Miro1-mutant iPSC-derived Neurons reveal novel functions of Miro1 in mitochondrial respiration and dopamine handling

Dissertation
der Mathematisch-Naturwissenschaftlichen Fakultät
der Eberhard Karls Universität Tübingen
zur Erlangung des Grades eines
Doktors der Naturwissenschaften
(Dr. rer. nat.)

vorgelegt von
M. Sc. Lisa Schwarz
aus Pforzheim

Tübingen
2022

Gedruckt mit Genehmigung der Mathematisch-Naturwissenschaftlichen Fakultät der Eberhard Karls Universität Tübingen.

Tag der mündlichen Qualifikation: 21.12.2022
Dekan: Prof. Dr. Thilo Stehle
1. Berichterstatterin: Dr. Julia Fitzgerald
2. Berichterstatter: Prof. Dr. Boris Macek
3. Berichterstatterin: Prof. Dr. Yifat Merbl

Preface

This dissertation introduces three novel Miro1-mutant iPSC lines with following assessment of the phenotypic outcomes of each mutation in differentiated dopaminergic neurons to gain insight into Miro1 functions relevant for Parkinson's disease. The study was conducted from June 2018 until July 2022 under the supervision of Dr. Julia Fitzgerald in the Department of Neurodegenerative Diseases at the Hertie Institute for Clinical Brain Research, University of Tübingen. Prof. Dr. Boris Macek of the Interfaculty Institute for Cell Biology of the University of Tübingen and Prof. Dr. Yifat Merbl of the Department of Immunology at the Weizmann Institute of Science (Rehovot, Israel) were members of the doctoral committee. The project was part of the DFG-funded research training group "The multifaceted functions and dynamics of the mitochondrial outer membrane" (RTG2364) hosted by the University of Tübingen.

Acknowledgements

First, I would like to thank my supervisor Dr. Julia Fitzgerald for the opportunity to work on this challenging and interesting project. Thank you for the trust you put in me when you chose me as your PhD student. Thank you for always believing in me and supporting me, for your advice and guidance which helped me overcome difficulties and thrive into the scientist I am today. Your passion and persistence are remarkable and inspiring for everyone around you.

Furthermore, I would like to acknowledge Prof. Dr. Boris Macek and Prof. Dr. Yifat Merbl for being on my thesis committee. Thank you for your helpful advice and support throughout the years. I highly valued your expert input and the point of view you provided. I also would like to thank Prof. Dr. Tassula Proikaz-Cezanne to be my examiner, I always appreciated your scientific input during the bi-weekly seminars.

A huge thanks goes to the laboratory staff and the students who worked with us. I especially want to thank Maria Zarani for teaching me how to culture iPSCs and for her help not only with cell culture, but everything else as well. Special thanks go to Lara-Sophie Rieder and Lorenzo Davide Dodi for their work on my project and being incredible students. I also want to thank Orchid Ammar, Karan Sharma and especially Felix Knab for their help and support. It was a tremendous pleasure to have worked with all of you.

Additionally, I want to thank all MOMbrane students for being such a supportive and great group. You guys are incredible, and I am deeply grateful to have had you as peers. I especially want to thank Anna Lechado not only for her scientific input but also being a good listener.

My gratitude further goes to everyone who helped me advance my research. I want to thank Dr. Javier Jarazo and Dr. Zoé Hanss as well as Dr. Joachim Täger and Katleen Wild for their help with the CRISPR strategy and the subsequent gene-edit, respectively. I also want to thank Dr. Nicolas Casadei not only for his contribution during my PhD but also for his support before that.

Außerdem möchte ich meine tiefempfundene Dankbarkeit für meine Freunde ausdrücken, die mir immer zur Seite stehen, mir durch schwierige Zeiten halfen und die guten Zeiten so viel besser machen. Besonders dankbar bin ich für Alina und Lisa in meinem Leben, für ihre bedingungslose Unterstützung und ihren steten Zuspruch, vor allem während des letzten Jahres.

Nicht zuletzt möchte ich meiner Familie danken. Ich möchte den Eltern meines Partners danken dafür, dass sie immer an mich geglaubt haben und mich ermutigt haben. Vor allem aber möchte ich meinen Eltern danken für die unendliche Unterstützung, die bedingungslose Liebe und die konstante Ermutigung mein Leben lang. Ihr habt mich zu der Person gemacht, die ich heute bin. Mein Dank gilt auch meinen Geschwistern, für ihren steten Beistand und lebenslange Unterstützung. Da das Wichtigste immer zum Schluss kommt, möchte ich hier meinem Partner Marius danken, für die Sicherheit und die Ruhe, die du mir gibst, für die immerwährende Unterstützung und Ermutigung.

Table of Contents

1. Abbreviations

7-AAD	7- Aminoactinomycin D
ADP	Adenosine diphosphate
ATP	Adenosine triphosphate
ATP1A2	ATPase Na+/K+ transporting subunit alpha 2
ATP5A	ATP synthase subunit alpha, mitochondrial
CCCP	(3-Chlorophenyl)hydrazonomalononitrile
cEF-hand	C-terminal EF-hand domain (Miro1)
cGTPase	C-terminal GTPase domain (Miro1)
CHCHD2	Coiled-coil-helix-coiled-coil-Helix domain-containing protein 2
CHCHD10	Coiled-coil-helix-coiled-coil-Helix domain-containing protein 10
CNS	Central nervous system
CNV	Copy number variation
CRISPR	Clustered regularly interspaced short palindromic repeats
CTF	Corrected total fluorescence
D. melanogaster	Drosophila melanogaster
DA	Dopamine
DAT	Dopamine transporter
DJ1	Protein/nucleic acid deglycase DJ1
DMEM/F12	Dulbecco's modified eagle medium/Nutrient mixture F12
DMSO	Dimethyl sulfoxide
dMiro	Drosophila Miro
DNA	Deoxyribonucleic acid
Dnm1	Dynamin-1-like protein
DRD2	Dopamine receptor D2
Drp1	Density-regulated protein 1
EMRE	Essential MCU regulator
ER	Endoplasmic Reticulum
ERMES	ER-mitochondria encounter structure
FoxA2	Forkhead box protein A2
gRNA	guide RNA
GRP75	75 kDa glucose-regulated protein
GTP	Guanosine-5'-triphosphate
hDaNs	Human dopaminergic neurons
HIV	Human immunodeficiency virus
huES	Human embryonic stem cells
IP3R	Inositol triphosphate receptor
iPSC	induced pluripotent stem cell
k.o.	knock out

Klf4	Krüppel-like factor 4
LC3	Microtubule-associated protein 1A/1B-light chain 3
L-DOPA	Levodopa or l-3,4-dihydroxyphenylalanine
LRRK2	Leucine rich repeat kinase 2
Lys	Lysine
MAO-A/-B	Monoamine oxidase A/B
MAP2	Microtubule-associated protein 2
MCU	Mitochondrial calcium uniporter
MCUb	Mitochondrial calcium uniporter regulatory subunit MCUb
MCUR	MCU regulator
MDC	Mitochondrial-derived compartments
MDV	Mitochondrial-derived vesicles
MERCs	Mitochondria-ER contact
MFN	Mitofusin
Mic10	MICOS complex subunit MIC10
Mic60	MICOS complex subunit MIC60
MICOS	Mitochondrial contact site and cristae organizing system
MICU 1/2/3	Mitochondrial calcium uptake protein 1/2/3
MIM	Mitochondrial inner membrane
Miro	Mitochondrial Rho GTPase
MOM	Mitochondrial outer membrane
MQC	Mitochondrial quality control
mRNA	messenger RNA
MTCO1	Mitochondrially encoded cytochrome C Oxidase I
mtDNA	Mitochondrial DNA
MUL1	Mitochondrial ubiquitin ligase activator of NFKB 1
Myo19	Myosin XIX
NanoG	Nanog Homeobox
nEF-hand	N-terminal EF-hand domain (Miro1)
NET	Norepinephrine transporter
nGTPase	N-terminal GTPase domain (Miro1)
NPCs	Neural precursor cells
NDUFB8	NADH:Ubiquinone Oxidoreductase Subunit B8
Oct4	Octamer-binding transcription factor 4
Opa1	Optic atrophy protein 1
OPTN	Optineurin
OXPHOS	Oxidative phosphorylation
p62	Sequestosome-1
PARK2	Parkinson protein 2 (Parkin)
PAX6	Paired-box protein 6

PD	Parkinson’s disease
PBS	Phosphate buffered saline
PEX19	Peroxisomal biogenesis factor 19
PFA	Paraformaldehyde
PINK1	PTEN-induced kinase 1
pSer	phopho-Serine
PVDF	Polyvinylidene fluoride
RHOT1	Ras homolog family member T1
RNA	Ribonucleic acid
RT-qPCR	Quantitative reverse transcription polymerase chain reaction
S. cerevisiae	Saccharomyces cerevisiae
SDHB	Succinate Dehydrogenase Subunit B
Ser	Serine
SERT	Serotonine transporter
SH-SY5Y	Human Neuroblastoma cell line
siRNA	small-interfering RNA
SMA	Smooth muscle actin
SNCA	Synuclein alpha
SNpc	Substantia nigra pars compacta
Sox2	SRY-box 2
SSEA4	Stage-specific embryonic antigen-4
SYT2	Synaptotagmin 2
TCA	Tricarboxylic acid cycle
TH	Tyrosine hydroxylase
Thr	Threonine
TMD	Transmebrane domain
TMRM	Tetramethylrhodamine methyl ester perchlorate
Tom20	Translocase of outer membrane 20 kDa subunit
TOMM70	Translocase Of Outer Mitochondrial Membrane 70
Tra1-81	Epitope on Podocalyxin-like Protein 1
TRAK	Trafficking kinesin-binding protein
UQCRC2	Ubichinol-Cytochrome C Reductase Core Protein 2
VDAC	Voltage-dependent anion channels
VPS13D	Vacuolar protein sorting-associated protein 13D

2. Abstract

The mitochondrial outer membrane protein Miro1 is essential for neuronal development and maintenance, and recent research indicates that Miro1 might further be implicated in Parkinson's disease relevant neurodegenerative pathways. Miro1 is targeted by and interacts with several proteins connected to familial Parkinson's disease, such as PINK1 and Parkin (Hsieh et al. 2016; Kazlauskaite et al. 2014; Klosowiak et al. 2016; Shaltouki et al. 2018; Wang and Schwarz 2009; Weihofen et al. 2009). Additionally, rare variants in the encoding gene *RHOT1* were identified in sporadic Parkinson's disease patients (Berenguer-Escuder et al. 2019; Grossmann et al. 2019).

To better understand Miro1 involvement in Parkinson's disease relevant pathways, I gene-edited three Miro1 mutations into previously established, healthy human induced pluripotent stem cells (Marrone et al. 2018): heterozygous R272Q [sporadic Parkinson's disease (Grossmann et al. 2019)], homozygous S156A [preventing PINK1 phosphorylation (Wang et al. 2011)], and heterozygous K572R [preventing pSer65 Parkin ubiquitination (Kazlauskaite et al. 2014; Klosowiak et al. 2016)]. To investigate these mutations in a disease-relevant model, I differentiated neural precursor cell intermediates derived from the gene-edited stem cells into mid-brain specific dopaminergic neurons.

Analysis of the putative PINK1 phosphorylation site Ser156 (Wang et al. 2011) in neurons reveals that Miro1 S156A causes a reduction of Miro1 protein levels without affecting gene expression but impairing its degradation upon mitochondrial depolarization. This is accompanied by loss of mitochondrial membrane potential resulting in reduced mitochondrial respiration. These findings revealed a correlation between Miro1 and the level of respiratory chain complexes in differentiated, post-mitotic cells.

Miro1 R272Q found in a sporadic patient (Grossmann et al. 2019) shares the reduction of mitochondrial respiration, but links to mitochondrial calcium instead of membrane potential. Additionally, mitochondria are more fragmented and show partial loss of cristae structure. The data point towards Miro1 R272Q disrupting the interaction of Miro1 with the mitochondrial calcium uniporter to modulate mitochondrial calcium uptake thus altering cytosolic calcium handling. Consequently, decreased

neurotransmitter uptake and monoamine oxidase activity alter dopamine handling in neurons.

Inhibition of Parkin-mediated ubiquitination of Miro1 (Kazlauskaite et al. 2014; Klosowiak et al. 2016) in K572R neurons results in enlarged and fragmented mitochondria. This is concomitant with reduced membrane potential and increased turnover while Miro1 degradation and mitophagy are unaffected.

Taken together, these novel isogenic Miro1 models shed light on domain-specific functions of Miro1. Miro1 S156A highlights the relationship between Miro1 protein levels and oxidative phosphorylation in different cell types and specific vulnerability of post-mitotic neurons. In contrast, a putative mechanism in neurons for the disease-associated Miro1 mutation R272Q involves mitochondrial calcium handling linking to dopamine homeostasis. The gene-edited stem cells generated in this study serve as powerful platform to investigate Miro1 function in any cell type and the research with differentiated neurons provides new insight into Miro1 function in Parkinson’s disease relevant pathways.

3. Zusammenfassung

Das äußere mitochondriale Membranprotein Miro1 ist von zentraler Bedeutung für die Entwicklung von Neuronen und deren Erhalt. Zudem deutet jüngere Forschung darauf hin, dass Miro1 in für Morbus Parkinson relevanten neurodegenerativen Signalwegen eine Rolle spielen könnte. Miro1 ist Ziel von und interagiert mit einigen Proteinen, wie PINK1 und Parkin, die mit dem familiärem Parkinson-Syndrom assoziiert sind (Hsieh et al. 2016; Kazlauskaite et al. 2014; Klosowiak et al. 2016; Shaltouki et al. 2018; Wang and Schwarz 2009; Weihofen et al. 2009). Außerdem wurden Genvarianten in dem Miro1-codierendem Gen *RHOT1* in Patienten mit idiopathischem Parkinson-Syndrom identifiziert (Berenguer-Escuder et al. 2019; Grossmann et al. 2019).

Um die Beteiligung von Miro1 in für das Parkinson-Syndrom relevanten Signalwegen zu untersuchen, habe ich drei Miro1 Mutationen in zuvor etablierte, gesunde humane induzierte pluripotente Stammzellen (Marrone et al. 2018) eingeführt: heterozygote R272Q [idiopathisches Parkinson-Syndrom (Grossmann et al. 2019)], homozygote S156A [Verhinderung PINK1 Phosphorylierung (Wang et al. 2011)], und heterozygote K572R [Verhinderung pSer65 Parkin Ubiquitinierung (Kazlauskaite et al. 2014; Klosowiak et al. 2016)]. Um diese Mutationen in einem für die Erkrankung bedeutsamen Modell zu untersuchen, habe ich aus den geneditierten Stammzellen gewonnene neurale Vorläuferzellen in mittelhirnspezifische dopaminerge Neurone ausdifferenziert.

Die Analyse der möglichen PINK1 Phosphorylierungsstelle Ser156 (Wang et al. 2011) in Neuronen zeigt, dass Miro1 S156A eine Reduktion von Miro1 Proteinlevels bewirkt, ohne Veränderung der Genexpression. Zudem ist der Abbau von Miro1 nach mitochondrialer Depolarisation gestört. Dies wird von einem Verlust des mitochondrialen Membranpotentials begleitet, was eine Verminderung der mitochondrialen Atmung bewirkt. Diese Ergebnisse enthüllen eine Korrelation zwischen Miro1 und dem Level and Atmungskettenkomplexen in differenzierten, postmitotischen Zellen.

Miro1 R272Q, welches in einem Patienten mit idiopathischem Parkinson-Syndrom gefunden wurde (Grossmann et al. 2019) teilt den Phänotyp der reduzierten oxidativen Phosphorylierung, jedoch ist dies mit mitochondrialem Calcium verbunden anstelle des Membranpotentials. Zudem sind die Mitochondrien fragmentierter und zeigen einen teilweisen Verlust der Cristae. Die Daten deuten darauf hin, dass Miro1 R272Q die

Interaktion zwischen Miro1 und dem mitochondrialen Calciumuniporter zur Modulation der mitochondrialen Calciumaufnahme stört, was den Umgang mit zytosolischem Calcium verändert. In der Konsequenz führen eine Reduktion der Neurotransmitteraufnahme und Monoaminoxidaseaktivität zu einer Veränderung der Dopaminhandhabe in Neuronen.

Die Verhinderung der parkinvermittelten Ubiquitinierung von Miro1 (Kazlauskaite et al. 2014; Klosowiak et al. 2016) in K572R Neuronen resultiert in vergrößerten und fragmentierten Mitochondrien. Zudem ist das mitochondriale Membranpotential reduziert und der Umsatz von Mitochondrien erhöht, allerdings ist der Abbau von Miro1 sowie Mitophagie nicht verändert.

Zusammengefasst liefern diese neuen isogenen Miro1 Modelle neue Erkenntnisse über domänenspezifische Funktionen von Miro1. Miro1 S156A verdeutlicht die Beziehung zwischen Miro1 Proteinlevels und oxidativer Phosphorylierung in unterschiedlichen Zelltypen und die spezifische Vulnerabilität von postmitotischen Neuronen. Im Gegensatz dazu involviert ein möglicher Mechanismus für die krankheitsassoziierte Miro1 Mutation R272Q mitochondrialen Calciumumgang im Zusammenhang mit Dopaminhomöostase. Die geneditierten Stammzellen, die in dieser Studie generiert wurden, stellen eine bedeutende Plattform dar, um die Funktion von Miro1 in jedem Zelltyp zu untersuchen. Die Forschung mit differenzierten Neuronen zeigt neue Einblicke in die Rolle von Miro1 in für Morbus Parkinson relevanten Signalwegen.

4. List of Publications

Manuscript 1:

Generation of R272Q, S156A and K572R RHOT1/Miro1 mutations in iPSCs from a healthy individual using FACS-assisted CRISPR/Cas9 genome editing

Lisa Schwarz, Nicolas Casadei and Julia C. Fitzgerald

Stem Cell Res 55: 102469; doi: 10.1016/j.scr.2021.102469; PMID: 34359002

Manuscript 2:

Steady-state levels of Miro1 Linked to Phosphorylation at Serine 156 and Mitochondrial Respiration in Dopaminergic Neurons

Lisa Schwarz and Julia C. Fitzgerald

Cells 11(8); doi: 10.3390/cells11081269; PMID: 35455950

Manuscript 3:

Miro1 R272Q Disrupts Mitochondrial Calcium Handling and Neurotransmitter Uptake in Dopaminergic Neurons

Lisa Schwarz, Lorenzo D. Dodi, Lara-Sophie Rieder, Petra Fallier-Becker, Nicolas Casadei and Julia C. Fitzgerald

Submitted in Frontiers in Molecular Neuroscience June 10th, 2022

This thesis describes and discusses the results of the manuscript under revision (revision stage as of August 24th, 2022).

Manuscript 3 was accepted November 11th, 2022, and published December 2nd, 2022

5. Personal Contribution

Manuscript 1: Generation of R272Q, S156A and K572R RHOT1/Miro1 mutations in iPSCs from a healthy individual using FACS-assisted CRISPR/Cas9 genome editing

I designed and generated the CRISPR/Cas9 constructs for gene editing the iPSCs which included cloning and sequencing of the plasmids. I further performed the gene editing of the iPSCs, including selection of clones, processing of clones, sequencing and performing off-target analysis as well as characterization of the finalized iPSC lines. Except for the exome sequencing, I performed all experiments for the paper. I wrote the first draft of the manuscript and designed the figure.

Manuscript 2: Steady-state levels of Miro1 Linked to Phosphorylation at Serine 156 and Mitochondrial Respiration in Dopaminergic Neurons

Using the gene-edited iPSCs, I generated NPCs for differentiation of hDaNs with characterization of both NPCs and hDaNs. Except for the differentiation of SH-SH5Y neuroblastoma cells and subsequent *RHOT1* knock-down, I performed all experiments and was involved in designing them. I analyzed and interpreted the data generated for first submission. Further, I wrote the first draft of the manuscript and designed all figures.

In summary, I did methodology, formal analysis, investigation, data curation, original draft writing, visualization and contributed to validation.

Manuscript 3: Miro1 R272Q Disrupts Mitochondrial Calcium Handling and Neurotransmitter Uptake in Dopaminergic Neurons

Using the gene-edited iPSCs, I generated NPCs for differentiation of hDaNs with characterization of both NPCs and hDaNs. Except for mitochondrial movement, calcium imaging, electron microscopy and transcriptomics, I performed all experiments and was involved in designing them. For the experiments I did, I analyzed and interpreted the data. I was involved in the writing of the original draft as well as contributing to reviewing and editing of the manuscript before submission. I further designed all figures.

In summary, I was involved in methodology, validation, formal analysis investigation, data curation, writing the original draft and reviewing and editing it as well as visualization.

6. Introduction

6.1. Mitochondrial GTPase Miro1

6.1.1. Human Miro proteins

Human Miro1 and Miro2 (encoded by *RHOT1* and *RHOT2*, respectively) were identified by searching for unknown Rho-GTPases after the human genome project facilitated the discovery of novel genes (Fransson, Ruusala, and Aspenstrom 2003); following ontogenetic analysis revealed that Miro proteins form a distinct Ras-like family (Boureux et al. 2007). They are highly conserved across species with orthologues found in *S. cerevisiae* (Gem1) and *D. melanogaster* (dMiro), and ubiquitously expressed (Fransson, Ruusala, and Aspenstrom 2003).

Notably, human Miro1 and Miro2 are not redundant (Lopez-Domenech et al. 2018; Lopez-Domenech et al. 2016) and involved in distinct pathways (Kay et al. 2019) highlighted by the lethality of Miro1 k.o. while Miro2 k.o. is viable (Lopez-Domenech et al. 2016; Nguyen et al. 2014).

6.1.2. Structure of (mammalian) Miro proteins

Human Miro1 and Miro2 are both 618 amino acids in length with a mass of 70 kDa sharing 60% sequence homology (Fransson, Ruusala, and Aspenstrom 2003). They possess two GTPase domains (nGTPase aa1-170, cGTPase aa411-580) surrounding two central EF-hand domains (nEF-hand aa180-275, cEF-hand aa411-580) with a C-terminal transmembrane domain [TMD aa592-618, Figure 1, (Frederick et al. 2004; Fransson, Ruusala, and Aspenstrom 2006; Klosowiak et al. 2016)]. Mammals have four isoforms of Miro1: isoforms 2, 3 and 4 harbour insertion 1 (32 aa), insertion 2 (41 aa) or both, respectively, located between the cGTPase domain and TMD (Okumoto et al. 2018).

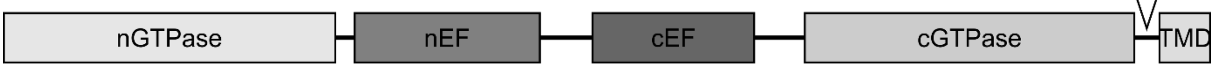

Figure 1: Structure of Miro proteins. N-terminal GTPase domain (nGTPase), followed by two EF-hand domains (nEF-hand and cEF-hand), a second GTPase (cGTPase) and a C-terminal transmembrane domain (TMD). Splice variants have insertions upstream of the TMD (Klosowiak et al. 2016; Okumoto et al. 2018).

The nGTPase is related to Rho GTPases (Fransson, Ruusala, and Aspenstrom 2003), coordinates magnesium (Smith et al. 2020) and shows differences in key catalytic residues compared to Ras GTPases (Peters et al. 2018; Smith et al. 2020). Human Miro proteins show EF-hand-dependent hydrolysis of GTP by the nGTPase domain (Peters et al. 2018), which has conformational freedom, possibly contributing to association with binding partners (Smith et al. 2020). The cGTPase resembles Ras GTPase structures (Klosowiak et al. 2013) with only 22% identity to the nGTPase domain (Smith et al. 2020). The cGTPase domain exhibits hydrolyzing activity for both GTP and ATP independent of calcium-binding (Peters et al. 2018), and forms a previously unreported interface with the cEF-hand domain (Klosowiak et al. 2013).

Each EF-hand domain consists of a canonical EF-hand sequence stabilized by a hidden helix-loop-helix motif and a ligand-mimicking domain; both EF-hand domains are linked to allow side-by-side orientation (Klosowiak et al. 2013). While both EF-hand domains have one calcium-binding site (Klosowiak et al. 2016), binding of calcium or magnesium was only observed in the canonical sequence of the cEF-hand domain of dMiro (Klosowiak et al. 2013).

6.1.3. Domain functions of mammalian Miro1

Studies investigating Miro1 function indicate that GTPase domains confer activity regulated by EF-hand calcium binding. While it is difficult to distinguish functions of nEF- and cEF-hand domains, the distinct structure of each GTPase domain relates to their function.

The nGTPase contribution to roles of Miro1 is quite well understood and confers Miro1-mediated tethering to binding partners most likely aided by the conformational freedom of the domain (Smith et al. 2020). This is important in mitochondrial movement (MacAskill, Brickley, et al. 2009) and the formation of mitochondria-endoplasmic reticulum (ER) contacts [MERCs, (Guillen-Samander et al. 2021)], but also contributes to maintenance of the mitochondrial network in mitotic cells (Fransson, Ruusala, and Aspenstrom 2006). How the cGTPase domain contributes to these aspects of Miro1 function needs more research, but it might relay EF-hand regulation because it forms an interface with the cEF-hand domain (Klosowiak et al. 2013).

Since the EF-hand domains are structurally similar (Klosowiak et al. 2013), most studies do not differentiate between both. It is likely, that calcium-binding modulates Miro1 interaction with binding partners, regulating Miro1 function as well as how Miro1 acts on other proteins (Fatiga et al. 2021; Macaskill, Rinholm, et al. 2009; Nemani et al. 2018; Niescier et al. 2018; Safiulina et al. 2019; Saotome et al. 2008; Wang and Schwarz 2009). Miro1 functions as well as the respective contribution of each domain are described in the following sections in greater detail.

6.1.4. Localization of Miro proteins

Miro proteins mostly localize to mitochondria (Fransson, Ruusala, and Aspenstrom 2003; Fransson, Ruusala, and Aspenstrom 2006; MacAskill, Brickley, et al. 2009); they are tail-anchored in the mitochondrial outer membrane (MOM) with the functional domains exposed to the cytosol (Fransson, Ruusala, and Aspenstrom 2006; Frederick et al. 2004). At mitochondria, mammalian Miro proteins form clusters close to mitochondrial contact site and cristae organisation system (MICOS) structures and were shown to interact with themselves and each other (Modi et al. 2019).

While isoforms 1 and 3 of Miro1 localize to mitochondria, isoforms 2 and 4 are targeted to peroxisomes (Okumoto et al. 2018) by nGTPase-dependent interaction with PEX19 (Covill-Cooke et al. 2020; Castro et al. 2018; Okumoto et al. 2018).

6.1.5. Mitochondrial movement in mammalian cells

One of the main functions of Miro proteins is enabling mitochondrial movement along microtubules and actin filament (Lopez-Domenech et al. 2016; Lopez-Domenech et al. 2018; Oeding et al. 2018).

For initiating movement of mitochondria along microtubules, Miro1/2 recruit TRAK/1/2 (Fransson, Ruusala, and Aspenstrom 2006; Glater et al. 2006; MacAskill, Brickley, et al. 2009), coiled-coiled domain proteins associating with motor proteins and localizing to mitochondria (Beck et al. 2002; Brickley et al. 2005). In mammalian neurons, Miro1 directly binds kinesin which can be independent of TRAK1/2 (Macaskill, Rinholm, et al. 2009), but both Miro1/2 and TRAK1/2 are required for mitochondrial movement (van Spronsen et al. 2013). Movement directionality, but not speed and distance is conferred by motor proteins of the Kinesin1 and Dynein families (van Spronsen et al. 2013).

Mitochondria stop upon elevation of cytosolic calcium via calcium-sensing of Miro1 EF-hand domains (MacAskill, Brickley, et al. 2009; Saotome et al. 2008; Wang and Schwarz 2009) by either detachment of the complex from microtubules because Miro1 binds the N-terminal motor domain of Kinesin (Wang and Schwarz 2009), or dissociation of Miro-TRAK complex from Kinesin (Macaskill, Rinholm, et al. 2009). More recent studies indicate that mitochondrial matrix calcium uptake by the mitochondrial calcium uniporter (MCU) via interaction with Miro1, in contrast to elevated cytosolic levels of calcium, is the main determinant of mitochondrial stopping (Chang, Niescier, and Min 2011; Niescier et al. 2018).

6.1.6. Mitochondrial dynamics in mammalian cells

Mitochondrial dynamics describe the continuous adaptation of the tubular network to different conditions including nutrient availability and metabolic state [reviewed in (Tilokani et al. 2018)]. While the MOM is a signalling hub for mitochondria, the mitochondrial inner membrane (MIM) hosts oxidative phosphorylation (OXPHOS) complexes for ATP generation [reviewed in (Giacomello et al. 2020)].

Mitochondrial fission, fusion and ultrastructure

The most important proteins in mitochondrial dynamics are GTPases Drp1 and Dnm1 (fission) as well as Mitofusins and Opa1 [fusion outer and inner membrane, respectively; reviewed in (Tilokani et al. 2018; Yapa et al. 2021)]. Opa1 further aids in maintaining mitochondrial ultrastructure [reviewed in (Colina-Tenorio et al. 2020)].

MIM folding is directed by the MICOS [reviewed in (Anand, Reichert, and Kondadi 2021; Colina-Tenorio et al. 2020; Giacomello et al. 2020)], a highly conserved multiprotein complex located at crista junctions in contact with the MOM [reviewed in (Anand, Reichert, and Kondadi 2021)]. Subcomplexes Mic60 and Mic10 are core components [reviewed in (Colina-Tenorio et al. 2020; Mukherjee, Ghosh, and Meinecke 2021)] associating with other Mic subcomplexes; while yeast MICOS is well understood, human MICOS composition remains to be fully identified [reviewed in (Giacomello et al. 2020)]. The Mic60-subcomplex maintains cristae junctions and can assemble independent of mitochondrial contact to the ER, the Mic10-subcomplex promotes formation of lamella and requires MERCs for its assembly (Stephan et al. 2020; Tirrell et al. 2020). MICOS localize close to MERCs (Tirrell et al. 2020) and further require CHCHD10 and CHCHD2 for assembly [reviewed in (Mukherjee, Ghosh, and Meinecke 2021)].

Miro 1 and mitochondrial dynamics

Both mammalian Miro proteins interact with Mitofusins (Fatiga et al. 2021; Misko et al. 2010) and regulate their function (Fatiga et al. 2021). While Miro1 nGTPase domain is required for maintenance of the mitochondrial network (Fransson, Ruusala, and Aspenstrom 2003; Fransson, Ruusala, and Aspenstrom 2006; Modi et al. 2019; Saotome et al. 2008), EF-hand calcium sensing prevents mitochondrial fusion via Mitofusins upon elevation of mitochondrial matrix calcium (Fatiga et al. 2021; Saotome et al. 2008), and promotes mitochondrial fragmentation (Nemani et al. 2018; Saotome et al. 2008). Additionally, Miro1 interacts with components of the MICOS complex to contribute to maintenance of mitochondrial ultrastructure (Modi et al. 2019), which could further be supported by Miro1 interaction with Myo19 (Lopez-Domenech et al. 2018; Oeding et al. 2018) functioning as a tether for ultrastructure organization and interacting with MICOS (Shi et al. 2022).

6.1.7. Mitochondria-ER contacts

Mitochondria contact several cellular structures such as the plasma membrane, the endosomal/lysosomal system and peroxisomes, but also the ER [reviewed in (Giacomello et al. 2020)].

In yeast, the ER-mitochondria encounter structure (ERMES) is mediated by a distinct complex and functions in calcium and phospholipid exchange between both organelles (Kornmann et al. 2009). It was further hypothesized that ERMES contributes to mitochondrial protein import and genome replication as well as regulation of mitochondrial physiology [reviewed in (Kornmann and Walter 2010)].

In mammalian cells, MERCs are less well characterized, but studies revealed that contact between both organelles is mediated by several proteins including Mitofusins on both sides and mitochondrial VDAC contacting ER IP3R via GRP75 [(de Brito and Scorrano 2008), reviewed in (Csordas, Weaver, and Hajnoczky 2018; Giacomello et al. 2020)]. As mentioned above, MERCs are central for maintaining cristae structure, and they are further required for mitochondrial fission mediated by Drp1 [reviewed in (Giacomello et al. 2020; Tilokani et al. 2018)]. Yeast ERMES functions are conserved in mammalian MERCs and further include apoptosis, calcium homeostasis and lipid/phospholipid biosynthesis [reviewed in (De Mario et al. 2017; Giacomello et al. 2020)]. Mammalian MERCs additionally take part in autophagosome formation (Hamasaki et al. 2013).

The yeast orthologue Gem1 was identified as part of ERMES with both GTPase domains and the nEF-hand domain being required for tethering of the ER to mitochondrial membranes (Kornmann, Osman, and Walter 2011; Stroud et al. 2011). Like mediating mitochondrial movement, this function is conserved across species. In drosophila, dMiro is localized to MERCs via phosphorylation by Polo kinase (Lee et al. 2016) and in mammalian cells, both Miro proteins are required for MERCs (Modi et al. 2019). There, Miro1 helps tethering mitochondria to the ER by recruiting VPS13D to mitochondria (Guillen-Samander et al. 2021).

6.2. Significance of Miro1 in the brain

6.2.1. Neuronal mitochondrial bioenergetics

Significance of mitochondrial oxidative phosphorylation

Providing energy precisely at the sites where it is needed is one of the most important functions of mitochondria in neurons because maintenance of membrane potential relies on a myriad of pumps and exchangers requiring ATP [reviewed in (Devine and Kittler 2018; Llorente-Folch et al. 2015)]. While glycolysis is sufficient in cultured induced pluripotent stem cell (iPSC) -derived neural precursor cells (NPCs), glycolytic genes are downregulated during neuronal differentiation (Lins et al. 2022; Zheng et al. 2016) to favor OXPHOS as the main source of energy in neurons (Zheng et al. 2016); similarly, OXPHOS fuels neuronal activity in brain tissue (Hall et al. 2012). This highlights the necessity of proper mitochondrial localization throughout the neuron to locate mitochondria at active sites. Additionally, synaptic mitochondria adapt their morphology for scaling respiration (Perkins et al. 2010) which is essential for maintaining neurotransmission (Rangaraju, Calloway, and Ryan 2014).

Maintaining mitochondrial network in complex neuronal architecture

To replenish a synaptic pool of mitochondria, local biogenesis and renewal is one way to overcome the obstacle of complex neuronal architecture [reviewed in (Devine and Kittler 2018)]. In mature neurons, replication of mtDNA occurs mainly in perinuclear regions (David and Barrett 2000), but can also take place in axons (Amiri and Hollenbeck 2008). Synthesis of nuclear encoded proteins occurs both in the soma (Hevner and Wong-Riley 1991) and locally at synapses (Gioio et al. 2001). However, transport of mitochondria throughout neurons is still required. During neuronal development, mitochondria are transported along the axon depending on the growth behaviour to ensure supply of mitochondria to the growth cone (Morris and Hollenbeck 1993) and contribute to arborization by localizing at branching sites (Spillane et al. 2013). In mature neurons, localization of mitochondria further depends on local concentrations of ADP and calcium to facilitate recruitment to synapses (Macaskill, Rinholm, et al. 2009; Mironov 2007). Notably, most studies investigating Miro1 function in neurons utilized rat or mouse primary hippocampal neurons (Lopez-Domenech et al. 2018; Lopez-Domenech et al. 2016; Lopez-Domenech et al. 2021; MacAskill, Brickley, et al. 2009; Macaskill, Rinholm, et al. 2009; Modi et al. 2019; Niescier et al. 2018) or mouse cortical neurons (Nguyen et al. 2014); one study used mouse inhibitory interneurons (Kontou et al. 2021). Some research was conducted in iPSC-derived midbrain dopaminergic neurons (Berenguer-Escuder et al. 2020; Hsieh et al. 2016; Shaltouki et al. 2018). The importance of Miro1 functions for the brain is not restricted to execution of these functions in neurons, but also in astrocytes where positioning of mitochondria in processes contributes to astrocytic calcium handling which in turn is important for neuronal function (Stephen et al. 2015).

6.2.2. Miro1 in neuronal development and cell survival

Adequate distribution of mitochondria throughout the neuron depends on Miro1-mediated movement. This is essential for neuronal development and survival, highlighted by the lethality of Miro1 k.o. in mice while Miro2 k.o. mice are viable and fertile. Miro1 can compensate for loss of Miro2, but this is not reciprocated upon loss of Miro1, indicating that mammalian Miro proteins are not redundant. (Lopez-Domenech et al. 2016; Nguyen et al. 2014). Conditional loss of Miro1 in the central nervous system results in degeneration of upper motor neurons (Nguyen et al. 2014; Lopez-Domenech et al. 2016), suggesting that neurons with long processes are more susceptible to loss of Miro1-mediated mitochondrial distribution. This results in a severe impairment of mitochondrial trafficking which in turn is required for dendritic development and maintenance (Lopez-Domenech et al. 2016).

6.2.3. Calcium homeostasis in neurons

Calcium homeostasis is central for neuronal firing because it’s driven by calcium spikes [reviewed in (Devine and Kittler 2018)], regulated and buffered by mitochondrial calcium uptake (David and Barrett 2000; Tang and Zucker 1997), next to voltage-gated channels, ionotropic receptors and G-protein coupled receptors amongst others [reviewed in (Zampese and Surmeier 2020)]. Mitochondrial calcium uptake driven by the strong electrochemical gradient [reviewed in (Zampese and Surmeier 2020)] relies on the MCU (Baughman et al. 2011; Pan et al. 2013) which binds calcium with high affinity (Kirichok, Krapivinsky, and Clapham 2004) and is regulated by MICU1/2/3 [(Ashrafi et al. 2020; Mallilankaraman et al. 2012; Perocchi et al. 2010), reviewed in (Devine and Kittler 2018)]. Mitochondria localize to synapses in an activity-dependent and hence calcium-dependent manner mediated by Miro1 EF-hand domains

(Macaskill, Rinholm, et al. 2009) to clear cytosolic calcium during prolonged neuronal firing affecting synaptic plasticity and neuronal transmission (Vaccaro et al. 2017). Thus, availability and calcium buffering capacity of mitochondria directly affects neuronal activity [reviewed in (Devine and Kittler 2018)]. Notably, synaptic mitochondria have a lower capacity of buffering calcium than non-synaptic mitochondria (Brown, Sullivan, and Geddes 2006) which is why adequate mitochondrial calcium handling is particularly important in synapses. Additionally, restoration of baseline calcium levels depends on mitochondrial membrane potential [reviewed in (Devine and Kittler 2018)].

6.2.4. Miro1 in synaptic plasticity and neuronal calcium homeostasis

In synapses, calcium induces mitochondrial fragmentation and depolarization during neurotransmission which is distinct from depolarization-induced mitochondrial fragmentation (Brustovetsky, Li, and Brustovetsky 2009). Calcium-induced mitochondrial fragmentation is a mitochondrial quality control (MQC) mechanism mediated by Miro1 via calcium sensing of EF-hand domains (Nemani et al. 2018). Miro1 impacts mitochondrial calcium uptake by interacting with MCU: elevation of cytosolic calcium levels inhibits the interaction and results in cleavage of the MCU to facilitate mitochondrial calcium uptake (Niescier et al. 2018). While calcium influx into mitochondria is severely impaired in absence of the MCU (Baughman et al. 2011; Niescier et al. 2018), Miro1 also contributes to maintain homeostatic mitochondrial calcium handling affecting MCU activity depending on Miro1 EF-hand domains (Berenguer-Escuder et al. 2019; Chang, Niescier, and Min 2011; Lee et al. 2016; Safiulina et al. 2019). Adequate mitochondrial calcium buffering is not only important for restoring baseline cytosolic calcium levels, but also for the motility of mitochondria (Chang, Niescier, and Min 2011; Niescier et al. 2018). In fact, mitochondrial movement scales the strength of neuronal signals as well as release of synaptic vesicles (Sun et al. 2013). Synaptic localization of mitochondria increases the availability of synaptic vesicles enabling longer periods of stimulation (Sun et al. 2013; Verstreken et al. 2005). Apart from restoring excitability by clearing calcium, mitochondria further regulate neurotransmission by producing ATP, which determines recruitment of the reserve pool for synaptic vesicle release (Verstreken et al. 2005) and thus prolonged activity (Sun et al. 2013). In fact, a recent study showed that mitochondrial calcium uptake is required to fuel OXPHOS for maintenance of energy supply during neuronal activity (Ashrafi et al. 2020). Elevation of cytosolic calcium not only fuels OXPHOS, but further enhances ATP supply by activating pathways to increase efficiency [reviewed in (Llorente-Folch et al. 2015)].

6.2.5. Mitochondrial quality control mechanisms

There are several mitochondrial MQC mechanisms in place to cope with deterioration in mitochondrial fitness. An important aspect of MQC is the removal of damaged or dysfunctional mitochondria.

Mitophagy pathways

One of the main pathways for clearing defective organelles is macroautophagy, referred to as mitophagy when targeted to mitochondria [reviewed in (Ashrafi and Schwarz 2013; Barazzuol et al. 2020)]. Known mechanisms include receptor-mediated mitophagy, lipid-mediated mitophagy, ubiquitin-mediated mitophagy as well as the extensively studied PINK1/Parkin-pathway [reviewed in (Evans and Holzbaur 2020)]. In receptor-mediated autophagy, TMD-containing receptors integrate into the MOM to recruit the autophagic machinery (Hanna et al. 2012; Novak et al. 2010). Lipid-mediated mitophagy functions by translocation of the MIM lipid cardiolipin to the MOM and subsequent activation of autophagy [reviewed in (Evans and Holzbaur 2020)]. In ubiquitin-mediated mitophagy, Parkin (described below in PINK1/Parkin-mediated mitophagy) is substituted by other E3 ligases such as MUL1 (Li et al. 2008; Yun et al. 2014).

PINK1/Parkin-mediated mitophagy

PINK1/parkin-mediated mitophagy was extensively studied in mitotic cells (Narendra et al. 2008; Sterky et al. 2011; Van Laar et al. 2011; Vives-Bauza et al. 2010), but its occurrence in mature neurons was initially not observed (Van Laar et al. 2011). Following studies showed that in primary neurons, this pathway is slower and locally restricted (Ashrafi et al. 2014; Cai et al. 2012). However, due to the availability of other mitophagy pathways, loss of PINK1/Parkin-pathway can be compensated for *in vivo* [reviewed in (Evans and Holzbaur 2020)].

At polarized mitochondria, PINK1 is constantly turned over, but stabilized upon mitochondrial depolarization [reviewed in (Pickles, Vigie, and Youle 2018)], which also mediates mitochondrial stopping (Miller and Sheetz 2004). Stabilized PINK1 recruits

(Narendra et al. 2008; Vives-Bauza et al. 2010) and phosphorylates Parkin at Ser65 for activation of E3 ubiquitin ligase activity [reviewed in (Pickles, Vigie, and Youle 2018)]. Parkin ubiquitinates downstream targets mostly at the MOM, such as *MFN1/2*, *RHOT1/2*, *TOMM70* and *VDAC1/2/3* (Antico et al. 2021; Chan et al. 2011; Sarraf et al. 2013), but also proteins located in the matrix and MIM (Antico et al. 2021).

Parkin activity further depends on PINK1 phosphorylation of ubiquitin itself as a feed-forward mechanism (Kane et al. 2014; Koyano et al. 2014). Ubiquitination of mitochondrial proteins promotes autophagy (Geisler et al. 2010; Narendra et al. 2010; Narendra et al. 2008), but is preceded by removal of MOM proteins (Chan et al. 2011). The involvement of Miro1 in PINK1/Parkin mediated mitophagy is described in the next section 6.2.6.

Ubiquitinated MOM proteins activate p62 which triggers clustering of damaged mitochondria (Geisler et al. 2010; Lazarou et al. 2015; Narendra et al. 2010), and mitophagy receptors, such as OPTN, subsequently binding LC3 to prompt the formation of autophagosomes [(Lazarou et al. 2015), reviewed in (Stavoe and Holzbaur 2019)].

In neurons, autophagy occurs locally and autophagosomes travel to the cell body for lysosomal degradation [reviewed in (Kulkarni and Maday 2018)]. En route to the soma, autophagosomes mature in acquiring markers of late endosomes/lysosomes to be fully matured to autolysosomes in the cell body (Maday and Holzbaur 2014; Maday, Wallace, and Holzbaur 2012). In PINK1/Parkin-mediated mitophagy, mitochondria accumulate distally and are degraded via lysosomes in the soma (Ashrafi et al. 2014; Cai et al. 2012).

Mitochondrial-derived vesicles and compartments

Apart from mitophagy, other, less well understood MQC mechanisms include formation of mitochondrial-derived vesicles (MDVs) or mitochondrial-derived compartments (MDCs), two distinct mechanisms to degrade mitochondrial content [reviewed in (Giacomello et al. 2020)].

MDVs are organelle buds targeted to peroxisomes and lysosomes depending on their cargo [(Neuspiel et al. 2008), reviewed in (Sugiura et al. 2014)]. Mitochondria can form MDVs independent of depolarization and involvement of the autophagic machinery (Soubannier, McLelland, et al. 2012), thus they can even serve as substitute for LC3-

mediated mitophagy (Towers et al. 2021). Notably, PINK1 and Parkin contribute to formation of MDVs (McLelland et al. 2016), as does Miro1 (Konig et al. 2021).

MDCs were first described in yeast as a mechanism for removal of mitochondrial proteins and for coping with amino acid stress (Hughes et al. 2016; Schuler et al. 2021). Their formation is promoted by ERMES and Gem1 (English et al. 2020).

6.2.6. Miro1 in PINK1/Parkin-mediated mitophagy

Miro1 interacts with both PINK1 (Weihofen et al. 2009) and Parkin (Birsa et al. 2014; Lopez-Domenech et al. 2021; Safiulina et al. 2019; Shlevkov et al. 2016). Upon loss of mitochondrial membrane potential, it is targeted by both to arrest mitochondria resulting in untethering of Miro1 from kinesin (Wang et al. 2011) followed by its degradation (Birsa et al. 2014).

Miro1 possesses three putative PINK1 phosphorylation sites, Ser156, Thr298 and Thr299 and PINK1-mediated phosphorylation at Ser156 signals Miro1 degradation (Wang et al. 2011). These phosphorylation residues are highly conserved and contribute to dopaminergic neuron maintenance in *D. melanogaster* (Tsai et al. 2014). While some studies support the hypothesis that phosphorylation of Miro1 at Ser156 facilitates its degradation and mitophagy (Shlevkov et al. 2016; Wang et al. 2011), other studies were unable to replicate this (Birsa et al. 2014; Liu et al. 2012).

Miro1 harbours several Lysine residues targeted by pSer65 Parkin, of which Lys572 determines ubiquitination pattern (Kazlauskaite et al. 2014; Klosowiak et al. 2016). Additionally, Lys572 ubiquitination facilitates Parkin translocation to mitochondria and Miro1 ubiquitination (Safiulina et al. 2019). pSer65 Parkin ubiquitinates both Miro proteins independent of calcium- or nucleotide-binding, with ubiquitination of Miro1 occurring quicker (Klosowiak et al. 2016). Independent of PINK1 activation and Parkin recruitment, Miro proteins can recruit Parkin to mitochondria upon elevation of cytosolic calcium (Safiulina et al. 2019).

6.3. Miro1 relevance for Parkinson's disease (PD)

6.3.1. Parkinson's disease

PD is a complex, heterogenic neurodegenerative disorder mostly presenting with resting tremor, rigidity, bradykinesia, and postural instability [reviewed in (Ammal Kaidery and Thomas 2018; Obeso et al. 2017)]. Non-motor symptoms can include olfactory dysfunction, depression, constipation, hyposmia, sleep disturbances and other symptoms arising from a diseased autonomic nervous system [reviewed in (Obeso et al. 2017)].

The main pathological characteristic of PD are Lewy bodies and Lewy neurites which mainly consist of aggregated α-synuclein [reviewed in (Ammal Kaidery and Thomas 2018; Antony et al. 2013)]. Motor symptoms mostly arise from the progressive loss of dopaminergic neurons in the substantia nigra pars compacta [SNpc, reviewed in (Zampese and Surmeier 2020)], which, as a part of the basal ganglia, contributes to control of movements [reviewed in (Fazl and Fleisher 2018)]. However, the degeneration also affects other dopaminergic systems (e.g. the olfactory system) as well as brain regions relying on other neurotransmitters [reviewed in (Antony et al. 2013)].

A current challenge of both diagnosing and treating PD is the classification of patients into subsets [reviewed in (Obeso et al. 2017; Mestre et al. 2021)] to improve both. PD is uncurable, treatment strategies merely aim to slow down progression of the disease and alleviate symptoms by increasing dopamine (DA) content (e.g. levodopa) and/or using deep brain stimulation to compensate for loss of SNpc input into the striatum [reviewed in (Balestrino and Schapira 2019)].

The main risk factors for PD are age, environmental factors, and genetics. Several known variants of different genes increase the risk for developing PD and may be associated with other diseases [reviewed in (Day and Mullin 2021)]. Most PD cases occur sporadic, but 5-10% are due to monogenetic mutations. Common causes for monogenetic PD include *SNCA* (autosomal dominant, encoding α-synuclein), *LRRK2* (autosomal dominant, encoding LRRK2), *PINK1* (autosomal recessive, encoding PINK1), *PARK2* (autosomal recessive, encoding Parkin), *ATP13A2* (autosomal recessive, ATPase 13A2) and *PARK7* [autosomal recessive, encoding DJ1; reviewed in (Ammal Kaidery and Thomas 2018; Antony et al. 2013; Balestrino and Schapira 2019)].

6.3.2. PD heterogeneity highlighted by genetic forms

The complexity of PD is highlighted by its heterogeneity: age of onset of motor symptoms, clinical presentation, progression of symptoms, genetic background as well as responsiveness to treatments differ greatly between patients, both sporadic and genetic. Despite the differences between sporadic and genetic PD, assessing the clinical phenotypes of monogenetic forms helps to group patients into subtypes. Notably, while there are rare monogenetic forms of PD, where a single mutation is sufficient to cause the disease, genetic contribution includes uncommon and common variants increasing the risk for developing PD [reviewed in (Day and Mullin 2021)].

Mutations in PINK1 (Valente Enza et al. 2004), Parkin (Kitada et al. 1998) and DJ1 (Bonifati et al. 2003; van Duijn et al. 2001) cause early-onset PD, mutations in LRRK2 (Wszolek et al. 1995; Zimprich et al. 2004) cause late onset PD, mutations in α-synuclein (Polymeropoulos et al. 1997) cause PD with heterogenous age of onset. Early onset PD caused by mutations in PINK1, Parkin or DJ1 present with slowly progressive mild motor symptoms and good responsiveness to levodopa [(Ishikawa and Tsuji 1996; Rogaeva et al. 2004; van Duijn et al. 2001), reviewed in (Day and Mullin 2021)]. The pathogenicity of these mutations has been studied extensively, but our understanding for the underlying mechanisms is far from complete. The implication of PINK1/Parkin in MQC has been described in 6.2.5. However, both proteins have additional functions, such as regulation of OXPHOS component translation (Gehrke et al. 2015) and maintenance of mitochondrial function (Chung et al. 2016), putatively contributing to their pathogenicity. DJ1 also functions in MQC by sensing oxidative stress and reducing it (Inden et al. 2011; Taira et al. 2004; Tanti and Goswami 2014). DJ1 further acts similarly to PINK1/Parkin, though it cannot compensate for loss of PINK1 (Thomas et al. 2011). The function of LRRK2 is poorly understood, but research points towards a role in mitochondrial homeostasis and mitophagy [reviewed in (Rosenbusch and Kortholt 2016)]. Notably, the here discussed genes, *PINK1*, *PARK2*, *PARK7* and *LRRK2* have distinct functions, but seem to converge on MQC and mitochondrial degradation. As discussed in 6.2.5, loss of PINK1/Parkin mediated mitophagy can be compensated for *in vivo* [reviewed in (Evans and Holzbaur 2020)], indicating that there is a certain level of redundancy and flexibility. However, several genes mutated in genetic PD highlight the significance of mitochondrial integrity for SNpc neurons. Mitochondrial aspects of PD are further discussed in 6.3.4.

6.3.3. Specific susceptibility of SNpc neurons

PD is linked to mitochondria by environmental toxins causing PD due to mitochondrial dysfunction and by genes encoding proteins with mitochondrial functions (see previous section 6.3.2). Despite having gained significant insight in PD-associated mitochondrial pathways there is a gap of knowledge explaining why dysfunction of these pathways almost exclusively affects SNpc dopaminergic neurons.

Assessing PD-related neuronal degeneration in the midbrain revealed specific loss of neuromelanin-containing SNpc neurons, but not adjacent areas (Hirsch, Graybiel, and Agid 1988). The vulnerability of these neurons to mitochondrial dysfunction can be partially explained by their extensive arborization and number of synapses arising from unmyelinated axons [(Gauthier et al. 1999; Matsuda et al. 2009; Pacelli et al. 2015), reviewed in (Bolam and Pissadaki 2012)]. The burden of the sheer number of synapses is stressed by the fact, that the adjacent ventral tegmental area DA neurons are mostly spared in PD because they have by far less synapses [(Pacelli et al. 2015), reviewed in (Bolam and Pissadaki 2012)]. The architecture of SNpc neurons as well as their pace-making activity [reviewed in (Balestrino and Schapira 2019)] drastically increases energy demand concomitant the need for proper mitochondrial distribution. Additionally, the complexity of neuronal branching also increases energy costs and propagating signals requires both stimulation and calcium transients (Pissadaki and Bolam 2013). Interestingly, while SNpc neurons show increased mitochondrial density in axons (Pacelli et al. 2015), dendrites have significantly less mitochondria (Liang et al. 2007) due to oxidative stress induced by OXPHOS (Guzman et al. 2010). Synaptic activity-induced changes in cytosolic calcium burden SNpc neurons by fueling mitochondrial energy production [reviewed in (Zampese and Surmeier 2020)] resulting in increased OXPHOS activity of SNpc neurons (Pacelli et al. 2015).

6.3.4. Mitochondrial biology of PD

Investigation of PD-relevant pathways using different models stresses the significance of a functional mitochondrial network for SNpc neurons. Environmental toxins acting at mitochondria can induce PD [reviewed in (Grunewald, Kumar, and Sue 2019; Surmeier 2018)] and several genes mutated in familial PD encode for proteins linking to mitochondrial function [discussed in 6.3.2; reviewed in (Day and Mullin 2021; Exner et al. 2012)]. This is supported by findings in PD patients showing changes to components of the respiratory chain and mtDNA (Bender et al. 2006; Grunewald et al.

2016; Schapira et al. 1989). However, despite the knowledge about mitochondrial biology of PD it is not quite clear why these aspects specifically affect SNpc neurons resulting in their death. Because mitochondria are not only central to (SNpc) neurons, but also other cell types, mutations compromising different aspects of mitochondrial function result in a variety of clinical presentations with different severity [reviewed in (Yapa et al. 2021)]. Hence, whether mitochondrial dysfunction is cause or consequence of developing PD is controversial [reviewed in (Zampese and Surmeier 2020)]. An explanation for the contribution of mitochondria to driving pathogenesis of PD could include burdening of SNpc neurons by mitochondrial dysfunction, genetics and/or other risk factors resulting in pathogenic SNpc neurodegeneration (and α-synuclein accumulation) if a certain threshold is passed. Mitochondrial dysfunction can burden SNpc neurons by alterations in calcium homeostasis, energy production and mitochondrial quality control [reviewed in (Barazzuol et al. 2020)].

Calcium homeostasis

SNpc neurons are equipped with specific plasma membrane calcium channels to maintain a relatively high cytosolic calcium level driving mitochondrial OXPHOS, which greatly impacts synaptic output [reviewed in (Zampese and Surmeier 2020)]. Because higher cytosolic calcium in SNpc neurons increases mitochondrial stress, pharmacological reduction of cytosolic calcium decreases SNpc vulnerability and thus the risk for PD [reviewed in (Surmeier 2018)]. The delicate calcium homeostasis in these neurons is highlighted by PD genes: studies indicate that PINK1 and Parkin can affect mitochondrial calcium handling contributing to mitochondrial dysfunction [reviewed in (Barazzuol et al. 2020)]. Notably binding of calcium to α-synuclein promotes its aggregation and α-synuclein aggregates in turn can alter intracellular calcium signaling [reviewed in (Zampese and Surmeier 2020)].

Mitochondrial respiration

As previously discussed, mitochondrial respiration is particularly important in SNpc neurons to meet their high energetic demand (Pacelli et al. 2015; Pissadaki and Bolam 2013), but OXPHOS also produces oxidative stress which is further increased by DA metabolism [reviewed in (Surmeier 2018)]. Mitochondrial respiration is tied to PD by mitochondrial toxins [reviewed in (Grunewald, Kumar, and Sue 2019)], but this is still controversial because a genetic model for loss of complex I failed to induce degradation of dopaminergic neurons (Kim et al. 2015). However, a more recent study showed that deletion of a specific subunit of complex I replicated progressive, levodopa-responsive PD-like motor symptoms (Gonzalez-Rodriguez et al. 2021). These findings indicate that metabolic plasticity enables compensation for loss of OXPHOS (Gonzalez-Rodriguez et al. 2021; Kim et al. 2015) but results in decreased DA input into the striatum because SNpc neurons cannot meet their energetic demand without OXPHOS [(Gonzalez-Rodriguez et al. 2021; Pacelli et al. 2015), reviewed in (Bolam and Pissadaki 2012)].

Mitochondrial quality control

Because SNpc neurons rely heavily on mitochondria for energy supply and calcium buffering, tight MQC mechanisms are particularly important. This is highlighted (as discussed in 6.3.2) by the role of the PD proteins PINK1, Parkin, DJ1 and LRRK2 in mitophagy (see 6.2.5 and 6.3.2).

6.3.5. Miro1 in Parkinson's disease-relevant pathways

Miro1-mediated stopping of damaged mitochondria and subsequent degradation of these mitochondria as well as Miro1 is affected in PD (Hsieh et al. 2019; Hsieh et al. 2016; Liu et al. 2012; Shaltouki et al. 2018).

Apart from its involvement in PINK1/Parkin-mediated mitochondrial degradation, described in section 6.2.6, Miro1 also interacts with the two PD proteins LRRK2 and α-synuclein during mitophagy (Hsieh et al. 2016; Shaltouki et al. 2018). The importance of Miro1 removal from damaged mitochondria as well as its role in mitophagy is further highlighted by identifying Miro1 ubiquitination as necessary step for mitophagy (Lopez-Domenech et al. 2021) as well as a group of PD patients failing to degrade Miro1 from damaged mitochondria (Hsieh et al. 2019).

6.3.6. Rare Miro1 variants in sporadic Parkinson's disease

The involvement of Miro1 in PD-relevant pathways suggests that Miro1 dysfunction might contribute to the disease, but several studies failed to link Miro1 and PD genetically so far (Anvret et al. 2012; Nalls et al. 2019; Saeed 2018). However, recent studies identified Miro1 mutations in four sporadic PD patients: two female patients carried heterozygous mutations R272Q and R450C (Grossmann et al. 2019), respectively, and two male patients carried heterozygous mutations T351A and T610A (Berenguer-Escuder et al. 2019), respectively. R272Q is located in the ligand-mimicking domain of the nEF-hand domain, R450C is located near the middle of the cGTPase domain (Grossmann et al. 2019; Klosowiak et al. 2013; Klosowiak et al. 2016), T351A is located in the hidden helix-loop-helix motif of the cEF-hand domain and T610A is located in the transmembrane-domain (Berenguer-Escuder et al. 2019; Klosowiak et al. 2013; Klosowiak et al. 2016).

Patient-derived fibroblasts

Analysis of patient-derived fibroblasts compared to control fibroblasts matched in age and gender revealed commonalities in phenotypes in all four mutations. Similarities included altered calcium buffering concomitant with decreased contact sites between ER and mitochondria (Grossmann et al. 2019; Berenguer-Escuder et al. 2019). In T351A and T610A, Miro1 abundance at MERCS was decreased suggesting that this might contribute to reduced contact sites in these mutants (Berenguer-Escuder et al. 2019). R272Q and R450C mutations further exhibited significantly decreased mitochondrial mass and Miro1 protein levels, as well as increased mitochondrial turnover and clearance (Grossmann et al. 2019).

Dopaminergic neurons

Of the four fibroblast lines, Miro1 R272Q was successfully reprogrammed and differentiated into dopaminergic neurons (hDaNs). Phenotypic analysis highlights the differences in mitotic (fibroblasts) and post-mitotic cells (hDaNs), resulting in changes during differentiation (Berenguer-Escuder et al. 2020). While Miro1 R272Q fibroblasts showed a reduction in mitochondrial mass and Miro1 protein levels (Grossmann et al. 2019), this was not maintained in hDaNs (Berenguer-Escuder et al. 2020). The phenotype with decreased MERCs (Grossmann et al. 2019) was inverted in neurons, but hDaNs showed similar impairments in clearance of damaged mitochondria and impairment of calcium handling (Berenguer-Escuder et al. 2020; Grossmann et al. 2019).

7. Aims and Objectives

Miro1 is becoming increasingly important in PD research: (I) it interacts with PD proteins PINK1 and Parkin, (II) a recent study showed that Miro1 removal from mitochondria can be a determinant for classifying subsets of patients and (III) *RHOT1* variants were identified in sporadic PD. The overall aim of the study was to better understand the role of Miro1 in PD-relevant pathways to assess how (dys)function of Miro1 could contribute to the pathogenesis of PD. Using iPSC-derived dopaminergic neurons as a model, I aimed to dissect Miro1 function by introducing mutations in different domains of the protein.

The first goal was the introduction and characterization of four Miro1 mutations into a previously established iPSC line derived from a healthy donor: heterozygous Miro1 R272Q (found in a patient), heterozygous R450C (found in a patient), homozygous S156A (abolishes PINK1 phosphorylation site) and homozygous K572R (abolishes ubiquitination site).

The second goal was to use iPSC-derived Miro1-mutant dopaminergic neurons to investigate mutation-specific impact on mitochondrial functions including assessment of how the mutations affect known Miro1 roles such as mitochondrial movement, morphology, and degradation. I further aimed to investigate whether putative Miro1-mediated mitochondrial deficiencies might impact mitochondrial turnover, respiration, and calcium handling.

Because midbrain dopaminergic neurons rely heavily on proper distribution of mitochondria for energy supply as well as calcium buffering, the insights gained from this study will broaden our knowledge of Miro1 contribution to mitochondrial fitness and hence its role in PD-relevant mechanisms. A better understanding of these pathways allows us to use Miro1 functions for classification of patient subsets and for targeting of therapeutic advancements.

8. Results and Discussion

8.1. Manuscript 1: Generation of R272Q, S156A and K572R RHOT1/Miro1 mutations in iPSCs from a healthy individual using FACS-assisted CRISPR/Cas9 genome editing

Because of the increasing importance of Miro1 in PD-relevant pathways, we gene-edited three Miro1 mutations into previously established healthy iPSCs (Marrone et al. 2018): R272Q, one of the four mutations found in sporadic PD patients (Grossmann et al. 2019), S156A, which abolishes a PINK1 phosphorylation site (Wang et al. 2011), and K572R, which abolishes the main lysine targeted by pSer65 Parkin (Kazlauskaite et al. 2014; Klosowiak et al. 2016).

8.1.1. Introduction of R272Q, S156A and K572R mutations

For gene-editing, different strategies can be employed of which the CRISPR/Cas9 system is the most versatile (Ran et al. 2013). It comprises a Cas9 endonuclease which forms a complex with the CRISPR RNA containing a guide RNA (gRNA) sequence to mediate specificity (Jinek et al. 2012; Ran et al. 2013) with low tolerance for mismatches (Anderson et al. 2015; Ran et al. 2013). We used a novel CRISPR/Cas9 approach which relies on the transient insertion of removable selection markers. Using homology arms carrying the intended genomic alteration, a puromycin resistance and a fluorescent protein are inserted as selection markers at the Cas9-induced double-strand break and removed after selection of correctly edited clones using an excision-only PiggyBac transposase (Arias-Fuenzalida et al. 2017; Jarazo, Qing, and Schwamborn 2019). To increase gene-editing efficiency, we also introduced silent nucleotide changes to mutate the target sequence to prevent repetitive binding of the CRISPR machinery to the target sequence (Jarazo, Qing, and Schwamborn 2019).

Sanger sequencing of the gene-edited iPSCs shows successful introduction of heterozygous Miro1 R272Q, homozygous S156A and heterozygous K572R mutations (Manuscript 1 Figure 1A). We aimed for the heterozygous introduction of the Miro1 R272Q mutation because the PD patient also carries the mutation on one allele (Grossmann et al. 2019). For the same reason, we aimed to introduce Miro1 R450C heterozygous, but we failed to obtain clones carrying the mutation after exposing the iPSCs to the CRISPR/Cas9 machinery. Because the efficiency of a CRISPR/Cas9-mediated gene-edit depends on the distance between site of edit and induced double-strand break (Paquet et al. 2016), we think that the iPSCs failed to incorporate the mutation because the site of edit was too far away from the induced double-strand break. For the Miro1 S156A and K572R mutations, we aimed for a homozygous gene-edit to investigate the significance of these modification sites without residual wild-type Miro1 present. We were successful in obtaining homozygous Miro1 S156A, but not for Miro1 K572R where we obtained a heterozygous clone.

8.1.2. Validation of gene-edited Miro1-mutant iPSCs

Off-target analysis

To validate the gene-edit, we first analyzed potential off-target sites of the gRNAs used. Using online platforms Benchling (off-target score based on (Hsu et al. 2013)), Cas-OFF finder (Bae, Park, and Kim 2014) and CCTop (Stemmer et al. 2015), we identified putative off-target sites depending on the number of mismatches. Subsequent Sanger sequencing validated that all off-target sites analysed remained unchanged (Manuscript 1 Supplementary Figure A). Because we mutated the target region for the gRNA, diligent off-target analysis was particularly important. A study investigating the tolerance for mismatches found that two mismatches were hardly tolerated depending on their position within the gRNA (Anderson et al. 2015). The highest-ranking off-target sites in our analysis had two mismatches, and our results show that these mismatches were not tolerated.

To further validate absence of adverse effects of the gene-editing strategy, we showed the absence of random integration of the plasmid backbone (Manuscript 1 Supplementary Figure B) and successful removal of the fluorescent selection markers as well as normal morphology of the iPSC colonies (Manuscript 1 Supplementary Figure D).

Exome sequencing

Next, we assessed genomic integrity as well as genetic identity of the daughter iPSC lines compared to the maternal isogenic control. Using whole exome sequencing, we analysed variants with an allele frequency bigger than 30% as well as CNVs larger than 50 kb and found no differences between the Miro1-mutant iPSC lines and the isogenic control depicted in circos plots (Manuscript 1 Figure 1E). iPSCs have efficient and highly active DNA repair mechanisms, but like embryonic stem cells, they acquire mutations if cultured over an extended period of time (Laurent et al. 2011). Next to confirming that the iPSC lines are isogenic to each other and that the CRISPR/Cas9 strategy did not cause genomic alterations not picked up by the previous analyses, the exome sequencing further assesses acquisition of genomic changes due to extended cultivation.

In addition to the genetic tests, we validated the quality of the iPSCs by showing the absence of mycoplasma in the iPSC culture (Manuscript 1 Supplementary Figure C). Furthermore, the fibroblasts used to derive the isogenic control iPSCs were tested negative for infection with HIV, Hepatitis B and C (data available with the author) for higher safety when handling the cells.

8.1.3. Characterization and differentiation potential of Miro1 mutant iPSC lines

Next, we validated the maintenance of pluripotency after introducing the mutations by probing markers NanoG, Oct4 and Klf4 using RT-qPCR with RNA of human embryonic stem cells (huES) as reference sample and RNA from fibroblasts as negative control (Manuscript 1 Figure 1B). All four iPSC lines show strong expression levels of NanoG and Oct4, which are hardly expressed in fibroblasts; Klf4 expression is comparable in all iPSC lines and fibroblasts (Manuscript 1 Figure 1B), but Klf4 expression has previously been reported in fibroblasts (Takahashi et al. 2007). We further showed pluripotency by staining for markers Oct4, SSEA4 and Tra1-81, which is comparable between the maternal isogenic control and the derived Miro1 mutant iPSCs (Manuscript 1 Figure 1D). Additionally, we validated stemness by showing differentiation potential of the iPSCs to derive endodermal, mesodermal, and ecotdermal cells. Staining of induced germ layer formation shows comparable signals for FoxA2 (endoderm), SMA (mesoderm) and Nestin (ectoderm) in all four iPSC lines exhibiting similar cell morphologies in the respective germ layers (Manuscript 1 Figure 1D). Because iPSCs can acquire mutations in pluripotency as well as cell differentiation genes (Laurent et al. 2011), assessment of differentiation potential comprised an important validation factor after gene-editing.

8.1.4. Summary and conclusion

In summary, we generated three novel Miro1-mutant iPSC lines carrying Miro1 R272Q, Miro1 S156A and Miro1 K572R, respectively. Next to thorough analysis of putative adverse effects of the gene edit, we also validated the quality of the iPSCs as well as their differentiation potential. Our aim for introducing these mutations was to better understand PD-relevant disease mechanisms in differentiated dopaminergic neurons. But our models can also be used to assess PD mechanisms in other cell types such as astrocytes. Furthermore, Miro1 S156A and Miro1 K572R mutations can be used to investigate Miro1 function in any cell type which can be derived from iPSCs. This makes our iPSCs a powerful tool not only for PD research, but also for other research areas investigating Miro1.

8.2. Manuscript 2: Steady-state levels of Miro1 Linked to Phosphorylation at Serine 156 and Mitochondrial Respiration in Dopaminergic Neurons

Miro1 targeting by PINK1/Parkin during mitophagy (Wang et al. 2011) has become increasingly important since a subset of sporadic PD patients was found to retain Miro1 at depolarized mitochondria (Hsieh et al. 2019). In line with that, Miro1 removal from mitochondria was revealed as a required step for facilitation and execution of mitophagy (Lopez-Domenech et al. 2021). Miro1 has three putative PINK1 phosphorylation sites (Wang et al. 2011), of which Ser156 is most extensively studied (Birsa et al. 2014; Liu et al. 2012; Shlevkov et al. 2016; Wang et al. 2011).

However, whether pSer156 facilitates Miro1 degradation (Shlevkov et al. 2016; Wang et al. 2011) or not (Birsa et al. 2014; Liu et al. 2012) remains unclear. Furthermore, it has not been investigated whether phosphorylation at Ser156 has roles outside of mitophagy. To study this phosphorylation site in a PD-relevant model, we used previously established Miro1 S156A iPSCs to differentiate dopaminergic neurons. This study reveals that Miro1 S156A results in reduction of Miro1 protein levels which correlates with levels of OXPHOS complexes resulting in impaired mitochondrial respiration. The data indicate a novel link between Miro1 and OXPHOS which involves modification of the nGTPase domain of Miro1.

8.2.1. Miro1 S156A protein levels are reduced in dopaminergic neurons

For investigating the phenotypic outcome of Miro1 S156A, we first derived NPCs for differentiation into hDaNs. We characterized the NPCs by showing expression of markers Nestin, Sox2 and PAX6 using RT-qPCR (Manuscript 2 Supplementary Figure 1A) and immunofluorescence (Manuscript 2 Supplementary Figure 1B). These NPCs can give rise to both neural tube and neural crest lineages including dopaminergic neurons (Reinhardt et al. 2013).

We next differentiated NPCs into mature hDaNs showing expression of neuronal marker MAP2 and dopaminergic marker TH in RT-qPCR (Manuscript 2 Figure 1A) and immunofluorescence (Manuscript 2 Figure 1B).

Miro1 protein levels

Prior to assessing how Miro1 S156A affects different mitochondrial functions, we first tested Miro1 protein levels in hDaN lysates and found a significant reduction in Miro1 S156A hDaNs by approximately 42% compared to the isogenic control (Manuscript 2 Figure 1C). We then probed Tom20 protein levels as a proxy of mitochondrial mass to assess whether the reduction in Miro1 protein levels is due to a reduction in mitochondrial content, but Miro1 S156A shows similar Tom20 protein levels as the isogenic control (Manuscript 2 Figure 1D). Because reduced Miro1 protein levels could be due to a decrease in gene expression, we tested levels of *RHOT1* and *RHOT2* mRNA, but found no differences (Manuscript 2 Figure 1E).

Taken together, Miro1 S156A hDaNs exhibit depleted Miro1 protein levels without changes in gene expression or mitochondrial mass. One explanation could be a destabilizing effect of the S156A mutation on Miro1. Structural analysis of the nGTPase domain revealed that Ser156 is the first amino acid in a highly conserved motif promoting dimerization by forming an interface between two Miro1 nGTPase domains (Smith et al. 2020). It is not known whether the dimerization has functional consequences, but it could affect protein stability at the MOM and be regulated by phosphorylation at Ser156.

Because phosphorylation of Ser156 might contribute to Miro1 degradation rather than its stabilization (Shlevkov et al. 2016; Wang et al. 2011), it is also likely, that the reduction in Miro1 protein levels in Miro1 S156A hDaNs is a compensatory mechanism and hence an indirect result of preventing phosphorylation. Further experiments assessing dimerization of Miro1 S156A versus wild-type Miro1 as well as phosphorylation state of Ser156 under basal conditions will help to better understand the determinants for protein stabilization; cell-type-specific pathways as well as mitotic activity could also impact the outcome of altered Miro1 stability.

Mitochondrial morphology

Because Miro1 regulates mitochondrial morphology (Fatiga et al. 2021; Fransson, Ruusala, and Aspenstrom 2006; MacAskill, Brickley, et al. 2009), we next analyzed mitochondrial area, length, form factor and circularity. hDaNs stained with 100 nM MitoTracker green to label mitochondria were imaged, and analysis revealed similar characteristics (Manuscript 2 Figure 1F) with only mitochondrial length being significantly increased in Miro1 S156A hDaNs (Manuscript 2 Figure 1F). Assessing constitutively active or inactive nGTPase domains of Miro1 revealed that nGTPase activity is involved in regulating mitochondrial morphology (Fransson, Ruusala, and Aspenstrom 2006). Although Ser156 does not take part in nucleotide binding (Smith et al. 2020), dimerization of the protein could affect GTPase activity. This is supported by the finding that phosphomimetic Miro1 S156E induces mitochondrial fragmentation in fibroblasts (Shlevkov et al. 2016).

Mitochondrial movement

Because PINK1 activation upon mitochondrial depolarization and subsequent phosphorylation at Ser156 mediates mitochondrial stopping (Wang et al. 2011), we analyzed mitochondrial movement. Using time lapses of mitochondria stained with 100 nM MitoTracker green, we derived kymographs (Manuscript 2 Figure 1G) to assess fractions of stationary, oscillating, anterograde and retrograde moving mitochondria.

In both Miro1 S156A and isogenic control hDaNs, approximately 60% of mitochondria are stationary and approximately 30% are motile, with similar fractions of both directionalities (Manuscript 2 Figure 1H). This matches previous findings showing that 20-50% of mitochondria are motile in neurons (Ligon and Steward 2000; Miller and Sheetz 2004). Mean mitochondrial displacement of 6-8 µm was comparable between both directions and genotypes (Manuscript 2 Figure 1H) and is in line with measuring mitochondrial displacement of 4-10 µm in rat hippocampal neurons (Ligon and Steward 2000).

We further assessed mean mitochondrial speed using Fiji (Rasband,W.S., ImageJ, U. S. National Institutes of Health, Bethesda, MD, USA) plugin TrackMate (Tinevez et al. 2017) and found that mitochondria of both Miro1 S156A and isogenic control hDaNs were moving approximately 0.1 µm/sec (Manuscript 2 Figure 1I), which is in line with a previous finding in hDaNs (Berenguer-Escuder et al. 2020). Notably, mitochondria in primary neurons travel slightly faster with a speed of 0.5-0.6 µm/sec (Ligon and Steward 2000; Miller and Sheetz 2004).

Taken together, Miro1 S156A does not affect mitochondrial movement under baseline conditions, however, we did not test whether mitochondrial movement persists upon depolarization of mitochondria or other stressors. Phosphomimetic Miro1 S156E was sufficient to mediate mitochondrial stopping, however this study used overexpression of a construct with the wild-type protein present (Shlevkov et al. 2016). Considering that loss of Miro1 protein levels impairs mitochondrial movement (Lopez-Domenech et al. 2016; Nguyen et al. 2014), a putative effect of Miro1 S156A interfering with mitochondrial stopping and hence increasing motility might be masked by the reduction of Miro1 protein levels (Manuscript 2 Figure 1C).

8.2.2. Miro1 degradation during CCCP-induced mitophagy is impaired

CCCP-induced mitophagy

Because previous studies are inconsistent whether phosphorylation of Miro1 at Ser156 is required for mitophagy or its degradation (Birsa et al. 2014; Liu et al. 2012; Shlevkov et al. 2016; Wang et al. 2011), we next tested Miro1 degradation upon induced mitophagy. We treated hDaNs for 0/2/4/6/24 h with 10 µM CCCP to depolarize mitochondria and activate PINK1/Parkin. Additionally, we inhibited the proteasome for 6 h using 10 µM MG132 to assess the contribution of proteasomal degradation. We then analyzed Miro1 protein levels as well as Mitofusin and LC3, to assess removal of other MOM proteins (Sarraf et al. 2013) and induction of autophagy (Kabeya et al. 2000), respectively (Manuscript 2 Figure 2A).

In isogenic control hDaNs, Miro1 degradation is observable within 2 h of CCCP treatment with further reduction within 4 h and complete removal after 24 h (Manuscript 2 Figure 2B). Inhibition of the proteasome does not inhibit degradation of Miro1 levels indicating that this occurs via alternative pathways. In mitotic cells, parkin-ubiquitinated proteins are degraded via the ubiquitin-proteasome system (Chan et al. 2011), but in neurons, activation of Parkin for removal of MOM proteins results in activation of autophagy (Ashrafi et al. 2014; Cai et al. 2012). In contrast to isogenic control hDaNs, Miro1 protein levels do not change within the first six hours of CCCP treatment in Miro1 S156A hDaNs; complete removal of Miro1 after 24 h is maintained (Manuscript 2 Figure 2B).

These findings indicate that phosphorylation at Ser156 is required to facilitate Miro1 removal in early stages of mitophagy. To assess how other targets of PINK1/Parkin are degraded, we probed Mitofusin because it is ubiquitinated and degraded similar to Miro1 (Birsa et al. 2014; Sarraf et al. 2013). In isogenic control hDaNs, this is replicated while in Miro1 S156A degradation is slowed down (Manuscript 2 Figure 2C). However, induction of autophagy by LC3 is not affected by Miro1 S156A (Manuscript 2 Figure 2D).

Taken together, these results indicate, that Miro1 S156A hDaNs fail to degrade Miro1 upon depolarization and that removal of other MOM targets is mildly impaired. Because induction of autophagy occurs normally, we suggest that phosphorylation of Miro1 at Ser156 is important for removal of Miro1 during early stages of mitophagy, but not for autophagy which occurs at later stages to remove Miro1. Previous studies investigating the importance of Miro1 Ser156 phosphorylation used different cell lines as well as overexpression of the respective constructs with wild-type Miro1 still present (Birsa et al. 2014; Liu et al. 2012; Shlevkov et al. 2016; Wang et al. 2011). In contrast, Miro1 S156A hDaNs are homozygous which allows investigating the function of this phosphorylation site without presence of wild-type Miro1. Its ubiquitination by Parkin is required for mitophagy in mouse primary neurons (Lopez-Domenech et al. 2021) and it can recruit parkin to polarized mitochondria independent of PINK1 (Safiulina et al. 2019). While Miro1 S156A can be ubiquitinated by Parkin, it is degraded slower than wild-type Miro1 (Shlevkov et al. 2016). We observed an impairment in Miro1 degradation in Miro1 S156A hDaNs, but we did not assess Parkin recruitment to mitochondria or ubiquitination efficiency. We also did not test Miro1 phosphorylation at Thr289 and Thr299 (Wang et al. 2011). Their contribution to Miro1 function is yet unknown, so is the interplay between the three phosphorylation residues. One study indicates that phosphorylation at Thr298 and Thr299 might counteract phosphorylation at Ser156 resulting in reduced Miro1 ubiquitination and degradation (Shlevkov et al. 2016). Because these phosphorylation sites are still present in Miro1 S156A hDaNs, they might contribute to rendering Miro1 resistant to ionophore-induced degradation.

Mitochondrial membrane potential and turnover

To assess whether the impairment in Miro1 removal might be linked to a reduced sensitivity to mitochondrial depolarization, we assessed mitochondrial membrane potential. hDaNs stained with 25 nM TMRM and 100 nM MitoTracker green as control revealed a significant reduction of mitochondrial membrane potential in Miro1 S156A hDaNs (Manuscript 2 Figure 2E), which was replicated in flow cytometry with a non-significant reduction (Manuscript 2 Figure 2F).

Because the loss of mitochondrial membrane potential could trigger MQC mechanisms, we next assessed mitochondrial turnover. We transfected hDaNs with the pMitoTimer construct (Hernandez et al. 2013) encoding for a mitochondrial targeted fluorescent protein shifting fluorescence from green to red over 48 h; this provides information about import and degradation of mitochondrial proteins, respectively (Hernandez et al. 2013). Compared to isogenic control hDaNs, the ratio between import (green) and degradation (red) is significantly reduced in Miro1 S156A hDaNs (Manuscript 2 Figure 2G) indicating an increase in mitochondrial turnover. This is in line with our finding, that despite a loss of membrane potential (Manuscript 2 Figure 2E and F), there is no reduction of mitochondrial mass indicated by Tom20 (Manuscript 2 Figure 1D).

So far, little is known about the connection between Miro1 and mitochondrial membrane potential. One study reported mild hyperpolarization after overexpression of Miro1 (Safiulina et al. 2019) which would be in line with our findings that reduction of Miro1 protein levels results in depolarized mitochondria. While we did not observe changes in mitochondrial morphology indicative of compromised quality, we did not analyze mitochondrial ultrastructure. Miro1 interacts with MICOS structures and takes part in cristae organization (Modi et al. 2019) which in turn regulates assembly of OXPHOS complexes into supercomplexes as well as their stability and efficiency (Cogliati et al. 2013). Because respiratory chain complexes both contribute to and utilize the electrochemical gradient across the membrane [reviewed in (Huttemann et al. 2008)], a reduction in mitochondrial membrane potential might indicate deficiencies in mitochondrial respiration.

8.2.3. Miro1 S156A reduces mitochondrial respiration

To test this hypothesis, we next tested protein levels of OXPHOS complexes. In Miro1 S156A hDaN lysates, only complex I (NDUFB8) protein levels remained unchanged (Manuscript 1 Figure S1F). Complexes III (UQCRC2) and V (ATP5A) were reduced significantly by approximately 26% and 22%, respectively (Manuscript 2 Figure 3A), complexes II (SDHB) and IV (MTCO1) were mildly reduced (Manuscript 2 Figure S1F). Interestingly, we found that Miro1 protein levels correlate significantly with protein levels of complexes III (r=0.8857, *p*=0.0001) and V (r=0.7910, *p*=0.0022), but not complex IV (r=0.5181, *p*=0.0844) in hDaNs of both genotypes (Manuscript 2 Figure 3B).

We further asked whether the combined reduction of mitochondrial membrane potential and OXPHOS complexes has functional outcomes and analyzed mitochondrial respiration. In a basic mitochondrial stress test, we exposed hDaNs to subsequent injections of (I) Oligomycin (inhibition complex V), (II) CCCP (uncoupling) and (III) Rotenone with Antimycin A (inhibition of complexes I and III, respectively). This results in (I) minimizing, (II) maximizing and (III) shutting down mitochondrial oxygen consumption (Manuscript 2 Figure 3C). In Miro1 S156A hDaNs, mitochondria overall consume less oxygen (Manuscript 2 Figure 3C) and have a significantly reduced basal respiration (Manuscript 2 Figure 3D). Because maximum respiration is also decreased, spare respiratory capacity (which indicates capability of mitochondria to meet higher energetic demands) is unchanged in Miro1 S156A hDaNs compared to the isogenic control (Manuscript 2 Figure 3D).

We further tested extracellular acidification rate, which is an indicator of glycolysis. Because there are no differences in Miro1 S156A and isogenic control hDaNs (Manuscript 2 Figure S1C), there is likely no compensatory upregulation in glycolysis to counteract the reduction in OXPHOS in Miro1 S156A hDaNs.

Previous studies investigating Miro1 k.o. models did not identify deficiencies in mitochondrial respiration, in both fibroblasts in neurons (Lopez-Domenech et al. 2018; Nguyen et al. 2014). We hypothesize that in complete absence of Miro1, this is compensated for. In Miro1 S156A hDaNs however, either reduction of Miro1 protein itself or the mutation confers a reduction in protein levels of respiratory chain complexes concomitant with decreased mitochondrial respiration. Whether this deficit affects neuronal activity needs to be determined; because in Miro1 S156A hDaNs there is no compensatory upregulation of glycolysis, a deficit in ATP production might impair firing capacity of hDaNs. Phosphorylation at Ser156 might have roles outside Miro1 degradation during mitophagy and could be important for interaction with PINK1 and Parkin. These proteins can regulate synthesis of nuclear encoded OXPHOS components (Gehrke et al. 2015; Vincow et al. 2013) and Miro1 protein levels at the MOM might take part in this.

8.2.4. Miro1 protein levels link to OXPHOS is post-mitotic cells

Because a link between mitochondrial respiration and Miro1 has not yet been reported and studies in k.o. models did not observe changes in respiration (Lopez-Domenech et al. 2018; Nguyen et al. 2014), we wanted to determine whether the observed effect is specific to the mutation (S156A), or due to a susceptibility of postmitotic cells to Miro1 protein levels.

Miro1 S156A NPCs

We first tested Miro1 S156A NPCs (Manuscript 2 Figure S1A), which – in contrast to hDaNs – are mitotic and have a less complex morphology (Manuscript 2 Figures 1B and S1B). Under basal conditions, Miro1 protein levels are comparable between Miro1 S156A and isogenic control hDaNs (Manuscript 2 Figure 4A) concomitant with unchanged mitochondrial mass assessed using Tom20 (Manuscript 2 Figure S1D).

This indicates that the reduction in Miro1 protein levels observed in Miro1 S156A hDaNs is specific to postmitotic cells because this is not replicated in mitotic NPCs. We also found that the Miro1 S156A mutation is not sufficient to reduce complexes III and V in NPCs (Manuscript 2 Figure 4A); complexes I and IV remain unchanged as well (Manuscript 2 Figure S1D).

RHOT1 knock-down in undifferentiated and differentiated SH-SY5Y

To further determine whether a reduction in Miro1 protein levels in mitotic cells might suffice to affect OXPHOS complexes, we knocked down Miro1 in undifferentiated SH-SY5Y cells by approximately 37% (Manuscript 2 Figure 4B); assessing Tom20 we validated that the knock-down did not affect mitochondrial mass (Manuscript 2 Figure S1D).

As in Miro1 S156A NPCs, *RHOT1* knock-down in undifferentiated SH-SY5Y cells was insufficient to reduce protein levels of OXPHOS complexes (Manuscript 2 Figures 4B and S1E). Because neither the mutation nor the reduction in Miro1 protein levels affects respiratory chain complexes, we lastly asked whether this link depends on the mitotic state of cells. We repeated the knock-down of Miro1 in differentiated postmitotic SH-SY5Y cells and reduced Miro1 protein levels by approximately 24% without affecting Tom20 (Manuscript 2 Figure S1F). This resulted in a significant decrease of complexes IV and III, but not I or V (Manuscript 2 Figures 4C and S1F). Replicating the findings in hDaNs, Miro1 protein levels correlated with OXPHOS complexes (CIII r=0.8318, p=0.0104; CIV r=0.9630, p=0.0001).

Taken together, these findings support the hypothesis that the reduction of OXPHOS complexes found in Miro1 S156A hDaNs is due to the reduction in Miro1 protein levels and specific to the differentiation state of the cells. It further indicates that the reduction in Miro1 protein levels might be a compensatory effect of the mutation. Additionally, our findings reveal a novel link between Miro1 protein levels and OXPHOS complexes in differentiated cells which could be linked to PINK1/Parkin mediated renewal of OXPHOS complexes (Gehrke et al. 2015; Vincow et al. 2013). Notably, mitochondrial biogenesis correlates with cell size and depends on the mitotic state of cells (Zheng et al. 2016). Because metabolism switches from glycolysis to OXPHOS during neuronal differentiation (Hall et al. 2012; Zheng et al. 2016), these cells might be specifically vulnerable to Miro1 protein levels regarding stability of OXPHOS complexes. The fact that not all complexes are affected similarly might be explained by their different half-lives, which vary not only between complexes but also between tissues (Karunadharma et al. 2015). Taken together, our findings indicate that the differentiation state of cells confers different thresholds for tolerating loss of Miro1 protein depending on the aspect of Miro1 function.

8.3. Manuscript 3: R272Q Disrupts Mitochondrial calcium Handling and Neurotransmitter Uptake in Dopaminergic Neurons

Studies investigating Miro1 function revealed an involvement in PD-relevant pathways, but initial assessment of a genetic link was first negative (Anvret et al. 2012; Nalls et al. 2019; Saeed 2018), until four heterozygous variants were found in a cohort of sporadic PD patients (Berenguer-Escuder et al. 2019; Grossmann et al. 2019). We introduced heterozygous Miro1 R272Q into healthy iPSCs to better understand contributing factors facilitating pathogenesis of PD in dopaminergic neurons. Our data indicate, that Miro1 R272Q impairs mitochondrial calcium uptake most likely by disrupting interaction with MCU. While mitochondrial movement and Miro1 degradation are not affected, mitochondria were found to show altered morphology and cristae structure concomitant with decreased OXPHOS. Additionally, mitochondrial deficits result in alterations of dopamine handling highlighted by neurotransmitter uptake and transcriptomics indicating dysregulation of dopaminergic neurotransmission.

8.3.1. Miro1 R272Q does not affect mitochondrial movement or degradation

For investigation of changes in mitochondrial biology due to Miro1 R272Q relevant for PD, we differentiated iPSCs into hDaNs. We validated dopaminergic and neuronal identity by testing expression of TH and MAP2, respectively, using RT-qPCR (Manuscript 3 Supplementary Figure 1A), as well as immunofluorescence (Manuscript 3 Figure 1A). In differentiated hDaNs, 35-40% of MAP+ cells are also TH+ (Manuscript 3 Supplementary Figure 1B), in line with numbers reported previously (Bus et al. 2020; Hartfield et al. 2014; Seibler et al. 2011).

Miro1 protein levels and CCCP-induced mitophagy

We next assessed Miro1 protein levels in hDaN lysates and found no differences between Miro1 R272Q and isogenic control (Manuscript 3 Figure 1B). Additionally, we validated that gene expression of both *RHOT1* and *RHOT2* remained unchanged (Manuscript 3 Supplementary Figure 1C).

Because Miro1 removal from mitochondria is essential in mitophagy (Lopez-Domenech et al. 2021), we next tested whether either of these are affected. We depolarized mitochondria by treatment with 10 µM CCCP for 2/4/6/22 h to activate PINK1/Parkin and tested involvement of the proteasome by blocking it for 6 h with

10 µM MG132 in addition to the ionophore treatment. Immunoblotting analysis reveals that Miro1 protein levels in Miro1 R272Q hDaNs follow the same flux as in isogenic control hDaNs (Manuscript 3 Figure 1C). To rule out that removal of other MOM targets of PINK1/Parkin or the induction of autophagy are affected despite intact Miro1 removal, we probed Mitofusin (Sarraf et al. 2013) and LC3 (Kabeya et al. 2000), respectively. Both genotypes remove Mitofusin (Manuscript 3 Figure 1C) and activate LC3 similarly (Manuscript 3 Supplementary Figure 1D).

These findings indicate that Miro1 R272Q hDaNs do not have a deficit in mitophagy. However, Miro1 R272Q hDaNs derived from patient fibroblasts exhibited impairment in removing defective mitochondria by reduced co-localization of mitochondria and lysosomes after induction of oxidative stress (Berenguer-Escuder et al. 2020). Because we used CCCP to depolarize mitochondria, more experiments are required to test whether gene-edited Miro1 R272Q replicates this phenotype. Furthermore, we cannot exclude a putative effect of the genetic background which contributes to either the patient or the gene-edited phenotype. An isogenic gene-corrected control for the patient-derived Miro1 R272Q hDaNs as well as generation of animal models and assessing primary neurons might help to differentiate between mutation-specific effect and genetic burden.

Mitochondrial movement

After establishing that Miro1 protein levels are unchanged in Miro1 R272Q hDaNs, we next analyzed mitochondrial movement without stimuli. We stained mitochondria with 100 nM MitoTracker green and used time lapses to derive kymographs (Manuscript 3 Figure 1D) to determine the percentage of stationary, oscillating, anterograde and retrograde moving mitochondria. hDaNs of both genotypes have approximately 60% stationary mitochondria and 15-20% anterograde and retrograde moving mitochondria, respectively (Manuscript 3 Figure 1E), in line with previous findings (Ligon and Steward 2000; Miller and Sheetz 2004). Mitochondria of both Miro1 R272Q and isogenic control hDaNs travelled 7-9 µm on average (Manuscript 3 Figure 1E), in line with displacement measured previously (Ligon and Steward 2000). In agreement with unchanged mitochondrial motility, we found no differences in mitochondrial speed (Manuscript 3 Figure 1F) analyzed using Fiji plugin TrackMate (Tinevez et al. 2017).

Similar to our findings on Miro1 removal and mitophagy, the unchanged mitochondrial motility is not replicated in patient-derived Miro1 R272Q hDaNs, which show a significant reduction in mitochondrial speed (Berenguer-Escuder et al. 2020). While gene-edited Miro1 R272Q does not confer changes, we measured similar speeds of approximately 0.1 µm/sec (Manuscript 3 Figure 1F). As discussed above, we cannot rule out that the genetic background is a contributing factor to the observed differences. Analysis of stationary and motile fractions in the patient-derived Miro1 R272Q hDaNs as well as changing conditions such as cytosolic calcium might further help to differentiate mutation-specific effects from genetic background. Additionally, this might reveal a potential deficit in calcium-mediated mitochondrial stopping. Miro1 distributes mitochondria throughout the neuron in a calcium sensing-dependent manner (Macaskill, Rinholm, et al. 2009; Saotome et al. 2008; Wang and Schwarz 2009) which contributes to scaling neurotransmission (Vaccaro et al. 2017). A possible deficit in calcium-mediated mitochondrial stopping might compromise neuronal activity by decreasing abundance of mitochondria at synapses and thus the availability of synaptic vesicles (Sun et al. 2013; Verstreken et al. 2005).

8.3.2. Miro1 R272Q alters mitochondrial morphology and ultrastructure

Mitochondrial morphology

Miro1 contribution to regulating mitochondrial morphology includes calcium sensing via EF-hand domains (Fatiga et al. 2021; Nemani et al. 2018; Saotome et al. 2008). Since Miro1 R272Q is located near the end of the nEF-hand domain (Grossmann et al. 2019; Klosowiak et al. 2013) and could affect calcium sensing, we next analyzed mitochondrial morphology. Using images of hDaNs stained with 100 nM MitoTracker green (Manuscript 3 Figure 2A), we analyzed mitochondrial area, length, circularity, and form factor. Miro1 R272Q mitochondria are significantly smaller, both in area and length, concomitant with increased fragmentation and reduced form factor (Manuscript 2 Figure 2B). To assess whether this affects mitochondrial mass, we probed Tom20 but found no differences between Miro1 R272Q and isogenic control lysates (Manuscript 2 Figure 2C).

Mitochondrial ultrastructure

Having observed significant changes to mitochondrial morphology, we next looked at mitochondrial ultrastructure using electron microscopy. Representative images show that Miro1 R272Q mitochondria are partially or completely devoid of cristae

(Manuscript 3 Figure 2D). Blinded counting revealed that Miro1 R272Q hDaNs have significantly more mitochondria with disrupted cristae than isogenic control (Manuscript 3 Figure 2E). Notably, Miro1 hDaNs R272Q also have significantly more mitochondria per image (Manuscript 3 Supplementary Figure 1E), which is in line with increased fragmentation (Manuscript 3 Figure 2B).

These data suggest that the alterations in ultrastructure do not affect integrity of the MOM, because Tom20 protein levels are unchanged (Manuscript 3 Figure 2C), and that increased mitochondrial fragmentation (Manuscript 3 Figure 2B) might be a compensatory effect.

Mitochondrial turnover and sensitivity to apoptosis

To assess whether compromised mitochondrial ultrastructure affects mitochondrial turnover, we transfected hDaNs with pMitoTimer (Hernandez et al. 2013) encoding for a fluorescent protein indicating protein import (green) and degradation (red) by a shift of fluorescence. In line with our findings of altered mitochondrial morphology, Miro1 R272Q hDaNs show significantly increased mitochondrial turnover, indicated by a decreased red to green ratio (Manuscript 3 Figure 2F). Last, we checked whether Miro1 R272Q hDaNs have a higher susceptibility for apoptosis because of compromised mitochondrial morphology. We used 1 µM Staurosporine for 4 h to induce apoptosis and stained hDaNs with apoptotic marker Annexin V and necrotic marker 7-AAD. Staurosporine treatment significantly increased apoptosis in Miro1 R272Q hDaNs, but not isogenic control without increasing necrosis (Manuscript 3 Figure 2G).

Taken together, Miro1 R272Q results in alterations in mitochondrial morphology as well as mitochondrial turnover which are most likely a compensatory mechanism for partial loss of cristae. These data indicate that this elevates the sensitivity to apoptosis in hDaNs which suggests a burdening of these cells and renders them more sensitive to further mitochondrial deficits.

In line with our findings, patient-derived Miro1 R272Q show a higher mitochondrial fragmentation at baseline and after stimulation with calcium (Berenguer-Escuder et al. 2020). Whether mitochondrial ultrastructure is similarly altered in these cells as well was not investigated. We suggest that the above-described changes trigger compensatory mitochondrial fragmentation in gene-edited Miro1 R272Q hDaNs. Since mediation of mitochondrial fusion by Mitofusin depends on Miro1 EF-hand calcium-sensing (Fatiga et al. 2021), this might be compromised by R272Q because of its location in the nEF-hand domain (Grossmann et al. 2019; Klosowiak et al. 2013). It is further possible, that a putative deficit in calcium-sensing might also impair Miro1 interaction with MICOS complex (Modi et al. 2019), which is one of the central regulators of mitochondrial ultrastructure [reviewed in (Mukherjee, Ghosh, and Meinecke 2021)].

8.3.3. Miro1 R272Q alters calcium handling

Alterations in cytosolic calcium in Miro1 R272Q hDaNs

Because altered calcium handling due to Miro1 R272Q might link to the observed changes in mitochondrial morphology, we analyzed changes in cytosolic calcium indicated by FLUO-4 in response to 5 µM Thapsigargin while chelating extracellular calcium. We additionally treated hDaNs for 2 h with 2 µM Mitoxantrone, a specific MCU inhibitor (Arduino et al. 2017), to assess contribution of mitochondrial calcium uptake in buffering Thapsigargin-stimulated elevation of cytosolic calcium. This triggers a higher cytosolic calcium response in Miro1 R272Q hDaNs with delayed buffering compared to isogenic control hDaNs (Manuscript 3 Figure 3A left graph). Blocking mitochondrial calcium uptake with Mitoxantrone mildly affects isogenic control hDaNs but reverses the phenotype in Miro1 R272Q hDaNs (Manuscript 3 Figure 3A left graph). Notably, the slopes of increasing and decreasing cytosolic calcium were comparable between both phenotypes (Manuscript 3 Figure 3A right graph).

Miro1 contribution to calcium buffering in SH-SY5Y

To better understand Miro1 contribution to mitochondrial calcium uptake, we knocked down Miro1 protein in SH-SY5Y neuroblastoma cells (Schwarz and Fitzgerald 2022). For indication of cytosolic calcium, SH-SY5Ys were stained with FLUO-4 and for indication of mitochondrial matrix calcium, cells were transfected with the genetically encoded calcium indicator CMV-mito-jRCaMP1b (Ashrafi et al. 2020); all were treated for 2 h with 10 µM Mitoxantrone to block the MCU. Cytosolic calcium response is mildly decreased in *RHOT1* knock-down, and not affected by Mitoxantrone treatment in either control siRNA or *RHOT1* siRNA-treated cells (Manuscript 3 Figure 3B left graph). Mitochondrial calcium uptake however is increased upon reduction of Miro1 protein levels and Mitoxantrone treatment reverses this phenotype (Manuscript 3 Figure 3B right graph).

Taken together, our data are in line with previous findings that Miro1 affects mitochondrial calcium uptake (Chang, Niescier, and Min 2011; Lee et al. 2016; Saotome et al. 2008). This is regulated via the MCU (Baughman et al. 2011; Pan et al. 2013), which in turn is a subunit of a multiprotein complex comprising MCUb and regulatory units EMRE, MCUR1 and MICU1/2/3 [reviewed in (Alevriadou et al. 2021; Nemani, Shanmughapriya, and Madesh 2018)]. While EMRE and MCUR1 are positive regulators [reviewed in (Nemani, Shanmughapriya, and Madesh 2018)], MICUs sit in the intermembrane space functioning as gatekeepers [reviewed in (Alevriadou et al. 2021)]. A recent study showed that Miro1 and MCU interact biochemically, suggesting that the N-terminal end of MCU interacts with Miro1 until cleavage of the N-terminus (Niescier et al. 2018). Structural analysis of the N-terminal domain of human MCU confirms its localization in the mitochondrial matrix (Lee et al. 2015). However, the Miro1-interacting part is upstream of the N-terminal domain of MCU (Lee et al. 2015; Niescier et al. 2018) and cleavage of this region was shown to be required for MCU-mediated calcium uptake into mitochondria (Niescier et al. 2018).

Studies investigating how Miro1 affects mitochondrial calcium uptake are not quite consistent: in the complete absence of Miro1 mitochondrial matrix calcium showed a lower amplitude (Lee et al. 2016; Modi et al. 2019), but it is unclear how Miro1 EF-hand domains contribute to mitochondrial calcium uptake (Chang, Niescier, and Min 2011; Saotome et al. 2008). Mitochondria-ER contact sites also need to be taken into consideration because Miro1 double knock-out impairs mitochondrial calcium buffering due to alterations in MERCS (Modi et al. 2019) and patient-derived Miro1 R272Q hDaNs showed impairment of MERCS (Berenguer-Escuder et al. 2020). Notably, cytosolic calcium flux observed in gene-edited Miro1 R272Q hDaNs in response to Thapsigargin (Manuscript 3 Figure 3A left graph) is comparable to patient-derived Miro1 R272Q hDaN response to ionomycin (Berenguer-Escuder et al. 2020). All in all, we hypothesize that Miro1 R272Q changes mitochondrial calcium handling. Future experiments to shed light into interaction with MCU or MICUs as well as MERCS will provide further information about how Miro1 takes part in mitochondrial calcium buffering.

8.3.4. Consequences of reduced mitochondrial calcium uptake

Mitochondrial respiration

Since mitochondrial calcium uptake via the MCU regulates mitochondrial respiration [reviewed in (Llorente-Folch et al. 2015)] and Miro1 R272Q hDaNs show changes in mitochondrial ultrastructure, we next assessed functional consequences of this phenotype. Assessing protein levels of OXPHOS complexes, Miro1 R272Q hDaNs were found to have significantly reduced complex V (ATP5A) protein levels (Manuscript 3 Figure 4A) without changes in complexes III (UQCRC2) or IV (MTCO1, Manuscript 3 Supplementary Figure 1F). Image analysis of hDaNs stained with 25 nM TMRM and 100 nM MitoTracker green as control revealed that despite the alterations in cristae structure, Miro1 R272Q mitochondria maintain mitochondrial membrane potential (Manuscript 3 Supplementary Figure 1G).

We next tested if OXPHOS is affected by the observed mitochondrial changes. We modified a basic mitochondrial stress test measuring mitochondrial oxygen consumption and extracellular acidification rate (indicators for OXPHOS and glycolysis, respectively). Since we hypothesize that Miro1 R272Q hDaNs have altered mitochondrial calcium, we treated cells for 2 h with 20 µM Mitoxantrone to prevent mitochondrial calcium uptake. During the stress test, we first challenged hDaNs with either 5 µM ionomycin or medium as control, followed by subsequent injections of Oligomycin (inhibition complex V), CCCP (uncoupling) and Rotenone with Antimycin A (inhibition of complexes I and III, respectively). Miro1 R272Q hDaNs show overall decreased mitochondrial oxygen consumption, mimicked by Mitoxantrone treatment in the isogenic control (Manuscript 3 Figure 4B), but does not affect extracellular acidification rate (Manuscript 3 Supplementary Figure 1H). Basal respiration is reduced by depletion of mitochondrial calcium in isogenic control hDaNs and significantly reduced in Miro1 R272Q under basal conditions with decreased sensitivity to treatments (Manuscript 3 Figure 4C). The reactivity to ionomycin or Mitoxantrone can be explained by the presence of one copy of wild-type Miro1 in R272Q hDaNs because the mutation is heterozygous. Spare respiratory capacity is unaffected in untreated Miro1 R272Q hDaNs, but the increase in response to Mitoxantrone treatment is diminished (Manuscript 3 Figure 4C).

Taken together, these findings indicate that Miro1 R272Q reduces mitochondrial calcium content affecting mitochondrial respiration. Several enzymes in the mitochondrial matrix are tunable by calcium, such as the dehydrogenases of the citric acid cycle and complex V [reviewed in (Llorente-Folch et al. 2015)]. Additionally, bioenergetic state of mitochondria links to their morphology by elongation with increased respiration [reviewed in (Mishra and Chan 2016)].

This is in line with our findings indicating that Miro1 R272Q results in reduced mitochondrial matrix calcium compromising oxidative phosphorylation. The observed fragmentation could be a compensatory mechanism to save functional mitochondria. Because complex V accumulates in distinct areas within mitochondrial cristae and contributes to maintenance of ultrastructure [reviewed in (Mukherjee, Ghosh, and Meinecke 2021)], it is likely that reduction in complex V protein levels observed in Miro1 R272Q hDaNs contributes to loss of cristae structure. In turn, cristae organization regulates assembly of respiratory chain complexes into supercomplexes, as well as their stability and efficiency (Cogliati et al. 2013). Because this is believed to differentiate and specialize OXPHOS functions different cell types (Acin-Perez et al. 2008), it is possible that the observed effects might be neuron-specific due to their reliance on mitochondrial ATP production (Hall et al. 2012). In summary, this indicates that in Miro1 R272Q, disequilibrium of mitochondrial calcium might fuel a vicious circle resulting in the observed phenotype.

Transcriptomics

To better understand the consequences of the Miro1 mutation in R272Q hDaNs, we performed transcriptomics (Manuscript 3 Supplementary Figure 2A). We used the unbiased online pathway analysis tool GOrilla (Eden et al. 2007; Eden et al. 2009) and found dysregulation of neuronal pathways (Manuscript 3 Supplementary Figures Table 1). Checking genes involved in synaptic and plasma membrane signalling revealed changes in *SYT2*, *DRD2*, *MAO-A* and *-B* (Manuscript 3 Supplementary Figure 2B). Notably, genes connected to mitochondrial and/or Miro1 functions such as *TRAK1/2*, kinesins, *PINK1* and *PARK2* remained unchanged (Manuscript 3 Supplementary Figure 2B). In line with finding altered expression patterns of genes relevant for neuronal function, Qiagen Ingenuity software gene mapping highlights changes specific to dopaminergic presynaptic signalling (Manuscript 3 Supplementary Figure 2C). These findings are in line with a proteome-based analysis indicating that the human Miro1 interactome comprises various pathways linked to neuronal function and development (Kay et al. 2019).

Neurotransmitter uptake and DA content

To specifically test DA handling in Miro1 R272Q hDaNs, we next performed a neurotransmitter uptake assay (Jorgensen et al. 2008) and found reduced uptake by approximately 42% in Miro1 R272Q hDaNs under basal conditions (Manuscript 3 Figure 4D). Testing the contribution of DA availability and calcium to neurotransmitter uptake revealed that neither treatment with 50 µM L-DOPA for 24 h nor 5 µM ionomycin for 30 min, respectively, affected uptake (Manuscript 3 Figure 4D). However, blocking mitochondrial calcium uptake with 20 µM Mitoxantrone for 2 h decreased neurotransmitter uptake in both genotypes to an approximately similar level (Manuscript 3 Figure 4D; Friedman test with Dunn's multiple comparisons: isogenic control $p=0.0682$, Miro1 R272Q $p>0.9999$).

Because this assay measures uptake of a dye via monoaminergic transporters DAT, NET and SERT (Jorgensen et al. 2008), we next tested levels of DA and DAT specifically using immunofluorescence (Manuscript 3 Figure 4E). While in untreated hDaNs levels of DA are comparable between both genotypes, we found a significant increase in DAT staining (Manuscript 3 Figure 4F). Treatment with 5 µM ionomycin for 30 min does not affect overall levels of DA but inverses the DAT level phenotype in Miro1 R272Q hDaNs (Manuscript 3 Figure 4F). Notably, 24 h-treatment of hDaNs with 5 µM L-DOPA significantly increases DA levels in Miro1 R272Q hDaNs (Manuscript 3 Figure 4F).

DA degradation by MAO-A and -B

Because this might involve function of DA-degrading enzymes MAO-A and -B, we next assessed their activity in a fluorescent-based assay (Valley et al. 2006). For differentiation between MAO-A and -B, we titrated specific inhibitors Clorgyline and Deprenyl, respectively and found that hDaNs primarily exhibit activity for MAO-B, but also for MAO-A (Manuscript 3 Supplementary Figure 3A), matching the presence of both transcripts (Manuscript 3 Supplementary Figure 2B). In line with the downregulation of *MAO-B* found in transcriptomics (Manuscript 3 Supplementary Figure 2B), we found a significant reduction of protein levels in Miro1 R272Q hDaN lysate (Manuscript 3 Figure 4G) as well as isolated mitochondria (Manuscript 3 Supplementary Figure 3B) concomitant with reduced enzyme activity (Manuscript 3 Supplementary Figure 3C).

Taken together, Miro1 R272Q hDaNs exhibit altered DA handling by reduced MAO activity and neurotransmitter uptake via DAT. We hypothesize that this contributes to the changes in expression of synaptic genes. Our findings highlight the interplay between mitochondrial bioenergetics, calcium handling and neuronal activity. Scaling of energetic output to neuronal activity is required for synaptic transmission (Rangaraju, Calloway, and Ryan 2014) and a recent study showed that neuron-specific MICU3 can mediate ER-independent mitochondrial calcium uptake (Ashrafi et al. 2020). MCU can further stimulate OXPHOS by compensating for Complex I impairment by elevation of matrix calcium (Balderas et al. 2022) and regulates synaptic vesicle recycling (Marland et al. 2016). Interestingly, MAOs can move electrons generated by DA degradation into mitochondria for maintenance of mitochondrial membrane potential and respiration (Graves et al. 2020) and are sensitive to calcium (Cao, Li, and Mousseau 2009). Miro1 R272Q phenotype shows impairment in several of these mechanisms indicating that neuronal function might be affected. Testing spontaneous and stimulated neuronal activity as well as synaptic vesicle pools might help to specify the deficits of Miro1 R272Q hDaNs. Because SNpc neurons show increased respiration to meet their energetic demand (Pacelli et al. 2015) and their pace-making activity constitutes an additional energetic burden to maintain high ATP levels for prolonged activity (Sun et al. 2013), we propose that the bioenergetic deficit and reduced calcium buffering capacity might provide the link between Miro1 R272Q and the development of PD.

Notably, Miro1 R272Q could also affect recruitment of Parkin to mitochondria under basal conditions, which depends on Miro1 calcium-sensing (Safiulina et al. 2019). Parkin was previously linked to MAO, DAT, and neurotransmitter uptake (Itier et al. 2003; Jiang et al. 2006; Jiang, Ren, et al. 2012). Further experiments assessing Parkin localization within Miro1 R272Q hDaNs as well as its interaction with the mutant Miro1 will show whether this is indeed the case. Additionally, more work is needed to understand the relationship between Miro1 and MAO, whether they interact and how they regulate each other.

8.4. Unpublished data: Miro1 K572R phenotype preliminary data

8.4.1. Results and Discussion

Characterization of Miro1 K572R hDaNs

To study the effects of the heterozygous Miro1 K572R mutation in a PD relevant model, I used the iPSCs to derive NPCs for differentiation into hDaNs. I first characterized the differentiated hDaNs for their dopaminergic neuronal identity as well as Miro1 protein levels and expression. Assessing differentiation markers reveals positive immunofluorescence staining for neuronal marker MAP2 and dopaminergic maker TH (Figure 2A). Validation with RT-qPCR confirms comparable gene expression of neuronal marker MAP2, midbrain marker FoxA2 and dopaminergic marker TH (Figure 2B). Next, I tested Miro1 protein levels and found no differences between the genotypes (Figure 2C). Probing gene expression of *RHOT1* and *RHOT2* shows that neither is affected by Miro1 K572R (Figure 2D).

CCCP-induced mitophagy

Because Parkin ubiquitinates Miro1 during mitophagy (Kazlauskaite et al. 2014; Klosowiak et al. 2016) and this constitutes a necessary step for mitophagy (Lopez-Domenech et al. 2021), I tested next, if Miro1 degradation upon mitochondrial depolarization is affected in Miro1 K572R hDaNs. I treated hDaNs with 10 µM CCCP

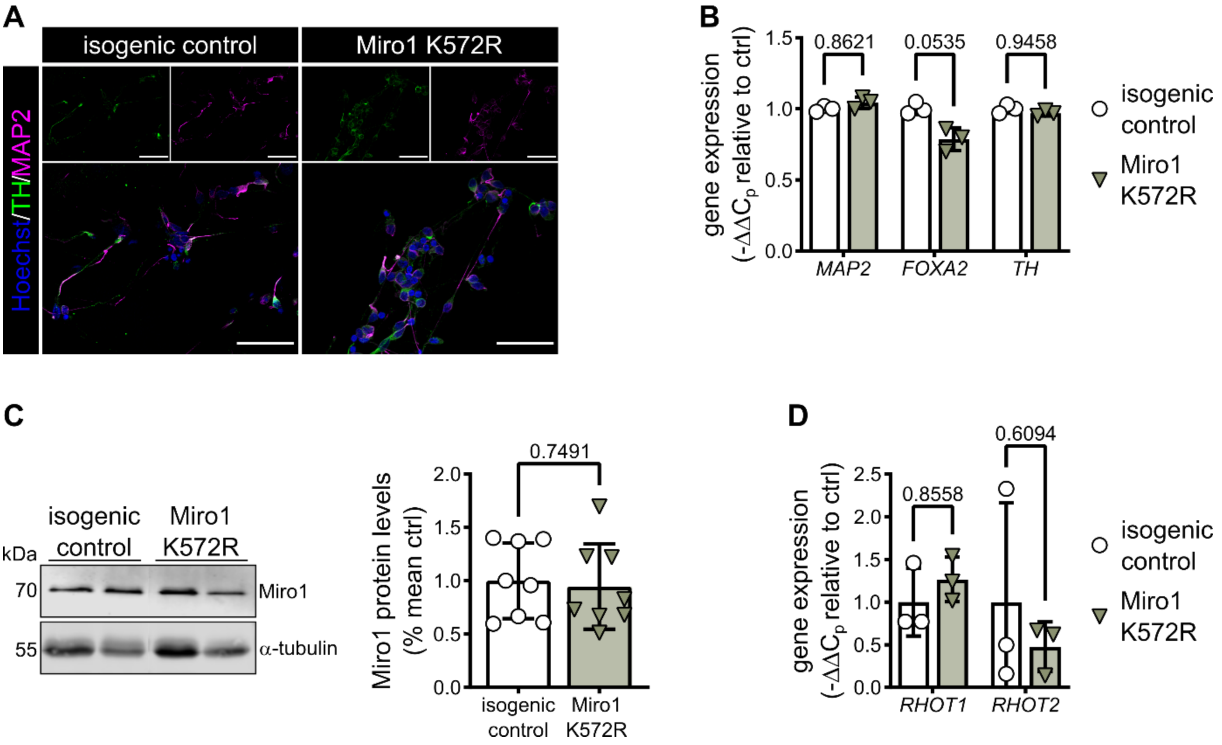

Figure 2: Characterization Miro1 K572R hDaNs. (A) Representative immunofluorescence image of hDaNs stained with TH and MAP2 to label dopaminergic and neuronal cells, respectively. Scale bar represents 50 µm. n_{Diff}=2 **(B)** Gene expression analysis of *MAP2*, *FOXA2* and *TH* as neuronal, midbrain and dopaminergic markers, respectively, with *GAPDH* as reference gene. Gene expression presented as $-\Delta\Delta C_p$ relative to the mean of the isogenic control. Data displayed as mean ± SD; n_{Diff}=3; Two-Way ANOVA with Šidák's multiple comparisons test. **(C)** Representative Western blot of Miro1 protein levels in hDaN lysates. Quantification of band intensity relative to α-tubulin, presented relative to mean of the isogenic control. Data displayed as mean ± SD; n_{Diff}=8; Paired t test (two-tailed) **(D)** Gene expression analysis of *RHOT1* and *RHOT2* with *GAPDH* as reference gene. Gene expression presented as $-\Delta\Delta C_p$ relative to the mean of the isogenic control. Data displayed as mean ± SD; n_{Diff}=3; Two-Way ANOVA with Šidák's multiple comparisons test.

for 2/4/6/22 h to induce PINK1/Parkin mitophagy; I also depolarized the hDaNs for 6 h with the addition of 10 µM MG132. Probing Miro1 on an immunoblot revealed that it is degraded similarly in both genotypes (Figure 3A).

This indicates, that heterozygous Miro1 K572R is not sufficient to impair Miro1 removal during CCCP-induced mitophagy. A previous study showed that while Miro1 K572R does not affect Parkin interaction with Miro1 it is required for thorough Miro1 ubiquitination (Safiulina et al. 2019). I did not observe higher molecular weight bands above Miro1 in my blots (Figure 3A) which might indicate ubiquitination. To assess whether K572R affects Miro1 modification, Miro1 immunoprecipitation with subsequent probing of ubiquitin and phospho-Serine or -Threonine might provide further insight. It is possible that due to the heterozygosity of the mutation, putative effects might be masked by to the presence of wild-type Miro1. I further did not assess levels or expression of mutated versus wild-type Miro1, which would provide further insight into how K572R can contribute to a phenotype. To complete assessment of mitophagy in Miro1 K572R hDaNs, I additionally probed Mitofusin and LC3 to check for removal of other MOM proteins (Sarraf et al. 2013) and induction of autophagy (Kabeya et al. 2000), respectively. Similar to Miro1 degradation, Mitofusin degradation and LC3 activation is comparable in Miro1 K572R and isogenic control hDaNs (Figure 3B), indicating that Miro1 K572R does not affect targeting of other MOM proteins or induction of autophagy.

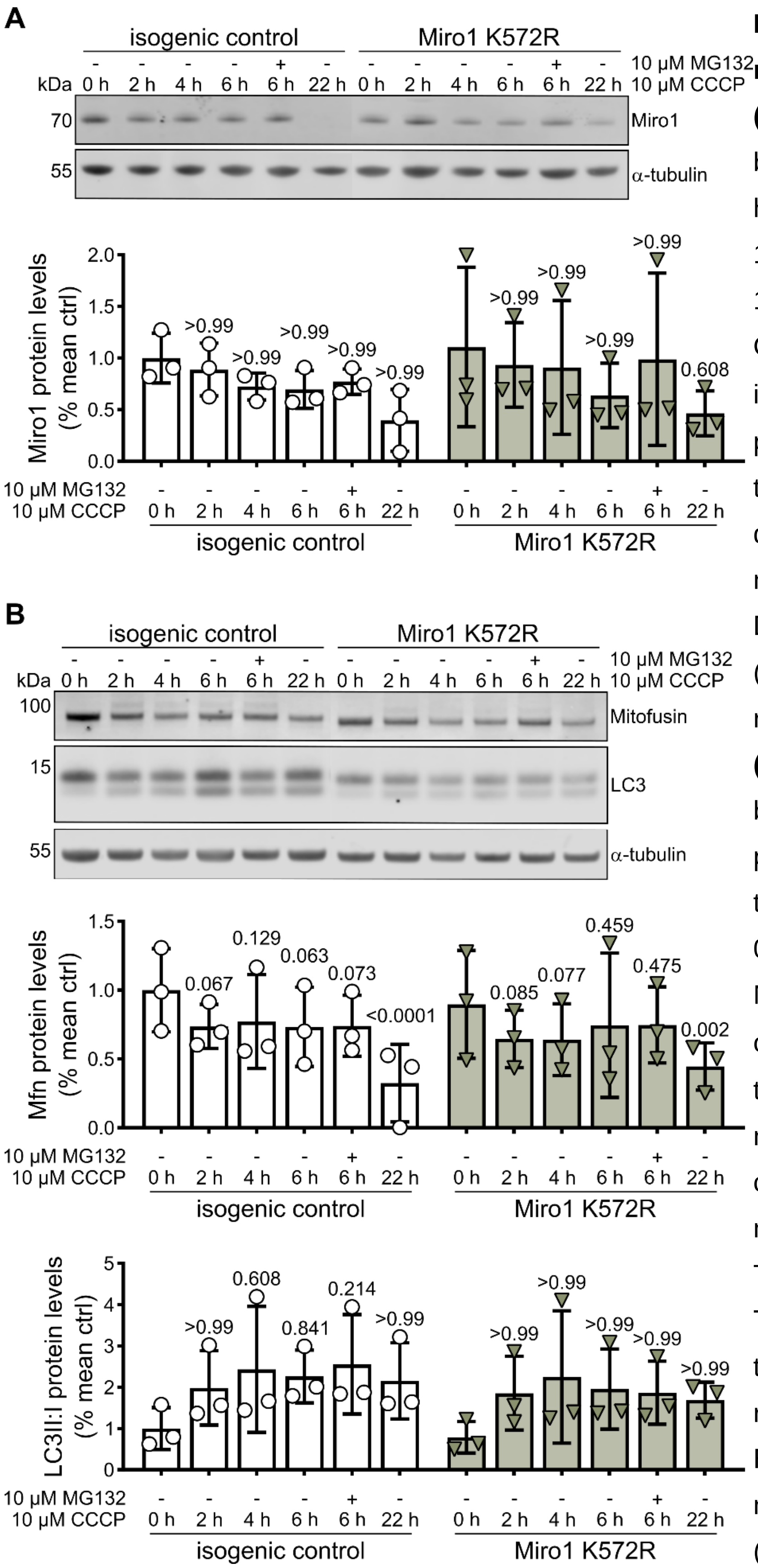

Figure 3: CCCP-induced mitophagy.

(A) Representative Western blot of Miro1 protein levels in hDaN lysates treated with 10 µM CCCP for 0/2/4/6/6 (+ 10 µM MG132)/22 h. Quantification of band intensity relative to α-tubulin, presented relative to mean of the 0 h isogenic control. Data displayed as mean ± SD; n_{Diff}=3; Friedman test with Dunn's multiple comparisons (compared to 0 h of the respective genotype)

(B) Representative Western blot of Mitofusin and LC3II/I protein levels in hDaN lysates treated with 10 µM CCCP for 0/2/4/6/6 (+ 10 µM MG132)/22 h. Quantification of band intensity relative to α-tubulin, presented relative to mean of the 0 h isogenic control. Data displayed as mean ± SD; n_{Diff}=3; Mitofusin: Two-Way ANOVA with Tukey's multiple comparisons test (compared to 0 h of the respective genotype); LC3: Friedman test with Dunn's multiple comparisons (compared to 0 h of the respective genotype)

Studies investigating the ubiquitination of different Lysine residues of Miro1 suggest that Lys572 orchestrates Miro1 ubiquitination (Kazlauskaite et al. 2014; Klosowiak et al. 2016), but it is possible that it acts in concert with four other Lysine residues to facilitate Miro1 degradation and autophagic clearance of mitochondria (Lopez-Domenech et al. 2021). It is likely, that heterozygous K572R is not sufficient to impair Miro1 degradation or mitophagy. However, it is unknown whether ubiquitination at this residue might take part in other Miro1 functions.

Mitochondrial quality parameters

To assess whether this is the case, I tested different mitochondrial parameters. I stained hDaNs with 100 nM MitoTracker green to label mitochondria for analysis of mitochondrial morphology. Miro1 K572R hDaNs have mitochondria with a significantly smaller area and branching as well as higher fragmentation compared to isogenic control hDaNs (Figure 4A). Notably, mean mitochondrial length is not affected which could indicate that mitochondria are larger while being more fragmented than those of the isogenic control (Figure 4A). Next, I tested whether these alterations in morphology are an indicator of stress and used TMRM for analysis of mitochondrial membrane potential. Indeed, Miro1 K572R mitochondria have a significant reduction in mitochondrial membrane potential (Figure 4B). To check whether this affects mitochondrial turnover, I transfected hDaNs with the pMitoTimer plasmid (Hernandez et al. 2013), which indicates the import of new protein in green and the decay in red by shifting fluorescence over 48 h. In Miro1 K572R hDaNs, the ratio between red and green is significantly reduced (Figure 4C) indicating that mitochondrial turnover is increased. Lastly, I probed protein levels of OXPHOS complexes as well as Tom20 as an indicator of mitochondrial mass. While Tom20 and Complex III protein levels are comparable between both genotypes, Complex V is significantly reduced and Complex IV mildly, by approximately 21% and 28%, respectively (Figure 4D).

Taken together, these data indicate that K572R might affect import and assembly of respiratory chain complexes concomitant with a loss of mitochondrial membrane potential. I observed alterations in mitochondrial morphology and increased turnover which could be a compensatory mechanism. Assessment of mitochondrial ultrastructure as well as mitochondrial bioenergetics will provide a more complete

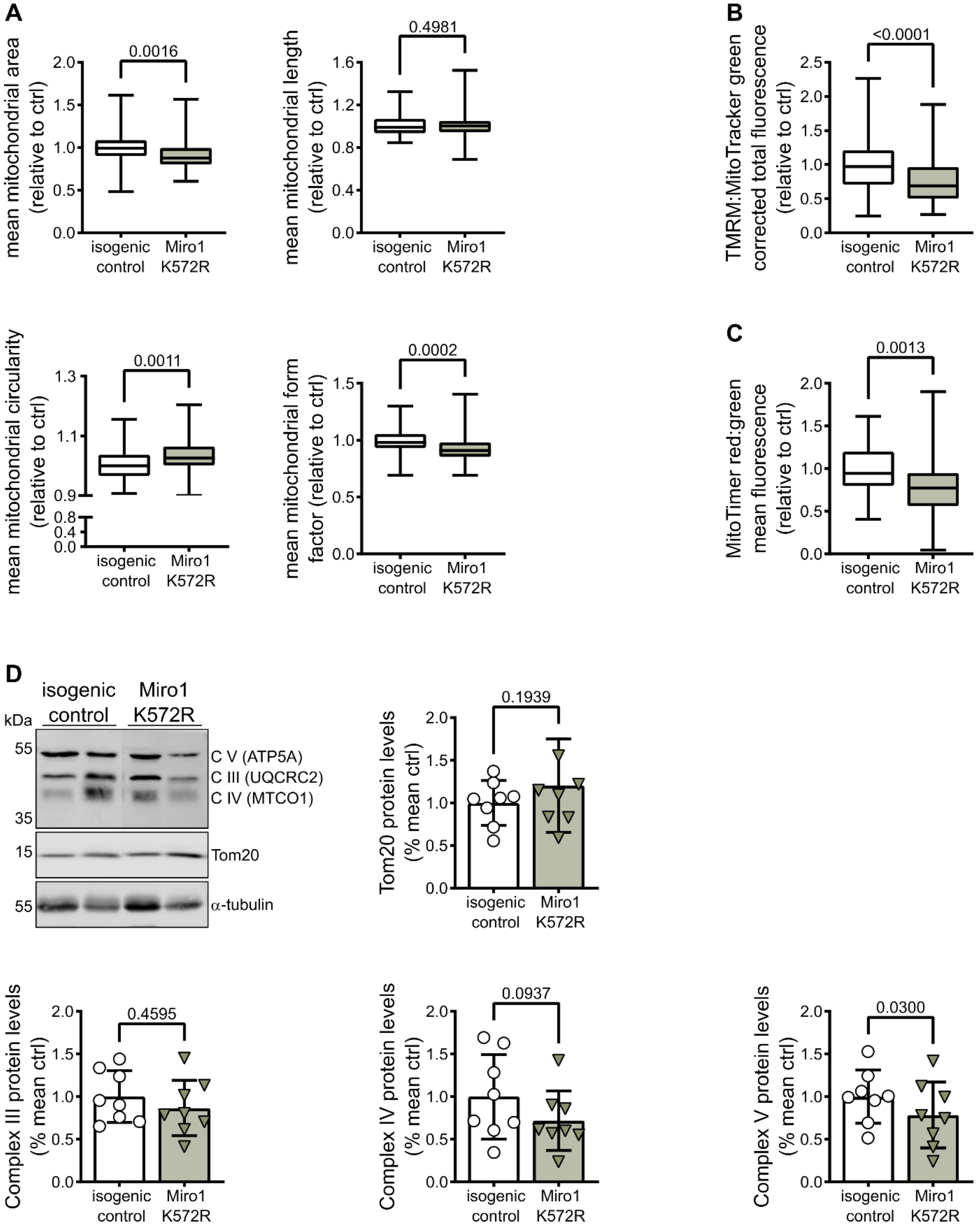

picture of mitochondrial fitness of Miro1 K572R hDaNs. Previous studies investigating Miro1 ubiquitination mainly focused on Miro1 degradation and mitophagy (Kazlauskaite et al. 2014; Klosowiak et al. 2016; Lopez-Domenech et al. 2021; Safiulina et al. 2019) and did not assess other mitochondrial parameters. A putative pathway how Miro1 K572R could affect respiratory chain complexes and mitochondrial

Figure 4: Mitochondrial quality parameters. (A) Mitochondrial morphology analysis of hDaNs stained with 100 nM MitoTracker green. Results presented relative to mean of the isogenic control. Data displayed as mean ± SD; n_{Diff}=3; area, length, and form factor: Mann-Whitney test (two-tailed); circularity: unpaired t test (two-tailed). **(B)** Mitochondrial membrane analysis of hDaNs stained with 25 nM TMRM and 100 nM MitoTracker green. Calculation of corrected total fluorescence of TMRM relative to MitoTracker green. Results presented relative to mean of the isogenic control. Data displayed as mean ± SD; n_{Diff}=3; Mann-Whitney test (two-tailed). **(C)** Analysis of mitochondrial turnover using pMitoTimer plasmid transfection. Calculation of ratio between mean grey value of red and green channels. Results presented relative to mean of the isogenic control. Data displayed as mean ± SD; n_{Diff}=3; Mann-Whitney test (two-tailed). **(D)** Representative Western blot of Tom20, Complex V (ATP5A), IV (MTCO1) and III (UQCRC2) protein levels in hDaN lysates. Quantification of band intensity relative to α-tubulin, presented relative to mean of the isogenic control. Data displayed as mean ± SD; n_{Diff}=8; Paired t test (two-tailed).

membrane potential is similar to the proposed mechanism of Miro1 S156A. Because PINK1 and Parkin regulate synthesis and turnover of OXPHOS complexes (Gehrke et al. 2015; Vincow et al. 2013), their interaction with Miro1 might contribute to this. While previous studies show that K572R does not prevent interaction between Miro1 and Parkin (Safiulina et al. 2019), it is possible that the interaction with PINK1 is affected. Further experiments assessing the interaction parameters under non-depolarizing conditions as well as the contribution of Miro1 modifications will shed light into how Miro1 takes part in regulating protein levels of respiratory chain complexes.

8.4.2. Experimental procedures

NPC generation and differentiation into hDaNs

For derivation of NPCs, iPSC colonies in mTeSR (Stemcell Technologies, #85850) were picked and put into an uncoated well with base medium [50% DMEM/F12 (Thermo Fisher Scientific, #11-330-057), 50% neurobasal (Thermo Fisher Scientific, 21103-049), 1% penicillin/streptomycin (Merck, #A2213),1% GlutaMax (Thermo Fisher Scientific, #35050-038), 1% B27 supplement without vitamin A; Thermo Fisher Scientific, #12587-010), and 0.5% N2 supplement (Thermo Fisher Scientific, #17502-048)] supplemented with 20 µM SB431542 (Selleckchem, #S1067-10 mg), 1 µM dorsomorphin (Axon Medchem, #Axon 1708 5 mg), 3 µM CHIR 99021 (Axon Medchem, #Axon1386 5 mg), and 0.5 µM PMA (Merck, #540220-5MG) for formation of embryonic bodies. These were transferred into NPC medium [base medium supplemented with 3 µM CHIR 99021, 200 µM Ascorbic Acid (Sigma-Aldrich, #A4544-25G) and 0.5 µM PMA] on day 3 and plated on Matrigel (Corning, #354230) on day 5. Outgrowing cells were passaged several times prior to storage or differentiation into hDaNs as described in (Bus et al. 2020) without priming neuronal differentiation by removing PMA.

hDaNs were used at differentiation day 16-19 for experiments. Mitophagy was induced by treatment with 10 µM CCCP in maturation medium for 0/2/4/6/22 h with the addition of 10 µM MG132 for 6 h; untreated cells received fresh maturation medium 22 h prior to harvest.

Immunofluorescence

Matrigel-coated coverslips were used for seeding of hDaNs; cells were fixed in 4% PFA and permeabilized with 0.5% TritonX-100 in PBS for 5 min for Tom20 staining. Blocking was achieved with 10% normal goat serum in 0.01% TritonX-100 in PBS, antibodies were diluted in 5% normal goat serum [primary antibodies: MAP2 1:2000 (abcam, #ab5392), TH 1:1000 (Pel Freez #P40101-150), Tom20 1:200 (Santa Cruz, #sc17764); secondary antibodies: 1:1000; Thermo Fisher, #A21449, #A11070, #A21463] and nuclei were stained with Hoechst (Molecular Devices, #H3569).

A Zeiss Imager.Z1 with an ApoTome.2 and an AxioCam MRm was used for acquisition of Z-stacks. Representative images of hDaN characterization were projected with maximum intensity prior to adjustment of brightness and contrast.

RT-qPCR

RNA from hDaN pellets was isolated using RNeasy kit (Qiagen, #74104) following the manufacturer’s instructions; homogenization was done using QIAshredder as described. Gene expression was quantified by RT-qPCR using QuantiTect SYBR green kit (Qiagen, #204243) following the manufacturer’s instructions.

Primers are listed in Table 1.

Table 1: Primers used in RT-qPCR

Gene	Forward	Reverse
GAPDH	CGAGATCCCTCCAAAATCAAG	GCAGAGATGATGACCCTTTTG
MAP2	CCGTGTGGACCATGGGGCTG	GTCGTCGGGGTGATGCCACG
TH	TGTCTGAGGAGCCTGAGATTCG	GCTTGTCCTTGGCGTCACTG
FOXA2	CCATGCACTCGGCTTCCAG	TGTTGCTCACGGAGGAGT
RHOT1	TGTCACCCCAGAGAGAGTTC	GCCTGCTGTCTTTGTCTGTT
RHOT2	ATTGAGACCTGCGTGGAGTG	AAGCGTTGAGCTCTTCGTCA

Immunoblotting

For lysis of hDaNs, either 1% Triton X-100 in PBS or in 50 mM Tris HCl pH 7.5/150 mM NaCl/1 mM EDTA/0.5% TritonX-100, both supplemented with cOmplete protease inhibitor (Millipore Sigma, #11873580001) and PhosStop phosphatase inhibitor (Sigma-Aldrich, #4906837001) were used. Passes through different needle sizes (5x 20G/8x 25G/10x 27G or 5x 25G/10x 27G) were used for homogenization. Immunoblotting was performed according to standard procedures; proteins were blotted onto a PVDF membrane (Merck, #IPVH00010). Primary antibodies [α-tubulin 1:5000 (Sigma, #AA13), Miro1 1:500 (Thermo Fisher, #PA-42646), Tom20 1:1000 (Santa Cruz, #sc11415), Total OXPHOS 1:1000 (abcam, #ab110413), LC3 1:1000 (Novusbio, #NB100-2220), Mitofusin 1:1000 (Abcam, ab#57602)] were labelled with fluorescent secondary antibodies (1:10,000; Li-cor, #926-32210, #926-32213, # 926-68071, # 926-68070) for detection with an Odyssey CLx (Licor) with Image Studio software (Licor). Band intensity was quantified using Image Studio Lite Ver 5.2 (Licor).

Analysis of mitochondrial membrane potential and morphology

For live cell imaging, approximately 150,000 hDaNs were seeded two-three days prior to microscopy on Matrigel-coated ibidi-dishes. Mitochondria were stained with 25 nM Image-iT™ TMRM reagent (Thermo Fisher Scientific, #I34361) to indicate mitochondrial membrane potential and 100 nM MitoTracker green (Thermo Fisher Scientific, #M7514) as reference for 7 min at 37°C with 5% CO_2.

A Leica DMi8 Microscope (40× objective) with LASX software was used for acquisition of Z-stacks (0.88 µm interval) of hDaNs in phenol-red free maturation medium.

Mitochondrial membrane potential and morphology were analyzed using Fiji: each channel was projected with average intensity and converted to 8-bit greyscale.

For mitochondrial morphology analysis using MitoTracker green images, an adapted protocol (Merrill, Flippo, and Strack 2017) was used with adaptations. In summary, after convolving [Kernel: (0 0 −1 0 0/0 −1 −1 −1 0/-1 −1 24 −1 −1/0 −1 −1 −1 0/0 0 −1 0 0)] and subtraction of background (rolling ball radius: 10 px), local contrast was enhanced (blocksize: 9; maximum slope: 4; unfast) prior to applying tubeness tool (sigma=0.24156) and subsequent despeckling. After conversion to 8-bit and thresholding to create a binary image, area, shape descriptors, perimeter (used to calculate $\text{form factor} = \text{perimeter}^2/4\pi \cdot \text{area}$) and fit ellipse of particles bigger than 1.5 px with a circularity of 0-1 was measured. For each shape descriptor, one data point represents the mean of all particles of one image.

Mitochondrial membrane potential was analyzed by first creating a binary image of MitoTracker green (subtract background with rolling ball of 15 px, then thresholding), then corrected total fluorescence ($\text{CTF}=\text{IndDen}_{\text{Particle}}$ - ($\text{area}_{\text{Particle}} \times$ mean grey $\text{value}_{\text{Background}}$) of each particle was calculated for MitoTracker green and TMRM prior to calculating the ratio for each particle. The mean per image was used as data point in statistics.

MitoTimer analysis for mitochondrial turnover

After seeding approximately 80,000 hDaNs on Matrigel-coated coverslips, transfection with pMitoTimer plasmid [Addgene, #52659; (Hernandez et al. 2013)] was performed using Fugene HD (Promega, #E2311), according to the manufacturer’s instructions after feeding hDaNs with fresh maturation medium 1-2 h earlier. Fixation and Tom20 labeling were performed as described above 48 h after transfection. Z-stacks (0.72 µm interval) were acquired as described above. Mean grey value of green and red channels was measured after projection with average intensity and conversion to 8-bit greyscale using binary Tom20 (generated by thresholding) to define the region of interest. Particles bigger than 1.5 px with circularity 0-1 were measured and the mean of one image was used to calculate the ratio between red and green.

Statistical analyses

GraphPad Prism 9.1.1 was used for statistical analyses. Data was first tested for normality using Shapiro-Wilk test and subsequently tested for significant differences using a parametric or non-parametric test appropriate for the dataset. Statistical tests used are indicated in the figure legends, as is the sample size as number of independent neuronal differentiations as biological replicates indicated as n_{Diff}.

9. Summary

9.1. General discussion: relevance of Miro1 function for PD pathways

In this study I have generated novel isogenic Miro1-mutant iPSC lines and assessed the phenotypic outcome in differentiated dopaminergic neurons. My findings provide new insights into the significance of Miro1 for neuronal health. Miro1 S156A triggers decrease in Miro1 protein levels depending on the mitotic state of the cell affecting mitochondrial respiration via OXPHOS protein complexes. While Miro1 R272Q also exhibits reduced mitochondrial respiration, this can be attributed to altered calcium homeostasis. Because of the specific vulnerability of SNpc dopaminergic neurons to changes in mitochondrial energy production and cytosolic calcium, this study provides valuable insight into Miro1 relevance to PD.

9.1.1. Miro1 S156A: the importance of mitochondrial respiration and MQC for neurons

Recent studies highlighted the significance of Miro1 for mitophagy showing that its ubiquitination is a necessary step (Lopez-Domenech et al. 2021) and that treatment with a Miro1 reducer rescues PD-associated impairments in mitophagy (Hsieh et al. 2019). Additionally, post mortem analysis of PD brains showed an increase of Miro1 protein correlating with an increase in α-synuclein (Shaltouki et al. 2018). However, complete loss of Miro1 is lethal, resulting in crippled neuronal morphology and severe deficits in mitochondrial motility (Lopez-Domenech et al. 2018; Lopez-Domenech et al. 2016; Nguyen et al. 2014). These findings indicate that levels of Miro1 are important for MQC, and both increase or decrease can have adverse effects.

Susceptibility of post-mitotic cells to loss of Miro1 function

In Miro1 S156A NPCs, Miro1 protein levels are comparable to the isogenic control, but during neuronal differentiation, Miro1 S156A hDaNs down-regulate Miro1 protein. Because in post-mitotic cells (hDaNs and differentiated SH-SY5Y), I observed a correlation between Miro1 protein levels and OXPHOS components, I hypothesize that decrease of Miro1 protein is a compensatory effect. It is likely, that adverse effects of Miro1 S156A have less impact in mitotic NPCs because specific aspects of Miro1 function are not as central to cellular fitness. Opposing the overall phenotype observed in Miro1 S156A hDaNs to undifferentiated NPCs would help understand whether the mitochondrial changes in hDaNs are due to reduced Miro1 protein levels or to the mutation. Additionally, testing the phosphorylation pattern of Miro1 under basal conditions and in response to different treatments, such as mitochondrial stress, and comparing hDaNs and NPCs, will provide insight into Miro1 modification depending on the mitotic state of the cell. Because previous studies investigating the effect of Ser156 on Miro1 degradation used different mitotic cell types including HEK, HeLa, SH-SY5Y and fibroblasts (Birsa et al. 2014; Liu et al. 2012; Shlevkov et al. 2016; Wang et al. 2011), it is not known whether the importance of Ser156 changes with differentiation. The body of evidence that post-mitotic neurons react differently to mutations or triggers grows increasingly bigger, which is in line with my findings. Additionally, it is not known, how Miro1 protein levels and turnover are regulated. Because loss of Miro1 is lethal (Lopez-Domenech et al. 2016; Nguyen et al. 2014), a certain expression level needs to be maintained. However, the minimum amount of Miro1 required depending on the mitotic state of the cell is unknown. My findings indicate that a reduction by approximately 42% is tolerated without affecting mitochondrial movement but at the expense of mitochondrial respiration. Because the importance of Miro1 in MQC is highlighted by its interaction with PD-proteins PINK1 (Weihofen et al. 2009), Parkin (Birsa et al. 2014; Lopez-Domenech et al. 2021; Safiulina et al. 2019; Shlevkov et al. 2016), LRRK2 (Hsieh et al. 2016) and α-synuclein (Shaltouki et al. 2018), and because Miro1 protein levels and its degradation are linked to PD (Hsieh et al. 2019; Hsieh et al. 2016; Shaltouki et al. 2018), determining how Miro1 protein levels are regulated can help to define treatment strategies targeting Miro1.

Miro1 Ser156 in PINK1/Parkin mediated mitophagy

Next, I found that Miro1 flux upon CCCP-induced mitophagy is altered in Miro1 S156A hDaNs. Since mitochondrial depolarization triggers PINK1/Parkin activation (see section 6.2.5) and Miro1 interacts with and is targeted by both (Birsa et al. 2014; Kazlauskaite et al. 2014; Klosowiak et al. 2016; Safiulina et al. 2019; Wang and Schwarz 2009; Weihofen et al. 2009), I aimed to shed light into the inconsistent findings about the importance of Ser156 phosphorylation (Birsa et al. 2014; Liu et al. 2012; Shlevkov et al. 2016; Wang et al. 2011). However, the physiological role of mitophagy in neurons is debated. The significance of mitochondria to produce energy and buffer calcium (see sections 6.2.1 and following) in neurons suggests that they are not dispensable and that a loss of mitochondrial quality would first trigger mechanisms to sequester the organelle for retention of functional parts. Indeed, mitochondria can dispose of dysfunctional proteins by budding of MDVs or formation of MDCs (Hughes et al. 2016; Neuspiel et al. 2008; Soubannier, McLelland, et al. 2012). So far, little is known about MDCs, and they have only been investigated in yeast (English et al. 2020; Hughes et al. 2016; Schuler et al. 2021). MDVs are formed in response to different kinds of mitochondrial stress which determines the cargo (Soubannier, Rippstein, et al. 2012). Notably, MDV formation can involve PINK1/Parkin and Miro1 (Konig et al. 2021; McLelland et al. 2016). Next to alternative pathways to mitophagy, PINK1 and Parkin can be circumvented by other pathways [reviewed in (Cummins and Gotz 2018; Evans and Holzbaur 2020)]; but it is the most extensively studied mitophagy pathway and does occur in cultured neurons (Ashrafi et al. 2014; Cai et al. 2012). Its role *in vivo* is highly debated because PINK1 and Parkin k.o. mammalian models failed to exhibit a deficiency in mitophagy [reviewed in (Evans and Holzbaur 2020)]. This indicates that because of the importance of mitochondrial quality to neurons, several parallel pathways are in place. To better understand alternative MQC pathways, Miro1 S156A contribution to MDV formation could be investigated. Next to using different stressors, other PD-relevant proteins, such as LRRK2 (Hsieh et al. 2016) and α-synuclein (Shaltouki et al. 2018) could be included in the analysis.

Because CCCP is an ionophore depolarizing mitochondria to activate PINK1, it is questionable whether this reflects physiological conditions. While CCCP is commonly used to induce mitophagy (Liu et al. 2012; Shlevkov et al. 2016), other treatments include Antimycin A, with (Safiulina et al. 2019) or without (Hsieh et al. 2019) Oligomycin, or removing antioxidants to induce oxidative stress (Berenguer-Escuder et al. 2020). Optimizing the time-course of treatment would further help to dissect when Miro1 degradation is induced and when mitophagy occurs. Additionally, experiments could include testing alternative protein degradation pathways and mitochondrial degradation mechanisms other than proteasomal degradation and LC3-activated autophagy, respectively. I did not add a vehicle control in the untreated condition to correct for a potential effect of ethanol (CCCP) or DMSO (MG132). However, because the maturation medium already contains DMSO as diluent for one of the additives and because the dilution of the CCCP/MG132 stock is quite high, I didn’t expect the vehicle to affect the readout of the experiments. But when assessing whether other mitochondrial stressors have similar effects, a vehicle control would make the results more comparable given that all treatment stocks are reconstituted in the same solvent (e.g. DMSO) and used with the same dilution factor. In addition to analyzing changes of protein levels in lysates, specifically checking Miro1 S156A phosphorylation and ubiquitination will help to understand the determinants of Miro1 modification during mitophagy.

In light of identifying a Miro1 reducer as a potential therapeutic target for a subset of PD patients that fails to translocate Parkin to mitochondria and degrade Miro1 during mitophagy (Hsieh et al. 2019), my findings complement this and provide a cell line which could be used as control. Notably, the Miro1 reducer does not decrease Miro1 protein levels per se but enables its degradation during mitophagy (Hsieh et al. 2019). Hence assessing responsiveness of Miro1 S156A would further help to understand the mechanism of this drug. Furthermore, the Miro1 reducer might rescue some Miro1 S156A phenotypes if facilitating Miro1 removal during mitophagy restores Miro1 protein levels.

The novel link between Miro1 protein levels and mitochondrial OXPHOS

Next to impaired Miro1 degradation my data provide a novel link between Miro1 steady-state protein levels in postmitotic cells and OXPHOS complexes. One putative pathway could involve PINK1 and Parkin, which modulate renewal of respiratory chain complexes (Gehrke et al. 2015; Vincow et al. 2013). Investigating whether Miro1 S156A can still interact with PINK1 and Parkin, respectively, and under which conditions will test this hypothesis.

Because respiratory chain complexes assemble into supercomplexes which in turn links to cristae structure (Cogliati et al. 2013), EM images of mitochondrial ultrastructure and biochemical analyses of supercomplexes such as two-dimensional blue native gel electrophoresis might help to explain whether this contributes to Miro1 S156A phenotype. Likewise, not only conducting these experiments in hDaNs, but also in NPCs provides insight into the differences and similarities between mitotic and postmitotic cells.

9.1.2. Miro1 R272Q: how calcium imbalance can burden neurons and affect neurotransmitter metabolism

Studies identifying *RHOT1* variants in sporadic PD patients (Berenguer-Escuder et al. 2019; Grossmann et al. 2019) strengthened the relevance of Miro1 function for PD after showing that Miro1 takes part in several PD pathways (Hsieh et al. 2016; Lopez-Domenech et al. 2021; Shaltouki et al. 2018; Wang et al. 2011; Weihofen et al. 2009). Assessing patient-derived Miro1 R272Q hDaNs showed that the mutation alters mitochondrial calcium handling (Berenguer-Escuder et al. 2020). Because SNpc neurons are pacemakers, yet can be excited to generate spikes, they are equipped with a unique combination of calcium channels to maintain these functions [reviewed in (Zampese and Surmeier 2020)]. Additionally, cytosolic calcium transients tune OXPHOS (Ashrafi et al. 2020) which is required to meet the high energetic demand of SNpc neurons [(Pacelli et al. 2015; Pissadaki and Bolam 2013), reviewed in (Bolam and Pissadaki 2012)]. Hence, they are particularly susceptible to alterations in (mitochondrial) calcium handling.

Gene-edited Miro1 R272Q and patient-derived Miro1 R272Q

I gene-edited Miro1 R272Q into a previously established healthy iPSC line to generate an isogenic pair for assessment of the phenotypic outcome of the mutation. Genetic variability in humans can contribute strongly to differences observed between a healthy and diseased patient. Because the patient-derived Miro1 R272Q hDaNs were compared to a healthy cell line with a different genetic background, I wanted to assess which phenotypes are observable in the isogenic pair I generated. Notably, the differences between gene-edited and patient-derived lines may not only be attributable to the controls (isogenic and healthy individual, respectively) used, but also to the different genetic background of the mutated lines. Comparing the phenotypes helps to determine which effects are conferred by the mutation.

Patient-derived Miro1 R272Q fibroblasts showed reduced Miro1 protein levels (Grossmann et al. 2019), but this phenotype was lost in hDaNs (Berenguer-Escuder et al. 2020). I did not observe reduced levels of Miro1 protein in gene-edited R272Q hDaNs. However, I neither found deficits in mitophagy or mitochondrial motility shown in patient-derived hDaNs (Berenguer-Escuder et al. 2020). Comparing all four lines to assess the significance of Miro1 protein levels is important, because my work in Miro1 S156A shows that neurons are sensitive to reduced Miro1 protein levels. Because this affects mitochondrial respiration and can also impact mitochondrial calcium handling (Chang, Niescier, and Min 2011; Lee et al. 2016; Modi et al. 2019; Saotome et al. 2008), Miro1 R272Q hDaNs might be sensitive to changes in Miro1 protein levels possibly exacerbating the phenotype.

Considering my hypothesis that Miro1 R272Q impairs Miro1 calcium sensing, these neurons should exhibit changes in mitochondrial motility. Patient-derived hDaNs showed significantly slower mitochondria (Berenguer-Escuder et al. 2020). Due to their complex architecture, (SNpc) neurons are sensitive to impairment of mitochondrial motility (see section 6.2.1 and following). Challenging responsiveness of Miro1-mediated movement to elevated levels of calcium or changes in ADP/ATP ratio will help to oppose gene-edited and patient-derived Miro1 R272Q phenotypes and the contribution of the mutation to this mechanism. Miro1 calcium sensing is important in mitochondrial quality control and necessary for recruiting Parkin to polarized mitochondria (Safiulina et al. 2019). I used CCCP to depolarize mitochondria for activation of PINK1/Parkin and analyzed whole cell lysates. Using alternative mitochondrial stressors, like oxidative stress [which was used to show impairment in mitophagy in patient-derived Miro1 R272Q hDaNs (Berenguer-Escuder et al. 2020)], as well as fractionation of cell homogenates or imaging will aid the assessment of Parkin recruitment to mitochondria and subsequent mitochondrial degradation.

Mitochondrial calcium handling in Miro1 R272Q hDaNs

Assessing dynamics of cytosolic calcium to Thapsigargin revealed that Miro1 R272Q hDaNs exhibit altered buffering. Blocking the MCU with Mitoxantrone had little effect on isogenic control hDaNs which raises the question whether the treatment was effective. For imaging analysis, hDaNs were treated with 2 µM Mitoxantrone instead of 20 µM which was used for neurotransmitter uptake assay and respiratory analysis. Because the neurons are seeded at a much lower density for imaging analysis, 20 µM Mitoxantrone was toxic. Thus, the concentration was reduced to 2 µM, which was the highest concentration tolerated at the cell density for imaging. Testing another inhibitor of the MCU such as Ru360 might help to determine whether Mitoxantrone treatment with a concentration of 2 µM is effective. Additionally, the variability between differentiations is quite big in this assay. Increasing the number of replicates could decrease variability and enhance data reliability. The initial aim was using genetically encoded calcium indicators targeted to the MOM or the matrix (Ashrafi et al. 2020) in hDaNs, but the transfection efficiency is too low to obtain reliable data. To overcome the obstacle of hDaN transfection, the genetically encoded calcium indicators could be gene-edited into iPSCs for constitutive expression. Another way to eliminate the necessity for transfection is switching cell types, hence SH-SY5Y were used as surrogate model with knock-down of Miro1 to simulate a deficiency in Miro1 function. While SH-SY5Y are a popular model for PD research, easy to transfect with efficient Miro1 knock-down, they have the disadvantage that Thapsigargin induces apoptosis in these cells (Nath et al. 1997). Testing mitochondrial matrix calcium in SH-SY5Y showed that knock-down of Miro1 increases matrix calcium. This is not in line with previous studies reporting that decrease of Miro1 protein levels results in reduced mitochondrial calcium buffering (Lee et al. 2016; Modi et al. 2019). The discrepancy between literature and my data might be explained by the sensitivity of SH-SY5Y to Thapsigargin. Taken together, gene-editing the isogenic control and Miro1 R272Q iPSCs to incorporate genetically encoded calcium indicators and using a higher number of biological replicates will strengthen the data and determine whether my hypothesis is correct. Notably, patient-derived Miro1 R272Q hDaNs also show changes in calcium dynamics (Berenguer-Escuder et al. 2020).

Mitochondrial calcium, morphology, and bioenergetics

Mitochondrial membrane potential is the main driving force for mitochondrial calcium uptake [reviewed in (Zampese and Surmeier 2020)] and unaltered in Miro1 R272Q hDaNs. Thus, I hypothesize that Miro1 is upstream of the MCU modulating mitochondrial calcium uptake, a function disrupted by Miro1 R272Q. This results in changes in mitochondrial morphology and mitochondrial bioenergetics.

Miro1 R272Q exhibit fragmented mitochondria partially devoid of cristae concomitant with reduced complex V protein levels and mitochondrial respiration. Previous studies show that calcium-sensitivity of Miro1 is required for mitochondrial morphology (Saotome et al. 2008) and that Miro1 interacts with MICOS subunits to maintain cristae structure (Modi et al. 2019).

It is possible, that mitochondrial sequestration in Miro1 R272Q hDaNs is a compensatory mechanism due to impaired cristae structure and mitochondrial respiration. Which of those is cause and effect remains to be investigated. Mild chronic inhibition of the MCU using low doses of Mitoxantrone might mimic the deficiency in mitochondrial calcium uptake in Miro1 R272Q. Respiratory analysis showed that blocking the MCU decreases mitochondrial respiration, thus longer exposure to Mitoxantrone would answer the question whether this results in depletion of cristae. Loss of Miro1 calcium sensitivity might impact its interaction with MICOS, but I did not assess this in Miro1 R272Q hDaNs. High resolution microscopy to observe whether Miro1 and MICOS clusters co-localize and whether this is sensitive to changes in cytosolic or mitochondrial calcium as well as corresponding pull-down assays to determine interaction will provide further information about the determinants of Miro1-MICOS interaction. Because mitochondrial respiration is not affected by loss of MICOS in HeLa cells (Stephan et al. 2020), it is possible, that both are linked by calcium in Miro1 R272Q hDaNs via complex V. Because complex V is tunable by calcium [reviewed in (Llorente-Folch et al. 2015)] and mitochondrial calcium uptake in neurons scales OXPHOS output to synaptic activity (Ashrafi et al. 2020), it is possible that a deficiency in mitochondrial calcium triggers complex V degradation. In line with this hypothesis, turnover of mitochondrial proteins is increased in Miro1 R272Q hDaNs. Notably, complex V forms dimers regulating cristae shape and MICOS distribution (Stephan et al. 2020), thus the decrease in complex V protein levels in Miro1 R272Q could contribute to alterations in ultrastructure. To test this hypothesis, chronic low-dose treatment with Mitoxantrone could be used to assess effects of mitochondrial calcium depletion on respiratory chain complexes.

Interestingly, transcriptomic analyses revealed dysregulation of *CHCHD2* in Miro1 R272Q hDaNs. CHCHD2 is required for MICOS assembly [reviewed in (Mukherjee, Ghosh, and Meinecke 2021)] and mutations in the encoding gene were identified in autosomal-dominant PD (Funayama et al. 2015). These mutations affect CHCHD10 and MICOS resulting in loss of mitochondrial cristae structure, OXPHOS complexes and mitochondrial respiration (Zhou et al. 2019). Whether *CHCHD2* downregulation in Miro1 R272Q is because of a disturbance of Miro1-MICOS interaction or due to other factors remains to be investigated. Determining how Miro1 or mitochondrial calcium impacts CHCHD2 and mitochondrial ultrastructure will provide further insight into the susceptibility of SNpc neurons to changes in cristae organization.

Taken together, I propose that R272Q impairs Miro1 calcium sensing resulting in mitochondrial fragmentation to compensate for decreased OXPHOS. This is further exacerbated by failing to properly maintain calcium-stimulated respiratory flexibility (Ashrafi et al. 2020) and energy synthesis upon impairment of the electron transport chain (Balderas et al. 2022) because R272Q disturbs Miro1-MCU interaction and thus mitochondrial calcium uptake. Impaired mitochondrial respiration can be compensated for by metabolic flexibility in neurons, even though this is not favorable in SNpc neurons because OXPHOS is required to meet the energetic demand (see section 6.3.4). Interestingly, mitochondrial calcium uptake can sustain mitochondrial respiration when complex I is impaired (Balderas et al. 2022).

Consequences for dopamine handling

Transcriptomic analysis of Miro1 R272Q indicates an impact of the mutation on synaptic and dopaminergic function.

Miro1 R272Q exhibit reduced neurotransmitter uptake through monoaminergic transporters, but DA levels remain unchanged and DAT signal is significantly elevated. While the DAT encoding gene was not differentially regulated in transcriptomics, *DRD2* was significantly upregulated. I did not test DRD2 protein levels, but an increase might explain the elevation in DAT protein levels because these proteins interact with each other (Lee et al. 2007). Because the regulation of both expression and function of DAT and DRD2 is complex, further experiments probing protein levels in cell lysates as well as imaging analysis to visualize subcellular localization will provide information about synaptic structures in Miro1 R272Q hDaNs. Imaging of synaptic structures to label synaptic vesicle pools can help to resolve DA distribution within the neurons. Because we found significantly reduced MAO activity, reduction in DAT activity might be a compensatory effect to prevent toxic levels of DA.

A connection between Miro1 and MAOs is not known, but calcium can affect MAO-A activity [reviewed in (Ramsay and Albreht 2021)]. It is possible, that Miro1 R272Q-mediated changes in calcium homeostasis dampens MAO activity. Another possible link between Miro1, calcium and MAO is Parkin. Miro1 can recruit Parkin to polarized mitochondria in a calcium-dependent manner (Safiulina et al. 2019) and Parkin can suppress expression of MAO and regulate DA utilization (Itier et al. 2003; Jiang et al. 2006; Jiang, Ren, et al. 2012). Testing levels of Parkin as well as localization in a calcium-dependent manner will help to support or deny this hypothesis. Additionally, it can be tested whether MAO activity can be modified by Parkin recruitment to mitochondria or calcium as well as assessing whether MAO and Miro1 interact biochemically. Notably, it was shown recently, that MAO-B activity can fuel the electron transport chain (Graves et al. 2020), thus reduced MAO activity might contribute to decreased mitochondrial respiration in Miro1 R272Q hDaNs.

9.2. Conclusion

In conclusion, the three novel Miro1-mutant iPSCs lines, R272Q, S156A and K572R provide a powerful platform to investigate Miro1 function in any cell type with an isogenic control. This will broaden our understanding of Miro1 function not only for neurodegenerative disease, but also for other diseases such as cancer (Jiang, He, et al. 2012) and diabetes (Chen et al. 2017).

I confirmed previous studies showing that phosphorylation at Ser156 is required for Miro1 degradation. This modification appears to be particularly important in post-mitotic hDaNs because they down-regulate Miro1 S156A most likely for compensation. Additionally, my data provides a novel link between Miro1 and respiratory chain protein levels indicating that Miro1 might regulate the latter. I propose that Miro1 takes part in MQC via phosphorylation at Ser156 stabilizing OXPHOS complexes and Miro1 steady-state protein levels. Gaining insight into how mitochondrial respiration is regulated in hDaNs helps to define factors contributing to SNpc vulnerability. While neurons are metabolically plastic and can compensate for loss of mitochondrial respiration, this is detrimental in SNpc neurons because they cannot meet their energetic demand [(Gonzalez-Rodriguez et al. 2021; Kim et al. 2015; Pacelli et al. 2015) reviewed in (Bolam and Pissadaki 2012)]. My findings support the notion that Miro1 is a putative target for novel treatment strategies. While complete loss of Miro1 is lethal (Lopez-Domenech et al. 2016; Nguyen et al. 2014) and an inability of removing Miro1 from damaged mitochondria is found in PD patients (Hsieh et al. 2019), modulating Miro1 protein levels are a delicate matter. The correlation to levels of respiratory chain complexes makes targeting Miro1 both more compelling and more difficult. The recently described Miro1 reducer is a promising therapeutic because it rescues impaired Miro1 removal from mitochondria without affecting steady-state Miro1 protein levels (Hsieh et al. 2019).

For the PD-associated Miro1 mutation R272Q I found a putative mechanism which involves dampened mitochondrial calcium regulation and respiration. This results in changes in DA metabolism and neuronal function indicated by deceased MAO-B activity and transcriptomics, respectively. I suggest that Miro1 R272Q impairs Miro1 calcium sensing thus affecting related mechanisms. This includes the interaction between Miro1 and MCU (Niescier et al. 2018) and regulation of mitochondrial morphology (Fatiga et al. 2021; Nemani et al. 2018; Saotome et al. 2008). My findings show that Miro1 R272Q confers deficits addressing the specific vulnerability of SNpc neurons. While mitochondria are central for calcium buffering and energy supply in all neurons (see section 6.2.1-4), in SNpc DA neurons, this has even greater significance because of their high energetic demand [(Pacelli et al. 2015), reviewed in (Bolam and Pissadaki 2012)] and their calcium handling dictated by pace-making and excitability [reviewed in (Zampese and Surmeier 2020)]. The knowledge gained by this study can be used to develop new strategies to define subsets of PD patients. While the methods to assess SNpc neurons directly are very limited, patient-derived fibroblasts are a useful tool to define subsets (Hsieh et al. 2019). Probing for differences in mitochondrial calcium handling and mitochondrial respiration in sporadic patients could be used to classify patients. Subsequent testing of treatment strategies to rescue this phenotype can include targeting the MCU to modulate mitochondrial calcium uptake and OXPHOS complexes to increase respiration.

9.3. Outlook

This study revealed that two Miro1 mutations, S156A and R272Q share the phenotype of reduced mitochondrial respiration despite having different causes. Further investigation how aspects of Miro1 function can impact mitochondrial energy production will help to understand potential side effects of PD treatment strategies aimed at Miro1. Future experiments opposing Miro1 S156A and R272Q phenotypes in neurotransmission and ATP availability/distribution throughout the neuron will shed light into how mitochondrial dysfunction can impact synaptic activity. Observing unstimulated spontaneous activity as well as the capacity to scale and maintain transmission during high frequency stimulation will uncover weaknesses in synaptic plasticity in Miro1 mutant hDaNs. Formation of midbrain specific organoids (Monzel et al. 2017) from Miro1 mutant NPCs for future experiments could serve as a model closer to the CNS. In summary, Miro1 S156A and R272Q hDaNs or midbrain-specific organoids are promising models to understand the interplay between the specific vulnerabilities of SNpc neurons to imbalances in calcium homeostasis, mitochondrial respiration, and mitochondrial quality control.

10. References

Acin-Perez, R., P. Fernandez-Silva, M. L. Peleato, A. Perez-Martos, and J. A. Enriquez. 2008. 'Respiratory active mitochondrial supercomplexes', *Mol Cell*, 32: 529-39.

Alevriadou, B. R., A. Patel, M. Noble, S. Ghosh, V. M. Gohil, P. B. Stathopulos, and M. Madesh. 2021. 'Molecular nature and physiological role of the mitochondrial calcium uniporter channel', *Am J Physiol Cell Physiol*, 320: C465-C82.

Amiri, M., and P. J. Hollenbeck. 2008. 'Mitochondrial biogenesis in the axons of vertebrate peripheral neurons', *Dev Neurobiol*, 68: 1348-61.

Ammal Kaidery, N., and B. Thomas. 2018. 'Current perspective of mitochondrial biology in Parkinson's disease', *Neurochem Int*, 117: 91-113.

Anand, R., A. S. Reichert, and A. K. Kondadi. 2021. 'Emerging Roles of the MICOS Complex in Cristae Dynamics and Biogenesis', *Biology (Basel)*, 10.

Anderson, E. M., A. Haupt, J. A. Schiel, E. Chou, H. B. Machado, Z. Strezoska, S. Lenger, S. McClelland, A. Birmingham, A. Vermeulen, and Av Smith. 2015. 'Systematic analysis of CRISPR-Cas9 mismatch tolerance reveals low levels of off-target activity', *J Biotechnol*, 211: 56-65.

Antico, Odetta, Alban Ordureau, Michael Stevens, Francois Singh, Raja S. Nirujogi, Marek Gierlinski, Erica Barini, Mollie L. Rickwood, Alan Prescott, Rachel Toth, Ian G. Ganley, J. Wade Harper, and Miratul M. K. Muqit. 2021. 'Global ubiquitylation analysis of mitochondria in primary neurons identifies endogenous Parkin targets following activation of PINK1', *Science advances*, 7: eabj0722-eabj22.

Antony, P. M., N. J. Diederich, R. Kruger, and R. Balling. 2013. 'The hallmarks of Parkinson's disease', *FEBS J*, 280: 5981-93.

Anvret, Anna, Caroline Ran, Marie Westerlund, Olof Sydow, Thomas Willows, Lars Olson, Dagmar Galter, and Andrea Carmine Belin. 2012. 'Genetic Screening of the Mitochondrial Rho GTPases MIRO1 and MIRO2 in Parkinson's Disease', *The open neurology journal*, 6: 1-5.

Arduino, D. M., J. Wettmarshausen, H. Vais, P. Navas-Navarro, Y. Cheng, A. Leimpek, Z. Ma, A. Delrio-Lorenzo, A. Giordano, C. Garcia-Perez, G. Medard, B. Kuster, J. Garcia-Sancho, D. Mokranjac, J. K. Foskett, M. T. Alonso, and F. Perocchi. 2017. 'Systematic Identification of MCU Modulators by Orthogonal Interspecies Chemical Screening', *Mol Cell*, 67: 711-23 e7.

Arias-Fuenzalida, J., J. Jarazo, X. Qing, J. Walter, G. Gomez-Giro, S. L. Nickels, H. Zaehres, H. R. Scholer, and J. C. Schwamborn. 2017. 'FACS-Assisted CRISPR-Cas9 Genome Editing Facilitates Parkinson's Disease Modeling', *Stem Cell Reports*, 9: 1423-31.

Ashrafi, G., J. de Juan-Sanz, R. J. Farrell, and T. A. Ryan. 2020. 'Molecular Tuning of the Axonal Mitochondrial Ca(2+) Uniporter Ensures Metabolic Flexibility of Neurotransmission', *Neuron*, 105: 678-87 e5.

Ashrafi, G., J. S. Schlehe, M. J. LaVoie, and T. L. Schwarz. 2014. 'Mitophagy of damaged mitochondria occurs locally in distal neuronal axons and requires PINK1 and Parkin', *J Cell Biol*, 206: 655-70.

Ashrafi, G., and T. L. Schwarz. 2013. 'The pathways of mitophagy for quality control and clearance of mitochondria', *Cell Death Differ*, 20: 31-42.

Bae, S., J. Park, and J. S. Kim. 2014. 'Cas-OFFinder: a fast and versatile algorithm that searches for potential off-target sites of Cas9 RNA-guided endonucleases', *Bioinformatics*, 30: 1473-5.

Balderas, E., D. R. Eberhardt, S. Lee, J. M. Pleinis, S. Sommakia, A. M. Balynas, X. Yin, M. C. Parker, C. T. Maguire, S. Cho, M. W. Szulik, A. Bakhtina, R. D. Bia, M. W. Friederich, T. M. Locke, J. L. K. Van Hove, S. G. Drakos, Y. Sancak, M. Tristani-Firouzi, S. Franklin, A. R. Rodan, and D. Chaudhuri. 2022. 'Mitochondrial calcium uniporter stabilization preserves energetic homeostasis during Complex I impairment', *Nat Commun*, 13: 2769.

Balestrino, R., and A. H. V. Schapira. 2019. 'Parkinson disease', *European Journal of Neurology*, 27: 27-42.

Barazzuol, L., F. Giamogante, M. Brini, and T. Cali. 2020. 'PINK1/Parkin Mediated Mitophagy, Ca(2+) Signalling, and ER-Mitochondria Contacts in Parkinson's Disease', *Int J Mol Sci*, 21.

Baughman, J. M., F. Perocchi, H. S. Girgis, M. Plovanich, C. A. Belcher-Timme, Y. Sancak, X. R. Bao, L. Strittmatter, O. Goldberger, R. L. Bogorad, V. Koteliansky, and V. K. Mootha. 2011. 'Integrative genomics identifies MCU as an essential component of the mitochondrial calcium uniporter', *Nature*, 476: 341-5.

Beck, M., K. Brickley, H. L. Wilkinson, S. Sharma, M. Smith, P. L. Chazot, S. Pollard, and F. A. Stephenson. 2002. 'Identification, molecular cloning, and characterization of a novel GABAA receptor-associated protein, GRIF-1', *J Biol Chem*, 277: 30079-90.

Bender, A., K. J. Krishnan, C. M. Morris, G. A. Taylor, A. K. Reeve, R. H. Perry, E. Jaros, J. S. Hersheson, J. Betts, T. Klopstock, R. W. Taylor, and D. M. Turnbull. 2006. 'High levels of mitochondrial DNA deletions in substantia nigra neurons in aging and Parkinson disease', *Nat Genet*, 38: 515-7.

Berenguer-Escuder, C., D. Grossmann, P. Antony, G. Arena, K. Wasner, F. Massart, J. Jarazo, J. Walter, J. C. Schwamborn, A. Grunewald, and R. Kruger. 2020. 'Impaired mitochondrial-endoplasmic reticulum interaction and mitophagy in Miro1-mutant neurons in Parkinson's disease', *Hum Mol Genet*, 29: 1353-64.

Berenguer-Escuder, C., D. Grossmann, F. Massart, P. Antony, L. F. Burbulla, E. Glaab, S. Imhoff, J. Trinh, P. Seibler, A. Grunewald, and R. Kruger. 2019. 'Variants in Miro1 Cause Alterations of ER-Mitochondria Contact Sites in Fibroblasts from Parkinson's Disease Patients', *J Clin Med*, 8.

Birsa, N., R. Norkett, T. Wauer, T. E. Mevissen, H. C. Wu, T. Foltynie, K. Bhatia, W. D. Hirst, D. Komander, H. Plun-Favreau, and J. T. Kittler. 2014. 'Lysine 27 ubiquitination of the mitochondrial transport protein Miro is dependent on serine 65 of the Parkin ubiquitin ligase', *J Biol Chem*, 289: 14569-82.

Bolam, J. P., and E. K. Pissadaki. 2012. 'Living on the edge with too many mouths to feed: why dopamine neurons die', *Mov Disord*, 27: 1478-83.

Bonifati, Vincenzo, Patrizia Rizzu, Marijke J. van Baren, Onno Schaap, Guido J. Breedveld, Elmar Krieger, Marieke C. J. Dekker, Ferdinando Squitieri, Pablo Ibanez, Marijke Joosse, Jeroen W. van Dongen, Nicola Vanacore, John C. van Swieten, Alexis Brice, Giuseppe Meco, Cornelia M. van Duijn, Ben A. Oostra, and Peter Heutink. 2003. 'Mutations in the DJ-1 Gene Associated with Autosomal Recessive Early-Onset Parkinsonism', *Science*, 299: 256-59.

Boureux, A., E. Vignal, S. Faure, and P. Fort. 2007. 'Evolution of the Rho family of ras-like GTPases in eukaryotes', *Mol Biol Evol*, 24: 203-16.

Brickley, K., M. J. Smith, M. Beck, and F. A. Stephenson. 2005. 'GRIF-1 and OIP106, members of a novel gene family of coiled-coil domain proteins: association in vivo and in vitro with kinesin', *J Biol Chem*, 280: 14723-32.

Brown, M. R., P. G. Sullivan, and J. W. Geddes. 2006. 'Synaptic mitochondria are more susceptible to Ca2+overload than nonsynaptic mitochondria', *J Biol Chem*, 281: 11658-68.

Brustovetsky, T., V. Li, and N. Brustovetsky. 2009. 'Stimulation of glutamate receptors in cultured hippocampal neurons causes Ca2+-dependent mitochondrial contraction', *Cell Calcium*, 46: 18-29.

Bus, C., L. Zizmare, M. Feldkaemper, S. Geisler, M. Zarani, A. Schaedler, F. Klose, J. Admard, C. J. Mageean, G. Arena, P. Fallier-Becker, A. Ugun-Klusek, K. K. Maruszczak, K. Kapolou, B. Schmid, D. Rapaport, M. Ueffing, N. Casadei, R. Kruger, T. Gasser, D. M. Vogt Weisenhorn, P. J. Kahle, C. Trautwein, C. J. Gloeckner, and J. C. Fitzgerald. 2020. 'Human Dopaminergic Neurons Lacking PINK1 Exhibit Disrupted Dopamine Metabolism Related to Vitamin B6 Co-Factors', *iScience*, 23: 101797.

Cai, Q., H. M. Zakaria, A. Simone, and Z. H. Sheng. 2012. 'Spatial parkin translocation and degradation of damaged mitochondria via mitophagy in live cortical neurons', *Curr Biol*, 22: 545-52.

Cao, X., X. M. Li, and D. D. Mousseau. 2009. 'Calcium alters monoamine oxidase-A parameters in human cerebellar and rat glial C6 cell extracts: possible influence by distinct signalling pathways', *Life Sci*, 85: 262-8.

Castro, I. G., D. M. Richards, J. Metz, J. L. Costello, J. B. Passmore, T. A. Schrader, A. Gouveia, D. Ribeiro, and M. Schrader. 2018. 'A role for Mitochondrial Rho GTPase 1 (MIRO1) in motility and membrane dynamics of peroxisomes', *Traffic*, 19: 229-42.

Chan, N. C., A. M. Salazar, A. H. Pham, M. J. Sweredoski, N. J. Kolawa, R. L. Graham, S. Hess, and D. C. Chan. 2011. 'Broad activation of the ubiquitin-proteasome system by Parkin is critical for mitophagy', *Hum Mol Genet*, 20: 1726-37.

Chang, K. T., R. F. Niescier, and K. T. Min. 2011. 'Mitochondrial matrix Ca2+ as an intrinsic signal regulating mitochondrial motility in axons', *Proc Natl Acad Sci U S A*, 108: 15456-61.

Chen, Lingling, Chunyan Liu, Jianfeng Gao, Zhiwen Xie, Lawrence W. C. Chan, Damien J. Keating, Yibin Yang, Jiazhong Sun, Fuling Zhou, Yongchang Wei, Xiuli Men, and Sijun Yang. 2017. 'Inhibition of Miro1 disturbs mitophagy and pancreatic β-cell function interfering insulin release via IRS-Akt-Foxo1 in diabetes', *Oncotarget; Vol 8, No 53*.

Chung, S. Y., S. Kishinevsky, J. R. Mazzulli, J. Graziotto, A. Mrejeru, E. V. Mosharov, L. Puspita, P. Valiulahi, D. Sulzer, T. A. Milner, T. Taldone, D. Krainc, L. Studer, and J. W. Shim. 2016. 'Parkin and PINK1 Patient iPSC-Derived Midbrain Dopamine Neurons Exhibit Mitochondrial Dysfunction and alpha-Synuclein Accumulation', *Stem Cell Reports*, 7: 664-77.

Cogliati, S., C. Frezza, M. E. Soriano, T. Varanita, R. Quintana-Cabrera, M. Corrado, S. Cipolat, V. Costa, A. Casarin, L. C. Gomes, E. Perales-Clemente, L. Salviati, P. Fernandez-Silva, J. A. Enriquez, and L. Scorrano. 2013. 'Mitochondrial cristae shape determines respiratory chain supercomplexes assembly and respiratory efficiency', *Cell*, 155: 160-71.

Colina-Tenorio, L., P. Horten, N. Pfanner, and H. Rampelt. 2020. 'Shaping the mitochondrial inner membrane in health and disease', *J Intern Med*, 287: 645-64.

Covill-Cooke, C., V. S. Toncheva, J. Drew, N. Birsa, G. Lopez-Domenech, and J. T. Kittler. 2020. 'Peroxisomal fission is modulated by the mitochondrial Rho-GTPases, Miro1 and Miro2', *EMBO Rep*, 21: e49865.

Csordas, G., D. Weaver, and G. Hajnoczky. 2018. 'Endoplasmic Reticulum-Mitochondrial Contactology: Structure and Signaling Functions', *Trends Cell Biol*, 28: 523-40.

Cummins, N., and J. Gotz. 2018. 'Shedding light on mitophagy in neurons: what is the evidence for PINK1/Parkin mitophagy in vivo?', *Cell Mol Life Sci*, 75: 1151-62.

David, G., and E. F. Barrett. 2000. 'Stimulation-evoked increases in cytosolic [Ca(2+)] in mouse motor nerve terminals are limited by mitochondrial uptake and are temperature-dependent', *The Journal of neuroscience : the official journal of the Society for Neuroscience*, 20: 7290-96.

Day, J. O., and S. Mullin. 2021. 'The Genetics of Parkinson's Disease and Implications for Clinical Practice', *Genes (Basel)*, 12.

de Brito, O. M., and L. Scorrano. 2008. 'Mitofusin 2 tethers endoplasmic reticulum to mitochondria', *Nature*, 456: 605-10.

De Mario, A., R. Quintana-Cabrera, D. Martinvalet, and M. Giacomello. 2017. '(Neuro)degenerated Mitochondria-ER contacts', *Biochem Biophys Res Commun*, 483: 1096-109.

Devine, Michael J., and Josef T. Kittler. 2018. 'Mitochondria at the neuronal presynapse in health and disease', *Nature Reviews Neuroscience*, 19: 63-80.

Eden, E., D. Lipson, S. Yogev, and Z. Yakhini. 2007. 'Discovering motifs in ranked lists of DNA sequences', *PLoS Comput Biol*, 3: e39.

Eden, E., R. Navon, I. Steinfeld, D. Lipson, and Z. Yakhini. 2009. 'GOrilla: a tool for discovery and visualization of enriched GO terms in ranked gene lists', *BMC Bioinformatics*, 10: 48.

English, A. M., M. H. Schuler, T. Xiao, B. Kornmann, J. M. Shaw, and A. L. Hughes. 2020. 'ER-mitochondria contacts promote mitochondrial-derived compartment biogenesis', *J Cell Biol*, 219.

Evans, C. S., and E. L. F. Holzbaur. 2020. 'Quality Control in Neurons: Mitophagy and Other Selective Autophagy Mechanisms', *J Mol Biol*, 432: 240-60.

Exner, N., A. K. Lutz, C. Haass, and K. F. Winklhofer. 2012. 'Mitochondrial dysfunction in Parkinson's disease: molecular mechanisms and pathophysiological consequences', *EMBO J*, 31: 3038-62.

Fatiga, F. F., L. J. Wang, T. Hsu, J. I. Capuno, and C. Y. Fu. 2021. 'Miro1 functions as an inhibitory regulator of MFN at elevated mitochondrial Ca(2+) levels', *J Cell Biochem*, 122: 1848-62.

Fazl, A., and J. Fleisher. 2018. 'Anatomy, Physiology, and Clinical Syndromes of the Basal Ganglia: A Brief Review', *Semin Pediatr Neurol*, 25: 2-9.

Fransson, A., A. Ruusala, and P. Aspenstrom. 2003. 'Atypical Rho GTPases have roles in mitochondrial homeostasis and apoptosis', *J Biol Chem*, 278: 6495-502.

Fransson, S., A. Ruusala, and P. Aspenstrom. 2006. 'The atypical Rho GTPases Miro-1 and Miro-2 have essential roles in mitochondrial trafficking', *Biochem Biophys Res Commun*, 344: 500-10.

Frederick, R. L., J. M. McCaffery, K. W. Cunningham, K. Okamoto, and J. M. Shaw. 2004. 'Yeast Miro GTPase, Gem1p, regulates mitochondrial morphology via a novel pathway', *J Cell Biol*, 167: 87-98.

Funayama, Manabu, Kenji Ohe, Taku Amo, Norihiko Furuya, Junji Yamaguchi, Shinji Saiki, Yuanzhe Li, Kotaro Ogaki, Maya Ando, Hiroyo Yoshino, Hiroyuki Tomiyama, Kenya Nishioka, Kazuko Hasegawa, Hidemoto Saiki, Wataru Satake, Kaoru Mogushi, Ryogen Sasaki, Yasumasa Kokubo, Shigeki Kuzuhara, Tatsushi Toda, Yoshikuni Mizuno, Yasuo Uchiyama, Kinji Ohno, and Nobutaka Hattori. 2015. 'CHCHD2 mutations in autosomal dominant late-onset Parkinson's disease: a genome-wide linkage and sequencing study', *The Lancet Neurology*, 14: 274-82.

Gauthier, Julie, Martin Parent, Martin Lévesque, and André Parent. 1999. 'The axonal arborization of single nigrostriatal neurons in rats', *Brain Research*, 834: 228-32.

Gehrke, S., Z. Wu, M. Klinkenberg, Y. Sun, G. Auburger, S. Guo, and B. Lu. 2015. 'PINK1 and Parkin control localized translation of respiratory chain component mRNAs on mitochondria outer membrane', *Cell Metab*, 21: 95-108.

Geisler, S., K. M. Holmstrom, D. Skujat, F. C. Fiesel, O. C. Rothfuss, P. J. Kahle, and W. Springer. 2010. 'PINK1/Parkin-mediated mitophagy is dependent on VDAC1 and p62/SQSTM1', *Nat Cell Biol*, 12: 119-31.

Giacomello, M., A. Pyakurel, C. Glytsou, and L. Scorrano. 2020. 'The cell biology of mitochondrial membrane dynamics', *Nat Rev Mol Cell Biol*, 21: 204-24.

Gioio, Anthony E., Maria Eyman, Hengshan Zhang, Zeno Scotto Lavina, Antonio Giuditta, and Barry B. Kaplan. 2001. 'Local synthesis of nuclear-encoded mitochondrial proteins in the presynaptic nerve terminal', *Journal of Neuroscience Research*, 64: 447-53.

Glater, E. E., L. J. Megeath, R. S. Stowers, and T. L. Schwarz. 2006. 'Axonal transport of mitochondria requires milton to recruit kinesin heavy chain and is light chain independent', *J Cell Biol*, 173: 545-57.

Gonzalez-Rodriguez, P., E. Zampese, K. A. Stout, J. N. Guzman, E. Ilijic, B. Yang, T. Tkatch, M. A. Stavarache, D. L. Wokosin, L. Gao, M. G. Kaplitt, J. Lopez-Barneo, P. T. Schumacker, and D. J. Surmeier. 2021. 'Disruption of mitochondrial complex I induces progressive parkinsonism', *Nature*, 599: 650-56.

Graves, S. M., Z. Xie, K. A. Stout, E. Zampese, L. F. Burbulla, J. C. Shih, J. Kondapalli, T. Patriarchi, L. Tian, L. Brichta, P. Greengard, D. Krainc, P. T. Schumacker, and D. J. Surmeier. 2020. 'Dopamine metabolism by a monoamine oxidase mitochondrial shuttle activates the electron transport chain', *Nat Neurosci*, 23: 15-20.

Grossmann, D., C. Berenguer-Escuder, M. E. Bellet, D. Scheibner, J. Bohler, F. Massart, D. Rapaport, A. Skupin, A. Fouquier d'Herouel, M. Sharma, J. Ghelfi, A. Rakovic, P. Lichtner, P. Antony, E. Glaab, P. May, K. S. Dimmer, J. C. Fitzgerald, A. Grunewald, and R. Kruger. 2019. 'Mutations in RHOT1 Disrupt Endoplasmic Reticulum-Mitochondria Contact Sites Interfering with Calcium Homeostasis and Mitochondrial Dynamics in Parkinson's Disease', *Antioxid Redox Signal*, 31: 1213-34.

Grunewald, A., K. R. Kumar, and C. M. Sue. 2019. 'New insights into the complex role of mitochondria in Parkinson's disease', *Prog Neurobiol*, 177: 73-93.

Grunewald, A., K. A. Rygiel, P. D. Hepplewhite, C. M. Morris, M. Picard, and D. M. Turnbull. 2016. 'Mitochondrial DNA Depletion in Respiratory Chain-Deficient Parkinson Disease Neurons', *Ann Neurol*, 79: 366-78.

Guillen-Samander, A., M. Leonzino, M. G. Hanna, N. Tang, H. Shen, and P. De Camilli. 2021. 'VPS13D bridges the ER to mitochondria and peroxisomes via Miro', *J Cell Biol*, 220.

Guzman, J. N., J. Sanchez-Padilla, D. Wokosin, J. Kondapalli, E. Ilijic, P. T. Schumacker, and D. J. Surmeier. 2010. 'Oxidant stress evoked by pacemaking in dopaminergic neurons is attenuated by DJ-1', *Nature*, 468: 696-700.

Hall, C. N., M. C. Klein-Flugge, C. Howarth, and D. Attwell. 2012. 'Oxidative phosphorylation, not glycolysis, powers presynaptic and postsynaptic mechanisms underlying brain information processing', *J Neurosci*, 32: 8940-51.

Hamasaki, M., N. Furuta, A. Matsuda, A. Nezu, A. Yamamoto, N. Fujita, H. Oomori, T. Noda, T. Haraguchi, Y. Hiraoka, A. Amano, and T. Yoshimori. 2013. 'Autophagosomes form at ER-mitochondria contact sites', *Nature*, 495: 389-93.

Hanna, R. A., M. N. Quinsay, A. M. Orogo, K. Giang, S. Rikka, and A. B. Gustafsson. 2012. 'Microtubule-associated protein 1 light chain 3 (LC3) interacts with Bnip3 protein to selectively remove endoplasmic reticulum and mitochondria via autophagy', *J Biol Chem*, 287: 19094-104.

Hartfield, Elizabeth M., Michiko Yamasaki-Mann, Hugo J. Ribeiro Fernandes, Jane Vowles, William S. James, Sally A. Cowley, and Richard Wade-Martins. 2014. 'Physiological Characterisation of Human iPS-Derived Dopaminergic Neurons', *PLoS One*, 9: e87388.

Hernandez, G., C. Thornton, A. Stotland, D. Lui, J. Sin, J. Ramil, N. Magee, A. Andres, G. Quarato, R. S. Carreira, M. R. Sayen, R. Wolkowicz, and R. A. Gottlieb. 2013. 'MitoTimer: a novel tool for monitoring mitochondrial turnover', *Autophagy*, 9: 1852-61.

Hevner, R. F., and M. T. Wong-Riley. 1991. 'Neuronal expression of nuclear and mitochondrial genes for cytochrome oxidase (CO) subunits analyzed by in situ hybridization: comparison with CO activity and protein', *The Journal of Neuroscience*, 11: 1942.

Hirsch, Etienne, Ann M. Graybiel, and Yves A. Agid. 1988. 'Melanized dopaminergic neurons are differentially susceptible to degeneration in Parkinson's disease', *Nature*, 334: 345-48.

Hsieh, C. H., L. Li, R. Vanhauwaert, K. T. Nguyen, M. D. Davis, G. Bu, Z. K. Wszolek, and X. Wang. 2019. 'Miro1 Marks Parkinson's Disease Subset and Miro1 Reducer Rescues Neuron Loss in Parkinson's Models', *Cell Metab*, 30: 1131-40 e7.

Hsieh, C. H., A. Shaltouki, A. E. Gonzalez, A. Bettencourt da Cruz, L. F. Burbulla, E. St Lawrence, B. Schule, D. Krainc, T. D. Palmer, and X. Wang. 2016. 'Functional Impairment in Miro Degradation and Mitophagy Is a Shared Feature in Familial and Sporadic Parkinson's Disease', *Cell Stem Cell*, 19: 709-24.

Hsu, P. D., D. A. Scott, J. A. Weinstein, F. A. Ran, S. Konermann, V. Agarwala, Y. Li, E. J. Fine, X. Wu, O. Shalem, T. J. Cradick, L. A. Marraffini, G. Bao, and F. Zhang. 2013. 'DNA targeting specificity of RNA-guided Cas9 nucleases', *Nat Biotechnol*, 31: 827-32.

Hughes, A. L., C. E. Hughes, K. A. Henderson, N. Yazvenko, and D. E. Gottschling. 2016. 'Selective sorting and destruction of mitochondrial membrane proteins in aged yeast', *Elife*, 5.

Huttemann, M., I. Lee, A. Pecinova, P. Pecina, K. Przyklenk, and J. W. Doan. 2008. 'Regulation of oxidative phosphorylation, the mitochondrial membrane potential, and their role in human disease', *J Bioenerg Biomembr*, 40: 445-56.

Inden, M., Y. Kitamura, K. Takahashi, K. Takata, N. Ito, R. Niwa, R. Funayama, K. Nishimura, T. Taniguchi, T. Honda, T. Taira, and H. Ariga. 2011. 'Protection against dopaminergic neurodegeneration in Parkinson's disease-model animals by a modulator of the oxidized form of DJ-1, a wild-type of familial Parkinson's disease-linked PARK7', *J Pharmacol Sci*, 117: 189-203.

Ishikawa, Atsushi, and Shoji Tsuji. 1996. 'Clinical analysis of 17 patients in 12 Japanese families with autosomal-recessive type juvenile parkinsonism', *Neurology*, 47: 160.

Itier, J. M., P. Ibanez, M. A. Mena, N. Abbas, C. Cohen-Salmon, G. A. Bohme, M. Laville, J. Pratt, O. Corti, L. Pradier, G. Ret, C. Joubert, M. Periquet, F. Araujo, J. Negroni, M. J. Casarejos, S. Canals, R. Solano, A. Serrano, E. Gallego, M. Sanchez, P. Denefle, J. Benavides, G. Tremp, T. A. Rooney, A. Brice, and J. Garcia de Yebenes. 2003. 'Parkin gene inactivation alters behaviour and dopamine neurotransmission in the mouse', *Hum Mol Genet*, 12: 2277-91.

Jarazo, J., X. Qing, and J. C. Schwamborn. 2019. 'Guidelines for Fluorescent Guided Biallelic HDR Targeting Selection With PiggyBac System Removal for Gene Editing', *Front Genet*, 10: 190.

Jiang, H., C. He, S. Geng, H. Sheng, X. Shen, X. Zhang, H. Li, S. Zhu, X. Chen, C. Yang, and H. Gao. 2012. 'RhoT1 and Smad4 are correlated with lymph node metastasis and overall survival in pancreatic cancer', *PLoS One*, 7: e42234.

Jiang, H., Q. Jiang, W. Liu, and J. Feng. 2006. 'Parkin suppresses the expression of monoamine oxidases', *J Biol Chem*, 281: 8591-9.

Jiang, H., Y. Ren, E. Y. Yuen, P. Zhong, M. Ghaedi, Z. Hu, G. Azabdaftari, K. Nakaso, Z. Yan, and J. Feng. 2012. 'Parkin controls dopamine utilization in human midbrain dopaminergic neurons derived from induced pluripotent stem cells', *Nat Commun*, 3: 668.

Jinek, Martin, Krzysztof Chylinski, Ines Fonfara, Michael Hauer, Jennifer A. Doudna, and Emmanuelle Charpentier. 2012. 'A programmable dual-RNA-guided DNA endonuclease in adaptive bacterial immunity', *Science (New York, N.Y.)*, 337: 816-21.

Jorgensen, S., E. O. Nielsen, D. Peters, and T. Dyhring. 2008. 'Validation of a fluorescence-based high-throughput assay for the measurement of neurotransmitter transporter uptake activity', *J Neurosci Methods*, 169: 168-76.

Kabeya, Yukiko, Noboru Mizushima, Takashi Ueno, Akitsugu Yamamoto, Takayoshi Kirisako, Takeshi Noda, Eiki Kominami, Yoshinori Ohsumi, and Tamotsu Yoshimori. 2000. 'LC3, a mammalian homologue of yeast Apg8p, is localized in autophagosome membranes after processing', *The EMBO Journal*, 19: 5720-28.

Kane, L. A., M. Lazarou, A. I. Fogel, Y. Li, K. Yamano, S. A. Sarraf, S. Banerjee, and R. J. Youle. 2014. 'PINK1 phosphorylates ubiquitin to activate Parkin E3 ubiquitin ligase activity', *J Cell Biol*, 205: 143-53.

Karunadharma, P. P., N. Basisty, Y. A. Chiao, D. F. Dai, R. Drake, N. Levy, W. J. Koh, M. J. Emond, S. Kruse, D. Marcinek, M. J. Maccoss, and P. S. Rabinovitch. 2015. 'Respiratory chain protein turnover rates in mice are highly heterogeneous but strikingly conserved across tissues, ages, and treatments', *FASEB J*, 29: 3582-92.

Kay, L. J., V. Sangal, G. W. Black, and M. Soundararajan. 2019. 'Proteomics and bioinformatics analyses identify novel cellular roles outside mitochondrial function for human miro GTPases', *Mol Cell Biochem*, 451: 21-35.

Kazlauskaite, A., V. Kelly, C. Johnson, C. Baillie, C. J. Hastie, M. Peggie, T. Macartney, H. I. Woodroof, D. R. Alessi, P. G. Pedrioli, and M. M. Muqit. 2014. 'Phosphorylation of Parkin at Serine65 is essential for activation: elaboration of a Miro1 substrate-based assay of Parkin E3 ligase activity', *Open Biol*, 4: 130213.

Kim, H. W., W. S. Choi, N. Sorscher, H. J. Park, F. Tronche, R. D. Palmiter, and Z. Xia. 2015. 'Genetic reduction of mitochondrial complex I function does not lead to loss of dopamine neurons in vivo', *Neurobiol Aging*, 36: 2617-27.

Kirichok, Yuriy, Grigory Krapivinsky, and David E. Clapham. 2004. 'The mitochondrial calcium uniporter is a highly selective ion channel', *Nature*, 427: 360-64.

Kitada, Tohru, Shuichi Asakawa, Nobutaka Hattori, Hiroto Matsumine, Yasuhiro Yamamura, Shinsei Minoshima, Masayuki Yokochi, Yoshikuni Mizuno, and Nobuyoshi Shimizu. 1998. 'Mutations in the parkin gene cause autosomal recessive juvenile parkinsonism', *Nature*, 392: 605-08.

Klosowiak, J. L., P. J. Focia, S. Chakravarthy, E. C. Landahl, D. M. Freymann, and S. E. Rice. 2013. 'Structural coupling of the EF hand and C-terminal GTPase domains in the mitochondrial protein Miro', *EMBO Rep*, 14: 968-74.

Klosowiak, J. L., S. Park, K. P. Smith, M. E. French, P. J. Focia, D. M. Freymann, and S. E. Rice. 2016. 'Structural insights into Parkin substrate lysine targeting from minimal Miro substrates', *Sci Rep*, 6: 33019.

Konig, T., H. Nolte, M. J. Aaltonen, T. Tatsuta, M. Krols, T. Stroh, T. Langer, and H. M. McBride. 2021. 'MIROs and DRP1 drive mitochondrial-derived vesicle biogenesis and promote quality control', *Nat Cell Biol*, 23: 1271-86.

Kontou, G., P. Antonoudiou, M. Podpolny, B. R. Szulc, I. L. Arancibia-Carcamo, N. F. Higgs, G. Lopez-Domenech, P. C. Salinas, E. O. Mann, and J. T. Kittler. 2021. 'Miro1-dependent mitochondrial dynamics in parvalbumin interneurons', *Elife*, 10.

Kornmann, B., C. Osman, and P. Walter. 2011. 'The conserved GTPase Gem1 regulates endoplasmic reticulum-mitochondria connections', *Proc Natl Acad Sci U S A*, 108: 14151-6.

Kornmann, B., and P. Walter. 2010. 'ERMES-mediated ER-mitochondria contacts: molecular hubs for the regulation of mitochondrial biology', *J Cell Sci*, 123: 1389-93.

Kornmann, Benoît, Erin Currie, Sean R. Collins, Maya Schuldiner, Jodi Nunnari, Jonathan S. Weissman, and Peter Walter. 2009. 'An ER-Mitochondria Tethering Complex Revealed by a Synthetic Biology Screen', *Science*, 325: 477-81.

Koyano, F., K. Okatsu, H. Kosako, Y. Tamura, E. Go, M. Kimura, Y. Kimura, H. Tsuchiya, H. Yoshihara, T. Hirokawa, T. Endo, E. A. Fon, J. F. Trempe, Y. Saeki, K. Tanaka, and N. Matsuda. 2014. 'Ubiquitin is phosphorylated by PINK1 to activate parkin', *Nature*, 510: 162-6.

Kulkarni, V. V., and S. Maday. 2018. 'Compartment-specific dynamics and functions of autophagy in neurons', *Dev Neurobiol*, 78: 298-310.

Laurent, L. C., I. Ulitsky, I. Slavin, H. Tran, A. Schork, R. Morey, C. Lynch, J. V. Harness, S. Lee, M. J. Barrero, S. Ku, M. Martynova, R. Semechkin, V. Galat, J. Gottesfeld, J. C. Izpisua Belmonte, C. Murry, H. S. Keirstead, H. S. Park, U. Schmidt, A. L. Laslett, F. J. Muller, C. M. Nievergelt, R. Shamir, and J. F. Loring. 2011. 'Dynamic changes in the copy number of pluripotency and cell proliferation genes in human ESCs and iPSCs during reprogramming and time in culture', *Cell Stem Cell*, 8: 106-18.

Lazarou, M., D. A. Sliter, L. A. Kane, S. A. Sarraf, C. Wang, J. L. Burman, D. P. Sideris, A. I. Fogel, and R. J. Youle. 2015. 'The ubiquitin kinase PINK1 recruits autophagy receptors to induce mitophagy', *Nature*, 524: 309-14.

Lee, Frank J. S., Lin Pei, Anna Moszczynska, Brian Vukusic, Paul J. Fletcher, and Fang Liu. 2007. 'Dopamine transporter cell surface localization facilitated by a direct interaction with the dopamine D2 receptor', *The EMBO Journal*, 26: 2127-36.

Lee, S., K. S. Lee, S. Huh, S. Liu, D. Y. Lee, S. H. Hong, K. Yu, and B. Lu. 2016. 'Polo Kinase Phosphorylates Miro to Control ER-Mitochondria Contact Sites and Mitochondrial Ca(2+) Homeostasis in Neural Stem Cell Development', *Dev Cell*, 37: 174-89.

Lee, Y., C. K. Min, T. G. Kim, H. K. Song, Y. Lim, D. Kim, K. Shin, M. Kang, J. Y. Kang, H. S. Youn, J. G. Lee, J. Y. An, K. R. Park, J. J. Lim, J. H. Kim, J. H. Kim, Z. Y. Park, Y. S. Kim, J. Wang, D. H. Kim, and S. H. Eom. 2015. 'Structure and function of the N-terminal domain of the human mitochondrial calcium uniporter', *EMBO Rep*, 16: 1318-33.

Li, W., M. H. Bengtson, A. Ulbrich, A. Matsuda, V. A. Reddy, A. Orth, S. K. Chanda, S. Batalov, and C. A. Joazeiro. 2008. 'Genome-wide and functional annotation of human E3 ubiquitin ligases identifies MULAN, a mitochondrial E3 that regulates the organelle's dynamics and signaling', *PLoS One*, 3: e1487.

Liang, C. L., T. T. Wang, K. Luby-Phelps, and D. C. German. 2007. 'Mitochondria mass is low in mouse substantia nigra dopamine neurons: implications for Parkinson's disease', *Exp Neurol*, 203: 370-80.

Ligon, Lee A., and Oswald Steward. 2000. 'Movement of mitochondria in the axons and dendrites of cultured hippocampal neurons', *Journal of Comparative Neurology*, 427: 340-50.

Lins, E. M., N. C. M. Oliveira, O. Reis, A. Ferrasa, R. Herai, A. R. Muotri, K. B. Massirer, and M. H. Bengtson. 2022. 'Genome-wide translation control analysis of developing human neurons', *Mol Brain*, 15: 55.

Liu, S., T. Sawada, S. Lee, W. Yu, G. Silverio, P. Alapatt, I. Millan, A. Shen, W. Saxton, T. Kanao, R. Takahashi, N. Hattori, Y. Imai, and B. Lu. 2012. 'Parkinson's disease-associated kinase PINK1 regulates Miro protein level and axonal transport of mitochondria', *PLoS Genet*, 8: e1002537.

Llorente-Folch, I., C. B. Rueda, B. Pardo, G. Szabadkai, M. R. Duchen, and J. Satrustegui. 2015. 'The regulation of neuronal mitochondrial metabolism by calcium', *J Physiol*, 593: 3447-62.

Lopez-Domenech, G., C. Covill-Cooke, D. Ivankovic, E. F. Halff, D. F. Sheehan, R. Norkett, N. Birsa, and J. T. Kittler. 2018. 'Miro proteins coordinate microtubule- and actin-dependent mitochondrial transport and distribution', *EMBO J*, 37: 321-36.

Lopez-Domenech, G., N. F. Higgs, V. Vaccaro, H. Ros, I. L. Arancibia-Carcamo, A. F. MacAskill, and J. T. Kittler. 2016. 'Loss of Dendritic Complexity Precedes

Neurodegeneration in a Mouse Model with Disrupted Mitochondrial Distribution in Mature Dendrites', *Cell Rep*, 17: 317-27.

Lopez-Domenech, G., J. H. Howden, C. Covill-Cooke, C. Morfill, J. V. Patel, R. Burli, D. Crowther, N. Birsa, N. J. Brandon, and J. T. Kittler. 2021. 'Loss of neuronal Miro1 disrupts mitophagy and induces hyperactivation of the integrated stress response', *EMBO J*, 40: e100715.

MacAskill, A. F., K. Brickley, F. A. Stephenson, and J. T. Kittler. 2009. 'GTPase dependent recruitment of Grif-1 by Miro1 regulates mitochondrial trafficking in hippocampal neurons', *Mol Cell Neurosci*, 40: 301-12.

Macaskill, A. F., J. E. Rinholm, A. E. Twelvetrees, I. L. Arancibia-Carcamo, J. Muir, A. Fransson, P. Aspenstrom, D. Attwell, and J. T. Kittler. 2009. 'Miro1 is a calcium sensor for glutamate receptor-dependent localization of mitochondria at synapses', *Neuron*, 61: 541-55.

Maday, S., and E. L. Holzbaur. 2014. 'Autophagosome biogenesis in primary neurons follows an ordered and spatially regulated pathway', *Dev Cell*, 30: 71-85.

Maday, S., K. E. Wallace, and E. L. Holzbaur. 2012. 'Autophagosomes initiate distally and mature during transport toward the cell soma in primary neurons', *J Cell Biol*, 196: 407-17.

Mallilankaraman, K., P. Doonan, C. Cardenas, H. C. Chandramoorthy, M. Muller, R. Miller, N. E. Hoffman, R. K. Gandhirajan, J. Molgo, M. J. Birnbaum, B. S. Rothberg, D. O. Mak, J. K. Foskett, and M. Madesh. 2012. 'MICU1 is an essential gatekeeper for MCU-mediated mitochondrial Ca(2+) uptake that regulates cell survival', *Cell*, 151: 630-44.

Marland, J. R., P. Hasel, K. Bonnycastle, and M. A. Cousin. 2016. 'Mitochondrial Calcium Uptake Modulates Synaptic Vesicle Endocytosis in Central Nerve Terminals', *J Biol Chem*, 291: 2080-6.

Marrone, L., C. Bus, D. Schondorf, J. C. Fitzgerald, M. Kubler, B. Schmid, P. Reinhardt, L. Reinhardt, M. Deleidi, T. Levin, A. Meixner, B. Klink, M. Glatza, C. J. Gloeckner, T. Gasser, and J. Sterneckert. 2018. 'Generation of iPSCs carrying a common LRRK2 risk allele for in vitro modeling of idiopathic Parkinson's disease', *PLoS One*, 13: e0192497.

Matsuda, W., T. Furuta, K. C. Nakamura, H. Hioki, F. Fujiyama, R. Arai, and T. Kaneko. 2009. 'Single nigrostriatal dopaminergic neurons form widely spread and highly dense axonal arborizations in the neostriatum', *J Neurosci*, 29: 444-53.

McLelland, G. L., S. A. Lee, H. M. McBride, and E. A. Fon. 2016. 'Syntaxin-17 delivers PINK1/parkin-dependent mitochondrial vesicles to the endolysosomal system', *J Cell Biol*, 214: 275-91.

Merrill, Ronald A., Kyle H. Flippo, and Stefan Strack. 2017. 'Measuring Mitochondrial Shape with ImageJ.' in, *Techniques to Investigate Mitochondrial Function in Neurons*.

Mestre, T. A., S. M. Fereshtehnejad, D. Berg, N. I. Bohnen, K. Dujardin, R. Erro, A. J. Espay, G. Halliday, J. J. van Hilten, M. T. Hu, B. Jeon, C. Klein, A. F. G. Leentjens, J. Marinus, B. Mollenhauer, R. Postuma, R. Rajalingam, M. Rodriguez-Violante, T. Simuni, D. J. Surmeier, D. Weintraub, M. P. McDermott, M. Lawton, and C. Marras. 2021. 'Parkinson's Disease Subtypes: Critical Appraisal and Recommendations', *J Parkinsons Dis*, 11: 395-404.

Miller, Kyle E., and Michael P. Sheetz. 2004. 'Axonal mitochondrial transport and potential are correlated', *Journal of Cell Science*, 117: 2791-804.

Mironov, S. L. 2007. 'ADP regulates movements of mitochondria in neurons', *Biophys J*, 92: 2944-52.

Mishra, P., and D. C. Chan. 2016. 'Metabolic regulation of mitochondrial dynamics', *J Cell Biol*, 212: 379-87.

Misko, A., S. Jiang, I. Wegorzewska, J. Milbrandt, and R. H. Baloh. 2010. 'Mitofusin 2 is necessary for transport of axonal mitochondria and interacts with the Miro/Milton complex', *J Neurosci*, 30: 4232-40.

Modi, S., G. Lopez-Domenech, E. F. Halff, C. Covill-Cooke, D. Ivankovic, D. Melandri, I. L. Arancibia-Carcamo, J. J. Burden, A. R. Lowe, and J. T. Kittler. 2019. 'Miro clusters regulate ER-mitochondria contact sites and link cristae organization to the mitochondrial transport machinery', *Nat Commun*, 10: 4399.

Monzel, A. S., L. M. Smits, K. Hemmer, S. Hachi, E. L. Moreno, T. van Wuellen, J. Jarazo, J. Walter, I. Bruggemann, I. Boussaad, E. Berger, R. M. T. Fleming, S. Bolognin, and J. C. Schwamborn. 2017. 'Derivation of Human Midbrain-Specific Organoids from Neuroepithelial Stem Cells', *Stem Cell Reports*, 8: 1144-54.

Morris, R. L., and P. J. Hollenbeck. 1993. 'The regulation of bidirectional mitochondrial transport is coordinated with axonal outgrowth', *Journal of Cell Science*, 104: 917-27.

Mukherjee, I., M. Ghosh, and M. Meinecke. 2021. 'MICOS and the mitochondrial inner membrane morphology - when things get out of shape', *FEBS Lett*, 595: 1159-83.

Nalls, Mike A., Cornelis Blauwendraat, Costanza L. Vallerga, Karl Heilbron, Sara Bandres-Ciga, Diana Chang, Manuela Tan, Demis A. Kia, Alastair J. Noyce, Angli Xue, Jose Bras, Emily Young, Rainer von Coelln, Javier Simón-Sánchez, Claudia Schulte, Manu Sharma, Lynne Krohn, Lasse Pihlstrøm, Ari Siitonen, Hirotaka Iwaki, Hampton Leonard, Faraz Faghri, J. Raphael Gibbs, Dena G. Hernandez, Sonja W. Scholz, Juan A. Botia, Maria Martinez, Jean-Christophe Corvol, Suzanne Lesage, Joseph Jankovic, Lisa M. Shulman, Margaret Sutherland, Pentti Tienari, Kari Majamaa, Mathias Toft, Ole A. Andreassen, Tushar Bangale, Alexis Brice, Jian Yang, Ziv Gan-Or, Thomas Gasser, Peter Heutink, Joshua M. Shulman, Nicholas W. Wood, David A. Hinds, John A. Hardy, Huw R. Morris, Jacob Gratten, Peter M. Visscher, Robert R. Graham, Andrew B.

Singleton, Team andMe Research, Consortium System Genomics of Parkinson's Disease, and Consortium International Parkinson's Disease Genomics. 2019. 'Identification of novel risk loci, causal insights, and heritable risk for Parkinson's disease: a meta-analysis of genome-wide association studies', *The Lancet. Neurology*, 18: 1091-102.

Narendra, D., L. A. Kane, D. N. Hauser, I. M. Fearnley, and R. J. Youle. 2010. 'p62/SQSTM1 is required for Parkin-induced mitochondrial clustering but not mitophagy; VDAC1 is dispensable for both', *Autophagy*, 6: 1090-106.

Narendra, D., A. Tanaka, D. F. Suen, and R. J. Youle. 2008. 'Parkin is recruited selectively to impaired mitochondria and promotes their autophagy', *J Cell Biol*, 183: 795-803.

Nath, Rathna, Kadee J. Raser, Iradj Hajimohammadreza, and Kevin K. W. Wang. 1997. 'Thapsigargin induces apoptosis in SH-SY5Y neuroblastoma cells and cerebrocortical cultures', *IUBMB Life*, 43: 197-205.

Nemani, N., E. Carvalho, D. Tomar, Z. Dong, A. Ketschek, S. L. Breves, F. Jana, A. M. Worth, J. Heffler, P. Palaniappan, A. Tripathi, R. Subbiah, M. F. Riitano, A. Seelam, T. Manfred, K. Itoh, S. Meng, H. Sesaki, W. J. Craigen, S. Rajan, S. Shanmughapriya, J. Caplan, B. L. Prosser, D. L. Gill, P. B. Stathopulos, G. Gallo, D. C. Chan, P. Mishra, and M. Madesh. 2018. 'MIRO-1 Determines Mitochondrial Shape Transition upon GPCR Activation and Ca(2+) Stress', *Cell Rep*, 23: 1005-19.

Nemani, N., S. Shanmughapriya, and M. Madesh. 2018. 'Molecular regulation of MCU: Implications in physiology and disease', *Cell Calcium*, 74: 86-93.

Neuspiel, M., A. C. Schauss, E. Braschi, R. Zunino, P. Rippstein, R. A. Rachubinski, M. A. Andrade-Navarro, and H. M. McBride. 2008. 'Cargo-selected transport from the mitochondria to peroxisomes is mediated by vesicular carriers', *Curr Biol*, 18: 102-8.

Nguyen, T. T., S. S. Oh, D. Weaver, A. Lewandowska, D. Maxfield, M. H. Schuler, N. K. Smith, J. Macfarlane, G. Saunders, C. A. Palmer, V. Debattisti, T. Koshiba, S. Pulst, E. L. Feldman, G. Hajnoczky, and J. M. Shaw. 2014. 'Loss of Miro1-directed mitochondrial movement results in a novel murine model for neuron disease', *Proc Natl Acad Sci U S A*, 111: E3631-40.

Niescier, R. F., K. Hong, D. Park, and K. T. Min. 2018. 'MCU Interacts with Miro1 to Modulate Mitochondrial Functions in Neurons', *J Neurosci*, 38: 4666-77.

Novak, I., V. Kirkin, D. G. McEwan, J. Zhang, P. Wild, A. Rozenknop, V. Rogov, F. Lohr, D. Popovic, A. Occhipinti, A. S. Reichert, J. Terzic, V. Dotsch, P. A. Ney, and I. Dikic. 2010. 'Nix is a selective autophagy receptor for mitochondrial clearance', *EMBO Rep*, 11: 45-51.

Obeso, J. A., M. Stamelou, C. G. Goetz, W. Poewe, A. E. Lang, D. Weintraub, D. Burn, G. M. Halliday, E. Bezard, S. Przedborski, S. Lehericy, D. J. Brooks, J. C. Rothwell, M.

Hallett, M. R. DeLong, C. Marras, C. M. Tanner, G. W. Ross, J. W. Langston, C. Klein, V. Bonifati, J. Jankovic, A. M. Lozano, G. Deuschl, H. Bergman, E. Tolosa, M. Rodriguez-Violante, S. Fahn, R. B. Postuma, D. Berg, K. Marek, D. G. Standaert, D. J. Surmeier, C. W. Olanow, J. H. Kordower, P. Calabresi, A. H. V. Schapira, and A. J. Stoessl. 2017. 'Past, present, and future of Parkinson's disease: A special essay on the 200th Anniversary of the Shaking Palsy', *Mov Disord*, 32: 1264-310.

Oeding, S. J., K. Majstrowicz, X. P. Hu, V. Schwarz, A. Freitag, U. Honnert, P. Nikolaus, and M. Bahler. 2018. 'Identification of Miro1 and Miro2 as mitochondrial receptors for myosin XIX', *J Cell Sci*, 131.

Okumoto, K., T. Ono, R. Toyama, A. Shimomura, A. Nagata, and Y. Fujiki. 2018. 'New splicing variants of mitochondrial Rho GTPase-1 (Miro1) transport peroxisomes', *J Cell Biol*, 217: 619-33.

Pacelli, C., N. Giguere, M. J. Bourque, M. Levesque, R. S. Slack, and L. E. Trudeau. 2015. 'Elevated Mitochondrial Bioenergetics and Axonal Arborization Size Are Key Contributors to the Vulnerability of Dopamine Neurons', *Curr Biol*, 25: 2349-60.

Pan, X., J. Liu, T. Nguyen, C. Liu, J. Sun, Y. Teng, M. M. Fergusson, Rovira, II, M. Allen, D. A. Springer, A. M. Aponte, M. Gucek, R. S. Balaban, E. Murphy, and T. Finkel. 2013. 'The physiological role of mitochondrial calcium revealed by mice lacking the mitochondrial calcium uniporter', *Nat Cell Biol*, 15: 1464-72.

Paquet, D., D. Kwart, A. Chen, A. Sproul, S. Jacob, S. Teo, K. M. Olsen, A. Gregg, S. Noggle, and M. Tessier-Lavigne. 2016. 'Efficient introduction of specific homozygous and heterozygous mutations using CRISPR/Cas9', *Nature*, 533: 125-9.

Perkins, G. A., J. Tjong, J. M. Brown, P. H. Poquiz, R. T. Scott, D. R. Kolson, M. H. Ellisman, and G. A. Spirou. 2010. 'The micro-architecture of mitochondria at active zones: electron tomography reveals novel anchoring scaffolds and cristae structured for high-rate metabolism', *J Neurosci*, 30: 1015-26.

Perocchi, F., V. M. Gohil, H. S. Girgis, X. R. Bao, J. E. McCombs, A. E. Palmer, and V. K. Mootha. 2010. 'MICU1 encodes a mitochondrial EF hand protein required for Ca(2+) uptake', *Nature*, 467: 291-6.

Peters, D. T., L. Kay, J. Eswaran, J. H. Lakey, and M. Soundararajan. 2018. 'Human Miro Proteins Act as NTP Hydrolases through a Novel, Non-Canonical Catalytic Mechanism', *Int J Mol Sci*, 19.

Pickles, S., P. Vigie, and R. J. Youle. 2018. 'Mitophagy and Quality Control Mechanisms in Mitochondrial Maintenance', *Curr Biol*, 28: R170-R85.

Pissadaki, E. K., and J. P. Bolam. 2013. 'The energy cost of action potential propagation in dopamine neurons: clues to susceptibility in Parkinson's disease', *Front Comput Neurosci*, 7: 13.

Polymeropoulos, Mihael H., Christian Lavedan, Elisabeth Leroy, Susan E. Ide, Anindya Dehejia, Amalia Dutra, Brian Pike, Holly Root, Jeffrey Rubenstein, Rebecca Boyer, Edward S. Stenroos, Settara Chandrasekharappa, Aglaia Athanassiadou, Theodore Papapetropoulos, William G. Johnson, Alice M. Lazzarini, Roger C. Duvoisin, Giuseppe Di Iorio, Lawrence I. Golbe, and Robert L. Nussbaum. 1997. 'Mutation in the α-Synuclein Gene Identified in Families with Parkinson's Disease', *Science*, 276: 2045-47.

Ramsay, Rona R., and Alen Albreht. 2021. 'Questions in the Chemical Enzymology of MAO', *Chemistry*, 3: 959-78.

Ran, F. A., P. D. Hsu, J. Wright, V. Agarwala, D. A. Scott, and F. Zhang. 2013. 'Genome engineering using the CRISPR-Cas9 system', *Nat Protoc*, 8: 2281-308.

Rangaraju, V., N. Calloway, and T. A. Ryan. 2014. 'Activity-driven local ATP synthesis is required for synaptic function', *Cell*, 156: 825-35.

Reinhardt, P., M. Glatza, K. Hemmer, Y. Tsytsyura, C. S. Thiel, S. Hoing, S. Moritz, J. A. Parga, L. Wagner, J. M. Bruder, G. Wu, B. Schmid, A. Ropke, J. Klingauf, J. C. Schwamborn, T. Gasser, H. R. Scholer, and J. Sterneckert. 2013. 'Derivation and expansion using only small molecules of human neural progenitors for neurodegenerative disease modeling', *PLoS One*, 8: e59252.

Rogaeva, Ekaterina, Janel Johnson, Anthony E. Lang, Cindy Gulick, Katrina Gwinn-Hardy, Toshitaka Kawarai, Christine Sato, Angharad Morgan, John Werner, Robert Nussbaum, Agnes Petit, Michael S. Okun, Aideen McInerney, Ronald Mandel, Justus L. Groen, Hubert H. Fernandez, Ron Postuma, Kelly D. Foote, Shabnam Salehi-Rad, Yan Liang, Sharon Reimsnider, Anurag Tandon, John Hardy, Peter St George-Hyslop, and Andrew B. Singleton. 2004. 'Analysis of the PINK1 Gene in a Large Cohort of Cases With Parkinson Disease', *Archives of Neurology*, 61: 1898-904.

Rosenbusch, K. E., and A. Kortholt. 2016. 'Activation Mechanism of LRRK2 and Its Cellular Functions in Parkinson's Disease', *Parkinsons Dis*, 2016: 7351985.

Saeed, M. 2018. 'Genomic convergence of locus-based GWAS meta-analysis identifies AXIN1 as a novel Parkinson's gene', *Immunogenetics*, 70: 563-70.

Safiulina, D., M. Kuum, V. Choubey, N. Gogichaishvili, J. Liiv, M. A. Hickey, M. Cagalinec, M. Mandel, A. Zeb, M. Liiv, and A. Kaasik. 2019. 'Miro proteins prime mitochondria for Parkin translocation and mitophagy', *EMBO J*, 38.

Saotome, Masao, Dzhamilja Safiulina, György Szabadkai, Sudipto Das, Asa Fransson, Pontus Aspenstrom, Rosario Rizzuto, and György Hajnóczky. 2008. 'Bidirectional Ca2+-dependent control of mitochondrial dynamics by the Miro GTPase', *Proceedings of the National Academy of Sciences of the United States of America*, 105: 20728-33.

Sarraf, S. A., M. Raman, V. Guarani-Pereira, M. E. Sowa, E. L. Huttlin, S. P. Gygi, and J. W. Harper. 2013. 'Landscape of the PARKIN-dependent ubiquitylome in response to mitochondrial depolarization', *Nature*, 496: 372-6.

Schapira, A. H. V., J. M. Cooper, D. Dexter, P. Jenner, J. B. Clark, and C. D. Marsden. 1989. 'MITOCHONDRIAL COMPLEX I DEFICIENCY IN PARKINSON'S DISEASE', *The Lancet*, 333: 1269.

Schuler, M. H., A. M. English, T. Xiao, T. J. Campbell, J. M. Shaw, and A. L. Hughes. 2021. 'Mitochondrial-derived compartments facilitate cellular adaptation to amino acid stress', *Mol Cell*, 81: 3786-802 e13.

Schwarz, L., and J. C. Fitzgerald. 2022. 'Steady-State Levels of Miro1 Linked to Phosphorylation at Serine 156 and Mitochondrial Respiration in Dopaminergic Neurons', *Cells*, 11.

Seibler, P., J. Graziotto, H. Jeong, F. Simunovic, C. Klein, and D. Krainc. 2011. 'Mitochondrial Parkin recruitment is impaired in neurons derived from mutant PINK1 induced pluripotent stem cells', *J Neurosci*, 31: 5970-6.

Shaltouki, A., C. H. Hsieh, M. J. Kim, and X. Wang. 2018. 'Alpha-synuclein delays mitophagy and targeting Miro rescues neuron loss in Parkinson's models', *Acta Neuropathol*, 136: 607-20.

Shi, P., X. Ren, J. Meng, C. Kang, Y. Wu, Y. Rong, S. Zhao, Z. Jiang, L. Liang, W. He, Y. Yin, X. Li, Y. Liu, X. Huang, Y. Sun, B. Li, and C. Wu. 2022. 'Mechanical instability generated by Myosin 19 contributes to mitochondria cristae architecture and OXPHOS', *Nat Commun*, 13: 2673.

Shlevkov, E., T. Kramer, J. Schapansky, M. J. LaVoie, and T. L. Schwarz. 2016. 'Miro phosphorylation sites regulate Parkin recruitment and mitochondrial motility', *Proc Natl Acad Sci U S A*, 113: E6097-E106.

Smith, K. P., P. J. Focia, S. Chakravarthy, E. C. Landahl, J. L. Klosowiak, S. E. Rice, and D. M. Freymann. 2020. 'Insight into human Miro1/2 domain organization based on the structure of its N-terminal GTPase', *J Struct Biol*, 212: 107656.

Soubannier, V., G. L. McLelland, R. Zunino, E. Braschi, P. Rippstein, E. A. Fon, and H. M. McBride. 2012. 'A vesicular transport pathway shuttles cargo from mitochondria to lysosomes', *Curr Biol*, 22: 135-41.

Soubannier, V., P. Rippstein, B. A. Kaufman, E. A. Shoubridge, and H. M. McBride. 2012. 'Reconstitution of mitochondria derived vesicle formation demonstrates selective enrichment of oxidized cargo', *PLoS One*, 7: e52830.

Spillane, M., A. Ketschek, T. T. Merianda, J. L. Twiss, and G. Gallo. 2013. 'Mitochondria coordinate sites of axon branching through localized intra-axonal protein synthesis', *Cell Rep*, 5: 1564-75.

Stavoe, A. K. H., and E. L. F. Holzbaur. 2019. 'Autophagy in Neurons', *Annu Rev Cell Dev Biol*, 35: 477-500.

Stemmer, M., T. Thumberger, M. Del Sol Keyer, J. Wittbrodt, and J. L. Mateo. 2015. 'CCTop: An Intuitive, Flexible and Reliable CRISPR/Cas9 Target Prediction Tool', *PLoS One*, 10: e0124633.

Stephan, T., C. Bruser, M. Deckers, A. M. Steyer, F. Balzarotti, M. Barbot, T. S. Behr, G. Heim, W. Hubner, P. Ilgen, F. Lange, D. Pacheu-Grau, J. K. Pape, S. Stoldt, T. Huser, S. W. Hell, W. Mobius, P. Rehling, D. Riedel, and S. Jakobs. 2020. 'MICOS assembly controls mitochondrial inner membrane remodeling and crista junction redistribution to mediate cristae formation', *EMBO J*, 39: e104105.

Stephen, T. L., N. F. Higgs, D. F. Sheehan, S. Al Awabdh, G. Lopez-Domenech, I. L. Arancibia-Carcamo, and J. T. Kittler. 2015. 'Miro1 Regulates Activity-Driven Positioning of Mitochondria within Astrocytic Processes Apposed to Synapses to Regulate Intracellular Calcium Signaling', *J Neurosci*, 35: 15996-6011.

Sterky, F. H., S. Lee, R. Wibom, L. Olson, and N. G. Larsson. 2011. 'Impaired mitochondrial transport and Parkin-independent degeneration of respiratory chain-deficient dopamine neurons in vivo', *Proc Natl Acad Sci U S A*, 108: 12937-42.

Stroud, D. A., S. Oeljeklaus, S. Wiese, M. Bohnert, U. Lewandrowski, A. Sickmann, B. Guiard, M. van der Laan, B. Warscheid, and N. Wiedemann. 2011. 'Composition and topology of the endoplasmic reticulum-mitochondria encounter structure', *J Mol Biol*, 413: 743-50.

Sugiura, A., G. L. McLelland, E. A. Fon, and H. M. McBride. 2014. 'A new pathway for mitochondrial quality control: mitochondrial-derived vesicles', *EMBO J*, 33: 2142-56.

Sun, T., H. Qiao, P. Y. Pan, Y. Chen, and Z. H. Sheng. 2013. 'Motile axonal mitochondria contribute to the variability of presynaptic strength', *Cell Rep*, 4: 413-19.

Surmeier, D. J. 2018. 'Determinants of dopaminergic neuron loss in Parkinson's disease', *FEBS J*, 285: 3657-68.

Taira, T., Y. Saito, T. Niki, S. M. Iguchi-Ariga, K. Takahashi, and H. Ariga. 2004. 'DJ-1 has a role in antioxidative stress to prevent cell death', *EMBO Rep*, 5: 213-8.

Takahashi, K., K. Tanabe, M. Ohnuki, M. Narita, T. Ichisaka, K. Tomoda, and S. Yamanaka. 2007. 'Induction of pluripotent stem cells from adult human fibroblasts by defined factors', *Cell*, 131: 861-72.

Tang, Yun-gui, and Robert S. Zucker. 1997. 'Mitochondrial Involvement in Post-Tetanic Potentiation of Synaptic Transmission', *Neuron*, 18: 483-91.

Tanti, G. K., and S. K. Goswami. 2014. 'SG2NA recruits DJ-1 and Akt into the mitochondria and membrane to protect cells from oxidative damage', *Free Radic Biol Med*, 75: 1-13.

Thomas, K. J., M. K. McCoy, J. Blackinton, A. Beilina, M. van der Brug, A. Sandebring, D. Miller, D. Maric, A. Cedazo-Minguez, and M. R. Cookson. 2011. 'DJ-1 acts in parallel to the PINK1/parkin pathway to control mitochondrial function and autophagy', *Hum Mol Genet*, 20: 40-50.

Tilokani, L., S. Nagashima, V. Paupe, and J. Prudent. 2018. 'Mitochondrial dynamics: overview of molecular mechanisms', *Essays Biochem*, 62: 341-60.

Tinevez, J. Y., N. Perry, J. Schindelin, G. M. Hoopes, G. D. Reynolds, E. Laplantine, S. Y. Bednarek, S. L. Shorte, and K. W. Eliceiri. 2017. 'TrackMate: An open and extensible platform for single-particle tracking', *Methods*, 115: 80-90.

Tirrell, P. S., K. N. Nguyen, K. Luby-Phelps, and J. R. Friedman. 2020. 'MICOS subcomplexes assemble independently on the mitochondrial inner membrane in proximity to ER contact sites', *J Cell Biol*, 219.

Towers, C. G., D. K. Wodetzki, J. Thorburn, K. R. Smith, M. C. Caino, and A. Thorburn. 2021. 'Mitochondrial-derived vesicles compensate for loss of LC3-mediated mitophagy', *Dev Cell*, 56: 2029-42 e5.

Tsai, P. I., M. M. Course, J. R. Lovas, C. H. Hsieh, M. Babic, K. E. Zinsmaier, and X. Wang. 2014. 'PINK1-mediated phosphorylation of Miro inhibits synaptic growth and protects dopaminergic neurons in Drosophila', *Sci Rep*, 4: 6962.

Vaccaro, V., M. J. Devine, N. F. Higgs, and J. T. Kittler. 2017. 'Miro1-dependent mitochondrial positioning drives the rescaling of presynaptic Ca2+ signals during homeostatic plasticity', *EMBO Rep*, 18: 231-40.

Valente Enza, Maria, M. Abou-Sleiman Patrick, Viviana Caputo, M. K. Muqit Miratul, Kirsten Harvey, Suzana Gispert, Zeeshan Ali, Domenico Del Turco, Rita Bentivoglio Anna, G. Healy Daniel, Alberto Albanese, Robert Nussbaum, Rafael González-Maldonado, Thomas Deller, Sergio Salvi, Pietro Cortelli, P. Gilks William, S. Latchman David, J. Harvey Robert, Bruno Dallapiccola, Georg Auburger, and W. Wood Nicholas. 2004. 'Hereditary Early-Onset Parkinson's Disease Caused by Mutations in PINK1', *Science*, 304: 1158-60.

Valley, M. P., W. Zhou, E. M. Hawkins, J. Shultz, J. J. Cali, T. Worzella, L. Bernad, T. Good, D. Good, T. L. Riss, D. H. Klaubert, and K. V. Wood. 2006. 'A bioluminescent assay for monoamine oxidase activity', *Anal Biochem*, 359: 238-46.

van Duijn, C. M., M. C. Dekker, V. Bonifati, R. J. Galjaard, J. J. Houwing-Duistermaat, P. J. Snijders, L. Testers, G. J. Breedveld, M. Horstink, L. A. Sandkuijl, J. C. van Swieten, B. A. Oostra, and P. Heutink. 2001. 'Park7, a novel locus for autosomal recessive early-onset parkinsonism, on chromosome 1p36', *Am J Hum Genet*, 69: 629-34.

Van Laar, V. S., B. Arnold, S. J. Cassady, C. T. Chu, E. A. Burton, and S. B. Berman. 2011. 'Bioenergetics of neurons inhibit the translocation response of Parkin following rapid mitochondrial depolarization', *Hum Mol Genet*, 20: 927-40.

van Spronsen, M., M. Mikhaylova, J. Lipka, M. A. Schlager, D. J. van den Heuvel, M. Kuijpers, P. S. Wulf, N. Keijzer, J. Demmers, L. C. Kapitein, D. Jaarsma, H. C. Gerritsen, A. Akhmanova, and C. C. Hoogenraad. 2013. 'TRAK/Milton motor-adaptor proteins steer mitochondrial trafficking to axons and dendrites', *Neuron*, 77: 485-502.

Verstreken, P., C. V. Ly, K. J. Venken, T. W. Koh, Y. Zhou, and H. J. Bellen. 2005. 'Synaptic mitochondria are critical for mobilization of reserve pool vesicles at Drosophila neuromuscular junctions', *Neuron*, 47: 365-78.

Vincow, E. S., G. Merrihew, R. E. Thomas, N. J. Shulman, R. P. Beyer, M. J. MacCoss, and L. J. Pallanck. 2013. 'The PINK1-Parkin pathway promotes both mitophagy and selective respiratory chain turnover in vivo', *Proc Natl Acad Sci U S A*, 110: 6400-5.

Vives-Bauza, C., C. Zhou, Y. Huang, M. Cui, R. L. de Vries, J. Kim, J. May, M. A. Tocilescu, W. Liu, H. S. Ko, J. Magrane, D. J. Moore, V. L. Dawson, R. Grailhe, T. M. Dawson, C. Li, K. Tieu, and S. Przedborski. 2010. 'PINK1-dependent recruitment of Parkin to mitochondria in mitophagy', *Proc Natl Acad Sci U S A*, 107: 378-83.

Wang, X., and T. L. Schwarz. 2009. 'The mechanism of Ca2+ -dependent regulation of kinesin-mediated mitochondrial motility', *Cell*, 136: 163-74.

Wang, X., D. Winter, G. Ashrafi, J. Schlehe, Y. L. Wong, D. Selkoe, S. Rice, J. Steen, M. J. LaVoie, and T. L. Schwarz. 2011. 'PINK1 and Parkin target Miro for phosphorylation and degradation to arrest mitochondrial motility', *Cell*, 147: 893-906.

Weihofen, A., K. J. Thomas, B. L. Ostaszewski, M. R. Cookson, and D. J. Selkoe. 2009. 'Pink1 forms a multiprotein complex with Miro and Milton, linking Pink1 function to mitochondrial trafficking', *Biochemistry*, 48: 2045-52.

Wszolek, Z. K., B. Pfeiffer, J. R. Fulgham, J. E. Parisi, B. M. Thompson, R. J. Uitti, D. B. Calne, and R. F. Pfeiffer. 1995. 'Western Nebraska Family (Family D) with Autosomal Dominant Parkinsonism', *Neurology*, 45: 502.

Yapa, N. M. B., V. Lisnyak, B. Reljic, and M. T. Ryan. 2021. 'Mitochondrial dynamics in health and disease', *FEBS Lett*, 595: 1184-204.

Yun, J., R. Puri, H. Yang, M. A. Lizzio, C. Wu, Z. H. Sheng, and M. Guo. 2014. 'MUL1 acts in parallel to the PINK1/parkin pathway in regulating mitofusin and compensates for loss of PINK1/parkin', *Elife*, 3: e01958.

Zampese, E., and D. J. Surmeier. 2020. 'Calcium, Bioenergetics, and Parkinson's Disease', *Cells*, 9.

Zheng, X., L. Boyer, M. Jin, J. Mertens, Y. Kim, L. Ma, L. Ma, M. Hamm, F. H. Gage, and T. Hunter. 2016. 'Metabolic reprogramming during neuronal differentiation from aerobic glycolysis to neuronal oxidative phosphorylation', *Elife*, 5.

Zhou, W., D. Ma, A. X. Sun, H. D. Tran, D. L. Ma, B. K. Singh, J. Zhou, J. Zhang, D. Wang, Y. Zhao, P. M. Yen, E. Goh, and E. K. Tan. 2019. 'PD-linked CHCHD2 mutations impair CHCHD10 and MICOS complex leading to mitochondria dysfunction', *Hum Mol Genet*, 28: 1100-16.

Zimprich, A., S. Biskup, P. Leitner, P. Lichtner, M. Farrer, S. Lincoln, J. Kachergus, M. Hulihan, R. J. Uitti, D. B. Calne, A. J. Stoessl, R. F. Pfeiffer, N. Patenge, I. C. Carbajal, P. Vieregge, F. Asmus, B. Muller-Myhsok, D. W. Dickson, T. Meitinger, T. M. Strom, Z. K. Wszolek, and T. Gasser. 2004. 'Mutations in LRRK2 cause autosomal-dominant parkinsonism with pleomorphic pathology', *Neuron*, 44: 601-7.

11. Appendix

Manuscript 1:

Generation of R272Q, S156A and K572R RHOT1/Miro1 mutations in iPSCs from a healthy individual using FACS-assisted CRISPR/Cas9 genome editing

Lisa Schwarz, Nicolas Casadei and Julia C. Fitzgerald

Stem Cell Res 55: 102469; doi: 10.1016/j.scr.2021.102469; PMID: 34359002

Supplementary Figure

Manuscript 2:

Steady-state levels of Miro1 Linked to Phosphorylation at Serine 156 and Mitochondrial Respiration in Dopaminergic Neurons

Lisa Schwarz and Julia C. Fitzgerald

Cells 11(8); doi: 10.3390/cells11081269; PMID: 35455950

Supplementary Figure

Manuscript 3:

Miro1 R272Q Disrupts Mitochondrial calcium Handling and Neurotransmitter Uptake in Dopaminergic Neurons

Lisa Schwarz, Lorenzo D. Dodi, Lara-Sophie Rieder, Petra Fallier-Becker, Nicolas Casadei and Julia C. Fitzgerald

Submitted in *Frontiers in Molecular Neuroscience* June 10th, 2022; this paper was under revision when this thesis was submitted and accepted November 11th, 2022, published December 2nd, 2022. Section 0 describes and discusses the results of this manuscript under revision (appended manuscript and supplementary documents represent revision stage as of August 24th, 2022).

Supplementary Figures

Supplementary Methods

Stem Cell Research 55 (2021) 102469

Contents lists available at ScienceDirect

Stem Cell Research

journal homepage: www.elsevier.com/locate/scr

Lab Resource: Genetically-Modified Multiple Cell Lines

Generation of R272Q, S156A and K572R RHOT1/Miro1 point mutations in iPSCs from a healthy individual using FACS-assisted CRISPR/Cas9 genome editing

Lisa Schwarz [a], Nicolas Casadei [b,c], Julia C. Fitzgerald [a,*]

[a] *Department of Neurodegeneration, Hertie Institute for Clinical Brain Research, The University of Tübingen, Germany*
[b] *Institute of Medical Genetics and Applied Genomics, The University of Tübingen, Germany*
[c] *NGS Competence Center Tübingen, The University of Tübingen, Germany*

ABSTRACT

The GTPase Miro1 is tail anchored into the mitochondrial outer membrane and tethers mitochondria to molecular motors which is crucial for mitochondrial transport. Miro1 contains two EF hand, ion binding domains important for calcium sequestration. Miro1 is associated with Parkinson's disease (PD) due to its suggested interaction with PINK1 and Parkin. Rare variants in *RHOT1* (encoding Miro1) were found in PD patients but Miro1′s function in the brain is understudied. We gene edited three point mutations in healthy iPSCS

EF hand R272Q was identified in a PD patient, S156A abolishes the proposed PINK1 phosphorylation site, K572R abolishes the main lysine targeted by pSer65-parkin.

Resource Table:

Unique stem cell lines identifier	HIHTFi001-A HIHTFi001-B HIHTFi001-C
Alternative name(s) of stem cell lines	R272Q (HIHTFi001-A) S156A (HIHTFi001-B) K572R (HIHTFi001-C)
Institution	Hertie Institute for Clinical Brain Research, University of Tübingen
Contact information of the reported cell line distributor	Julia Fitzgerald Julia.Fitzgerald@uni-tuebingen.de
Type of cell lines	iPSC
Origin	Human
Additional origin info *(applicable for human ESC or iPSC)*	Age 77 Sex female
Cell Source	Fibroblasts
Method of reprogramming	episomal (Marrone et al. 2018)
Clonality	Clonal
Evidence of the reprogramming transgene loss (including genomic copy if applicable)	(Marrone et al. 2018)
Cell culture system used	see Methods
Type of Genetic Modification	CRISPR/Cas9-mediated point mutation
Associated disease	S156A & K572R No formal disease association R272Q OMIM # 168600 PARKINSON DISEASE, LATE-ONSET PD (Grossmann et al. 2019)
Gene/locus	R272Q *RHOT1* c.815G > A p.Arg272Gln (heterozygous) OMIM # 168600 S156A *RHOT1* c.466 T > G p.Ser156Ala (homozygous) K572R *RHOT1* c.1714_1716AAA > CGG p.Lys572Arg (heterozygous)
Method of modification/site-specific nuclease used	CRISPR/Cas9
Site-specific nuclease (SSN) delivery method	Plasmid transfection
All genetic material introduced into the cells	Crispr/Cas9 plasmid DONOR plasmids
Analysis of the nuclease-targeted allele status	Sanger sequencing mutation site Exome sequencing
Method of the off-target nuclease activity surveillance	Sanger sequencing off-target sites Exome sequencing
Name of transgene	N/A

(*continued on next column*)

(*continued*)

(*continued on next page*)

---

* Corresponding author.
E-mail address: Julia.Fitzgerald@uni-tuebingen.de (J.C. Fitzgerald).

https://doi.org/10.1016/j.scr.2021.102469
Received 16 June 2021; Accepted 15 July 2021
Available online 25 July 2021

(*continued*)

Eukaryotic selective agent resistance (including inducible/gene expressing cell-specific)	N/A
Inducible/constitutive system details	N/A
Date archived/stock date	December 2019; February/May 2020
Cell line repository/bank	N/A
Ethical/GMO work approvals	Ethical approval, University of Tübingen. Consent and ethical approval according to The Hertie Institute for Clinical Brain Research Biobank. # 146120098O1.
Addgene/public access repository recombinant DNA sources' disclaimers (if applicable)	CRISPR/Cas9 plasmid pX330-U6-Chimeric_BB-CBh-hSpCas9 was a gift from Feng Zhang (Addgene plasmid # 42,230 http://n2t.net/addgene:42230 RRID:Addgene_42230) Repair template plasmidspDONOR-tagBFP-PSM-EGFP was a gift from Jens Schwamborn (Addgene plasmid # 100,603 http://n2t.net/addgene:100603 RRID:Addgene_100603) pDONOR-tagBFP-PSM-dTOMATO was a gift from Jens Schwamborn (Addgene plasmid # 100,604 http://n2t.net/addgene:100604 RRID:Addgene_100604)

1. Introduction

1.1. *Resource utility*

Miro1 has been linked to the neurodegenerative disease Parkinson's disease (PD) and therefore we generated isogenic iPSC models to elucidate three possible Miro1 related PD mechanisms. EF hand R272Q models a heterozygous mutation found in a PD patient, S156A and K572R are functional mutations introduced to study the possible interaction with the PINK1-Parkin pathway. Table 1

1.2. *Resource details*

In this study we gene edited point mutations in *RHOT1* (encoding Miro1) in healthy iPSCs using FACS-assisted CRISPR/Cas9 genome editing (Arias-Fuenzalida et al., 2017). We previously characterised the healthy donor iPSCs (Marrone et al., 2018). In summary, iPSCs were transfected with a CRISPR/Cas9 plasmid as well as repair template plasmids, which additionally inserted selection markers at the site of edit. The insertion of the selection markers was reversible resulting in a scarless gene edit at the respective mutation sites. Three different mutations were introduced

Heterozygous R272Q was found in a PD patient (Grossmann et al., 2019) homozygous S156A is a phospho null mutant for a putative PINK1 phosphorylation site (Wang et al., 2011) heterozygous K572R is a ubiquitin null muatant for the preferred lysine targeted by pS65-parkin (Klosowiak et al., 2016). The R272Q mutation is localised within the first EF hand domain, the S156A mutation in the first GTPase domain and the K572R in the second GTPase domain (Fig. 1A).

iPSC clones carrying scarless gene edit were Sanger sequenced to validate the presence of mutation showing that the gene edit was correctly introduced (Fig. 1A). Sanger sequencing of the most likely off-target sites for each gRNA revealed that all sites remained unchanged (Supplementary Fig. A). To validate the genomic integrity and identity of the isogenic iPSC lines, exome sequencing was performed and no abnormalities were detected (Fig. 1E). For the interpretation of the variants, we excluded genetic variants present in the isogenic control or with an allele frequency smaller than 30%. We also ignored CNVs smaller than 50 kb.

We further validated the absence of random integration events as well as selection markers (Supplementary Figs. B and D). The iPSCs tested negative for mycoplasma (Supplementary Fig. C). The fibroblast source of the iPSCs tested negative for HIV, HBV and HCV. The iPSCs have normal morphology (Supplementary Fig. D).

The expression of pluripotency markers was assessed by quantitative RT-PCR (Fig. 1B) and immunofluorescence (Fig. 1C). The iPSC lines show comparable expression of pluripotency markers Oct4, NanoG and Klf4 between the parental iPSC line (isogenic control) and all three daughter cells lines R272Q, S156A and K572R (Fig. 1B). We demonstrated differentiation potential by trilineage differentiation assay and subsequent assessment of endodermal (FoxA2), mesodermal (SMA) and ectodermal (Nestin) cell lineage markers (Fig. 1D).

Table 1
Characterization and validation.

Classification	Test	Result	Data
Morphology	Photography	Normal	Supplementary Fig. D
Pluripotency status evidence for the described cell line	Qualitative analysis	Immunocytochemistry of pluripotency markers Oct4, SSEA4, Tra1-81	Fig. 1 panel C
	Quantitative analysis	RT-qPCR for Oct4, NanoG and Klf4	Fig. 1 panel B
Karyotype	Karyotype (G-banding) and higher-resolution, array-based assays	Exome sequencing	Fig. 1 panel E
Genotyping for the desired genomic alteration/ allelic status of the gene of interest	PCR across the edited site or targeted allele-specific PCR	Sanger sequencing for each mutation	Fig. 1 panel A
	Transgene-specific PCR	N/A	N/A
Verification of the absence of random plasmid integration events	PCR/Southern	PCR plasmid backbone and junction between backbone and PSM	Supplementary Fig. B
Parental and modified cell line genetic identity evidence	STR analysis, microsatellite PCR (mPCR) or specific (mutant) allele seq	Exome sequencing	Fig. 1 panel E
Mutagenesis/genetic modification outcome analysis	Sequencing (genomic DNA PCR or RT-PCR product)		Fig. 1 panel A
	PCR-based analyses	N/A	N/A
	Southern Blot or WGS western blotting (for knock-outs, KOs)	N/A	N/A
Off-target nuclease analysis-	PCR across top 5/10 predicted top likely off-target sites, whole genome/exome sequencing	Sanger sequencing of top off-target sites	Supplementary Fig. A
Specific pathogen-free status	Mycoplasma	PCR-based Mycoplasma test	Negative Supplementary Fig. C
Multilineage differentiation potential	e.g. embryoid body formation OR Teratoma formation OR Scorecard OR Directed differentiation	Trilineage Differentiation	Fig. 1 panel D
Donor screening (OPTIONAL)	HIV 1, Hepatitis B, Hepatitis C	Negative	Not shown but available with author
Genotype – additional histocompatibility info (OPTIONAL)	Blood group genotyping	N/A	N/A
	HLA tissue typing	N/A	N/A

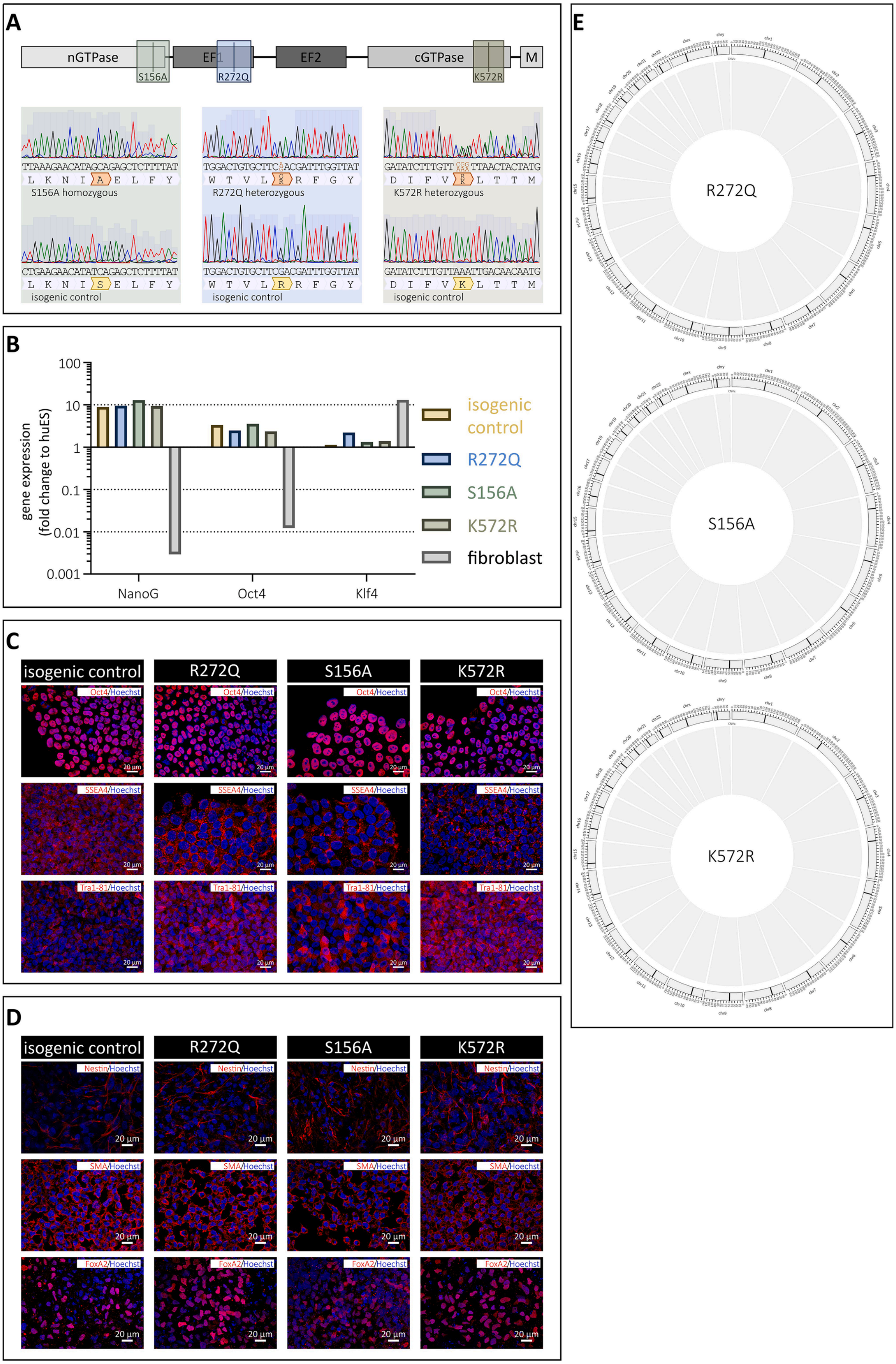

(caption on next page)

Fig. 1. A) Diagram of Miro1 protein structure showing the location of S156A in the N-terminal GTPase domain, R272Q in the first EF hand domain and K572R in the C-terminal GTPase domain. Confirmation of introduced mutations by Sanger sequencing. B) Gene expression of NanoG, Oct4 and Klf4 in the three Miro1 mutant iPSC lines, the isogenic, healthy control and healthy human fibroblasts as a negative control. The gene expression is shown as fold change to a human embryonic stem cell (huES) template control. C) Immunofluorescence of iPSCs stained for pluripotency markers Oct4, SSEA4 and Tra1-81. D) Immunofluorescence of trilineage differentiation from iPSCs. Stained for germ layer markers, Nestin (ectoderm), SMA (mesoderm), FoxA2 (endoderm). E) Genomic integrity and identity of iPSCs using exome sequencing and depicted using circos plots.

Table 2
Reagents details.

Antibodies and stains used for immunocytochemistry/flow-cytometry			
	Antibody	Dilution	Company Cat # and RRID
Pluripotency markers	Mouse Anti-Tra1-81	1:100	Millipore Cat# MAB4381, RRID AB_177638
	Mouse Anti-SSEA4	1:100	Millipore Cat# MAB4304, RRID AB_177629
	Goat Anti-Oct4	1:200	Abcam Cat# ab27985, RRID AB_776898
Differentiation markers	Mouse Anti-Nestin	1:150	R and D systems Cat# MAB1259, RRID AB_ 2251304
	Mouse Anti-SMA	1:100	Agilent Cat# M0851, RRID AB_2223500
	Rabbit Anti-FoxA2	1:200	Millipore Cat# 07-633, RRID AB_390153
Secondary antibodies	Alexa Fluor 568 Donkey Anti-mouse IgG	1:1000	Thermo Fisher Scientific Cat# A10037, RRID AB_2534013
	Alexa Fluor 568 Donkey Anti-goat IgG	1:1000	Thermo Fisher Scientific Cat #A11057, RRID AB_2534104
	Alexa Fluor 546 Goat Anti-rabbit IgG Alexa	1:1000	Thermo Fisher Scientific Cat# A-11010, RRID:AB_2534077
Nuclear stain	Hoechst33258	1:10,000	Thermo Fisher Scientific Cat# H3569
Site-specific nuclease			
Nuclease information	Cas9	Endonuclease	
Delivery method	Plasmid	Nucleofection 4D Nucleofector (Lonza)	
Selection/enrichment strategy	Antibiotic resistance	Puromycin selection	
	Fluorescent proteins	Imaging of colonies and subsequent selection FACS for purification	
Primers and Oligonucleotides used in this study			
	Target	Forward/Reverse primer (5′-3′)	
Pluripotency markers	Oct4	CCCCAGGGCCCCATTTTGGTACC/ACCTCAGTTTGAATGCATGGGAGAGC	
	NanoG	CCTGTGATTTGTGGGCCTG/GACAGTCTCCGTGTGAGGCAT	
	Klf4	ACCCATCCTTCCTGCCCGATCAGA/TTGGTAATGGAGCGGCGGGACTTG	
Housekeeping genes	GAPDH	CGAGATCCCTCCAAAATCAAG/GCAGAGATGATGACCCTTTTG	
Genotyping	R272Q	tagactggatccAATGCAAAGCTAGCATCCGT/tagactgtcgacTCCCAATTAGCTTGAAGCCC	
	S156A	tagactggatccAAACCTGTGTGGAGGTATGC/tagactgtcgacTTCCAGCCCCTATAAACACAGC	
	K572R	tagactggatccGCCTTTTGGTTCACTTTTTCGC/tagactgtcgacTTATGGCATTCAAACCAAACTTGC	
Random integration	Vector backbone	TTTGTCCCAAATCTGGCGGA/GCCAGGCATCTTGAGGTTCT	
	Vector junction homology	gctgcctatcagaaggtggtg/cgacggattcgcgctatttag	
gRNA oligonucleotide sequence	R272Q	GAGGGAGACACGAAACTACT	
	S156A	AGAGCTCTGATATGTTCTTC	
	K572R	CTTTGTTAAATTGACAACAA	
Genomic target sequence(s)	R272Q	GAGGGAGACACGAAACTACT TGG (+) (Chr. 17 DSB at pos. 32194037)	
	S156A	AGAGCTCTGATATGTTCTTC AGG (−) (Chr. 17 DSB at pos. 32183191)	
	K572R	CTTTGTTAAATTGACAACAA TGG (+) (Chr. 17 DSB at pos. 32208294)	
Off-target site primers	R272Q OT1	Ctctctgtgtagccacctgc/GGAAGGGCTCCACTGTCTTC	
	R272Q OT2	CTAAGACTGCCCCCAACCAG/GTTGCACGAAGCATGGTCTG	
	R272Q OT3	ACTGTACACTGGCAAAGGCT/ACCTGGATCAGAACCTCGGA	
	R272Q OT4	GACAGGCTGAACCCCATGAA/CAACTGGCCCTCCCAGATTT	
	R272Q OT5	TGCCATTCCAGTCAAAGCCT/GGCTTTCTTTGGGCTAGATGG	
	R272Q OT6	AGCCAGCTTGAATTCCTCCC/CCTCTCCAGTCGTGGGAAAC	
	R272Q OT7	GCTGTCGTGTGAGGAGGAAA/GGAGAAGCAGACAGACCACC	
	R272Q OT8	TGCAATGGCCAAGGAAGGAT/CATCCCCTGGGAAAGCAGAG	
	S156A OT1	Ctaggtgtggccaagagattgtttg/cagagtgatggccaaagctgc	
	S156A OT2	GCTGGGTAATGAGCATGAGTTA/AACGTTAACTCCATCTTGGGCT	
	S156A OT3	AAGGAGGCCAGCTGGAGATA/CAACCAACAAAACGACCCCC	
	S156A OT4	CATAGAAGTGAGTGAGCACCGT/TTTTGCTCATTGTGTACCTGAAGC	
	S156A OT5	GCAAGTGCCAACCTTTCCAG/TCGCAGTTTTGATGCTCCCT	
	S156A OT6	CTACCCACCTCTGCCCTACT/CTGACATGCCACCCTCTCTC	
	K572R OT1	AGAGTCACTGCAGAGGAGGT/CCGTGGCAACGGCTTAAAAT	
	K572R OT2	Tactgaaggttgggtggctg/agagcctgaaaacgaaacca	
	K572R OT3	Tgaggtggctttgtgtgggaat/gacgaggagttgcttcaacaaaac	
	K572R OT4	Ggttgcagtggttgtgcaat/aggaatcactgcaggtgtgg	
	K572R OT5	Gctggttgctaaagggtgga/aggtgacaccaatgctcact	
	K572R OT6	Agagaactctgaccaatacactgtt/ggagttgctttttaggagtgagc	
	K572R OT7	Cttgaacaacgaggcattgct/tgccacactgacagatcctt	
	K572R OT8	Ttccaataccgtgcgctcat/ctgctgcatcaagggactct	
	K572R OT9	Caggttggtgattgccgaag/gtaaagagctgacgcgttgtt	
	K572R OT10	Ctgagtcttcggcaagccat/ccctcatggactttgaggca	
Plasmids	Donor plasmids for repair templates	pDONOR-tagBFP-PSM-EGFP was a gift from Jens Schwamborn (Addgene plasmid # 100,603 http://n2t.net/addgene:100603 RRID:Addgene_100603) pDONOR-tagBFP-PSM-dTOMATO was a gift from Jens Schwamborn (Addgene plasmid # 100,604 http://n2t.net/addgene:100604 RRID:Addgene_100604)	

RRID Requirement for antibodies use http://antibodyregistry.org/ to retrieve RRID for antibodies and include ID in the table as shown in examples.

2. Materials and methods

2.1. Culturing and gene editing of iPSCs

iPSCs were cultured on Vitronecin (Stemcell Technologies, Cat# 07180/07183) or Matrigel (Coring, Cat# 354230) in E8 flex (Thermo Fisher, Cat# A2858501) for maintenance and mTeSR (Stemcell Technologies, Cat# 85850) for transfection/sorting/freezing/differentiation. Medium was supplemented with 10 μM Y27632 (Selleckchem, Cat# S1049) for passaging and 20 μM Y27632 and 10% DMSO for freezing. For transfection of CRISPR/Cas9 (1.5 μg DNA) and repair template plasmids (2.5 μg DNA each), 10^6 cells were transfected using 4D Nucleofector kit (Lonza, Cat# V4XP-3024) using the 4-D Nucleofector program "P3 primary cells" with pulse CB-150. Medium was switched to E8-Flex the second day and transfected cells were selected using puromycin (InvivoGen, Cat# ant-pr-1). After two weeks, high-content imaging (Operetta CLS High-Content Analysis System, Perkin Elmer) was performed to identify colonies showing indicators for correct integration

subsequent sorting (mTeSR +20 μM Y27632) of colonies excluded remaining non-fluorescent cells. PCR screening (Thermo Fisher, Cat# EP0705) and in-house Sanger sequencing (BigDye Terminator

Thermo Fisher, Cat# 4337456) were used to identify correctly edited clones showing no random integration and presence of the desired mutation, respecitvely. Transfection (STEMGENT, Cat# 00-0069) with an excision-only PiggyBac transposase removed positive selection markers. The transposase mRNA was a kind gift from Javier Jarazo from the laboratory of Jens Schwamborn, LCSB, Luxembourg. Non-fluorescent colonies were obtained by cloning and scarlessly edited clones were in-house Sanger sequenced to validate gene editand to check off-target sites for each gRNA.

2.2. Exome sequencing and genotypic identity

DNA from iPSCs was isolated using the DNeasy blood and tissue kit (Qiagen Cat#69504) following the manufacturer's instructions. DNA libraries were prepared using 50 ng of genomic DNA and the Twist Library Preparation using enzymatic fragmentation combined with the Core Exome and RefSeq enrichment (Twist Bioscience) on the automated liquid handler Beckman Biomeck i7, according to manufacturer's instructions. Raw data was processed using the in-house megSAP Pipeline (https://github.com/imgag/megSAP,version 0.2-480-gbbdd7699) combined with ngs-bits package (https://github.com/imgag/ngs-bits). Briefly, sequencing reads were aligned to the human reference genome (GRCh37) by BWA-MEM, variants were called using Strelka2 and annotated with VEP. For SCNA detection ClinCNV (version 1.16) was used. For evidence of genotypic identity, discriminative SNPs were used to compute the genotype correlation using an in-house tool which extracts high-coverage SNPs and computes the correlation for all sample pairings (see supplementary information).

2.3. Pluripotency assessment

For immunofluorescence stainings, iPSCs on coverslips were fixed with 4% PFA and stained following standard protocols using specific antibodies and Hoechst nuclear stain (Table 2). Transcript levels of pluripotency markers was assessed using RT-qPCR. RNA was isolated using RNeasy kit (Qiagen, Cat# 74104) according to manufacturer's instructions. Using the Quantitect RT-qPCR kit (Qiagen, Cat# 204243), reaction was perfomed with LightCylcer 480 SYBR Green I Master (Roche). Ct values were normalized to GAPDH and huES as reference to calculate the fold change ($2^{-\Delta\Delta ct}$). Pluripotency was further demonstrated by differentiation into three germlayers using STEMDiff Trilineage differentiation kit (Stemcell Technologies, Cat#05230) following the manufacturer's instructions. Immunofluorescence staining for specific markers was perfomed as described above using specific antibodies (Table 2).

Declaration of Competing Interest

The authors declare that they have no known competing financial interests or personal relationships that could have appeared to influence the work reported in this paper.

Acknowledgements

This study was funded by the Deutsche Forschungsgemeinschaft (DFG, German Research Foundation) – Research Training Group MOMbrane 654651/GRK2364. Thanks to German Demidov (Institute of Medical Genetics and Applied Genomics, The University of Tübingen) for his help with the analysis of the exome sequencing data. NGS sequencing methods were performed with the support of the DFG-funded NGS Competence Center Tübingen (INST 37/1049-1).

Appendix A. Supplementary data

Supplementary data to this article can be found online at https://doi.org/10.1016/j.scr.2021.102469.

References

Arias-Fuenzalida, J., Jarazo, J., Qing, X., Walter, J., Gomez-Giro, G., Nickels, S.L., Zaehres, H., Scholer, H.R., Schwamborn, J.C., 2017. FACS-Assisted CRISPR-Cas9 Genome Editing Facilitates Parkinson's Disease Modeling. Stem Cell Reports 9, 1423–1431.

Grossmann, D., Berenguer-Escuder, C., Bellet, M.E., Scheibner, D., Bohler, J., Massart, F., Rapaport, D., Skupin, A., Fouquier d'Herouel, A., Sharma, M., Ghelfi, J., Rakovic, A., Lichtner, P., Antony, P., Glaab, E., May, P., Dimmer, K.S., Fitzgerald, J.C., Grunewald, A., Kruger, R., 2019. Mutations in RHOT1 Disrupt Endoplasmic Reticulum-Mitochondria Contact Sites Interfering with Calcium Homeostasis and Mitochondrial Dynamics in Parkinson's Disease. Antioxid Redox Signal 31, 1213–1234.

Klosowiak, J.L., Park, S., Smith, K.P., French, M.E., Focia, P.J., Freymann, D.M., Rice, S. E., 2016. Structural insights into Parkin substrate lysine targeting from minimal Miro substrates. Sci Rep 6, 33019.

Marrone, L., Bus, C., Schondorf, D., Fitzgerald, J.C., Kubler, M., Schmid, B., Reinhardt, P., Reinhardt, L., Deleidi, M., Levin, T., Meixner, A., Klink, B., Glatza, M., Gloeckner, C.J., Gasser, T., Sterneckert, J., 2018. Generation of iPSCs carrying a common LRRK2 risk allele for in vitro modeling of idiopathic Parkinson's disease. PLoS One 13, e0192497.

Wang, X., Winter, D., Ashrafi, G., Schlehe, J., Wong, Y.L., Selkoe, D., Rice, S., Steen, J., LaVoie, M.J., Schwarz, T.L., 2011. PINK1 and Parkin target Miro for phosphorylation and degradation to arrest mitochondrial motility. Cell 147, 893–906.

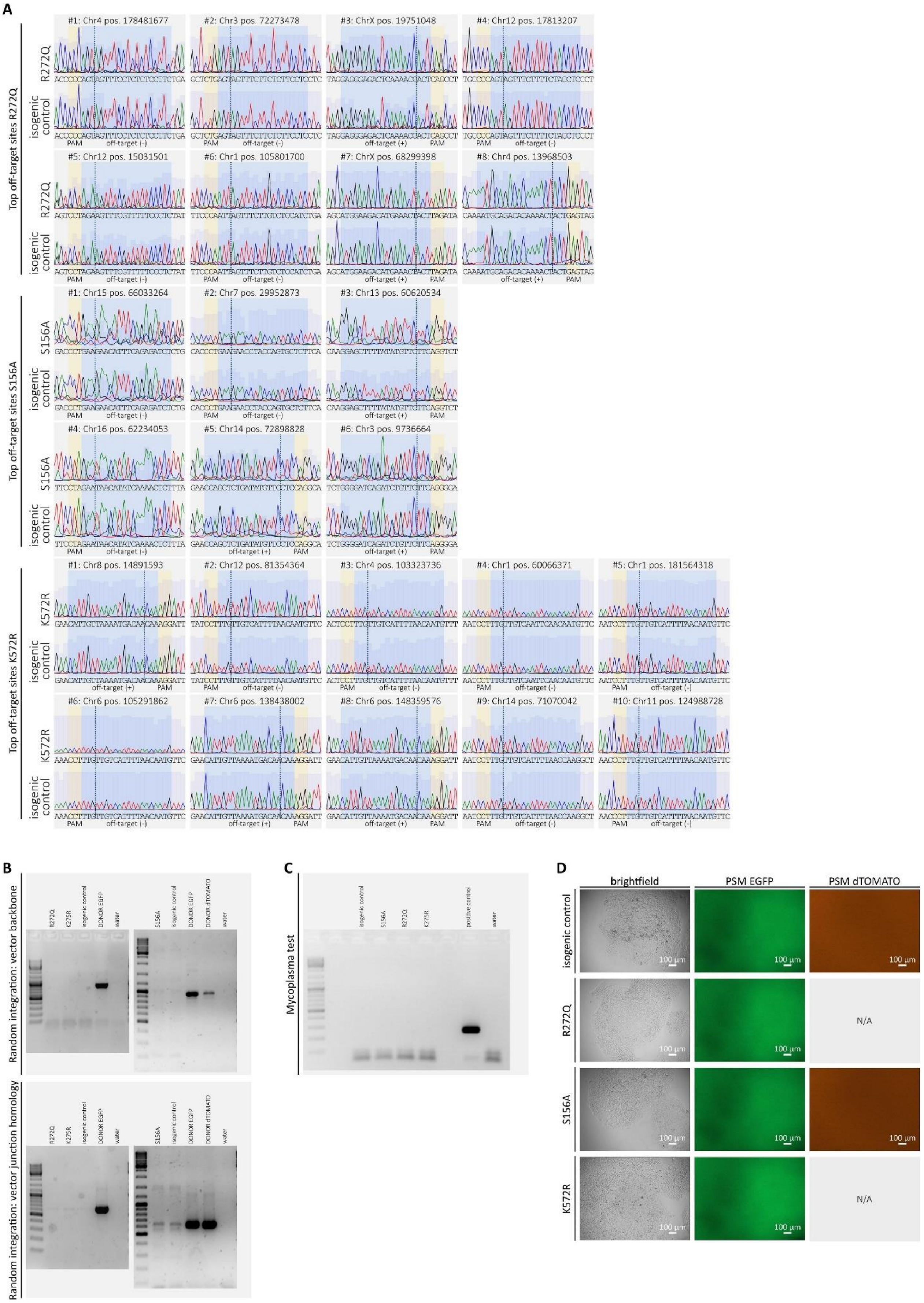
A
Top off-target sites R272Q
R272Q
isogenic control
#1: Chr4 pos. 178481677
#2: Chr3 pos. 72273478
#3: ChrX pos. 19751048
#4: Chr12 pos. 17813207
#5: Chr12 pos. 15031501
#6: Chr1 pos. 105801700
#7: ChrX pos. 68299398
#8: Chr4 pos. 13968503
PAM
off-target (-)
off-target (+)
Top off-target sites S156A
S156A
#1: Chr15 pos. 66033264
#2: Chr7 pos. 29952873
#3: Chr13 pos. 60620534
#4: Chr16 pos. 62234053
#5: Chr14 pos. 72898828
#6: Chr3 pos. 9736664
Top off-target sites K572R
K572R
#1: Chr8 pos. 14891593
#2: Chr12 pos. 81354364
#3: Chr4 pos. 103323736
#4: Chr1 pos. 60066371
#5: Chr1 pos. 181564318
#6: Chr6 pos. 105291862
#7: Chr6 pos. 138438002
#8: Chr6 pos. 148359576
#9: Chr14 pos. 71070042
#10: Chr11 pos. 124988728
B
Random integration: vector backbone
Random integration: vector junction homology
R272Q
K275R
isogenic control
DONOR EGFP
water
S156A
DONOR dTOMATO
C
Mycoplasma test
isogenic control
S156A
R272Q
K275R
positive control
water
D
brightfield
PSM EGFP
PSM dTOMATO
isogenic control
R272Q
S156A
K572R
100 µm
N/A

cells

Communication

Steady-State Levels of Miro1 Linked to Phosphorylation at Serine 156 and Mitochondrial Respiration in Dopaminergic Neurons

Lisa Schwarz and Julia C. Fitzgerald *

Department of Neurodegeneration, Hertie Institute for Clinical Brain Research, University of Tuebingen, 72076 Tuebingen, Germany; l.schwarz@uni-tuebingen.de
* Correspondence: julia.fitzgerald@uni-tuebingen.de

Abstract: Miro1 has emerged as an interesting target to study Parkinson's disease-relevant pathways since it is a target of PINK1 and Parkin. Miro1 is a mitochondrial GTPase with the primary function of facilitating mitochondrial movement, and its knockout in mice is postnatally lethal. Here, we investigated the effect of the artificial *RHOT1*/Miro1 S156A mutation since it is a putative PINK1 phosphorylation site shown to be involved in Miro1 degradation and mitochondrial arrest during mitophagy. We gene-edited a homozygous phospho-null Miro1 S156A mutation in induced pluripotent stem cells to study the mutation in human dopaminergic neurons. This mutation causes a significant depletion of Miro1 steady-state protein levels and impairs further Miro1 degradation upon CCCP-induced mitophagy. However, mitochondrial mass measured by Tom20 protein levels, as well as mitochondrial area, are not affected in Miro1 S156A neurons. The mitochondria are slightly lengthened, which is in line with their increased turnover. Under basal conditions, we found no discernable effect of the mutation on mitochondrial movement in neurites. Interestingly, the S156A mutation leads to a significant reduction of mitochondrial oxygen consumption, which is accompanied by a depletion of OXPHOS complexes III and V. These effects are not mirrored by Miro1 knockdown in neuroblastoma cells, but they are observed upon differentiation. Undifferentiated Miro1 S156A neural precursor cells do not have decreased Miro1 levels nor OXPHOS complexes, suggesting that the effect of the mutation is tied to development. In mature dopaminergic neurons, the inhibition of Miro1 Ser156 phosphorylation elicits a mild loss of mitochondrial quality involving reduced mitochondrial membrane potential, which is sufficient to induce compensatory events involving OXPHOS. We suggest that the mechanism governing Miro1 steady-state levels depends on differentiation state and metabolic demand, thus underscoring the importance of this pathway in the pathobiology of Parkinson's disease.

Keywords: Miro1; PINK1; Parkinson's disease; mitochondria

check for updates

Citation: Schwarz, L.; Fitzgerald, J.C. Steady-State Levels of Miro1 Linked to Phosphorylation at Serine 156 and Mitochondrial Respiration in Dopaminergic Neurons. *Cells* **2022**, *11*, 1269. https://doi.org/10.3390/cells11081269

Academic Editor: Albert Quintana

Received: 31 January 2022
Accepted: 4 April 2022
Published: 8 April 2022

1. Introduction

The atypical GTPase Miro1 is located at the outer mitochondrial membrane and possesses two central EF-hand calcium-binding domains with two surrounding GTPase domains [1–3]. Its primary function is facilitation of mitochondrial movement by anchoring mitochondria via the adaptor proteins TRAK1/2 to molecular motors such as kinesin [2,4,5].

Mammalian cells have two Miro proteins exhibiting similar functions, but they are non-redundant [1,6]. Miro1 knockout is postnatally lethal in mice, while Miro2 knockout is tolerated [7]. Hippocampal cultures from Miro2 knockout mice exhibit unaltered mitochondrial trafficking, while this is markedly reduced in Miro1 knockout neurons [6]. These findings highlight the importance of Miro1 in neurons, as well as the necessity of proper mitochondrial distribution for neuronal development and health. Since mitochondria are mostly synthesized in the soma, they need to be distributed to the cell's periphery [8]. Mitochondrial stopping is also mediated by Miro1 through calcium binding upon elevation of cytosolic calcium [9–13], which is thought to be important for the arrest of mitochondria at sites of high energy demand [8].

Miro1 takes part in several other mitochondrial functions, including mitochondrial calcium buffering and mitochondrial quality control. Miro1 interacts with PINK1 [14] and Parkin [15]; mutations in the encoding genes *PINK1* and *PARK2* cause autosomal recessive Parkinson's disease [16–18]. PINK1 initiates mitophagy upon mitochondrial depolarization and recruits Parkin for the ubiquitination of a subset of mitochondrial substrates [19,20]. The subsequent phosphorylation of the ubiquitin chains by PINK1 activates autophagy [21,22]. The phosphorylation of Miro1 by PINK1, followed by its ubiquitination by Parkin, induces Miro1 removal from depolarized mitochondria and degradation by the proteasome [15,23–25]. PINK1 and Parkin also inhibit mitochondrial movement upon mitochondrial depolarization by untethering mitochondria from the microtubules [23,26].

In the context of PINK1-mediated degradation, three residues have been identified for Miro1 phosphorylation (Ser156, Thr298, and Thr299), of which Ser156 was found to be required for degradation [23,26]. However, studies investigating the significance of Ser156 phosphorylation in induced mitophagy are contradictory. While some studies indicate that phosphorylation at Ser156 facilitates Miro1 degradation [23,26], other studies were not able to reproduce this result [15,24]. Because these studies focused on Miro1 degradation, it is not known whether this phosphorylation site has other functions. One limitation was that these studies used the expression of constructs that only show transient effects with the wild-type protein still present. The mechanisms governing Miro1 retention at or degradation at mitochondria are of particular relevance: a study shows that a large subset of Parkinson's disease patients' fibroblasts fail to remove Miro1 following mitochondrial depolarization [27].

We previously established induced pluripotent stem cell (iPSC) lines where we introduced *RHOT1*/Miro1 mutations, including S156A, into healthy iPSCs using CRISPR/Cas9 gene editing [28].

Here, we show the effect of the phospho-null mutant S156A in human dopaminergic neurons, the cell type affected in Parkinson's disease. Our results confirm the findings of previous studies, in which preventing Miro1 phosphorylation at this site affects Miro1 degradation, slowing the flux of mitophagy in dopaminergic neurons. This is accompanied by mild, but consistently reduced, mitochondrial membrane potential, basal respiration, and OXPHOS complex levels without any effect on respiratory capacity or mitochondrial movement. This only occurs in differentiated neurons which cannot rely on canonical mitophagy.

2. Materials and Methods

2.1. Generation Neural Precursor Cells (NPCs) and Differentiation in Midbrain Dopaminergic Neurons (hDaNs)

NPCs were derived from iPSCs as previously described [29] with the following adjustments: EBs were started in base medium (50% DMEM/F12 (Thermo Fisher Scientific (Waltham, MA, USA), #11-330-057), 50% neurobasal (Thermo Fisher Scientific (Waltham, MA, USA), 21103-049), 1% penicillin/streptomycin (Merck (Darmstadt, Germany), #A2213), 1% GlutaMax (Thermo Fisher Scientific (Waltham, MA, USA), #35050-038), 1% B27 supplement (without vitamin A; Thermo Fisher Scientific (Waltham, MA, USA), #12587-010), and 0.5% N2 supplement (Thermo Fisher Scientific (Waltham, MA, USA), #17502-048)), supplemented with 20 µM SB431542 (Selleckchem (Houston, TX, USA), #S1067-10 mg), 1 µM dorsomorphin (Axon Medchem (Groningen, The Netherlands), #Axon 1708 5 mg), 3 µM CHIR 99021 (Axon Medchem (Groningen, Netherlands), #Axon1386 5 mg), and 0.5 µM PMA (Merck (Darmstadt, Germany), #540220-5MG). On day 3, EBs were put in NPC medium (base medium supplemented with 3 µM CHIR 99021, 200 µM ascorbic acid (Sigma-Aldrich (St. Louis, MO, USA), #A4544-25G), and 0.5 µM PMA) and plated on Matrigel (Corning (Corning, NY, USA), #354230) on day 5. After several passages, NPCs were differentiated into human, mid-brain-specific dopaminergic neurons as previously described [30], with the alteration that NPCs were not primed by removing the PMA from the NPC media prior to differentiation. Dopaminergic neurons were used at day 16–19. The number of individual differentiations used in experiments is indicated as n_{Diff}.

For the induction of mitophagy, hDaNs were treated for 2, 4, 6, or 24 h with a final concentration of 10 µM CCCP in the neuronal maturation medium, or for 6 h with 10 µM CCCP plus 10 µM MG132. Untreated hDaNs received fresh neuronal maturation medium for 24 h.

2.2. RT-qPCR

RNA was isolated using the RNEasy kit (Qiagen (Hilden, Germany), #74104), following the manufacturer's instructions, including the homogenization step using QIAshredder. For RT-qPCR, the Quantitect SYBR-green kit (Qiagen (Hilden, Germany), #204243) was used, following the manufacturer's instructions. Primers used for RT-qPCR are listed in Table 1.

Table 1. Primers used for RT-qPCR.

Gene	Forward	Reverse
GAPDH	CGAGATCCCTCCAAAATCAAG	GCAGAGATGATGACCCTTTTG
NESTIN	GGCAGCGTTGGAACAGAGGTTGGA	CTCTAAACTGGAGTGGTCAGGGCT
SOX2	TTCACATGTCCCAGCACTACCAGA	TCACATGTGTGAGAGGGGCAGTGTGC
PAX6	GTGTCCAACGGATGTGTGAG	CTAGCCAGGTTGCGAAGAAC
TH	TGTCTGAGGAGCCTGAGATTCG	GCTTGTCCTTGGCGTCACTG
MAP2	CCGTGTGGACCATGGGGCTG	GTCGTCGGGGTGATGCCACG
RHOT1	TGTCACCCCAGAGAGAGTTC	GCCTGCTGTCTTTGTCTGTT
RHOT2	ATTGAGACCTGCGTGGAGTG	AAGCGTTGAGCTCTTCGTCA

2.3. Immunofluorescence Staining

NPCs and hDaNs were seeded on Matrigel-coated coverslips and fixed with 4% PFA in PBS. For nuclear marker Sox2, cells were permeabilized with neat methanol for 5 min at −20 °C. For mitochondrial marker Tom20, cells were permeabilized with 0.5% TritonX-100 in PBS for 5 min at room temperature. After washing with wash buffer (0.01% TritonX-100 in PBS), cells were blocked using 10% normal goat serum in wash buffer. Antibodies were diluted in 5% normal goat serum in wash buffer. Primary antibodies (MAP2 1:2000 (abcam (Cambridge, UK), #ab5392), Tyrosine Hydroxylase (TH) 1:1000 (Pel-Freez (Rogers, AR, USA) #P40101-150), Tom20 1:200 (Santa Cruz Biotechnology (Dallas, TX, USA), #sc17764), Nestin 1:150 (R&D systems (Wiesbaden, Germany), #MAB1259), and Sox2 1:1000 (abcam (Cambridge, UK), #ab97959)) were incubated overnight at 4 °C, and secondary antibodies (1:1000; Thermo Fisher Scientific (Waltham, MA, USA), #A21449, #A11070, #A21463, #A11010) for 1–2 h at room temperature. Nuclei were counterstained with Hoechst (Molecular Devices (Urstein, Austria), #H3569). Coverslips were mounted on glass slides using Dako fluorescent mounting medium (Aligent (Santa Clara, CA, USA), #S3023). Slides were imaged using a Zeiss Imager.Z1 equipped with an ApoTome.2 and an AxioCam MRm. Representative images were processed using ZEN software (blue edition, Zeiss (Oberkochen, Germany)). For representative images of MAP2/TH and Nestin/Sox2 staining, Z-stacks were projected (maximum intensity), brightness and contrast were adjusted, and a scale bar was inserted.

2.4. SDS-PAGE and Western Blotting

For cell lysis, a lysis buffer containing 1% Triton X-100 in PBS with cOmplete protease inhibitor (Sigma-Aldrich (St. Louis, MO, USA), #11873580001) and PhosStop phosphatase inhibitor (Sigma-Aldrich (St. Louis, MO, USA), #4906837001) were used. hDaN and differentiated SH-SY5Y lysates were homogenized using 25G (5 passes) and 27G (10 passes) needles. SH-SY5Y lysates were homogenized by repetitive vortexing. NPCs were homogenized using 20G (5 passes), 25G (5 passes), and 27G (10 passes) needles. Electrophoresis and immunoblotting onto PVDF membranes (MilliporeSigma (Burlington, MA, USA), #IPVH00010) were done following standard protocols. Primary antibodies were diluted in 5% milk or Roche blocking solution diluted in Tris-buffered saline containing 0.05% Tween20 (TBST). The antibodies used in this study are as follows: α-vinculin 1:5000 (Sigma-Aldrich (St. Louis, MO, USA), #V9131), α-tubulin 1:5000 (Sigma-Aldrich (St. Louis, MO, USA), #AA13), Miro1 1:500 (Thermo Fisher Scientific (Waltham, MA, USA), #PA-42646), Tom20 1:1000 (Santa Cruz Biotechnology (Dallas, TX, USA), #sc11415), Total OXPHOS 1:1000 (Abcam (Cambridge, UK), #ab110413), Mitofusin 1:1000 (Abcam (Cambridge, UK), ab#57602) and LC3 1:1000 (Novus Biologicals (Littleton, CO, USA), #NB100-2220). Fluorescent secondary antibodies were diluted in 5% milk in TBST (1:10,000; LI -COR Biosciences, (Lincoln, NE, USA), #926-32210, #926-32213, #926-68071, and #926-68070). Proteins on the membranes were detected using an Odyssey CLx infrared imaging system (LI -COR Biosciences, (Lincoln, NE, USA)) with Image Studio software (LI -COR Biosciences, (Lincoln, NE, USA)). Intensity of protein bands was quantified using Image Studio Lite Ver 5.2 (LI -COR Biosciences, (Lincoln, NE, USA)). Intensity of the protein bands was normalized to the intensity of the loading control protein band on the same membrane (α-tubulin or α-vinculin).

2.5. Imaging Analysis of Mitochondrial Morphology and Membrane Potential

Approximately 150,000 hDaNs were seeded onto Matrigel-coated 35 mm ibidi dishes two to three days prior to imaging. Two dishes were seeded per differentiation, and imaging was conducted on two consecutive days ($n_{Diff} = 3$; 2 days of imaging per line, 10 images per day). Prior to imaging, hDaNs were stained with 100 nM MitoTracker green (Thermo Fisher Scientific (Waltham, MA, USA), #M7514) and 25 nM Image-iT™ TMRM reagent (Thermo Fisher Scientific (Waltham, MA, USA), #I34361) in maturation medium and incubated for 7 min at 37 °C with 5% CO_2. For imaging, medium was replaced with maturation medium without phenol red (Neurobasal: Thermo Fisher Scientific (Waltham, MA, USA), #12348017; DMEM/F12: Thermo Fisher Scientific (Waltham, MA, USA), #21041025). Z-stacks were taken with a slice interval of 0.88 μm using a Leica DMi8 Microscope (40× objective) with the LASX software under a controlled environment (37 °C with 5% CO_2).

Images were analyzed using Fiji (Rasband, W.S., ImageJ, U. S. National Institutes of Health, Bethesda, MD, USA). Z-stacks were projected using average intensity and all slices. Images were converted to 8-bit greyscale.

Mitochondrial morphology was analyzed as previously described [31] with alterations. In detail, greyscale images of MitoTracker green channel were convolved (process–filters–convolve; Kernel: $0\ 0\ -1\ 0\ 0/0\ -1\ -1\ -1\ 0/-1\ -1\ 24\ -1\ -1/0\ -1\ -1\ -1\ 0/0\ 0\ -1\ 0\ 0$), the background was subtracted (process—subtract background: rolling ball radius 10 px), and local contrast was enhanced (process—enhance local contrast (CLAHE): blocksize 9, maximum slope 4, fast unselected). Next, the tubeness tool (plugins–analyze–tubeness: sigma = 0.24156, use calibration information) was used, and images were despeckled (process–noise–despeckle) and converted into 8-bit. The processed images were converted into a binary image by applying thresholding (a similar threshold between images was maintained). An analysis of area, shape descriptors, perimeter, and fit ellipse as measurements was performed on particles bigger than 1.5 px (circularity: 0–1). The output of measurement was further processed in Excel to calculate descriptors: Area [μm^2]: area; form factor (degree of branching): $\frac{perimeter^2}{4\pi \cdot area}$; length [μm]: aspect ratio; circularity: circularity; for each descriptor, the mean of one image was calculated and used as data point in statistics.

For the analysis of mitochondrial membrane potential, MitoTracker green images were processed by subtracting the background (process—subtract background: rolling ball radius 15 px). Next, images were converted to a binary image using thresholding (a similar threshold between images was maintained). A binary image was used as a mask to quantify the integrated density of both the MitoTracker green and TMRM channel (set measurements: integrated density, redirect to MitoTracker green/TMRM greyscale image; analyze particles: size 1.5 px—infinity; circularity: 0–1; outlines were saved). The background was measured for each channel and corrected total fluorescence (CTF) for each particle analyzed was calculated as follows: CTF = $\text{IndDen}_{\text{Particle}} - (\text{area}_{\text{Particle}} \times \text{mean grey value}_{\text{Background}})$. The mean CTF of one image was used as a data point for statistics.

2.6. Imaging Analysis of Mitochondrial Movement

Approximately 100,000 hDaNs were seeded onto 35 mm ibidi dishes double-coated with poly-L-ornithine (Sigma-Aldrich (St. Louis, MO, USA), #P8638-25MG) and Matrigel three to four days prior to imaging. Two dishes were seeded per differentiation, and imaging was conducted on two consecutive days (n_{Diff} = 3; 2 days of imaging per genotype, 8–9 time-lapses per day). Prior to imaging, hDaNs were stained with 100 nM MitoTracker green in maturation medium and incubated 7 min at 37 °C with 5% CO_2. For imaging, the medium was replaced with maturation medium without phenol red. Time lapses were taken in 5 s intervals for 5 min (61 frames) using a Leica DMi8 Microscope (40× objective) with the LASX software under a controlled environment (37 °C with 5% CO_2).

Images were analyzed and processed using Fiji. Time lapses were checked for cellular drift by overlay of the first and last frames. Per imaging day, 10 immobile processes were selected for analysis and subsequently cropped and straightened using plugin straighten (line width: 30 px, applied to entire stack; [32]). The orientation of each straightened process was maintained to have anterograde movement from left to right.

For manual analysis, kymographs were generated by re-slicing (default settings) the straightened processes, then Z-projecting the stack (max intensity) and inverting the LUT; brightness and contrast were adjusted prior to analysis. Tracks were analyzed using the line tool to connect the start and the end of each track. Displacement was calculated using the Pythagorean theorem and mitochondria were classified as stationary (displacement $\leq$ 2 µm), mobile (displacement > 2 µm), or oscillating (displacement $\leq$ 2 µm; amplitude (from displacement line to peak of largest amplitude) > 1.5 µm). For each imaging day, the sum of all tracks analyzed was used to calculate fractions of motile, oscillating, anterograde, and retrograde mitochondria; mean displacement of motile mitochondria was calculated from all tracks of one imaging day.

For analysis of mean mitochondrial speed, automated analysis using the TrackMate [33] plugin was performed. First, straightened processes were processed using bleach correction (histogram matching) and enhancement of contrast (process—enhance contrast: 2.5%, normalized, applied to all slices). For TrackMate analysis, the calibration information was used, then the LoG detector was chosen. Next, the detector was set for an estimated blob diameter of 1 µm with threshold 0 and sub-pixel localization. Initial thresholding was not applied, HyperStack Displayer was used, and spots were filtered using the automatic settings (threshold was adjusted manually when automated detection was not appropriate). For tracking of particles, the Linear motion LAP tracker was used with an initial and subsequent search radius of 5 µm, and the max frame gap was set to two frames. The mean average speed of all tracks analyzed per process was used as one data point for statistics.

2.7. Imaging Analysis of Mitochondrial Turnover Using MitoTimer Construct

Approximately 80,000 hDaNs seeded on Matrigel-coated glass coverslips were transfected with pMitoTimer plasmid (Addgene (Watertown, MA, USA) plasmid #52659; RRID: Addgene_52659; [34]) using Fugene HD transfection reagent (Promega (Madison, WI, USA), #E2311), according to the manufacturer's instructions. hDaNs received fresh maturation medium 1–2 h prior to transfection. hDaNs were fixed 48 h after transfection and stained with Tom20 as mitochondrial marker, as described above. Slides were imaged using a Zeiss Imager.Z1 equipped with an ApoTome.2 and an AxioCam MRm. Z-stacks were taken with a 0.72 µm interval with fixed exposure times (Hoechst: 15 ms; green: 150 ms; red: 50 ms; Tom20: 1000 ms). Per differentiation (n_{Diff} = 3), 14 images were analyzed.

Images were analyzed using Fiji. Z-stacks were projected using average intensity and all slices. Images were converted to 8-bit greyscale. Tom20 greyscale images were converted to binary images using thresholding and used as a mask to quantify fluorescence intensity of green and red channels (set measurements: mean grey value, redirect to green or red channel; analyze particles: size 1.5 px—infinity, circularity 0–1, outlines were saved). The mean grey value of all particles from one image was used to calculate the ratio between green and red channels for that image, which was used as one data point for statistics.

2.8. Flow Cytometry

Dissociated hDaNs using Accutase (PAN-Biotech (Aidenbach, Germany), #P10-21100) were stained with a final concentration of 100 nM MitoTracker deep red (Thermo Fisher Scientific (Waltham, MA, USA), #M22426) and 100 nM Image-iT™ TMRM for 15 min at 37 °C. hDaNs were measured in neuronal maturation medium without phenol red using a MACSQuant (Mytenyi Biotec (Bergisch Gladbach, Germany)). The mean average fluorescence signal of each channel was divided by the background fluorescence of unstained hDaNs in the same channel to account for autofluorescence.

2.9. Respiratory Analyses

For respiratory analyses, a basic mitochondrial stress test measuring oxygen consumption rate (OCR) and extracellular acidification rate (ECAR) was performed using a Seahorse XF96 Extracellular Flux Analyzer (Agilent (Santa Clara, CA, USA)). Approximately 60,000–120,000 neurons were seeded per well into a Matrigel-coated Seahorse cell plate 2–5 days prior to the experiment. For the measurement, the medium was replaced with DMEM base medium (without phenol red; Sigma-Aldrich (St. Louis, MO, USA), #D5030 1L) supplemented with 4.5 mg/mL D-Glucose, 0.22 mg/mL pyruvate, and 2 mM glutamine. After eight measurements of basal respiration, hDaNs were challenged with subsequent injections to give final concentrations of (a) 0.8 µM Oligomycin, (b) 2.7 µM CCCP, and (c) 0.8 µM Rotenone with 4 µM Antimycin A. Each injection was followed by three measurements. OCR and ECAR measurement were normalized to the number of hDaNs seeded for each experiment. Basal respiration was calculated by subtracting the mean of the OCR measurements after injection (c) from the OCR of the third measurement of baseline. Maximal respiration was calculated by subtracting the mean of the OCR measurements after injection (c) from the mean of the OCR measurements after injection (b). Spare respiratory capacity was calculated as the percentage of maximal respiration of basal respiration.

2.10. Miro1 Knockdown in Undifferentiated SH-SY5Y

SH-SY5Y cells were maintained in DMEM/F12 supplemented with 10% heat-inactivated FBS, 1% NEAA (Thermo Fisher Scientific (Waltham, MA, USA), #1140-035), and 1% penicillin/streptomycin. For siRNA transfection, cells were seeded 24 h prior to transfecting three consecutive days before harvest and three days after the first transfection (representative blot Miro1 and Tom20). The protocol was modified by transfecting the cells once and harvesting them three days later. Transfection with non-targeting siRNA (Dharmacon (Lafayette, CO, USA) SMART Pool; #D-001206-14-05) and *RHOT1* siRNA (Dharmacon (Lafayette, CO, USA) SMART Pool, #M-010365-01-0005) was performed using 25 ng siRNA with 2 µL transfection reagent (Dharmacon (Lafayette, CO, USA), #T-2001-01) per well, following the manufacturer's instructions.

2.11. Miro1 Knockdown in Differentiated SH-SY5Y

For differentiation, SH-SY5Y cells were seeded on Matrigel. Differentiation was induced by adding DMEM/F12 supplemented with 10 µM all-trans retinoic acid, 1% heat inactivated FBS, 1% NEAA, and 1% penicillin/streptomycin. At day 4 of differentiation, SH-SY5Y were transfected with 50 ng non-targeting or *RHOT1* Dharmacon SMART Pool siRNA (described above) and 4 µL transfection reagent per well with antibiotic-free medium.

The medium was replaced with fresh differentiation medium the next day. Differentiated SH-SY5Y were harvested at day 7 of differentiation (three days after transfection).

2.12. Statistical Analysis

GraphPad Prism 9 (ver. 9.1.1) was used for statistics. Data are shown as mean ± standard deviation (SD) and were tested for (log)normal using the Shapiro–Wilk test. Normally distributed data were analyzed using a paired *t* test (one-tailed or two-tailed) or 2way ANOVA with Tukey's multiple comparisons. Non-normally distributed data were analyzed using (multiple) Wilcoxon tests, Mann-Whitney test, or Friedman's test with Dunn's multiple comparisons. Experiments with hDaNs were performed using individual differentiations indicated as n_{Diff}. The correlation between Miro1 and Complexes V/IV/III (detected on the same membrane) was done in Prism by computing Pearson correlation coefficients and subsequent simple linear regression.

3. Results

3.1. Miro1 S156A Protein Levels Are Reduced in Dopaminergic Neurons

For investigating Miro1 S156A in dopaminergic neurons, we used previously established, gene edited, homozygous Miro1 S156A iPSCs. We showed that the gene editing did not result in unintended genomic damage and that Miro1 S156A iPSCs were isogenic to the maternal control iPSCs [28].

For differentiation of mid-brain-patterned dopaminergic neurons, we first derived neural precursor cells (NPCs) from Miro1 S156A [28] and isogenic control [35] iPSCs. We validated the identity of the NPCs using RT-qPCR and immunofluorescence (Figure S1A) before differentiation into hDaNs. Dopaminergic identity and neuronal maturity of hDaNs were validated showing expression of Tyrosine Hydroxylase (TH) and MAP2, respectively, using RT-qPCR (Figure 1A) and immunofluorescence staining (Figure 1B).

Because previous studies found that phosphorylation at Ser156 is required for Miro1 degradation during induced mitophagy [23,26], we first asked whether the mutation might affect steady-state protein levels. Mean Miro1 protein levels are significantly decreased in Miro1 S156A hDaNs to 58% of the isogenic control (Figure 1C). The reduction of protein levels could be explained by a concomitant reduction of mitochondrial mass, but Tom20 protein levels used as a marker revealed no difference between Miro1 S156A and isogenic control hDaNs (Figure 1D). To determine whether the reduction of Miro1 protein levels is due to a reduction in gene expression, we assessed mRNA levels of *RHOT1*. We also probed *RHOT2* expression to assess compensatory upregulation of Miro2. Both *RHOT1* and *RHOT2* are expressed similarly in Miro1 S156A hDaNs and the isogenic control (Figure 1E). In summary, Miro1 S156A results in significantly reduced Miro1 protein that is not due to a change in mitochondrial mass or gene expression.

This indicates that S156A either has a destabilizing effect on steady-state levels of Miro1 or elicits a compensatory mechanism in mature neurons to reduce Miro1 protein.

In yeast and drosophila, Gem1/dMiro was shown to regulate mitochondrial morphology via its N-terminal GTPase domain [1,36,37], and a study in rat hippocampal neurons showed that this domain also confers this effect in mammalian cells [4]. Because Ser156 is located in the N-terminal GTPase domain, we assessed whether mitochondrial morphology is affected. We found that in Miro1 S156A hDaNs, mitochondrial morphology is mildly changed by a slight increase in area but significant elongation of mitochondria. Mitochondrial fragmentation and branching were not altered (Figure 1F). Since Miro1 protein is reduced in S156A hDaNs, we next assessed mitochondrial movement. Analysis of kymographs generated from neurites of live neurons (Figure 1G) revealed that there are no differences in the number of mitochondria in motion, nor in the directionality of movement nor the distance that mitochondria travel (Figure 1H). Assessing whether Ser156 is important for regulating the speed of mitochondria under basal conditions, we found that Miro1 S156A mitochondria travel as fast as isogenic control mitochondria (Figure 1I). These findings are in line with previous data that show that S156A alone is not sufficient to increase mitochondrial movement. In stimulated conditions, however, preventing phosphorylation at Ser156 impairs mitochondrial stopping mediated by PINK1 and parkin [23].

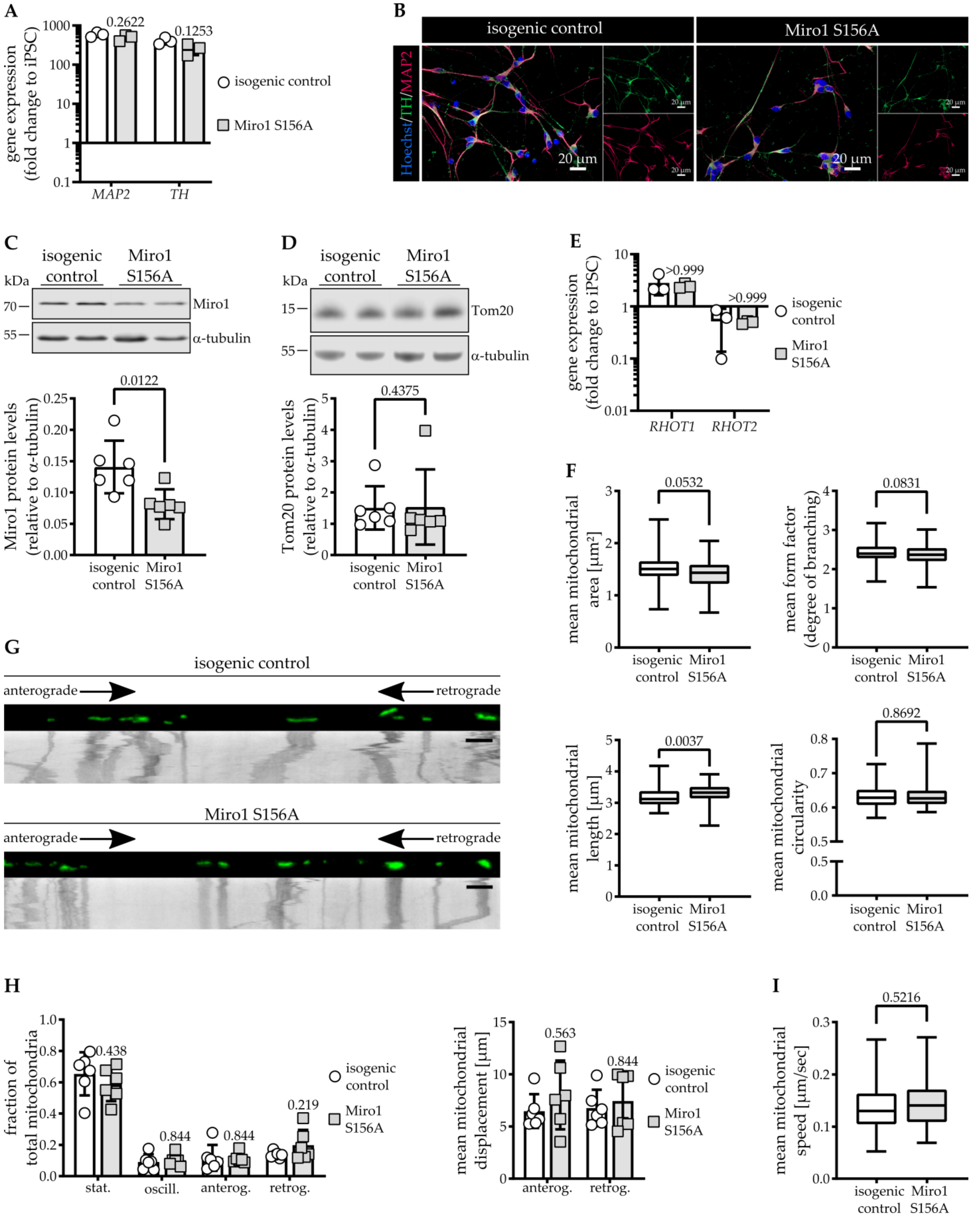

Figure 1. Reduction of Miro1 protein levels in Miro1 S156A hDaNs. (**A**) RT-qPCR showing expression

of dopaminergic neuronal markers in hDaNs as fold change to iPSCs. Error bars depict SD (n_{Diff} = 3); 2way ANOVA with Tukey's multiple comparisons. (**B**) Representative immunofluorescence staining showing the mature neuronal marker MAP2 and dopaminergic marker TH in hDaNs (n_{Diff} = 3). (**C**) Representative Western blot showing Miro1 in hDaN lysate. Quantification of intensity of Miro1 Western blot bands normalized to α-tubulin. Error bars depict SD (n_{Diff} = 6); paired *t* test, two-tailed. (**D**) Representative Western blot showing Tom20 in hDaN lysate. Quantification of intensity of Tom20 Western blot bands normalized to α-tubulin. Error bars depict SD (n_{Diff} = 6); Wilcoxon test matched pairs signed rank test. (**E**) RT-qPCR showing gene expression of *RHOT1/2* in hDaNs as fold change to iPSCs. Error bars depict SD (n_{Diff} = 3); Wilcoxon matched pairs signed rank test with two-stage linear step-up procedure of Benjamini, Krieger, and Yekutieli. (**F**) Imaging analysis of mitochondrial morphology in hDaNs stained with 100 nM MitoTracker green. Error bars depict SD (n_{Diff} = 3). Mitochondrial area and from factor: unpaired *t* test, two-tailed; Mitochondrial length and circularity; Mann-Whitney test. (**G**) First frame of representative movie with corresponding kymograph below for analysis of mitochondrial movement in processes of hDaNs stained with 100 nM MitoTracker green. Scale bar represents 10 µm. (**H**) Kymograph analysis of stationary, oscillating, anterograde, and retrograde mitochondrial fractions and mean displacement of anterograde and retrograde moving mitochondria. Error bars depict SD (n_{Diff} = 3); Wilcoxon matched pairs signed rank test with two-stage linear step-up procedure of Benjamini, Krieger, and Yekutieli. (**I**) Analysis of mitochondrial mean speed using Fiji plugin TrackMate. Error bars depict SD (n_{Diff} = 3); Mann-Whitney test.

Taken together, we found that Miro1 S156A results in longer mitochondria in hDaNs; however, despite the reduction of Miro1 protein levels, mitochondrial movement is not affected under basal conditions.

3.2. Miro1 Degradation during CCCP-Induced Mitophagy Is Imparied by S156A Mutation

Previous studies are not conclusive on whether S156A affects Miro1 degradation upon activation of mitophagy, or if it is only relevant during low levels of PINK1/Parkin activation [15,24,26]. Hence, we next tested if Miro1 degradation is impaired. We treated hDaNs with the ionophore CCCP to induce mitophagy for different time points with the addition of the proteasome inhibitor MG132 at 6 h. In isogenic control hDaNs, we observed a decrease of Miro1 protein levels after 2 h of induction and depletion of Miro1 after 24 h of treatment (Figure 2A,B). The addition of the proteasome inhibitor did not prevent Miro1 degradation, suggesting removal via alternative pathways. However, in Miro1 S156A hDaNs, depolarization of mitochondria does not result in further Miro1 protein degradation and inhibition of the proteasome mildly increased protein levels (Figure 2A,B). After 24 h of CCCP treatment, Miro1 is depleted, comparable to the isogenic control.

These findings indicate that the flux of Miro1 during mitophagy is impaired in S156A hDaNs.

To assess whether removal of other mitochondrial outer membrane targets of PINK1 and Parkin is impaired in Miro1 S156A hDaNs, we looked at the removal of Mitofusin. It is both ubiquitinated by Parkin [38,39] and degraded [15,38] in a similar manner to Miro1. In the isogenic control, Mitofusin degradation follows a similar degradation pattern as Miro1, but in Miro1 S156A mutant hDaNs, its degradation is slower. After 24 h, Mitofusin is depleted in both lines (Figure 2A,C). Next, we assessed levels of full-length and cleaved LC3 to measure activation of the autophagic machinery. We found that cleavage of LC3 in Miro1 S156A hDaNs occurs in a similar manner to isogenic control hDaNs (Figure 2A,D). These findings show that even though removal of Miro1 is changed in S156A hDaNs and degradation of mitochondria outer membrane targets like Mitofusin occurs slower, removal of damaged mitochondria via autophagy is not affected.

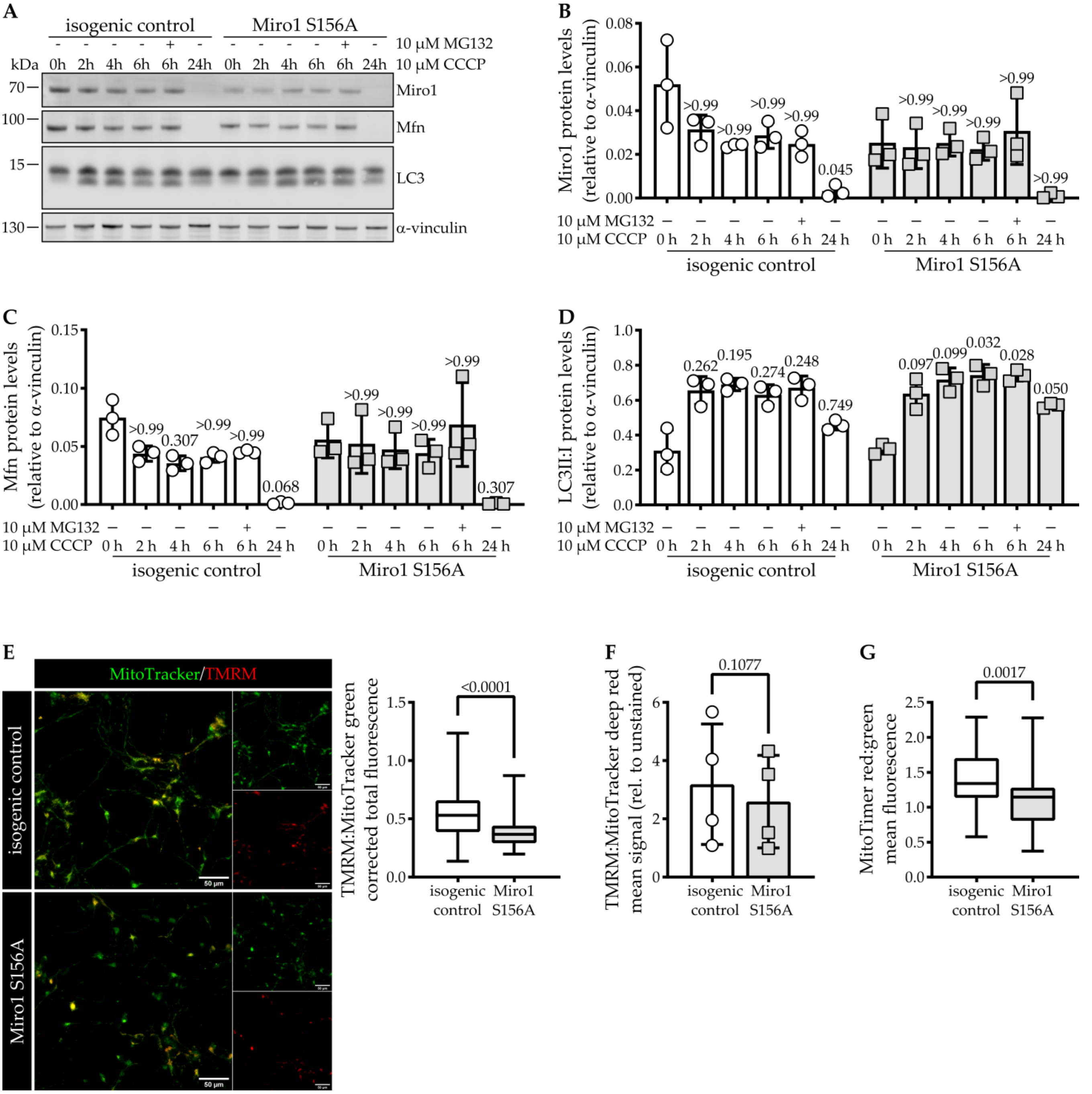

Figure 2. Miro1 degradation is impaired in Miro1 S156A hDaNs. (**A**) Representative Western blot showing Miro1, Mitofusin, and LC3 in hDaN lysate. Neurons were treated with a final concentration of 10 µM CCCP for 0, 2, 4, 6 (±10 µM MG132), or 24 h to induce mitophagy. (**B**) Quantification of intensity of Miro1 Western blot bands normalized to α-vinculin. Error bars depict SD (n_{Diff} = 3); Friedman's test with Dunn's multiple comparisons relative to 0 h of the respective genotype. (**C**) Quantification of the intensity of Mitofusin Western blot bands normalized to α-vinculin. Error bars depict SD (n_{Diff} = 3); Friedman's test with Dunn's multiple comparisons relative to 0 h of the respective genotype. (**D**) Ratio of LC3II:LC3I quantification of the intensity of LC3 Western blot bands normalized to α-vinculin. Error bars depict SD (n_{Diff} = 3); 2way ANOVA with Tukey's multiple comparisons. (**E**) Imaging analysis of mitochondrial membrane potential in hDaNs stained with 25 nM TMRM and 100 nM MitoTracker green. Representative live cell image of TMRM and MitoTracker

green staining. Quantification of corrected total fluorescence of TMRM relative to MitoTracker green. Error bars depict SD ($n_{Diff} = 3$); Mann-Whitney test. (**F**) Flow cytometric measurement of mitochondrial membrane potential in hDaNs stained with 100 nM TMRM and 100 nM MitoTracker deep red. Mean TMRM signal relative to MitoTracker deep red normalized to unstained signal. Error bars depict standard deviation ($n_{Diff} = 4$); paired *t* test, two-tailed. (**G**) Imaging analysis of mitochondrial renewal in hDaNs using MitoTimer plasmid. Quantification of mean red fluorescence relative to mean green fluorescence. Error bars depict SD ($n_{Diff} = 3$); Mann-Whitney test.

To assess whether the impairment of Miro1 degradation could be explained by a reduced sensitivity to CCCP, we looked at mitochondrial membrane potential. In live cell imaging of hDaNs stained with the mitochondrial membrane indicator TMRM and MitoTracker green as control, we found that Miro1 S156A hDaNs have a significantly reduced mitochondrial membrane potential (Figure 2E). These findings were confirmed by flow cytometry analysis of hDaNs stained with TMRM and MitoTracker deep red (Figure 2F). Because the loss of mitochondrial membrane potential could affect mitochondrial quality, we used the MitoTimer construct, which shifts from green to red fluorescence over a duration of 48 h, to assess mitochondrial turnover. The ratio between red and green fluorescence provides information about import and degradation of a mitochondrial matrix marker protein [34]. In Miro1 S156A hDaNs, the ratio between degradation (red) and import (green) is significantly decreased compared to isogenic control hDaNs (Figure 2G), indicating that the decrease of mitochondrial membrane potential is accompanied by an increase in mitochondrial turnover.

3.3. Miro1 S156A Reduces Mitochondrial Respiration in hDaNs

Having found that mitochondrial membrane potential is decreased concomitant with an increase in mitochondrial renewal in Miro1 S156A hDaNs, we next assessed whether this could be explained by a change in OXPHOS complexes and whether it affects mitochondrial respiration.

We found that levels of complex V (ATP5A) in Miro1 S156A hDaNs are significantly reduced by approximately 22% and complex III (UQCRC2) is reduced by approximately 26% compared to the isogenic control (Figure 3A). Complexes IV (MTCO1) and II (SDHB) are mildly reduced, and only levels of complex I (NDUFB8) remain unchanged (Figure S1F). Interestingly, in hDaNs, Miro1 protein levels correlate significantly with complex V ($r = 0.7910$, $p = 0.0022$) and complex III ($r = 0.8857$, $p = 0.0001$), the correlation with complex IV protein levels is not significant ($r = 0.5181$, $p = 0.0844$) in hDaNs (Figure 3B).

To assess whether the reduction in membrane potential and complexes V and IV has functional consequences, we analyzed mitochondrial respiration. Miro1 S156A mutant hDaNs overall consume less oxygen (Figure 3C) and have a significant reduction in basal respiration to approximately 35% of the isogenic control (Figure 3D, left graph). However, spare respiratory capacity is only mildly decreased by 13% (Figure 3D, middle graph). This results from a concomitant decrease in maximal respiration in Miro1 S156A hDaNs (Figure 3D, right graph).

Measurement of extracellular acidification rate (ECAR) indicates whether the cells shift their energy production to glycolysis upon reduction of mitochondrial respiration. We did not observe a shift to glycolysis in S156A hDaNs (Figure S1C). These findings indicate that in S156A Miro1 hDaNs, OXPHOS is impaired without compensatory increase in glycolysis, but the response to changing energy demands (which is reflected by spare respiratory capacity) is maintained.

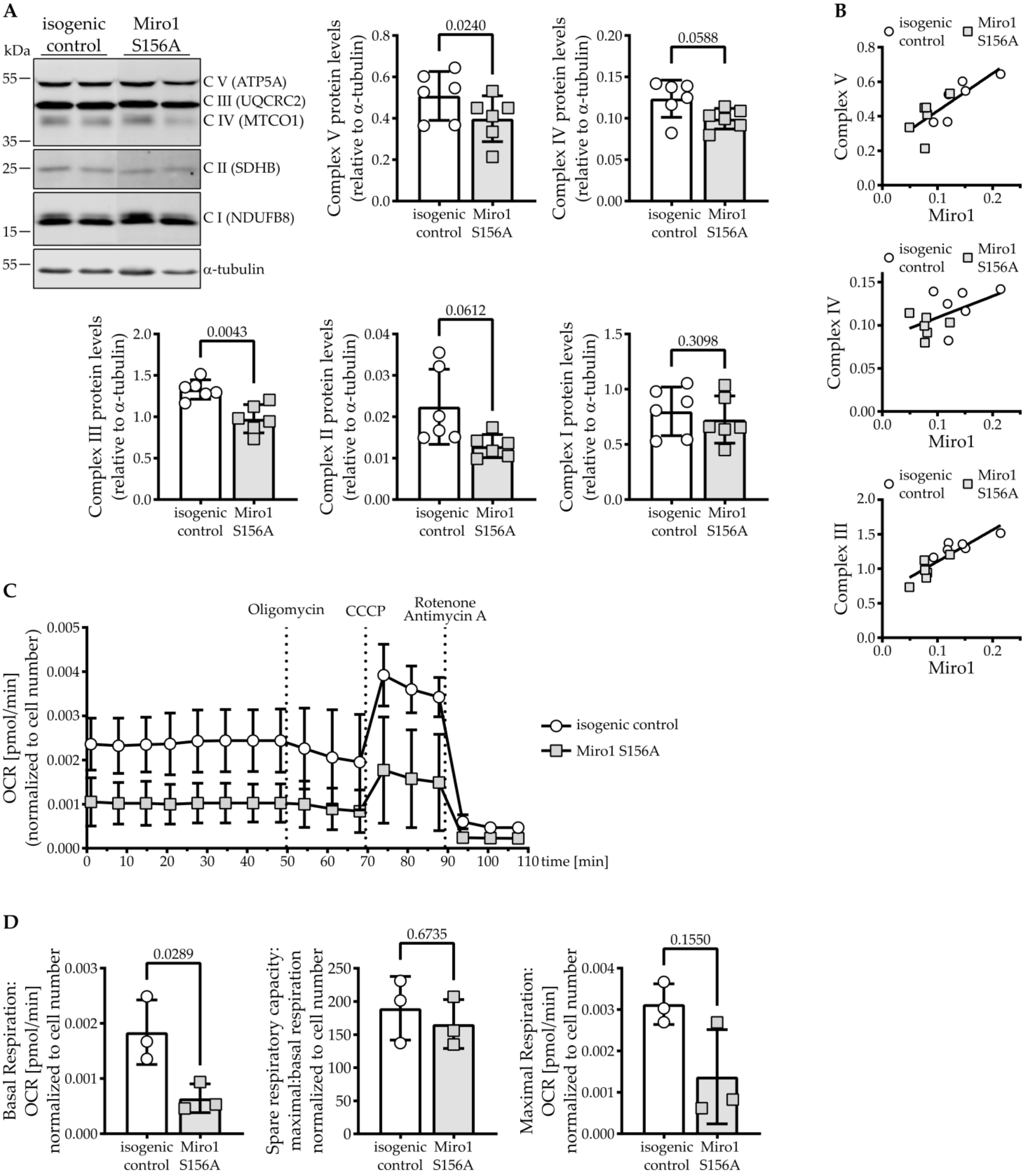

Figure 3. Miro1 S156A reduces mitochondrial respiration in hDaNs. (**A**) Representative Western blot showing complex V/IV/III/II/I in hDaN lysate. Quantification of the intensity of bands normalized to α-tubulin. Error bars depict standard deviation (n_{Diff} = 6); paired *t* test, two-tailed. (**B**) Correlation of Miro1 protein levels to complex V/IV/III protein levels in hDaN lysate (n_{Diff} = 6). (**C**) Respiratory analysis of mitochondrial oxygen consumption in hDaNs. Neurons were challenged with Oligomycin, CCCP, and rotenone with antimycin A at the indicated times. Oxygen consumption rate was normalized to the number of cells seeded. Error bars indicate standard deviation (n_{Diff} = 3). (**D**) Basal respiration, spare respiratory capacity, and maximal respiration calculated from respiratory analysis. Error bars indicate standard deviation (n_{Diff} = 3); paired *t* test, two-tailed.

3.4. The S156A Mutation Reduces Miro1 Protein Levels Affecting OXPHOS in Postmitotic Differentiated Cells

Since S156A leads to a reduction of Miro1 protein accompanied by a reduction of OXPHOS in hDaNs, we next assessed whether this effect is due to a specific vulnerability of postmitotic neuronal cells or a mutation-specific effect. To do this, we measured Miro1 protein levels, as well as Tom 20 protein levels as an indicator for mitochondrial mass, in S156A neural precursor cells. The NPCs are (in contrast to hDaNs) mitotic, undifferentiated, and have a less complex morphology (Figures 1B and S1B). In untreated NPCs, Miro1 S156A does not result in a reduction in Miro1 steady-state protein levels (Figure 4A), and Tom20 protein levels are comparable between Miro1 S156A and the isogenic control NPCs (Figure S1D). In NPCs, the S156A mutation alone is not sufficient to reduce OXPHOS complexes V and III (Figure 4A). OXPHOS complexes IV and I also remain unchanged (Figure S1D). We then knocked down Miro1 protein in mitotic, undifferentiated SH-SY5Y neuroblastoma cells to 63% of the control ($p = 0.0326$) by transfecting siRNA pools, which had no effect on either Tom20 protein levels (Figure S1E) or OXPHOS complexes (Figures 4B and S1E). These data support the notion that Miro1 reduction is necessary for the decrease of the OXPHOS complexes observed in hDaNs. We next performed Miro1 knockdown in post-mitotic, differentiated SH-SY5Y neuroblastoma cells to 76% of the control ($p = 0.0039$), which had no effect on Tom20 levels (Figure S1F). Reduced Miro1 levels in differentiated neuroblastoma cells did significantly reduce OXPHOS complexes III and IV, but not complexes I or V (Figures 4C and S1F). In line with the data from hDaNs, Miro1 levels correlate with reduced mitochondrial respiratory complexes (CIII $r = 0.8318$, $p = 0.0104$; CIV $r = 0.9630$, $p = 0.0001$). These data highlight the relevance of Miro1 depletion depending on the differentiation state of neurons.

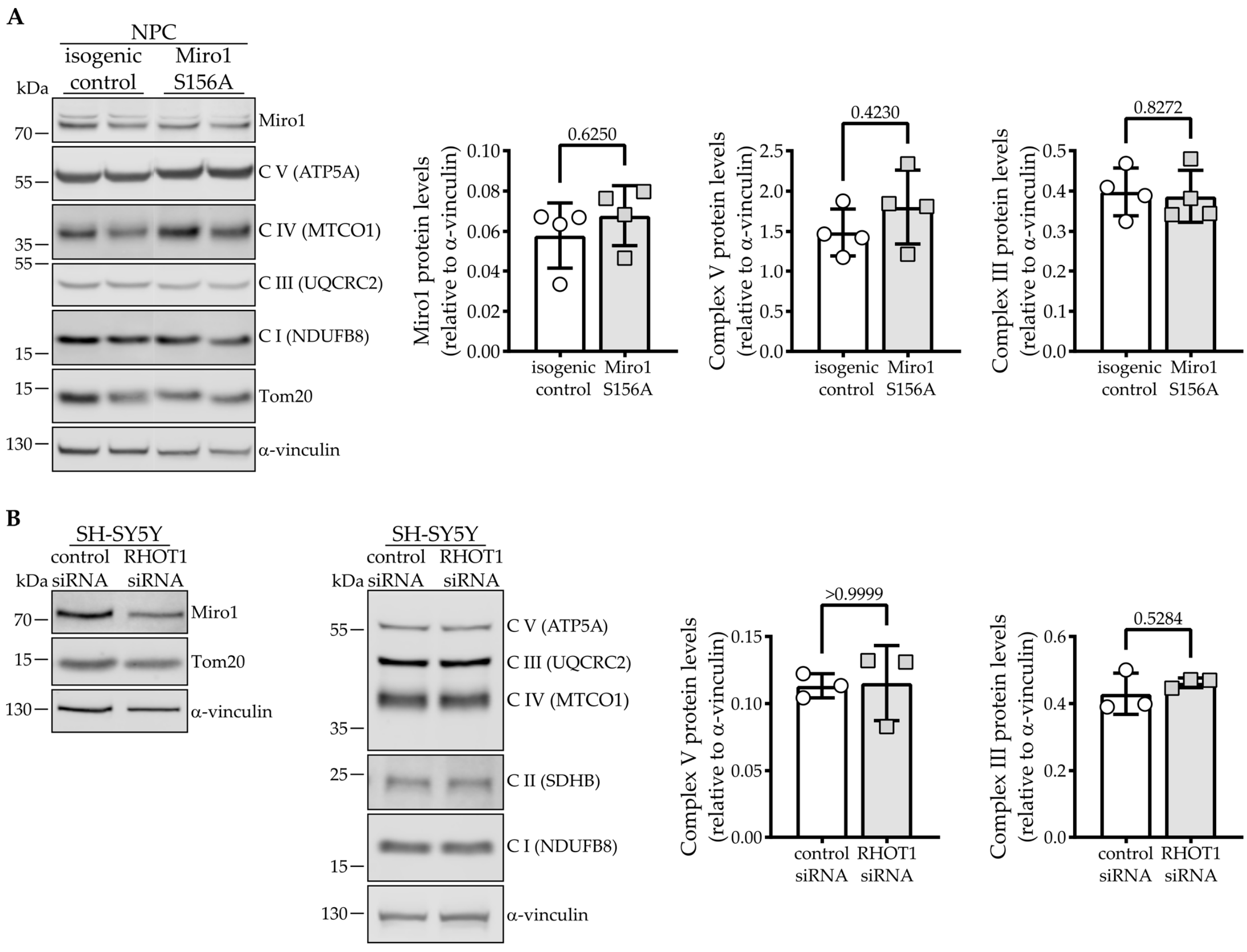

Figure 4. *Cont.*

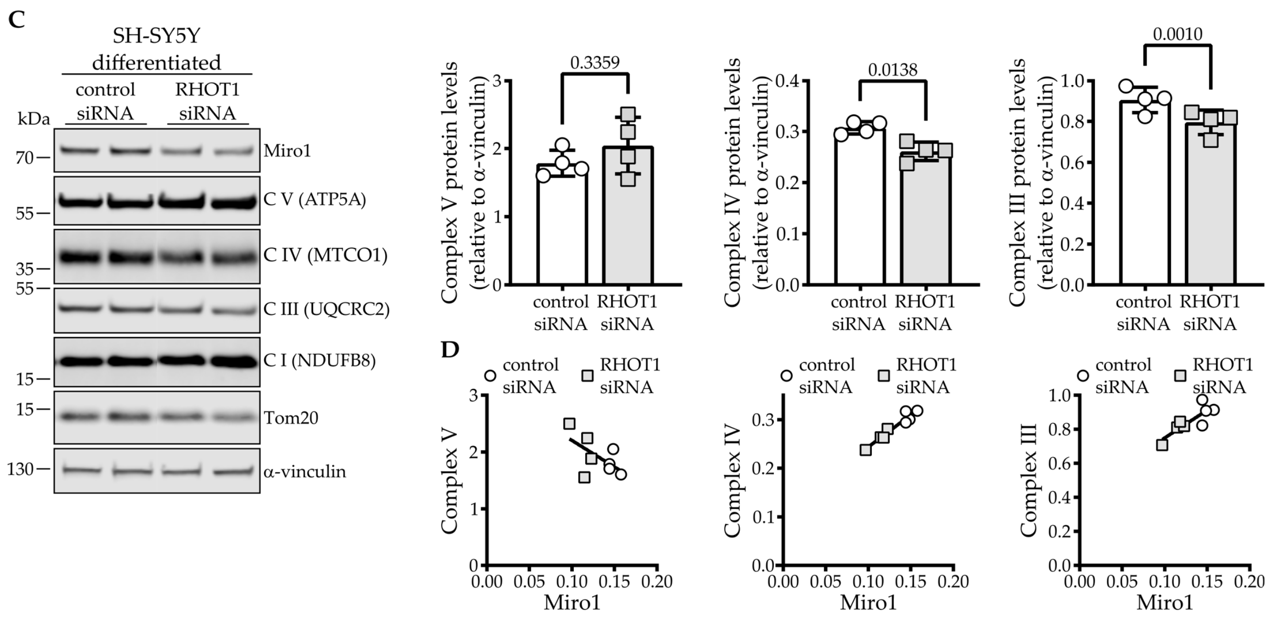

Figure 4. The S156A mutation reduces Miro1 protein levels affecting OXPHOS in postmitotic differentiated cells. (**A**) Representative Western blot showing Miro1, Tom20, complex V/IV/III/I in NPCs. Quantification of intensity of Miro1, complex V and III bands normalized to α-vinculin. Error bars depict standard deviation (n = 4); Miro1: Wilcoxon test matched pairs signed rank test; complexes V and III: paired *t* test, two-tailed. (**B**) RHOT1 knockdown in undifferentiated SH-SY5Y cells. Representative Western blot showing Miro1, Tom20, complex V/IV/III/II/I in undifferentiated SH-SY5Y cells transfected with RHOT1 or non-targeting siRNA. Quantification of intensity of complex V and III bands normalized to α-vinculin. Error bars depict standard deviation (n = 3); complex V: Wilcoxon test matched pairs signed rank test.; complex III: paired *t* test, two-tailed. (**C**) RHOT1 knockdown in differentiated SH-SY5Y cells. Representative Western blot showing Miro1, Tom20, complex V/IV/III/I in differentiated SH-SY5Y cells transfected with RHOT1 or non-targeting siRNA. Quantification of intensity of complex V/IV/III bands normalized to α-vinculin. Error bars depict standard deviation (n = 4); paired *t* test, two-tailed. (**D**) Correlation of Miro1 protein levels to complex V/IV/III protein levels in differentiated SH-SY5Y cells (n = 4).

4. Discussion

In a previous study, the induction of mitophagy failed to trigger Miro1 degradation and/or Parkin recruitment to mitochondria in a significant number of Parkinson's disease patients' fibroblasts. Treatment with a Miro1 reducer compound restored Miro1 removal and translocation of Parkin to mitochondria [27]. Another study showed that Miro1 degradation is required for proper mitochondrial clearance during mitophagy [40]. Phosphorylation at Ser156 facilitates Miro1 removal under non-stimulated conditions [26]. However, the overexpression of Miro1 S156A or S156E constructs did not alter Miro1 protein levels [15]. All of these studies used different mitotic cell models such as fibroblasts, HeLa, HEK, and SH-SY5Y, and the Ser156 studies used transfection of the respective Miro1 constructs (S156A or S156E) with the endogenous protein present. Some studies additionally transfected with PINK1 and/or Parkin to assess mitophagy and mitochondrial motility. These co-transfection experiments revealed that Ser156 is important for PINK1-Parkin-mediated phosphorylation of Miro1 and the subsequent removal of Miro1 during mitophagy, but it was not clear whether Ser156 phosphorylation is required for regulating endogenous Miro1 levels.

In our model, hDaNs constitutively express S156A mutant Miro1 without wild-type Miro1 present, and we did not change the expression levels of PINK1 or Parkin by transfection of constructs. We found a significant reduction of Miro1 protein levels in Miro1 S156A hDaNs without a reduction in gene expression. Because we found no differences in mitochondrial mass, we hypothesized that the baseline reduction of Miro1 protein could be a result of either increased degradation as a compensatory mechanism or a destabilizing effect of the mutation. The fact that neural precursors with the same mutation do not have reduced Miro1 levels argues in favor of compensation during development. It is also possible that the addition of a mitochondrial stressor is needed to expose the mutation-specific effect on Miro1 steady-state levels in mitotic cells.

Previous studies have shown that chemical-induced mitochondrial depolarization in healthy cells is followed by Miro1 phosphorylation and removal [15,26,27]. In the complete absence of Miro1, mitophagy is also impaired and the ubiquitination of Miro1 was shown to be a requirement for executing mitophagy in mouse primary neurons [40]. While this indicates that Ser156 phosphorylation does not affect Miro1 ubiquitination during chemically induced mitophagy [15,24], one study indicated that this might be relevant for Parkin recruitment and moderate Parkin activation [26]. In our study, the S156A mutation inhibits the flux of CCCP-induced mitophagy marked by impaired Miro1 and delayed Mitofusin degradation, presumably because the reduced mitochondrial membrane potential and depleted Miro1 levels have already engaged mitochondrial quality control systems. Parkin targets both Miro1 and Mitofusin for degradation, and the removal of the outer mitochondrial membrane targets precedes activation of autophagy and is mainly mediated by proteasomal degradation [41]. Here, inhibition of the proteasome has little or no effect on these substrates in both S156A and the control neurons, suggesting that degradation of Miro1 and Mitofusin can occur independently of the proteasome in hDaNs. The mutation does not prevent the CCCP-induced removal of Miro1 completely since it is degraded after 24h of treatment. This can be explained by the activation of the autophagosomal system. Little is known about the effect of phosphorylation at Thr298 and Thr299 of Miro1, but a study indicates that they might oppose the effect of phosphorylation at Ser156 [26]. Since Miro1 cannot be phosphorylated at Ser156, additional phosphorylation at Thr298 and Thr299 might contribute to failure of Miro1 degradation in S156A hDaNs during the first six hours of treatment. Taken together, the findings of this study are particularly interesting since they confirm the importance of Miro1 Ser156 phosphorylation in dopaminergic neurons. This is important because degradation of Miro1 is impaired in a subset of Parkinson's disease patients [27] and in α-synuclein mutant neurons [42].

We suggest that even a partial reduction of Miro1 steady-state levels is sufficient to impair mitophagy, but not mitochondrial movement. Together with Miro1 knockout studies in mice [40,43], our data support the notion that Miro1 has an essential role in PINK1-Parkin-mediated mitophagy. In dopaminergic neurons, the S156A mutation causes partial (40–50%) but incomplete depletion of Miro1 steady-state levels. Under physiological conditions, there are likely to be thresholds of Miro1 levels for maintaining certain functions, like mitochondrial movement, which cannot be modelled by chemically forced mitophagy or complete loss of the protein via knockout. Although Miro1 is essential for multiple processes, the whole removal of mitochondria via classical mitophagy could be the most dispensable process in mature neurons. Since previous experiments were performed in different cell types (SH-SY5Y [15], HeLa [24], and HEK/rat embryonic fibroblasts [26]), a greater significance of Ser156 phosphorylation during induced mitophagy might be attributed to the specific physiology of iPSC-derived hDaNs. It will be interesting to further detail the effect of this mutation in different cell types, including iPSCs, iPSC-derived astrocytes, or iPSC-derived cortical neurons. Furthermore, co-culturing or crossing Miro1 and PINK1 models may help in further dissecting the mechanism of Miro1 phosphorylation and subsequent events at the MOM.

Our data show a novel connection between Miro1 phosphorylation, Miro1 levels, and mitochondrial respiration. During differentiation, iPSCs switch energy production from glycolysis to OXPHOS to maintain the ATP levels required for neuronal activity [8]. The reduction of basal and maximal respiration in Miro1 S156A mutant neurons suggests that neurons might not be able to meet energetic demand during prolonged neuronal activation, which, in turn, might impair synaptic transmission. So far, only very few studies have looked at the of role Miro1 in regulating OXPHOS proteins and function. Studies in Miro1 knockout mouse fibroblasts (MEFs) found no effect on mitochondrial respiration [7,44], indicating that depletion of Miro1 does not alter their mitochondrial bioenergetics. In line with these findings, we showed that in undifferentiated SH-SH5Y cells, knockdown of Miro1 does not reduce complex IV and V protein levels. S156A might also impair Miro1 interaction with Parkin [23,26], and it is possible that PINK1/parkin signaling might confer the effect on respiration and levels of respiratory complexes since PINK1 and Parkin regulate synthesis of OXPHOS complexes [45]. We hypothesize that as part of mitochondrial quality control, phosphorylation of Miro1 at Ser156 promotes the synthesis of OXPHOS subunits or their regulation via Miro1 steady-state levels.

Supplementary Materials: The following supporting information can be downloaded at: https://www.mdpi.com/article/10.3390/cells11081269/s1, Figure S1: Characterization of Miro1 S156A Neural Precursor cells (NPCs).

Author Contributions: Conceptualization, J.C.F.; methodology, L.S.; validation, L.S. and J.C.F.; formal analysis L.S.; investigation, L.S and J.C.F.; resources, J.C.F.; data curation, L.S.; writing—original draft preparation, L.S.; writing—review and editing, J.C.F.; visualization, L.S.; supervision, J.C.F.; project administration, J.C.F.; funding acquisition, J.C.F. All authors have read and agreed to the published version of the manuscript.

Funding: This study was funded by the Deutsche Forschungsgemeinschaft (DFG, German Research Foundation)—Research Training Group MOMbrane 654651/GRK2364.

Institutional Review Board Statement: The study was conducted in accordance with the Declaration of Helsinki and approved by the Ethics Committee of The University of Tübingen (Ethical approval, 14612009801), in accordance with The Hertie Institute for Clinical Brain Research Biobank (protocols for informed consent, ethics, and data protection).

Informed Consent Statement: Informed consent was obtained from all subjects involved in the study. The consent of individuals for scientific research and publication of research is covered by the consent forms held at The Hertie Institute for Clinical Brain Research Biobank, Tübingen, and have been approved by the University of Tübingen Ethics committee. The anonymity of the healthy individual whose donated cells were used in this study is protected.

Data Availability Statement: Not applicable.

Acknowledgments: We thank Karan Sharma, a member of our laboratory for the discussions and critical evaluation of the manuscript. We thank Maike Nagel from the Schüle laboratory (Hertie Institute for Clinical Brain Research, Tübingen) for providing all-trans retinoic acid. We thank our former lab member, Lara-Sophie Rieder, for the establishment of mitochondrial movement analysis.

Conflicts of Interest: The authors declare no conflict of interest.

References

1. Fransson, A.; Ruusala, A.; Aspenstrom, P. Atypical Rho GTPases have roles in mitochondrial homeostasis and apoptosis. *J. Biol. Chem.* **2003**, *278*, 6495–6502. [CrossRef] [PubMed]
2. Fransson, S.; Ruusala, A.; Aspenstrom, P. The atypical Rho GTPases Miro-1 and Miro-2 have essential roles in mitochondrial trafficking. *Biochem. Biophys. Res. Commun.* **2006**, *344*, 500–510. [CrossRef] [PubMed]
3. Klosowiak, J.L.; Focia, P.J.; Chakravarthy, S.; Landahl, E.C.; Freymann, D.M.; Rice, S.E. Structural coupling of the EF hand and C-terminal GTPase domains in the mitochondrial protein Miro. *EMBO Rep.* **2013**, *14*, 968–974. [CrossRef] [PubMed]
4. MacAskill, A.F.; Brickley, K.; Stephenson, F.A.; Kittler, J.T. GTPase dependent recruitment of Grif-1 by Miro1 regulates mitochondrial trafficking in hippocampal neurons. *Mol. Cell Neurosci.* **2009**, *40*, 301–312. [CrossRef] [PubMed]
5. Russo, G.J.; Louie, K.; Wellington, A.; Macleod, G.T.; Hu, F.; Panchumarthi, S.; Zinsmaier, K.E. Drosophila Miro is required for both anterograde and retrograde axonal mitochondrial transport. *J. Neurosci.* **2009**, *29*, 5443–5455. [CrossRef]
6. Lopez-Domenech, G.; Higgs, N.F.; Vaccaro, V.; Ros, H.; Arancibia-Carcamo, I.L.; MacAskill, A.F.; Kittler, J.T. Loss of Dendritic Complexity Precedes Neurodegeneration in a Mouse Model with Disrupted Mitochondrial Distribution in Mature Dendrites. *Cell Rep.* **2016**, *17*, 317–327. [CrossRef]
7. Nguyen, T.T.; Oh, S.S.; Weaver, D.; Lewandowska, A.; Maxfield, D.; Schuler, M.H.; Smith, N.K.; Macfarlane, J.; Saunders, G.; Palmer, C.A.; et al. Loss of Miro1-directed mitochondrial movement results in a novel murine model for neuron disease. *Proc. Natl. Acad. Sci. USA* **2014**, *111*, E3631–E3640. [CrossRef]

8. Devine, M.J.; Kittler, J.T. Mitochondria at the neuronal presynapse in health and disease. *Nat. Rev. Neurosci.* **2018**, *19*, 63–80. [CrossRef]
9. Chang, K.T.; Niescier, R.F.; Min, K.T. Mitochondrial matrix Ca^{2+} as an intrinsic signal regulating mitochondrial motility in axons. *Proc. Natl. Acad. Sci. USA* **2011**, *108*, 15456–15461. [CrossRef]
10. Macaskill, A.F.; Rinholm, J.E.; Twelvetrees, A.E.; Arancibia-Carcamo, I.L.; Muir, J.; Fransson, A.; Aspenstrom, P.; Attwell, D.; Kittler, J.T. Miro1 is a calcium sensor for glutamate receptor-dependent localization of mitochondria at synapses. *Neuron* **2009**, *61*, 541–555. [CrossRef]
11. Niescier, R.F.; Hong, K.; Park, D.; Min, K.T. MCU Interacts with Miro1 to Modulate Mitochondrial Functions in Neurons. *J. Neurosci.* **2018**, *38*, 4666–4677. [CrossRef] [PubMed]
12. Saotome, M.; Safiulina, D.; Szabadkai, G.; Das, S.; Fransson, A.; Aspenstrom, P.; Rizzuto, R.; Hajnóczky, G. Bidirectional Ca^{2+}-dependent control of mitochondrial dynamics by the Miro GTPase. *Proc. Natl. Acad. Sci. USA* **2008**, *105*, 20728–20733. [CrossRef] [PubMed]
13. Wang, X.; Schwarz, T.L. The mechanism of Ca^{2+}-dependent regulation of kinesin-mediated mitochondrial motility. *Cell* **2009**, *136*, 163–174. [CrossRef] [PubMed]
14. Weihofen, A.; Thomas, K.J.; Ostaszewski, B.L.; Cookson, M.R.; Selkoe, D.J. Pink1 forms a multiprotein complex with Miro and Milton, linking Pink1 function to mitochondrial trafficking. *Biochemistry* **2009**, *48*, 2045–2052. [CrossRef]
15. Birsa, N.; Norkett, R.; Wauer, T.; Mevissen, T.E.; Wu, H.C.; Foltynie, T.; Bhatia, K.; Hirst, W.D.; Komander, D.; Plun-Favreau, H.; et al. Lysine 27 ubiquitination of the mitochondrial transport protein Miro is dependent on serine 65 of the Parkin ubiquitin ligase. *J. Biol. Chem.* **2014**, *289*, 14569–14582. [CrossRef] [PubMed]
16. Exner, N.; Lutz, A.K.; Haass, C.; Winklhofer, K.F. Mitochondrial dysfunction in Parkinson's disease: Molecular mechanisms and pathophysiological consequences. *EMBO J.* **2012**, *31*, 3038–3062. [CrossRef] [PubMed]
17. Kitada, T.; Asakawa, S.; Hattori, N.; Matsumine, H.; Yamamura, Y.; Minoshima, S.; Yokochi, M.; Mizuno, Y.; Shimizu, N. Mutations in the parkin gene cause autosomal recessive juvenile parkinsonism. *Nature* **1998**, *392*, 605–608. [CrossRef]
18. Valente Enza, M.; Abou-Sleiman Patrick, M.; Caputo, V.; Muqit Miratul, M.K.; Harvey, K.; Gispert, S.; Ali, Z.; Del Turco, D.; Bentivoglio Anna, R.; Healy Daniel, G.; et al. Hereditary Early-Onset Parkinson's Disease Caused by Mutations in PINK1. *Science* **2004**, *304*, 1158–1160. [CrossRef]
19. Geisler, S.; Holmstrom, K.M.; Skujat, D.; Fiesel, F.C.; Rothfuss, O.C.; Kahle, P.J.; Springer, W. PINK1/Parkin-mediated mitophagy is dependent on VDAC1 and p62/SQSTM1. *Nat. Cell Biol.* **2010**, *12*, 119–131. [CrossRef]
20. Narendra, D.; Kane, L.A.; Hauser, D.N.; Fearnley, I.M.; Youle, R.J. p62/SQSTM1 is required for Parkin-induced mitochondrial clustering but not mitophagy; VDAC1 is dispensable for both. *Autophagy* **2010**, *6*, 1090–1106. [CrossRef]
21. Kane, L.A.; Lazarou, M.; Fogel, A.I.; Li, Y.; Yamano, K.; Sarraf, S.A.; Banerjee, S.; Youle, R.J. PINK1 phosphorylates ubiquitin to activate Parkin E3 ubiquitin ligase activity. *J. Cell Biol.* **2014**, *205*, 143–153. [CrossRef] [PubMed]
22. Koyano, F.; Okatsu, K.; Kosako, H.; Tamura, Y.; Go, E.; Kimura, M.; Kimura, Y.; Tsuchiya, H.; Yoshihara, H.; Hirokawa, T.; et al. Ubiquitin is phosphorylated by PINK1 to activate parkin. *Nature* **2014**, *510*, 162–166. [CrossRef] [PubMed]
23. Wang, X.; Winter, D.; Ashrafi, G.; Schlehe, J.; Wong, Y.L.; Selkoe, D.; Rice, S.; Steen, J.; LaVoie, M.J.; Schwarz, T.L. PINK1 and Parkin target Miro for phosphorylation and degradation to arrest mitochondrial motility. *Cell* **2011**, *147*, 893–906. [CrossRef] [PubMed]
24. Liu, S.; Sawada, T.; Lee, S.; Yu, W.; Silverio, G.; Alapatt, P.; Millan, I.; Shen, A.; Saxton, W.; Kanao, T.; et al. Parkinson's disease-associated kinase PINK1 regulates Miro protein level and axonal transport of mitochondria. *PLoS Genet.* **2012**, *8*, e1002537. [CrossRef]
25. Kazlauskaite, A.; Kelly, V.; Johnson, C.; Baillie, C.; Hastie, C.J.; Peggie, M.; Macartney, T.; Woodroof, H.I.; Alessi, D.R.; Pedrioli, P.G.; et al. Phosphorylation of Parkin at Serine65 is essential for activation: Elaboration of a Miro1 substrate-based assay of Parkin E3 ligase activity. *Open Biol.* **2014**, *4*, 130213. [CrossRef]
26. Shlevkov, E.; Kramer, T.; Schapansky, J.; LaVoie, M.J.; Schwarz, T.L. Miro phosphorylation sites regulate Parkin recruitment and mitochondrial motility. *Proc. Natl. Acad. Sci. USA* **2016**, *113*, E6097–E6106. [CrossRef]
27. Hsieh, C.H.; Li, L.; Vanhauwaert, R.; Nguyen, K.T.; Davis, M.D.; Bu, G.; Wszolek, Z.K.; Wang, X. Miro1 Marks Parkinson's Disease Subset and Miro1 Reducer Rescues Neuron Loss in Parkinson's Models. *Cell Metab.* **2019**, *30*, 1131.e1137–1140.e1137. [CrossRef]
28. Schwarz, L.; Casadei, N.; Fitzgerald, J.C. Generation of R272Q, S156A and K572R RHOT1/Miro1 point mutations in iPSCs from a healthy individual using FACS-assisted CRISPR/Cas9 genome editing. *Stem Cell Res.* **2021**, *55*, 102469. [CrossRef]
29. Reinhardt, P.; Glatza, M.; Hemmer, K.; Tsytsyura, Y.; Thiel, C.S.; Hoing, S.; Moritz, S.; Parga, J.A.; Wagner, L.; Bruder, J.M.; et al. Derivation and expansion using only small molecules of human neural progenitors for neurodegenerative disease modeling. *PLoS ONE* **2013**, *8*, e59252. [CrossRef]
30. Bus, C.; Zizmare, L.; Feldkaemper, M.; Geisler, S.; Zarani, M.; Schaedler, A.; Klose, F.; Admard, J.; Mageean, C.J.; Arena, G.; et al. Human Dopaminergic Neurons Lacking PINK1 Exhibit Disrupted Dopamine Metabolism Related to Vitamin B6 Co-Factors. *iScience* **2020**, *23*, 101797. [CrossRef]
31. Merrill, R.A.; Flippo, K.H.; Strack, S. Measuring Mitochondrial Shape with ImageJ. In *Techniques to Investigate Mitochondrial Function in Neurons*; Neuromethods; Springer: Berlin, Germany, 2017; pp. 31–48.
32. Kocsis, E.; Trus, B.L.; Steer, C.J.; Bisher, M.E.; Steven, A.C. Image averaging of flexible fibrous macromolecules: The clathrin triskelion has an elastic proximal segment. *J. Struct. Biol.* **1991**, *107*, 6–14. [CrossRef]

33. Tinevez, J.Y.; Perry, N.; Schindelin, J.; Hoopes, G.M.; Reynolds, G.D.; Laplantine, E.; Bednarek, S.Y.; Shorte, S.L.; Eliceiri, K.W. TrackMate: An open and extensible platform for single-particle tracking. *Methods* **2017**, *115*, 80–90. [CrossRef] [PubMed]
34. Hernandez, G.; Thornton, C.; Stotland, A.; Lui, D.; Sin, J.; Ramil, J.; Magee, N.; Andres, A.; Quarato, G.; Carreira, R.S.; et al. MitoTimer: A novel tool for monitoring mitochondrial turnover. *Autophagy* **2013**, *9*, 1852–1861. [CrossRef] [PubMed]
35. Marrone, L.; Bus, C.; Schondorf, D.; Fitzgerald, J.C.; Kubler, M.; Schmid, B.; Reinhardt, P.; Reinhardt, L.; Deleidi, M.; Levin, T.; et al. Generation of iPSCs carrying a common LRRK2 risk allele for in vitro modeling of idiopathic Parkinson's disease. *PLoS ONE* **2018**, *13*, e0192497. [CrossRef]
36. Babic, M.; Russo, G.J.; Wellington, A.J.; Sangston, R.M.; Gonzalez, M.; Zinsmaier, K.E. Miro's N-terminal GTPase domain is required for transport of mitochondria into axons and dendrites. *J. Neurosci.* **2015**, *35*, 5754–5771. [CrossRef]
37. Frederick, R.L.; McCaffery, J.M.; Cunningham, K.W.; Okamoto, K.; Shaw, J.M. Yeast Miro GTPase, Gem1p, regulates mitochondrial morphology via a novel pathway. *J. Cell Biol.* **2004**, *167*, 87–98. [CrossRef]
38. Sarraf, S.A.; Raman, M.; Guarani-Pereira, V.; Sowa, M.E.; Huttlin, E.L.; Gygi, S.P.; Harper, J.W. Landscape of the PARKIN-dependent ubiquitylome in response to mitochondrial depolarization. *Nature* **2013**, *496*, 372–376. [CrossRef]
39. Chan, N.C.; Salazar, A.M.; Pham, A.H.; Sweredoski, M.J.; Kolawa, N.J.; Graham, R.L.; Hess, S.; Chan, D.C. Broad activation of the ubiquitin-proteasome system by Parkin is critical for mitophagy. *Hum. Mol. Genet.* **2011**, *20*, 1726–1737. [CrossRef]
40. Lopez-Domenech, G.; Howden, J.H.; Covill-Cooke, C.; Morfill, C.; Patel, J.V.; Burli, R.; Crowther, D.; Birsa, N.; Brandon, N.J.; Kittler, J.T. Loss of neuronal Miro1 disrupts mitophagy and induces hyperactivation of the integrated stress response. *EMBO J.* **2021**, *40*, e100715. [CrossRef]
41. Alshaabi, H.; Shannon, N.; Gravelle, R.; Milczarek, S.; Messier, T.; Cunniff, B. Miro1-mediated mitochondrial positioning supports subcellular redox status. *Redox Biol.* **2021**, *38*, 101818. [CrossRef]
42. Shaltouki, A.; Hsieh, C.H.; Kim, M.J.; Wang, X. Alpha-synuclein delays mitophagy and targeting Miro rescues neuron loss in Parkinson's models. *Acta Neuropathol.* **2018**, *136*, 607–620. [CrossRef] [PubMed]
43. López-Doménech, G.; Covill-Cooke, C.; Howden, J.H.; Birsa, N.; Morfill, C.; Brandon, N.J.; Kittler, J.T. Miro ubiquitination is critical for efficient damage-induced PINK1/Parkin-mediated mitophagy. *bioRxiv* **2018**, 414664. [CrossRef]
44. Schuler, M.H.; Lewandowska, A.; Caprio, G.D.; Skillern, W.; Upadhyayula, S.; Kirchhausen, T.; Shaw, J.M.; Cunniff, B. Miro1-mediated mitochondrial positioning shapes intracellular energy gradients required for cell migration. *Mol. Biol. Cell* **2017**, *28*, 2159–2169. [CrossRef] [PubMed]
45. Gehrke, S.; Wu, Z.; Klinkenberg, M.; Sun, Y.; Auburger, G.; Guo, S.; Lu, B. PINK1 and Parkin control localized translation of respiratory chain component mRNAs on mitochondria outer membrane. *Cell Metab.* **2015**, *21*, 95–108. [CrossRef]

cells

Communication

Steady-State Levels of Miro1 Linked to Phosphorylation at Serine 156 and Mitochondrial Respiration in Dopaminergic Neurons

Lisa Schwarz and Julia C. Fitzgerald *

Department of Neurodegeneration, Hertie Institute for Clinical Brain Research, University of Tuebingen, 72076 Tuebingen, Germany; l.schwarz@uni-tuebingen.de
* Correspondence: julia.fitzgerald@uni-tuebingen.de

Supplementary Figure 1. Characterization of Miro1 S156A Neural Precursor cells (NPCs)

Figure S 1: (**A**) RT-qPCR showing expression of neural precursor markers *NES*, *SOX2* and *PAX6* in NPCs as fold change to iPSCs. Error bars depict SD (n=3); Wilcoxon matched pairs signed rank test with two-stage linear step-up procedure of Benjamini, Krieger and Yekutieli. (**B**) Representative immunofluorescence staining showing neural precursor marker Sox2 and Nestin in NPCs. (**C**) ECAR in hDaNs. Neurons were challenged with Oligomycin, CCCP and Rotenone with Antimycin A at the indicated times. ECAR was normalized to number of cells seeded. Error bars indicate standard deviation (n_{Diff}=3). (**D**) Quantification of intensity of Tom20, Complex IV and I Western blot bands in NPCs normalized to α-vinculin. Error bars depict standard deviation (n=4); Complex IV: Wilcoxon test matched pairs signed rank test.; Tom20 and Complex I: Paired *t* test, two-tailed. **(C)** RHOT1 knockdown in undifferentiated SH-SY5Y cells. Quantification of intensity of Miro1, Tom20, Complex IV and I Western blot bands normalized to α-vinculin. Error bars depict standard deviation (n=3); Miro1: paired *t* test, one-tailed; Tom20, Complex IV/ II/I: Paired *t* test, two-tailed. **(D)** RHOT1 knockdown in differentiated SH-SY5Y cells. Quantification of intensity of Miro1, Tom20 and Complex I Western blot bands normalized to α-vinculin. Error bars depict standard deviation (n=4); Miro1: paired *t* test, one-tailed; Tom20 and Complex I: Paired *t* test, two-tailed.

Cells **2022**, *11*, 1269. https://doi.org/10.3390/cells11081269

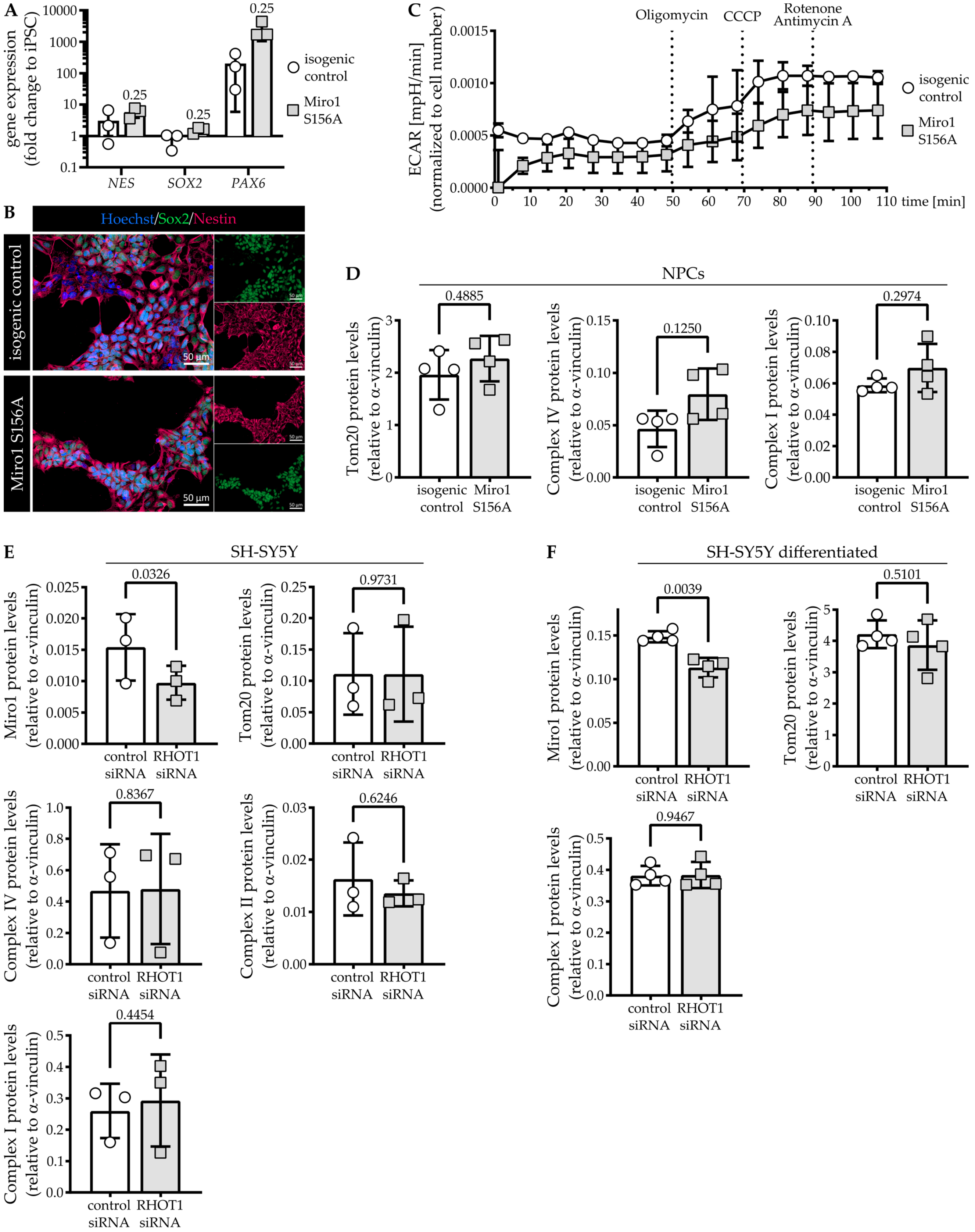
A
gene expression (fold change to iPSC)
10000
1000
100
10
1
0.1
0.25
0.25
0.25
NES
SOX2
PAX6
○ isogenic control
▨ Miro1 S156A
B
Hoechst/Sox2/Nestin
isogenic control
Miro1 S156A
50 µm
50 µm
C
ECAR [mpH/min] (normalized to cell number)
0.0015
0.0010
0.0005
0.0000
Oligomycin
CCCP
Rotenone Antimycin A
0
10
20
30
40
50
60
70
80
90
100
110 time [min]
○ isogenic control
▨ Miro1 S156A
D
NPCs
0.4885
0.1250
0.2974
Tom20 protein levels (relative to α-vinculin)
Complex IV protein levels (relative to α-vinculin)
Complex I protein levels (relative to α-vinculin)
isogenic control
Miro1 S156A
E
SH-SY5Y
0.0326
0.9731
0.8367
0.6246
0.4454
Miro1 protein levels (relative to α-vinculin)
Tom20 protein levels (relative to α-vinculin)
Complex IV protein levels (relative to α-vinculin)
Complex II protein levels (relative to α-vinculin)
Complex I protein levels (relative to α-vinculin)
control siRNA
RHOT1 siRNA
F
SH-SY5Y differentiated
0.0039
0.5101
0.9467
Miro1 protein levels (relative to α-vinculin)
Tom20 protein levels (relative to α-vinculin)
Complex I protein levels (relative to α-vinculin)
control siRNA
RHOT1 siRNA

frontiers

Miro1 R272Q Disrupts Mitochondrial Calcium Handling and Neurotransmitter Uptake in Dopaminergic Neurons

Lisa Schwarz[1], Lorenzo D. Dodi[1], Lara-Sophie Rieder[1], Petra Fallier-Becker[2], Nicolas Casadei[3,4], Julia C. Fitzgerald[1*]

[1] Mitochondrial Biology of Parkinson’s Disease Laboratory, Hertie Institute for Clinical Brain Research, Department of Neurodegenerative Diseases, University of Tübingen, Tübingen, Germany

[2] Institute of Pathology and Neuropathology, University of Tübingen, Tübingen, Germany

[3] Institute of Medical Genetics and Applied Genomics, University of Tübingen

[4] NGS Competence Center Tübingen, Tübingen, Germany

*** Correspondence:**
Julia C. Fitzgerald
Julia.Fitzgerald@uni-tuebingen.de

Keywords: Miro1, Parkinson’s disease, mitochondria, calcium, dopaminergic neuron.

Abstract

The Rho GTPase Miro1, located at the mitochondrial outer membrane is known to properly distribute mitochondria to synapses, aid calcium buffering and initiate PINK1-Parkin mediated mitophagy. Several heterozygous *RHOT1*/Miro1 variants were identified in sporadic Parkinson’s disease patients. Miro1 R272Q is located within a calcium binding domain, but the functional outcome of this point mutation and its contribution to the development of disease are unclear. To address this, we introduced a heterozygous *RHOT1*/Miro1 R272Q point mutation in healthy induced pluripotent stem cells. In dopaminergic neurons, Miro1 R272Q does not affect Miro1 protein levels, CCCP-induced mitophagy, nor mitochondrial movement yet causes the fragmentation of mitochondria with reduction of cristae and ATP5A. Inhibition of the mitochondrial calcium uniporter phenocopied Miro1 R272Q and Miro1 knockdown induced reduction of calcium buffering. Altered mitochondrial calcium uptake is associated with reduced mitochondrial respiration and reduced catecholamine neurotransmitter uptake. Synaptic changes are not coupled to dopamine distribution or dopamine transporters but are linked to Miro1 R272Q-related calcium handling concomitant with defective dopamine regulation at the mitochondrial surface by monoamine oxidase. We conclude that the Miro1 R272Q heterozygous point mutation dampens mitochondrial-calcium regulation and mitochondrial capacity via events at the outer membrane that are sufficient to disrupt dopaminergic function.

1 Introduction

Miro1 is a GTPase anchored in the outer mitochondrial membrane (Fransson et al., 2003) by a C-terminal transmembrane domain (Fransson et al., 2006). One of its main functions in mammalian cells is mediating mitochondrial transport along the cytoskeleton (Fransson et al., 2006, MacAskill et al., 2009a, Russo et al., 2009). In neurons, this is of special significance because mitochondria are mostly synthesized in the soma and hence need to be distributed to the cell’s periphery. Miro1 arrests mitochondria at sites of synaptic activity by calcium binding (Macaskill et al., 2009b, Wang and Schwarz, 2009). Since this is also essential in neuronal development (Lopez-Domenech et al., 2016, Nguyen et al., 2014), it is not surprising that no homozygous *RHOT1*/Miro1 loss of function mutations are reported in humans. This is supported by a study showing that Miro1 knockout is postnatally lethal in mice (Nguyen et al., 2014).

Although genome-wide association studies failed to identify *RHOT1* (the gene encoding Miro1) as a risk locus for Parkinson's disease (PD) (Anvret et al., 2012, Nalls et al., 2019, Saeed, 2018), rare *RHOT1* variants identified by exome sequencing (Berenguer-Escuder et al., 2019, Grossmann et al., 2019) have provided insight into the complex biology of PD. One of the four heterozygous mutations found in sporadic PD patients (Berenguer-Escuder et al., 2019, Grossmann et al., 2019), Miro1 R272Q, lies within the ligand mimicking domain of the N-terminal EF-hand domain. The role of Miro1 in PD became more prominent after the finding that a subset of sporadic PD patient fibroblasts retains Miro1 at mitochondria upon mitochondrial depolarization (Hsieh et al., 2019). This is relevant, because Miro1 acts in the same signaling pathway as PD proteins PINK1, Parkin and LRRK2 (Hsieh et al., 2016, Klosowiak et al., 2016, Sarraf et al., 2013, Wang et al., 2011, Weihofen et al., 2009). Work is underway to test compounds that modulate Miro1 levels at the mitochondria (Hsieh et al., 2019) and our group previously correlated levels of Miro1 to mitochondrial respiratory complexes in post mitotic neurons (Schwarz and Fitzgerald, 2022).

Prompted by studies showing the necessity of Miro1 or its EF-hand domain for mitochondrial morphology and calcium dynamics (Chang et al., 2011, Lopez-Domenech et al., 2021, Modi et al., 2019, Nemani et al., 2018, Vaccaro et al., 2017, Konig et al., 2021), we hypothesized that heterozygous Miro1 R272Q could impair mitochondrial quality via disruption of mitochondrial calcium homeostasis. We wanted to study whether disruption of calcium sensing in neurons could affect mitochondrial movement, and whether this could partly explain the neuronal dysfunction observed in the PD patients (Berenguer-Escuder et al., 2020, Grossmann et al., 2019) We previously introduced the heterozygous Miro1 R272Q mutation into healthy induced pluripotent stem cells (iPSCs) to generate an isogenic pair, characterized the cells and performed whole genome sequencing to show genomic integrity and genetic identity (Schwarz et al., 2021). In this study we found that mitochondrial transport is not affected by Miro1 R272Q, whereas mitochondrial energetics disrupted by a R272Q-calcium phenotype is concomitant with synaptic changes including disrupted neurotransmitter homeostasis.

2 Materials and Methods

2.1 Generation of NPCs and differentiation in hDaNs

We used previously established and fully characterized Heterozygous Miro1 R272Q and isogenic control iPSCs (Schwarz et al., 2021). Small molecule-induced neural precursor cell (NPC) derivation from iPSC colonies and subsequent differentiation into human midbrain-specific neurons (hDaNs) was described in (Schwarz and Fitzgerald, 2022), adapted from (Reinhardt et al., 2013). This protocol generates mid-brain specific dopaminergic neurons from iPSCs via NPC intermediates. Approximately 35-40% of the resulting MAP2 positive, mature neurons are tyrosine hydroxylase (TH) positive. hDaNs were used at day 16-19 for experiments. Treatments were diluted in maturation medium, untreated hDaNs received fresh maturation medium for the duration of the longest treatment. Mitophagy was induced with 10 µM CCCP for 2/4/6 (+ 10 µM MG132)/22 h.

2.2 RT-qPCR

RNeasy kit (Qiagen, #74104) following the manufacturer's instructions was used for RNA isolation and QuantiTect SYBR green kit (Qiagen, #204243) following the manufacturer's instructions for RT-qPCR. Primer sequences are listed in Supplementary Methods Table 1.

2.3 Immunofluorescence

hDaNs were stained following standard procedures with primary antibodies (MAP2 1:2000 (abcam, #ab5392), TH 1:1000 (Pel Freez #P40101-150), Tom20 1:200 (Santa Cruz, #sc17764)) and secondary antibodies (1:1000; Thermo Fisher, #A21449, #A11070, #A21463). For details and analysis of TH+ neurons see Supplementary methods.

2.4 Immunoblotting

hDaNs were lysed in either 1% Triton X-100 in PBS or in 50mM Tris HCl pH7.5/150 mM NaCl/1 mM EDTA/0.5% TritonX-100, both supplemented with cOmplete protease inhibitor (Millipore Sigma, #11873580001) and PhosStop phosphatase inhibitor (Sigma-Aldrich, #4906837001), and homogenized by subsequent passes through needles (5x 20G/8x 25G/10x 27G or 5x 25G/10x 27G). Following standard procedures, proteins were separated and blotted onto PVDF membranes (Merck, #IPVH00010), then incubated with primary (α-tubulin 1:5000 (Sigma, #AA13), α-vinculin 1:5000 (Sigma, #V9131), Miro1 1:500 (Thermo Fisher, #PA-42646), Tom20 1:1000 (Santa Cruz, #sc11415), Total OXPHOS 1:1000 (abcam, #ab110413), LC3 1:1000 (Novusbio, #NB100-2220), Mitofusin 1:1000 (Abcam, ab#57602), MAO-B 1:1000 (abcam, #ab137778) and secondary antibodies (1:10,000; Li-cor, #926-32210, #926-32213, # 926-68071, # 926-68070) and detected with an Odyssey CLx (Licor) using Image Studio software (Licor). Image Studio Lite Ver 5.2 (Licor) was used for quantification of intensity of bands.

2.5 Analysis mitochondrial movement

Mitochondria labelled with MitoTracker were imaged under controlled environment (37°C/5% CO_2) and analyzed using fiji (Rasband, W.S., ImageJ, U. S. National Institutes of Health, Bethesda, MD, USA). For details see Supplementary methods.

2.6 Mitochondrial morphology and membrane potential

Mitochondria labelled with MitoTracker green Image-iT™ TMRM were imaged under controlled environment (37°C/5% CO_2). Mitochondrial morphology was assessed as previously described protocol (Merrill et al., 2017) with alterations. Mitochondrial membrane potential was calculated as the ratio of TMRM to MitoTracker green signal. For details see Supplementary methods.

2.7 Electron microscopy

hDANs were fixed in 2.5% glutaraldehyde in 0.1 M Sodium Cacodylate Buffer (pH 7.4, PLANO, Wetzlar, Germany), overnight at 4 °C. For details see Supplementary methods. Processed ultrathin sections of 60 nm were examined using an EM 10-Electron microscope (Zeiss, Germany). 80 EM images from three independent hDaN differentiations were numbered and mitochondria were counted blind. For details see Supplementary methods.

2.8 MitoTimer analysis

hDaNs transfected with pMitoTimer plasmid (Addgene, #52659; (Hernandez et al., 2013)) were imaged using Zeiss Imager.Z1 equipped with an ApoTome.2 and an AxioCam MRm. For details see Supplementary methods.

2.9 Flow cytometry

hDaNs were treated with 1 µM Staurosporine for 4 h, dissociated and stained with AnnexinV and 7-AAD (BioLegend, #640926) following the manufacturer's instructions. Mean fluorescence was measured in phenol red-free maturation medium using a MACSQuant (Myltenyi Biotec) and corrected for background fluorescence.

2.10 Respiratory analysis

Prior to measuring oxygen consumption rate (OCR) and extracellular acidification rate (ECAR) in a mitochondrial stress test using a Seahorse XF96 Extracellular Flux Analyzer (Agilent), hDaNs were treated with 20 µM Mitoxantrone (Arduino et al., 2017) for 2 h prior to the measurement. For details see Supplementary methods.

2.11 Calcium imaging

Cytosolic calcium was imaged using FLUO-4 and mitochondrial matrix calcium by transfection with CMV-Mito4x-jRCaMP1b (Addgene, #127873; (Ashrafi et al., 2020)). Cells were pre-treated with Mitoxantrone and calcium release was triggered using Thapsigargin. For details see Supplementary methods.

2.12 Neurotransmitter transporter uptake assay

For neurotransmitter transporter uptake assay (Molecular Devices, #R8173, Jorgensen, Nielsen et al. 2008), hDaNs at day 22 or 24 of differentiation were treated for either 24 h with 50 µM L-DOPA, 0.5 h with 5 µM ionomycin or 2 h with 20 µM Mitoxantrone in maturation medium. Uptake was measured following manufacturer's instructions in Hank's buffered salt solution for 45 min at 37°C with a 30 sec interval using a SpectraMax M2e plate reader (Molecular devices) and normalized to t=0.

2.13 Dopamine staining and image analysis

hDaNs were stained with Dopamine (1:500, Immusmol, #IS1005), DAT (1:1000, Millipore, #MAB369) and MAP2 and Z-stacks were imaged using Zeiss Imager.Z1 equipped with an ApoTome.2 and an AxioCam MRm. For details see Supplementary methods.

2.14 Measurement of MAO enzyme activity

MAO enzyme activity was measured using a luminescence-based assay on isolated mitochondria and activity of citrate synthase was used as control. For details see Supplementary methods.

2.15 Transcriptomics

High quality RNA was isolated from independent hDaN differentiations as described above, subjected to PolyA enrichment followed by sequencing. For further procedure, see Supplementary methods.

2.16 Statistics

For statistical analyses, GraphPad Prism 9 (9.1.1) was used. Data are presented as mean ± standard deviation (SD) and (log)normal distribution was tested using the Shapiro–Wilk test. Appropriate statistical tests were used as indicated in the figure legends.

3 Results

3.1 Miro1 R272Q has no effect on mitochondrial movement nor Miro1 degradation during mitophagy

We previously established Miro1 R272Q and isogenic control iPSCs (Schwarz et al., 2021) which we differentiated into dopaminergic neurons. They show positive immunofluorescence for neuronal marker MAP2 and dopaminergic marker TH (Figure 1A); approximately 35-40% of MAP2+ cells are TH+ (Supplementary Figure 1B), which is similar to previously reported numbers (Bus et al., 2020, Hartfield et al., 2014, Seibler et al., 2011). We further confirmed expression of hDaN markers in RT-qPCR (Supplementary Figure 1A). To assess whether the mutation alters protein stability and expression, we first tested protein levels of Miro1 and expression of *RHOT1* and *RHOT2*. Miro1 R272Q hDaNs show similar levels of Miro1 protein (Figure 1B) as well as *RHOT1* and *RHOT2* mRNA (Supplementary Figure 1C) compared to isogenic control hDaNs. Because of its role in mitophagy (Lopez-Domenech et al., 2021, Wang et al., 2011), we next assessed Miro1 degradation by inducing mitophagy using the ionophore CCCP. In Miro1 R272Q hDaNs, Miro1 is degraded in a similar fashion as in the isogenic control (Figure 1C). Assessing Mitofusin degradation (Figure 1C) as a proxy of removal of other outer mitochondrial membrane targets, as well as LC3 (Supplementary Figure 1D) for the induction of autophagy, we found no differences between genotypes. To test alterations in mitochondrial movement under basal conditions, we imaged mitochondria in neuronal processes labelled with MitoTracker green. Analysis of derived kymographs (Figure 1D) showed no effect in the fractions of stationary, oscillating and anterograde/retrograde moving mitochondria (Figure 1E), as was the distance mitochondria travelled (Figure 1E) and their mean speed (Figure 1F). In summary, the heterozygous Miro1 R272Q mutation is not sufficient to affect Miro1 steady state protein levels, its degradation or mitochondrial movement.

3.2 Miro1 R272Q induces mitochondrial fragmentation and changes to cristae organization

Because R272Q lies in the first calcium-sensing domain and Miro1 calcium sensing was previously linked to mitochondrial morphology (Nemani et al., 2018, Saotome et al., 2008), we labelled mitochondria with MitoTracker green (Figure 2A) and analyzed mitochondrial morphology. Mitochondria in Miro1 R272Q hDaNs are significantly smaller and more fragmented compared to the isogenic control (Figure 2B). Notably, this did not result in a change of Tom20 protein levels (Figure 2C) which we assessed as a proxy of mitochondrial mass. Because Miro1 contributes to maintaining mitochondrial cristae structure (Modi et al., 2019), we assessed ultrastructure using electron microscopy. Compared to the isogenic control, mitochondria of Miro1 R272Q hDaNs had notably less cristae showing sections devoid of cristae altogether. (Figure 2D). Blinded quantification of mitochondria with disrupted cristae shows that their number is significantly increased in Miro1 R272Q hDaNs (Figure 2E). Notably, the total amount of mitochondria was also increased (Supplementary Figure 1E). These findings indicate that morphological changes observed in Miro1 R272Q mitochondria might compensate for alterations in ultrastructure and do not affect the integrity of the mitochondrial outer membrane. To assess consequences of this phenotype, we next tested mitochondrial turnover using pMitoTimer (Hernandez et al., 2013) which relies on shifting from green to red fluorescence. In Miro1 R272Q hDaNs, the ratio between red and green is significantly decreased (Figure 2F) indicating an upregulation of mitochondrial turnover. Next, we treated hDaNs for 4 h with 1 µM Staurosporine to test whether Miro1 R272Q hDaNs are more susceptible to apoptosis. Staining with apoptotic marker Annexin V and necrotic marker 7-AAD revealed that Staurosporine significantly increases apoptosis in Miro1 R272Q, but not in isogenic control hDaNs without a concomitant increase in necrosis (Figure 2G). Taken together, Miro1 R272Q changes in mitochondrial ultrastructure trigger compensatory increase in mitochondrial turnover and heighten sensitivity to apoptosis. Although this might not be sufficient to cause PD, it burdens hDaNs and renders them more susceptible for other contributing factors for the pathogenesis of PD.

3.3 Miro1 R272Q disrupts calcium uptake into mitochondria and calcium buffering

To assess whether changes in mitochondrial structure might be linked to altered calcium dynamics, we assessed calcium handling in hDaNs. We labelled cytosolic calcium using FLUO-4 and triggered calcium release from the ER with 5 µM Thapsigargin under chelation of extracellular calcium. To link the cytosolic calcium response to mitochondrial calcium buffering, hDaNs were treated with 2 µM Mitoxantrone (Arduino et al., 2017) to specifically inhibit the mitochondrial calcium uniporter (MCU). In Miro1 R272Q hDaNs, thapsigargin elicits a higher cytosolic calcium response while buffering is initiated later compared to isogenic control. While blocking the MCU only mildly affects the calcium response in isogenic control hDaNs, it reverses the phenotype in Miro1 R272Q (Figure 3A left graph). Notably, Miro1 R272Q only affects the magnitude of the cytosolic calcium response, not however, the slope of the increase or decrease (Figure 3A right graph). To better understand the role of Miro1 in mitochondrial calcium uptake upon Thapsigargin-mediated calcium release, we knocked down Miro1 in SH-SY5Y neuroblastoma cells (Schwarz and Fitzgerald, 2022). Cytosolic calcium was monitored using FLUO4 and mitochondrial matrix calcium was monitored using the genetically encoded calcium indicator CMV-mito-jRCaMP1b (Ashrafi et al., 2020) after treatment for 2 h with 10 µM Mitoxantrone. Reduction of Miro1 protein levels in SH-SY5Y only mildly decreases the cytosolic calcium response to Thapsigargin and blocking the MCU using Mitoxantrone does not change this effect (Figure 3B left graph). However, decreasing Miro1 protein levels increases mitochondrial calcium uptake upon Thapsigargin treatment (Figure 3B right graph). MCU treatment does delay mitochondrial calcium uptake in the control and reverses the phenotype in Miro1 knock-down (Figure 3B right graph). Taken together, we confirm previous findings that Miro1 modulates mitochondrial calcium uptake with the MCU (Chang et al., 2011, Niescier et al., 2018). In reducing Miro1 levels, we show disinhibition of calcium buffering in SH-SY5Y neuroblastoma cells with a mildly decreased cytosolic calcium response. Because the cytosolic calcium response is increased in Miro1 R272Q hDaNs and the location of the mutation in the first EF-hand domain suggests an effect on Miro1 calcium handling, we hypothesize that R272Q results in a decrease of mitochondrial calcium uptake.

3.4 Miro1 R272Q reduces mitochondrial respiratory capacity and neurotransmitter homeostasis

To test the functional consequences of both the altered mitochondrial structure and calcium handling observed in Miro1 R272Q hDaNs, we first assessed mitochondrial respiration. We tested levels of OXPHOS complexes and found a significant reduction of Complex V (Figure 4A), while Complexes IV and III were unaffected (Supplementary Figure 1F). Analyzing mitochondrial membrane potential using indicator TMRM, we found that the reduction in Complex V in Miro1 R272Q hDaNs does not affect mitochondrial membrane potential (Supplementary Figure 1G). We next measured mitochondrial respiration in a modified stress test; hDaNs were challenged with Oligomycin to inhibit Complex V, CCCP to depolarize mitochondria and Rotenone with Antimycin A to inhibit

Complexes I and III, respectively. To link mitochondrial respiration to mitochondrial calcium, uptake was blocked with 20 µM Mitoxantrone for 2 h and prior to injection of Oligomycin hDaNs were first challenged with 5 µM Ionomycin to deplete mitochondrial calcium with medium as control. Miro1 R272Q hDaNs show an overall reduction of mitochondrial oxygen consumption (Figure 4B), but no compensatory increase in glycolysis indicated by extracellular acidification rate (Supplementary Figure 1H). Our data indicate that this is due to an impaired mitochondrial calcium uptake because depletion of mitochondrial calcium by either ionomycin or Mitoxantrone decreases respiration in isogenic control hDaNs to approximately 58% (Two-way ANOVA, Tukey's multiple comparisons p=0.0316) and 62% (Two-way ANOVA, Tukey's multiple comparisons p=0.0482), respectively (Figure 4C); basal respiration of Miro1 R272Q is reduced to approximately 58%. Miro1 R272Q does respond to both ionomycin and Mitoxantrone treatment, to approximately 32% (Two-way ANOVA, Tukey's multiple comparisons p=0.1687) and 37% (Two-way ANOVA, Tukey's multiple comparisons p=0.2818) of untreated isogenic control, respectively (Figure 4C), but this is due to the heterozygosity of the mutation. Assessing spare respiratory capacity (ability of mitochondria to meet energetic demand), we found no differences between Miro1 R272Q and isogenic control at baseline (Figure 4C). Treatment with Mitoxantrone however increases spare respiratory capacity in isogenic control hDaNs by a factor of approximately 2 (Friedman test with Dunn's multiple comparisons p>0.9999), while the increase in Miro1 R272Q is only approximately 1.4-fold (Friedman test with Dunn's multiple comparisons p>0.9999, Figure 4C). Taken together, these results support our hypothesis that Miro1 R272Q impairs mitochondrial calcium uptake which in turn decreases mitochondrial respiration

To better understand the effects of Miro1 R272Q on hDaNs, we performed transcriptomics (Supplementary Figure 2A). Using unbiased pathway analysis tools revealed neuronal pathways (Supplementary Figures Table 1) which is highlighted by significant RNA expression changes in genes involved in synaptic and plasma membrane signaling (SYT2, DRD2, MAO-A, MAO-B) without significant changes to genes related to Miro1's function related to mitochondrial transport via adaptors and kinesins, as well as mitochondrial calcium handling and quality control (Supplementary Figure 2B). Gene mapping using Qiagen Ingenuity software to visualize changes in specific pathways showed changes to gene expression in dopaminergic presynaptic signaling (Supplementary Figure 2C). We then tested dopamine handling in Miro1 R272Q hDaNs. Neurotransmitter uptake through monoaminergic transporters was decreased under baseline conditions in Miro1 R272Q to approximately 58% (Figure 4D). Treatment with dopamine precursor L-DOPA nor ionomycin significantly affects uptake in either of the hDaN lines (Figure 4D). However, inhibition of mitochondrial calcium uptake by Mitoxantrone inhibits neurotransmitter uptake further in Miro1 R272Q by approximately 34 percentage points (Friedman test with Dunn's multiple comparisons p>0.9999) hDaNs as well as the isogenic control to an approximately similar level of 31% (Friedman test with Dunn's multiple comparisons p=0.0682; Figure 4D). We next used immunofluorescence to assess the distribution of Dopamine and dopamine transporter (DAT) Miro1 R272Q and isogenic control hDaNs (Figure 4E). Overall dopamine levels are unchanged under baseline conditions in Miro1 R272Q, but we found a significant increase in amounts of the dopamine transporter DAT (Figure 4F). Ionomycin treatment does not alter dopamine levels but does reverse DAT levels in Miro1 R272Q (Figure 4F). Exposing hDaNs to dopamine precursor L-DOPA elevates dopamine levels in Miro1 R272Q (Figure 4F). Because previous work showed that monoamine oxidase (MAO)-A activity is sensitive to calcium concentration (Cao et al., 2009), we further assessed dopamine degradation by looking at MAO-A and MAO-B. RNA expression of both was significantly downregulated in Miro1 R272Q neurons (Supplementary Figure 2B). Titration of specific MAO-A and MAO-B inhibitors Clorgyline and Deprenyl, respectively, showed that hDaNs contain mostly MAO-B activity but also MAO-A (Supplementary Figure 3A), which is in line with the presence of both transcripts (Supplementary Figure 2B). In lysates of Miro1 R272Q hDaNs, this leads to reduced MAO-B protein (Figure 4G). Concomitant with this, enzyme activity and MAO-B protein levels in isolated mitochondria are reduced (Supplementary Figure 3B), which matches reduced enzyme at isolated mitochondria (Supplementary Figure 3C). We hypothesize, that the consequences of altered mitochondrial calcium uptake by Miro1 R272Q could affect calcium sensitive, dopamine regulating enzymes at the mitochondrial outer membrane in differentiated dopaminergic neurons. This combined with reduced mitochondrial respiratory capacity may be responsible for the synaptic changes identified by expression profiling.

4 Discussion

Studies on *RHOT1*/Miro1 variants in sporadic PD patients (Berenguer-Escuder et al., 2019, Grossmann et al., 2019) underscored the relevance of Miro1's role in PD although previous studies failed to provide a genetic link (Anvret et al., 2012, Nalls et al., 2019, Saeed, 2018). Miro1 acts in well studied biological pathways in PD, interacting with PINK1, Parkin, LRRK2 and α-synuclein (Birsa et al., 2014, Hsieh et al., 2016, Klosowiak et al., 2016, Shaltouki et al., 2018, Wang et al., 2011) and is an important marker of PINK1-Parkin mediated mitophagy and mitochondrial morphogenesis (Hsieh et al., 2019, Konig et al., 2021, Lopez-Domenech et al., 2021). We previously showed that the putative Miro1-PINK1 phosphorylation site Ser156 is important for regulating steady state levels of Miro1 and mitophagy flux (Schwarz and Fitzgerald, 2022) in differentiated cells. In this study the R272Q mutation did not influence Miro1 steady state levels (Figure 1) and had no effect on Miro1 or Mitofusin degradation (Figure 1C) during six-hour treatment of hDaNs with CCCP. These findings are in contrast to Miro1 R272Q Parkinson's disease patient hDaNs, which showed reduced mitochondrial-lysosomal co-localization as a measure of mitophagy compared to healthy hDaNs (Berenguer-Escuder et al., 2019). We cannot rule out that the mutation influences Miro1 retention at the mitochondria with longer treatment or with Antimycin A or Oligomycin treatments that generate reactive oxygen species. It is also not clear whether something else, possibly the genetic background of the PD patient harboring the Miro1 R272Q variant could be driving additional biological burden. It will be interesting to see whether our observations can be replicated in gene corrected R272Q patient hDaN models and whether gene edited Miro1 R272Q animals display neurodegeneration, specifically of dopaminergic neurons in the *substantia nigra*. We hypothesized that the Miro1 R272Q mutation could be relevant in calcium-related Miro1 functions such as mitochondrial positioning because of its location within a calcium binding domain.

Work in primary hippocampal neurons proved that Miro1's calcium sensing properties are necessary for mitochondrial positioning at synapses (Macaskill et al., 2009b) which drives presynaptic Ca^{2+} signals during homeostatic plasticity (Vaccaro et al., 2017). In this study, the Miro1 R272Q point mutation was found to have no influence on mitochondrial movement throughout neurites (Figure 1D-F). Neuronal-specific Miro1 knockout in mice showed that Miro1 is not required for calcium-regulated mitochondrial movement but found reduced retrograde mitochondrial transport in axons and upper motor neuron development (Nguyen et al., 2014). Stephan and colleagues reported that Miro1 regulates intracellular calcium signaling through astrocyte-neuron interactions (Stephen et al., 2015). In this context it would be interesting to investigate heterozygous Miro1 PD variants in mouse or organoid models.

In contrast to work in Miro1 knockout mice (Nguyen et al., 2014), we found that the Miro1 R272Q point mutation reduced basal respiration of dopaminergic neurons (Figure 4B and C) and caused significant mitochondrial fragmentation (Figure 2B). In line with evidence from Miro1 knockout studies in mice and mouse-derived neurons, our study reports that Miro1 R272Q does not impact critical mitochondrial functions such as mitochondrial membrane potential (Supplementary Figure 1G). Instead, the mitochondrial phenotype appears to compensate for reduced respiration tied to calcium deregulation at the mitochondrial outer membrane (Figure 2 A and B). Mitochondrial compensation involves fragmentation (Figure 2B) and reorganization of cristae (Figure 2 D and E). Previous studies showed lack of Miro1 EF-hand affects mitochondrial morphology (Saotome et al., 2008) and that Miro1 associates with the MICOS complex to maintain cristae structure (Modi et al., 2019). It is possible that Miro1 R272Q-induced depletion of ATP5A levels shown here (Figure 4A) trigger changes to the mitochondrial cristae since ATP synthase promotes curvature at cristae rims (Mukherjee et al., 2021). However, in electron microscopy images shown here, sections of unaffected lamellar cristae are still visible in addition to empty parts of the organelle (Figure 2D), which would argue in favor of MICOS involvement. Interestingly, we did detect significantly reduced *CHCHD2* expression (Supplementary Figure 2B; mutations in *CHCHD2* are reported in PD in the Japanese population (Funayama et al., 2015)) but not for other members of the CHCHD family important for cristae architecture. We concluded that Miro1 R272Q likely disrupts calcium sensing at the mitochondrial outer membrane, which will lead to reduced calcium stimulated respiratory flexibility. We suggest that this could induce further mitochondrial compensation via failure to properly engage the MCU. Calcium entry via the MCU preserves energy synthesis when the electron transport chain is impaired (Balderas et al., 2022).

We link disruption of Miro1 interaction with the MCU to regulation of mitochondrial calcium buffering. A previous study found that Miro1 interacts with MCU to modulate mitochondrial calcium uptake (Niescier et al., 2018) and we suggest that Miro1 is upstream of MCU. While MCU is regulated by MICU1 in the inner mitochondrial membrane by sensing matrix calcium (Mallilankaraman et al., 2012), we hypothesize that Miro1 senses cytosolic calcium to modulate uptake via the MCU, which has been shown to bind calcium with a very high affinity (Kirichok et al., 2004). This hypothesis is supported by our finding, that Miro1 R272Q does not affect mitochondrial membrane potential (Supplementary Figure 1G), which is a main driving force for MCU-mediated calcium uptake (Santo-Domingo and Demaurex, 2010). Miro1 R272Q dampens the capacity of mitochondria to buffer changes in cytosolic calcium affecting mitochondrial respiratory capacity as well as dopamine handling and synaptic signaling. A recent study tied mitochondrial calcium uptake to tuning of oxidative phosphorylation in neurons to meet the increase in energetic demand during synaptic activity (Ashrafi et al., 2020). Our data points to significant impact of the R272Q mutation on synaptic and dopaminergic function. We show less catecholamine neurotransmitter uptake in R272Q hDaNs (Figure 4D) despite more DAT (Figure 4 E and F). Since we observed normal distribution of dopaminergic markers (Figure 1A, Supplementary Figure 1A and B) and dopamine (Figure 4 E and F) in both neuronal lines, we investigated whether dopamine degradation at the mitochondrial outer membrane could provide further evidence for the Miro1 R272Q calcium phenotype in PD. Significantly down-regulated MAO gene expression (Supplementary Figure 2B), protein levels (Figure 4G, Supplementary Figure 3C) and activity (Supplementary Figure 3B) are in line with recent work suggesting that MAO activity stimulates mitochondrial respiration to support the bio-energetic demands of phasic dopamine release (Graves et al., 2020). Interestingly, calcium regulates the anchoring of MAO at the mitochondrial surface, promoting the catalytic activity of MAO-A but not MAO-B (Ramsay and Albreht, 2021). In our study, both MAO-A and MAO-B are expressed in hDaNs (Supplementary Figure 2B), yet inhibitor titration suggests that MAO-B activity is dominant (Supplementary Figure 3A). Further work is therefore needed to understand the stoichiometry of MAOs in Miro1 loss-of-function models and whether Miro1 interacts directly with MAOs at the mitochondrial outer membrane.

5 Conflict of interest

The authors declare that the research was conducted in the absence of any commercial or financial relationships that could be construed as a potential conflict of interest.

6 Author contributions

Conceptualization: J.C.F.; Methodology: L.S., L.D.D., L.R., N.C; Software: L.D.D.; Validation: L.S., L.D.D., L.R.; Formal analysis: L.S., L.D.D., L.R., J.C.F., N.C; Investigation: L.S., L.D.D., L.R.; Resources: J.C.F., P.F-B., N.C; Data Curation: L.S., L.D.D., L.R., P.F-B., N.C; Writing – Original Draft: L.S., J.C.F.; Writing – Review & Editing: L.S., J.C.F.; Visualization: L.S.; Supervision: J.C.F.; Project administration: J.C.F.; Funding acquisition: J.C.F.

7 Funding

This study was funded by the Deutsche Forschungsgemeinschaft (DFG, German Research Foundation) Research Training Group MOMbrane 654651/GRK2364. NGS sequencing methods were performed with the support of the DFG-funded NGS Competence Center Tübingen (INST 37/1049-1).

8 Acknowledgements

The authors wish to thank Katja Schach, a student at The University of Tübingen for help in fixation of hDaNs and preparation of samples for electron microscopy. We also thank Gabriele Frommer-Kästle (Insitute of Pathology, University of Tübingen) for embedding and cutting the electron microscopy samples. We are extremely grateful to Jaime de Juan-Sanz (ICM – Paris Brain Institute) for kindly providing mitochondrial calcium constructs. The authors would like to thank Karan Sharma (University of Tübingen) for help in critically reviewing the manuscript.

9 Supplementary Material

Supplementary Figures and Supplementary methods.

10 Data Availability Statement

Not applicable.

11 References

ANVRET, A., RAN, C., WESTERLUND, M., SYDOW, O., WILLOWS, T., OLSON, L., GALTER, D. & BELIN, A. C. 2012. Genetic Screening of the Mitochondrial Rho GTPases MIRO1 and MIRO2 in Parkinson's Disease. *The open neurology journal,* 6**,** 1-5.

ARDUINO, D. M., WETTMARSHAUSEN, J., VAIS, H., NAVAS-NAVARRO, P., CHENG, Y., LEIMPEK, A., MA, Z., DELRIO-LORENZO, A., GIORDANO, A., GARCIA-PEREZ, C., MEDARD, G., KUSTER, B., GARCIA-SANCHO, J., MOKRANJAC, D., FOSKETT, J. K., ALONSO, M. T. & PEROCCHI, F. 2017. Systematic Identification of MCU Modulators by Orthogonal Interspecies Chemical Screening. *Mol Cell,* 67**,** 711-723 e7.

ASHRAFI, G., DE JUAN-SANZ, J., FARRELL, R. J. & RYAN, T. A. 2020. Molecular Tuning of the Axonal Mitochondrial Ca(2+) Uniporter Ensures Metabolic Flexibility of Neurotransmission. *Neuron,* 105**,** 678-687 e5.

BALDERAS, E., EBERHARDT, D. R., LEE, S., PLEINIS, J. M., SOMMAKIA, S., BALYNAS, A. M., YIN, X., PARKER, M. C., MAGUIRE, C. T., CHO, S., SZULIK, M. W., BAKHTINA, A., BIA, R. D., FRIEDERICH, M. W., LOCKE, T. M., VAN HOVE, J. L. K., DRAKOS, S. G., SANCAK, Y., TRISTANI-FIROUZI, M., FRANKLIN, S., RODAN, A. R. & CHAUDHURI, D. 2022. Mitochondrial calcium uniporter stabilization preserves energetic homeostasis during Complex I impairment. *Nat Commun,* 13**,** 2769.

BERENGUER-ESCUDER, C., GROSSMANN, D., ANTONY, P., ARENA, G., WASNER, K., MASSART, F., JARAZO, J., WALTER, J., SCHWAMBORN, J. C., GRUNEWALD, A. & KRUGER, R. 2020. Impaired mitochondrial-endoplasmic reticulum interaction and mitophagy in Miro1-mutant neurons in Parkinson's disease. *Hum Mol Genet,* 29**,** 1353-1364.

BERENGUER-ESCUDER, C., GROSSMANN, D., MASSART, F., ANTONY, P., BURBULLA, L. F., GLAAB, E., IMHOFF, S., TRINH, J., SEIBLER, P., GRUNEWALD, A. & KRUGER, R. 2019. Variants in Miro1 Cause Alterations of ER-Mitochondria Contact Sites in Fibroblasts from Parkinson's Disease Patients. *J Clin Med,* 8.

BIRSA, N., NORKETT, R., WAUER, T., MEVISSEN, T. E., WU, H. C., FOLTYNIE, T., BHATIA, K., HIRST, W. D., KOMANDER, D., PLUN-FAVREAU, H. & KITTLER, J. T. 2014. Lysine 27 ubiquitination of the mitochondrial transport protein Miro is dependent on serine 65 of the Parkin ubiquitin ligase. *J Biol Chem,* 289**,** 14569-82.

BUS, C., ZIZMARE, L., FELDKAEMPER, M., GEISLER, S., ZARANI, M., SCHAEDLER, A., KLOSE, F., ADMARD, J., MAGEEAN, C. J., ARENA, G., FALLIER-BECKER, P., UGUN-KLUSEK, A., MARUSZCZAK, K. K., KAPOLOU, K., SCHMID, B., RAPAPORT, D., UEFFING, M., CASADEI, N., KRUGER, R., GASSER, T., VOGT WEISENHORN, D. M., KAHLE, P. J., TRAUTWEIN, C., GLOECKNER, C. J. & FITZGERALD, J. C. 2020. Human Dopaminergic Neurons Lacking PINK1 Exhibit Disrupted Dopamine Metabolism Related to Vitamin B6 Co-Factors. *iScience,* 23**,** 101797.

CAO, X., LI, X. M. & MOUSSEAU, D. D. 2009. Calcium alters monoamine oxidase-A parameters in human cerebellar and rat glial C6 cell extracts: possible influence by distinct signalling pathways. *Life Sci,* 85**,** 262-8.

CHANG, K. T., NIESCIER, R. F. & MIN, K. T. 2011. Mitochondrial matrix Ca2+ as an intrinsic signal regulating mitochondrial motility in axons. *Proc Natl Acad Sci U S A,* 108**,** 15456-61.

FRANSSON, A., RUUSALA, A. & ASPENSTROM, P. 2003. Atypical Rho GTPases have roles in mitochondrial homeostasis and apoptosis. *J Biol Chem,* 278**,** 6495-502.

FRANSSON, S., RUUSALA, A. & ASPENSTROM, P. 2006. The atypical Rho GTPases Miro-1 and Miro-2 have essential roles in mitochondrial trafficking. *Biochem Biophys Res Commun,* 344**,** 500-10.

FUNAYAMA, M., OHE, K., AMO, T., FURUYA, N., YAMAGUCHI, J., SAIKI, S., LI, Y., OGAKI, K., ANDO, M., YOSHINO, H., TOMIYAMA, H., NISHIOKA, K., HASEGAWA, K., SAIKI, H., SATAKE, W., MOGUSHI, K., SASAKI, R., KOKUBO, Y., KUZUHARA, S., TODA, T., MIZUNO, Y., UCHIYAMA, Y., OHNO, K. & HATTORI, N. 2015. CHCHD2 mutations in autosomal dominant late-onset Parkinson's disease: a genome-wide linkage and sequencing study. *The Lancet Neurology,* 14**,** 274-282.

GRAVES, S. M., XIE, Z., STOUT, K. A., ZAMPESE, E., BURBULLA, L. F., SHIH, J. C., KONDAPALLI, J., PATRIARCHI, T., TIAN, L., BRICHTA, L., GREENGARD, P., KRAINC, D., SCHUMACKER, P. T. & SURMEIER, D. J. 2020. Dopamine metabolism by a monoamine oxidase mitochondrial shuttle activates the electron transport chain. *Nat Neurosci,* 23**,** 15-20.

GROSSMANN, D., BERENGUER-ESCUDER, C., BELLET, M. E., SCHEIBNER, D., BOHLER, J., MASSART, F., RAPAPORT, D., SKUPIN, A., FOUQUIER D'HEROUEL, A., SHARMA, M., GHELFI, J., RAKOVIC, A., LICHTNER, P., ANTONY, P., GLAAB, E., MAY, P., DIMMER, K. S., FITZGERALD, J. C., GRUNEWALD, A. & KRUGER, R. 2019. Mutations in RHOT1 Disrupt Endoplasmic Reticulum-Mitochondria Contact Sites Interfering with Calcium Homeostasis and Mitochondrial Dynamics in Parkinson's Disease. *Antioxid Redox Signal,* 31**,** 1213-1234.

HARTFIELD, E. M., YAMASAKI-MANN, M., RIBEIRO FERNANDES, H. J., VOWLES, J., JAMES, W. S., COWLEY, S. A. & WADE-MARTINS, R. 2014. Physiological Characterisation of Human iPS-Derived Dopaminergic Neurons. *PLOS ONE,* 9**,** e87388.

HERNANDEZ, G., THORNTON, C., STOTLAND, A., LUI, D., SIN, J., RAMIL, J., MAGEE, N., ANDRES, A., QUARATO, G., CARREIRA, R. S., SAYEN, M. R., WOLKOWICZ, R. & GOTTLIEB, R. A. 2013. MitoTimer: a novel tool for monitoring mitochondrial turnover. *Autophagy,* 9**,** 1852-61.

HSIEH, C. H., LI, L., VANHAUWAERT, R., NGUYEN, K. T., DAVIS, M. D., BU, G., WSZOLEK, Z. K. & WANG, X. 2019. Miro1 Marks Parkinson's Disease Subset and Miro1 Reducer Rescues Neuron Loss in Parkinson's Models. *Cell Metab,* 30**,** 1131-1140 e7.

HSIEH, C. H., SHALTOUKI, A., GONZALEZ, A. E., BETTENCOURT DA CRUZ, A., BURBULLA, L. F., ST LAWRENCE, E., SCHULE, B., KRAINC, D., PALMER, T. D. & WANG, X. 2016. Functional Impairment in Miro Degradation and Mitophagy Is a Shared Feature in Familial and Sporadic Parkinson's Disease. *Cell Stem Cell,* 19**,** 709-724.

KIRICHOK, Y., KRAPIVINSKY, G. & CLAPHAM, D. E. 2004. The mitochondrial calcium uniporter is a highly selective ion channel. *Nature,* 427**,** 360-364.

KLOSOWIAK, J. L., PARK, S., SMITH, K. P., FRENCH, M. E., FOCIA, P. J., FREYMANN, D. M. & RICE, S. E. 2016. Structural insights into Parkin substrate lysine targeting from minimal Miro substrates. *Sci Rep,* 6**,** 33019.

KONIG, T., NOLTE, H., AALTONEN, M. J., TATSUTA, T., KROLS, M., STROH, T., LANGER, T. & MCBRIDE, H. M. 2021. MIROs and DRP1 drive mitochondrial-derived vesicle biogenesis and promote quality control. *Nat Cell Biol,* 23**,** 1271-1286.

LOPEZ-DOMENECH, G., HIGGS, N. F., VACCARO, V., ROS, H., ARANCIBIA-CARCAMO, I. L., MACASKILL, A. F. & KITTLER, J. T. 2016. Loss of Dendritic Complexity Precedes Neurodegeneration in a Mouse Model with Disrupted Mitochondrial Distribution in Mature Dendrites. *Cell Rep,* 17**,** 317-327.

LOPEZ-DOMENECH, G., HOWDEN, J. H., COVILL-COOKE, C., MORFILL, C., PATEL, J. V., BURLI, R., CROWTHER, D., BIRSA, N., BRANDON, N. J. & KITTLER, J. T. 2021. Loss of neuronal Miro1 disrupts mitophagy and induces hyperactivation of the integrated stress response. *EMBO J,* 40**,** e100715.

MACASKILL, A. F., BRICKLEY, K., STEPHENSON, F. A. & KITTLER, J. T. 2009a. GTPase dependent recruitment of Grif-1 by Miro1 regulates mitochondrial trafficking in hippocampal neurons. *Mol Cell Neurosci,* 40**,** 301-12.

MACASKILL, A. F., RINHOLM, J. E., TWELVETREES, A. E., ARANCIBIA-CARCAMO, I. L., MUIR, J., FRANSSON, A., ASPENSTROM, P., ATTWELL, D. & KITTLER, J. T. 2009b. Miro1 is a calcium sensor for glutamate receptor-dependent localization of mitochondria at synapses. *Neuron,* 61**,** 541-55.

MALLILANKARAMAN, K., DOONAN, P., CARDENAS, C., CHANDRAMOORTHY, H. C., MULLER, M., MILLER, R., HOFFMAN, N. E., GANDHIRAJAN, R. K., MOLGO, J., BIRNBAUM, M. J., ROTHBERG, B. S., MAK, D. O., FOSKETT, J. K. & MADESH, M. 2012. MICU1 is an essential gatekeeper for MCU-mediated mitochondrial Ca(2+) uptake that regulates cell survival. *Cell,* 151**,** 630-44.

MERRILL, R. A., FLIPPO, K. H. & STRACK, S. 2017. Measuring Mitochondrial Shape with ImageJ. *Techniques to Investigate Mitochondrial Function in Neurons.*

MODI, S., LOPEZ-DOMENECH, G., HALFF, E. F., COVILL-COOKE, C., IVANKOVIC, D., MELANDRI, D., ARANCIBIA-CARCAMO, I. L., BURDEN, J. J., LOWE, A. R. & KITTLER, J. T. 2019. Miro clusters regulate ER-mitochondria contact sites and link cristae organization to the mitochondrial transport machinery. *Nat Commun,* 10**,** 4399.

MUKHERJEE, I., GHOSH, M. & MEINECKE, M. 2021. MICOS and the mitochondrial inner membrane morphology - when things get out of shape. *FEBS Lett,* 595**,** 1159-1183.

NALLS, M. A., BLAUWENDRAAT, C., VALLERGA, C. L., HEILBRON, K., BANDRES-CIGA, S., CHANG, D., TAN, M., KIA, D. A., NOYCE, A. J., XUE, A., BRAS, J., YOUNG, E., VON COELLN, R., SIMÓN-SÁNCHEZ, J., SCHULTE, C., SHARMA, M., KROHN, L., PIHLSTRØM, L., SIITONEN, A., IWAKI, H., LEONARD, H., FAGHRI, F., GIBBS, J. R., HERNANDEZ, D. G., SCHOLZ, S. W., BOTIA, J. A., MARTINEZ, M., CORVOL, J.-C., LESAGE, S., JANKOVIC, J., SHULMAN, L. M., SUTHERLAND, M., TIENARI, P., MAJAMAA, K., TOFT, M., ANDREASSEN, O. A., BANGALE, T., BRICE, A., YANG, J., GAN-OR, Z., GASSER, T., HEUTINK, P., SHULMAN, J. M., WOOD, N. W., HINDS, D. A., HARDY, J. A., MORRIS, H. R., GRATTEN, J., VISSCHER, P. M., GRAHAM, R. R., SINGLETON, A. B., ANDME RESEARCH, T., SYSTEM GENOMICS OF PARKINSON'S DISEASE, C. & INTERNATIONAL PARKINSON'S DISEASE GENOMICS, C. 2019. Identification of novel risk loci, causal insights, and heritable risk for Parkinson's disease: a meta-analysis of genome-wide association studies. *The Lancet. Neurology,* 18**,** 1091-1102.

NEMANI, N., CARVALHO, E., TOMAR, D., DONG, Z., KETSCHEK, A., BREVES, S. L., JANA, F., WORTH, A. M., HEFFLER, J., PALANIAPPAN, P., TRIPATHI, A., SUBBIAH, R., RIITANO, M. F., SEELAM, A., MANFRED, T., ITOH, K., MENG, S., SESAKI, H., CRAIGEN, W. J., RAJAN, S., SHANMUGHAPRIYA, S., CAPLAN, J., PROSSER, B. L., GILL, D. L., STATHOPULOS, P. B., GALLO, G., CHAN, D. C., MISHRA, P. & MADESH, M. 2018. MIRO-1 Determines Mitochondrial Shape Transition upon GPCR Activation and Ca(2+) Stress. *Cell Rep,* 23**,** 1005-1019.

NGUYEN, T. T., OH, S. S., WEAVER, D., LEWANDOWSKA, A., MAXFIELD, D., SCHULER, M. H., SMITH, N. K., MACFARLANE, J., SAUNDERS, G., PALMER, C. A., DEBATTISTI, V., KOSHIBA, T., PULST, S., FELDMAN, E. L., HAJNOCZKY, G. & SHAW, J. M. 2014. Loss of Miro1-directed mitochondrial movement results in a novel murine model for neuron disease. *Proc Natl Acad Sci U S A,* 111**,** E3631-40.

NIESCIER, R. F., HONG, K., PARK, D. & MIN, K. T. 2018. MCU Interacts with Miro1 to Modulate Mitochondrial Functions in Neurons. *J Neurosci,* 38**,** 4666-4677.

RAMSAY, R. R. & ALBREHT, A. 2021. Questions in the Chemical Enzymology of MAO. *Chemistry,* 3**,** 959-978.

REINHARDT, P., GLATZA, M., HEMMER, K., TSYTSYURA, Y., THIEL, C. S., HOING, S., MORITZ, S., PARGA, J. A., WAGNER, L., BRUDER, J. M., WU, G., SCHMID, B., ROPKE, A., KLINGAUF, J., SCHWAMBORN, J. C., GASSER, T., SCHOLER, H. R. & STERNECKERT, J. 2013. Derivation and expansion using only small molecules of human neural progenitors for neurodegenerative disease modeling. *PLoS One,* 8**,** e59252.

RUSSO, G. J., LOUIE, K., WELLINGTON, A., MACLEOD, G. T., HU, F., PANCHUMARTHI, S. & ZINSMAIER, K. E. 2009. Drosophila Miro is required for both anterograde and retrograde axonal mitochondrial transport. *J Neurosci,* 29**,** 5443-55.

SAEED, M. 2018. Genomic convergence of locus-based GWAS meta-analysis identifies AXIN1 as a novel Parkinson's gene. *Immunogenetics,* 70**,** 563-570.

SANTO-DOMINGO, J. & DEMAUREX, N. 2010. Calcium uptake mechanisms of mitochondria. *Biochim Biophys Acta,* 1797**,** 907-12.

SAOTOME, M., SAFIULINA, D., SZABADKAI, G., DAS, S., FRANSSON, A., ASPENSTROM, P., RIZZUTO, R. & HAJNÓCZKY, G. 2008. Bidirectional Ca2+-dependent control of mitochondrial dynamics by the Miro GTPase. *Proceedings of the National Academy of Sciences of the United States of America,* 105**,** 20728-20733.

SARRAF, S. A., RAMAN, M., GUARANI-PEREIRA, V., SOWA, M. E., HUTTLIN, E. L., GYGI, S. P. & HARPER, J. W. 2013. Landscape of the PARKIN-dependent ubiquitylome in response to mitochondrial depolarization. *Nature,* 496**,** 372-6.

SCHWARZ, L., CASADEI, N. & FITZGERALD, J. C. 2021. Generation of R272Q, S156A and K572R RHOT1/Miro1 point mutations in iPSCs from a healthy individual using FACS-assisted CRISPR/Cas9 genome editing. *Stem Cell Res,* 55**,** 102469.

SCHWARZ, L. & FITZGERALD, J. C. 2022. Steady-State Levels of Miro1 Linked to Phosphorylation at Serine 156 and Mitochondrial Respiration in Dopaminergic Neurons. *Cells,* 11.

SEIBLER, P., GRAZIOTTO, J., JEONG, H., SIMUNOVIC, F., KLEIN, C. & KRAINC, D. 2011. Mitochondrial Parkin recruitment is impaired in neurons derived from mutant PINK1 induced pluripotent stem cells. *J Neurosci,* 31**,** 5970-6.

SHALTOUKI, A., HSIEH, C. H., KIM, M. J. & WANG, X. 2018. Alpha-synuclein delays mitophagy and targeting Miro rescues neuron loss in Parkinson's models. *Acta Neuropathol,* 136**,** 607-620.

STEPHEN, T. L., HIGGS, N. F., SHEEHAN, D. F., AL AWABDH, S., LOPEZ-DOMENECH, G., ARANCIBIA-CARCAMO, I. L. & KITTLER, J. T. 2015. Miro1 Regulates Activity-Driven Positioning of Mitochondria within Astrocytic Processes Apposed to Synapses to Regulate Intracellular Calcium Signaling. *J Neurosci,* 35**,** 15996-6011.

VACCARO, V., DEVINE, M. J., HIGGS, N. F. & KITTLER, J. T. 2017. Miro1-dependent mitochondrial positioning drives the rescaling of presynaptic Ca2+ signals during homeostatic plasticity. *EMBO Rep,* 18**,** 231-240.

WANG, X. & SCHWARZ, T. L. 2009. The mechanism of Ca2+ -dependent regulation of kinesin-mediated mitochondrial motility. *Cell,* 136**,** 163-74.

WANG, X., WINTER, D., ASHRAFI, G., SCHLEHE, J., WONG, Y. L., SELKOE, D., RICE, S., STEEN, J., LAVOIE, M. J. & SCHWARZ, T. L. 2011. PINK1 and Parkin target Miro for phosphorylation and degradation to arrest mitochondrial motility. *Cell,* 147**,** 893-906.

WEIHOFEN, A., THOMAS, K. J., OSTASZEWSKI, B. L., COOKSON, M. R. & SELKOE, D. J. 2009. Pink1 forms a multiprotein complex with Miro and Milton, linking Pink1 function to mitochondrial trafficking. *Biochemistry,* 48**,** 2045-52.

12 Figures

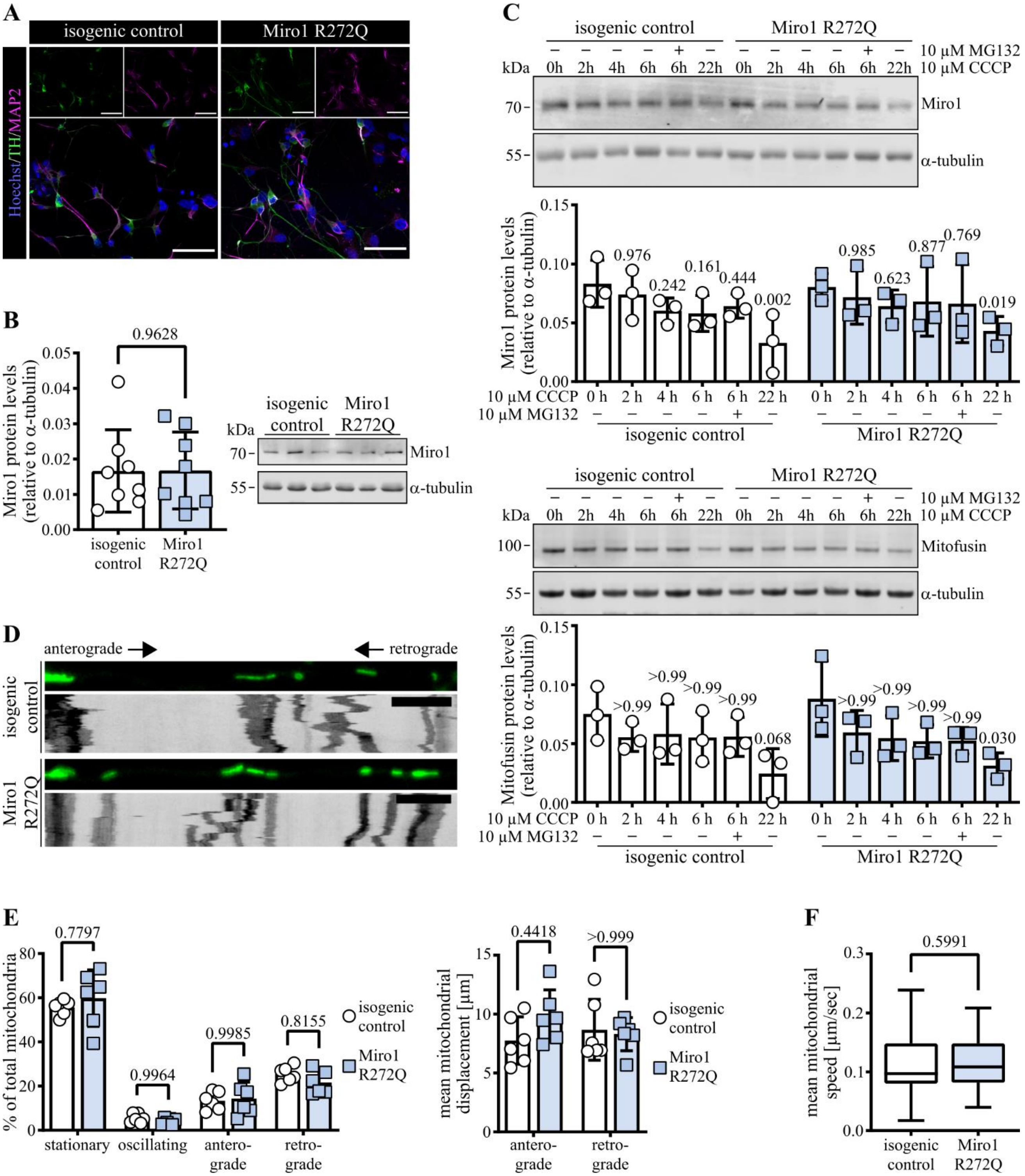

Figure 1: Miro1 R272Q does not change mitochondrial movement or Miro1 degradation upon CCCP-induced mitophagy. (A) Representative image of hDaNs stained with neuronal marker MAP2 and dopaminergic marker TH; n_{Diff}=3. Scale bar: 50 μM. **(B)** Miro1 protein levels in hDaN lysates. Representative blot and quantification of intensity of Miro1 bands relative to a-tubulin. n_{Diff}=8, data displayed as mean ± SD; paired t test (two-tailed). **(C)** Miro1 and Mitofusin protein

levels in hDaNs upon induction of mitophagy using 10 µM CCCP for 0/2/4/6 (+ 10 µM MG132)/22h. Representative blot and quantification of intensity of Miro1 and Mitofusin bands relative to a-tubulin. n_{Diff}=3, data displayed as mean ± SD; Miro1: Two-way ANOVA with Tukey's multiple comparisons; Mitofusin: Friedman test with Dunn's multiple comparisons. **(D)** Representative first frame of movie and derived kymograph for movement analysis of hDaNs stained with 100 nM MitoTracker green. Scale bar: 10 µM. **(E)** Kymograph analysis of mitochondrial movement to classify stationary/oscillating/anterograde/retrograde fractions and mean displacement of mitochondria. n_{Diff}=3 (2 datasets per differentiation), data displayed as mean ± SD; Fractions: Two-way ANOVA with Šídák's multiple comparisons; Displacement: Friedman test with Dunn's multiple comparisons. **(F)** Mean mitochondrial speed analyzed using TrackMate fiji plugin. n_{Diff}=3 ($n_{Processes}$=60), data displayed as mean ± SD; Mann-Whitney test

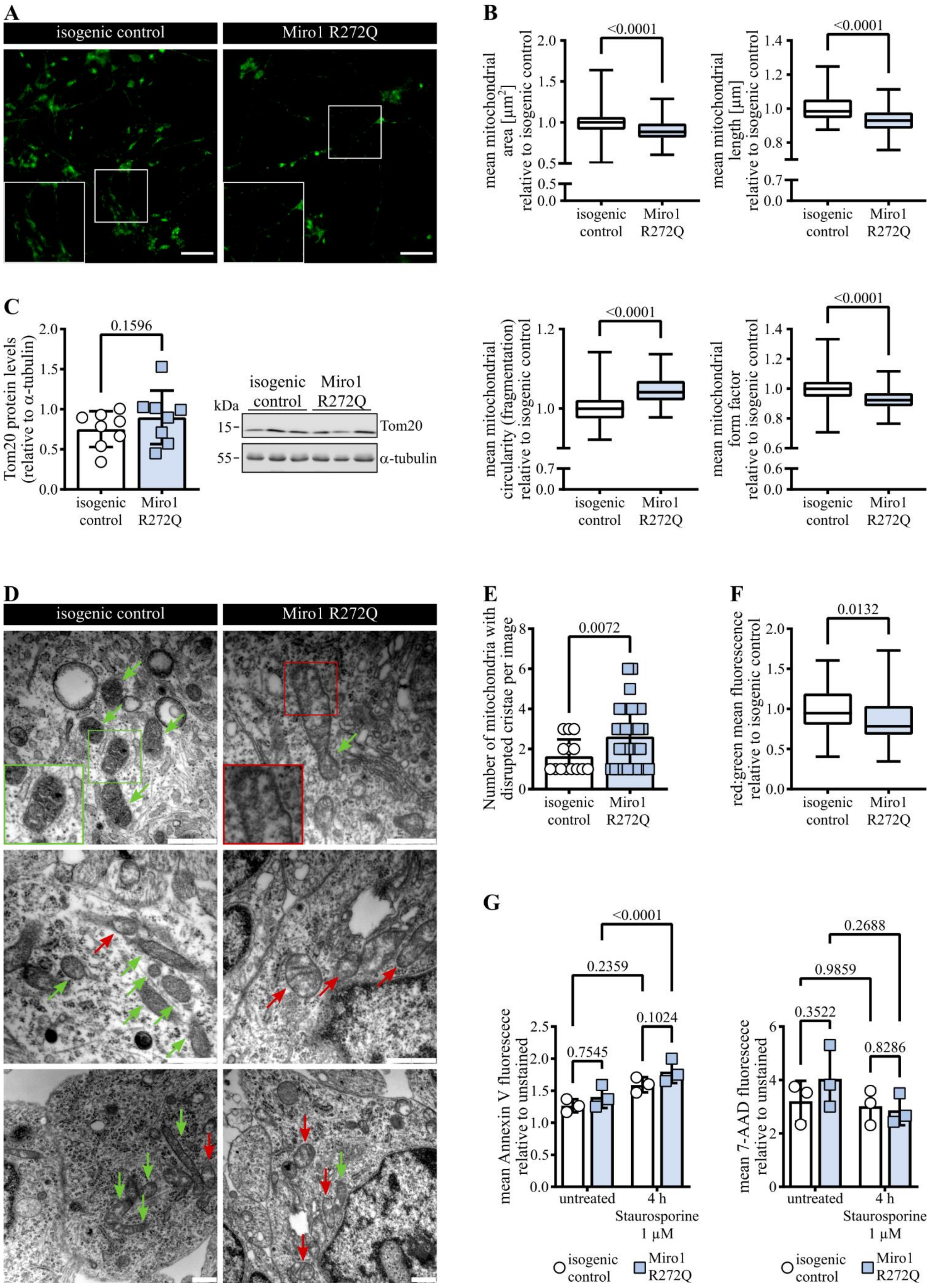
A
isogenic control
Miro1 R272Q
B
<0.0001
mean mitochondrial area [µm²] relative to isogenic control
2.0
1.5
1.0
0.5
0.5
0.0
isogenic control
Miro1 R272Q
<0.0001
mean mitochondrial length [µm] relative to isogenic control
1.4
1.2
1.0
0.8
0.7
0.0
isogenic control
Miro1 R272Q
C
0.1596
Tom20 protein levels (relative to α-tubulin)
2.0
1.5
1.0
0.5
0.0
isogenic control
Miro1 R272Q
kDa
isogenic control
Miro1 R272Q
15
Tom20
55
α-tubulin
<0.0001
mean mitochondrial circularity (fragmentation) relative to isogenic control
1.2
1.0
0.7
0.0
isogenic control
Miro1 R272Q
<0.0001
mean mitochondrial form factor relative to isogenic control
1.4
1.2
1.0
0.8
0.6
0.6
0.0
isogenic control
Miro1 R272Q
D
isogenic control
Miro1 R272Q
E
0.0072
Number of mitochondria with disrupted cristae per image
8
6
4
2
0
isogenic control
Miro1 R272Q
F
0.0132
red:green mean fluorescence relative to isogenic control
2.0
1.5
1.0
0.5
0.0
isogenic control
Miro1 R272Q
G
<0.0001
0.2359
0.7545
0.1024
mean Annexin V fluorescece relative to unstained
2.5
2.0
1.5
1.0
0.5
0.0
untreated
4 h Staurosporine 1 µM
○ isogenic control
□ Miro1 R272Q
0.2688
0.9859
0.3522
0.8286
mean 7-AAD fluorescece relative to unstained
6
4
2
0
untreated
4 h Staurosporine 1 µM
○ isogenic control
□ Miro1 R272Q

Figure 2: Miro1 R272Q alters mitochondrial morphology concomitant with changes in cristae organization. (A) Representative image of hDaNs stained with 100 nM MitoTracker green to label mitochondria for analysis of mitochondrial morphology. Scale bar: 50 µM. **(B)** Analysis of mitochondrial morphology of hDaNs stained with 100 nM MitoTracker green to assess mitochondrial area, length, fragmentation, and form factor. Values of one differentiation normalized to mean of isogenic control of the same differentiation. $n_{Diff}=3$ (20 images per differentiation), data displayed as mean ± SD; Mann-Whitney test. **(C)** Tom20 protein levels in hDaN lysates. Representative blot and quantification of intensity of Tom20 bands relative to a-tubulin. $n_{Diff}=8$, data displayed as mean ± SD; paired t test (two-tailed). **(D)** Representative electron microscopy of hDaNs. Red arrows indicate mitochondria with regions devoid of cristae, green arrows indicate mitochondria with maintained cristae. Scale bar: 500 nm. **(E)** Blinded quantification of mitochondria with disrupted cristae structure per EM image. $n_{Diff}=3$, data displayed as mean ± SD; Welch's t test (two-tailed). **(F)** Assessment of mitochondrial renewal in hDaNs by transfection with pMitoTimer. Quantification of mean red:green fluorescence and normalization of values of one differentiation to mean of isogenic control of the same differentiation. $n_{Diff}=3$ ($n_{images}=42$), data displayed as mean ± SD; Mann-Whitney test. **(G)** Flow cytometric assessment of susceptibility to apoptosis. hDaNs treated for 4 h with 1 µM Staurosporine were stained with apoptotic marker Annexin V and necrotic marker 7-AAD. Mean fluorescence of each channel normalized to unstained signal. $n_{Diff}=3$, data displayed as mean ± SD; Two-way ANOVA with Tukey's multiple comparisons.

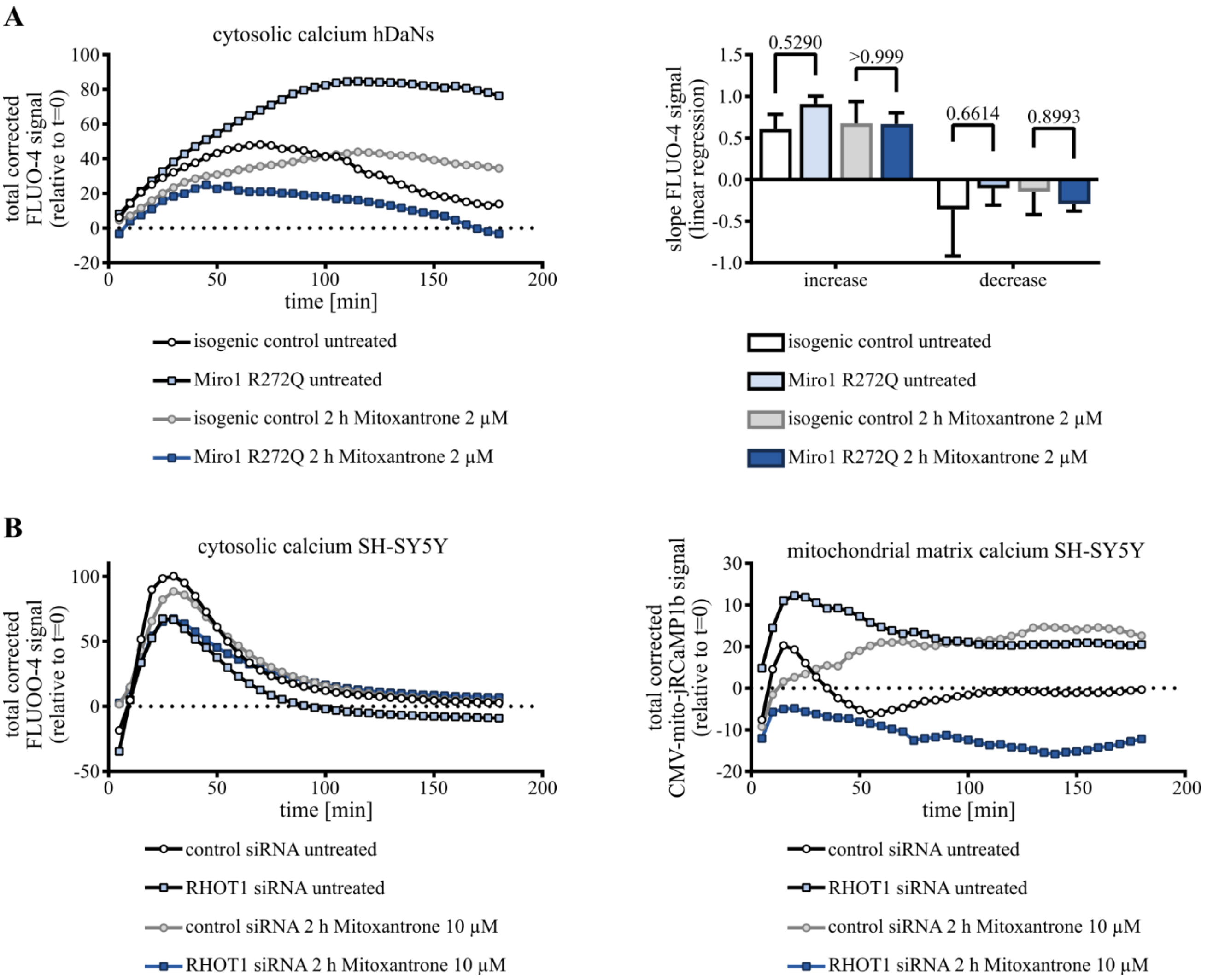

Figure 3: Miro1 R272Q alters calcium dynamics. (A) Cytosolic calcium trace in hDaNs after stimulation with 5 µM Thapsigargin. hDaNs were treated for 2 h with 2 µM Mitoxantrone and stained with cytosolic calcium indicator FLUO-4. Quantification of total corrected FLOU-4 signal and normalized relative to t=0. n_{Diff}=3, data displayed as mean. **(B)** Increasing and decreasing slope of FLUO-4 signal in hDaNs in response to thapsigargin calculated using linear regression. n_{Diff}=3, data displayed as mean ± SD; Two-way ANOVA with Tukey's multiple comparisons. **(C)** Calcium trace in SH-SY5Y after stimulation with 5 µM Thapsigargin. SH-SY5Ys were transfected with non-targeting or RHOT1 siRNA to knock down Miro1. SH-SY5Y were treated for 2 h with 10 µM Mitoxantrone. Cytosolic calcium was indicated using FLUO-4, mitochondrial matrix calcium was indicated by transfection with CMV-Mito4x-jRCaMP1b. Quantification of total corrected signal and normalized relative to t=0. n=2-3, data displayed as mean.

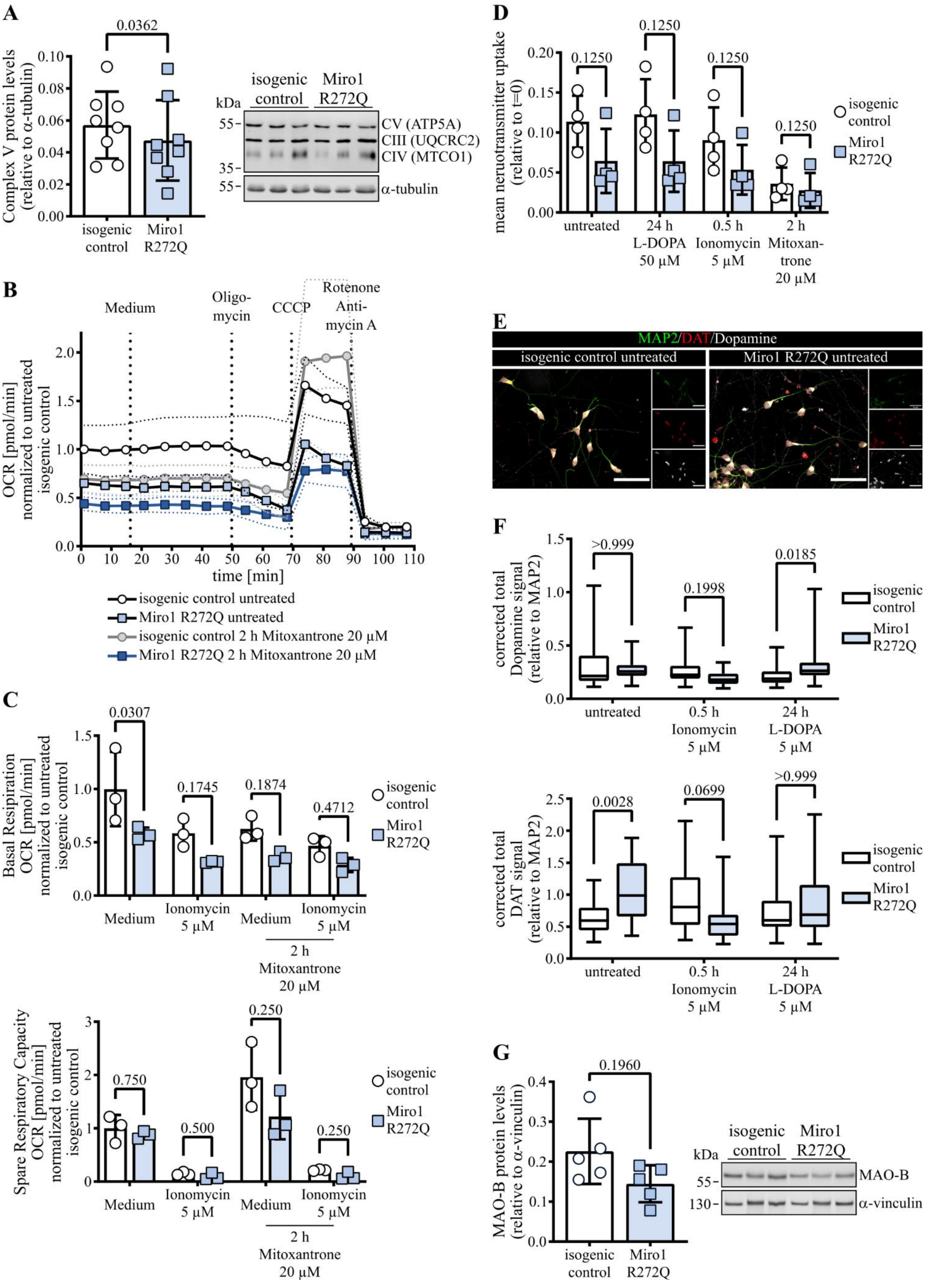
A
0.0362
Complex V protein levels (relative to α-tubulin)
0.10
0.08
0.06
0.04
0.02
0.00
isogenic control
Miro1 R272Q
kDa
55-
35-
55-
CV (ATP5A)
CIII (UQCRC2)
CIV (MTCO1)
α-tubulin
B
Medium
Oligo-mycin
CCCP
Rotenone Anti-mycin A
OCR [pmol/min] normalized to untreated isogenic control
2.0
1.5
1.0
0.5
0.0
0
10
20
30
40
50
60
70
80
90
100
110
time [min]
isogenic control untreated
Miro1 R272Q untreated
isogenic control 2 h Mitoxantrone 20 µM
Miro1 R272Q 2 h Mitoxantrone 20 µM
C
Basal Respiration OCR [pmol/min] normalized to untreated isogenic control
0.0307
0.1745
0.1874
0.4712
1.5
1.0
0.5
0.0
Medium
Ionomycin 5 µM
Medium
Ionomycin 5 µM
2 h Mitoxantrone 20 µM
isogenic control
Miro1 R272Q
Spare Respiratory Capacity OCR [pmol/min] normalized to untreated isogenic control
0.750
0.500
0.250
0.250
3
2
1
0
Medium
Ionomycin 5 µM
Medium
Ionomycin 5 µM
2 h Mitoxantrone 20 µM
isogenic control
Miro1 R272Q
D
mean neruotransmitter uptake (relative to t=0)
0.1250
0.1250
0.1250
0.1250
0.20
0.15
0.10
0.05
0.00
untreated
24 h L-DOPA 50 µM
0.5 h Ionomycin 5 µM
2 h Mitoxan-trone 20 µM
isogenic control
Miro1 R272Q
E
MAP2/DAT/Dopamine
isogenic control untreated
Miro1 R272Q untreated
F
corrected total Dopamine signal (relative to MAP2)
>0.999
0.1998
0.0185
1.5
1.0
0.5
0.0
untreated
0.5 h Ionomycin 5 µM
24 h L-DOPA 5 µM
isogenic control
Miro1 R272Q
corrected total DAT signal (relative to MAP2)
0.0028
0.0699
>0.999
2.5
2.0
1.5
1.0
0.5
0.0
untreated
0.5 h Ionomycin 5 µM
24 h L-DOPA 5 µM
isogenic control
Miro1 R272Q
G
0.1960
MAO-B protein levels (relative to α-vinculin)
0.4
0.3
0.2
0.1
0.0
isogenic control
Miro1 R272Q
kDa
55-
130-
MAO-B
α-vinculin

Figure 4: Impairment of mitochondrial calcium links to mitochondrial respiration and dopamine handling. (A) Complex V protein levels in hDaN lysates. Representative blot showing Complexes V, IV and III and quantification of intensity of Complex V bands relative to a-tubulin. n_{Diff}=8, data displayed as mean ± SD; paired t test (two-tailed). **(B)** Respiratory analysis of hDaNs treated 2 h with 20 µM Mitoxantrone. Injection of medium, Oligomycin, CCCP and Rotenone with Antimycin A as indicated. Oxygen consumption rate was normalized to number of cells seeded and to mean of t=0 in isogenic control. n_{Diff}=3, data displayed as mean ± SD. **(C)** Basal respiration and spare respiratory capacity in response to injection of either medium or 5 µM ionomycin in hDaNs treated 2 h with 20 µM Mitoxantrone calculated from respiratory analysis. n_{Diff}=3, data displayed as mean ± SD; basal respiration: Two-way ANOVA with Šídák's multiple comparisons; spare respiratory capacity: Wilcoxon matched-pairs signed rank test with two-stage linear step-up procedure of Benjamini, Krieger and Yekutieli. **(D)** Neurotransmitter transporter uptake assay. hDaNs were treated either for 24 h with 50 µM L-DOPA, for 30 min with 5 µM Ionomycin or for 2 h with 20 µM Mitoxantrone. Slopes was calculated from uptake normalized to t=0. n_{Diff}=3, data displayed as mean ± SD; Wilcoxon matched-pairs signed rank test with two-stage linear step-up procedure of Benjamini, Krieger and Yekutieli. **(E)** Representative image of untreated hDaNs stained with Dopamine, DAT and MAP2. n_{Diff}=3. Scale bar: 50 µM. **(F)** Quantification of corrected total Dopamine and DAT fluorescence normalized to MAP2. hDaNs were treated either for 30 min with 5 µM Ionomycin or for 24 h with 5 µM L-DOPA. n_{Diff}=3 (n_{images}=30), data displayed as mean ± SD; Kruskal-Wallis with Dunn's multiple comparisons. **(G)** MAO-B protein levels in hDaN lysates. Representative blot and quantification of intensity of MAO-B bands relative to a-vinculin. n_{Diff}=5, data displayed as mean ± SD; paired t test (two-tailed).

Supplementary Figures

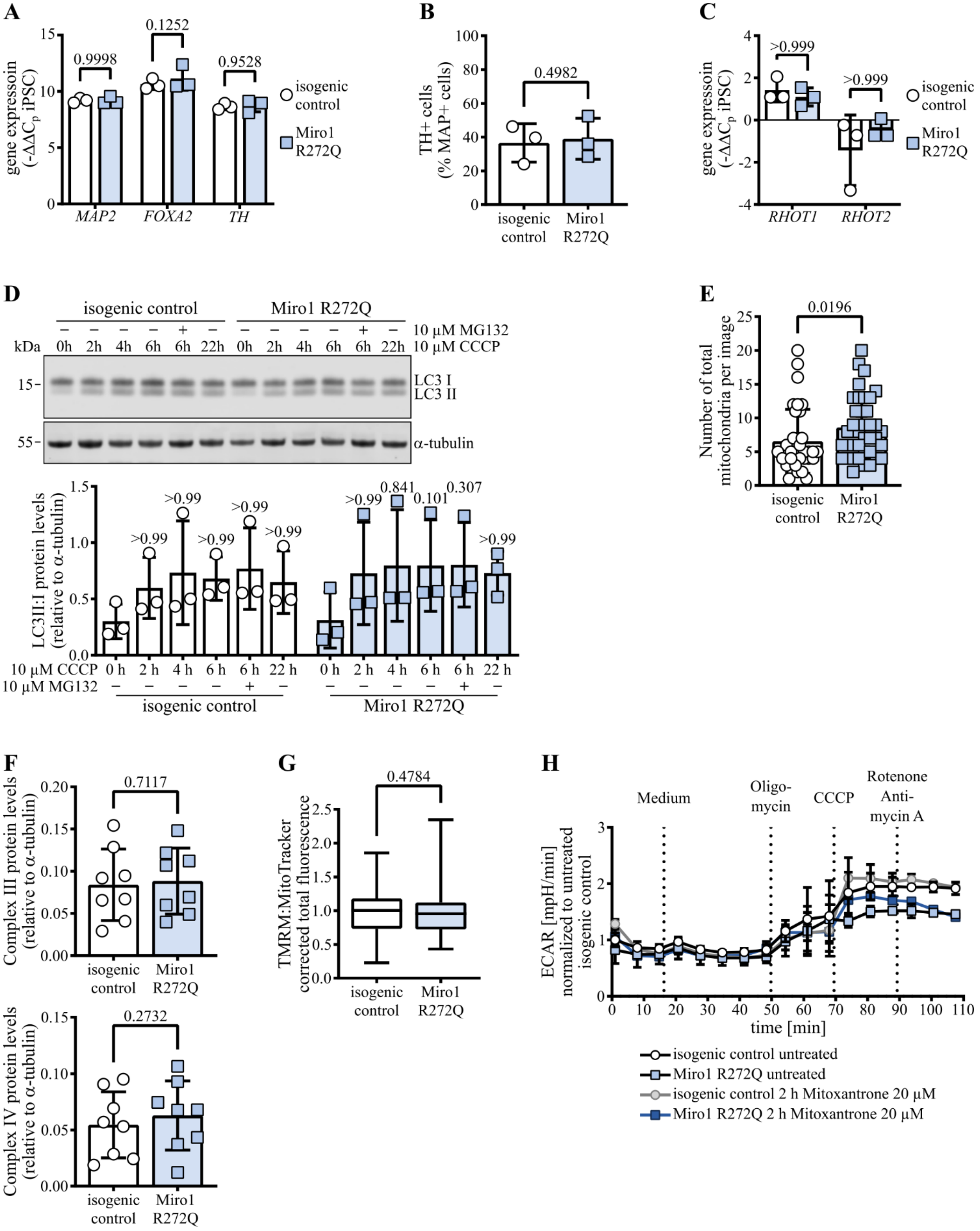

Supplementary Figure 1: **(A)** Analysis of gene expression of hDaN markers MAP2, FoxA2 and TH using RT-qPCR. Calculation of -$\Delta\Delta C_t$ relative to iPSCs. n_{Diff}=3, data displayed as mean ± SD; Two-way ANOVA with Šídák's multiple comparisons. **(B)** Quantification of MAP+ and TH+ cells to assess percentage of TH+ cells. n_{Diff}=3, data displayed as mean ± SD; paired t test (two-tailed). **(C)** Analysis of gene expression of RHOT1 and RHOT2 using RT-qPCR. Calculation of -$\Delta\Delta C_t$ relative to iPSCs. n_{Diff}=3, data displayed as mean ± SD; Friedman test with Dunn's multiple comparisons. **(D)** Ratio of LC3II to LC3I protein levels in hDaNs upon induction of mitophagy using 10 µM CCCP for 0/2/4/6 (+ 10 µM MG132)/22h. Representative blot and quantification of intensity of LC3II/I bands relative to α-tubulin. n_{Diff}=3, data displayed as mean ± SD; Friedman test with Dunn's multiple comparisons. **(E)** Blinded quantification of mitochondria total mitochondria per EM image. nDiff=3, data displayed as mean ± SD; Mann-Whitney test. **(F)** Complex III/IV protein levels in hDaN lysates. Quantification of intensity of Complex III/IV bands relative to α-tubulin. n_{Diff}=8, data displayed as mean ± SD; paired t test (two-tailed). **(G)** Image analysis of mitochondrial membrane potential. hDaNs stained with 25 nM TMRM and 100 nM MitoTracker green. Quantification of corrected total fluorescence of TMRM:MitoTracker green. Normalization of values of one differentiation to mean of isogenic control of the same differentiation. n_{Diff}=3 (n_{images}=60), data displayed as mean ± SD; Mann-Whitney test. **(H)** Extracellular acidification rate measured during respiratory analysis. Injection of medium, Oligomycin, CCCP and Rotenone with Antimycin A as indicated. Oxygen consumption rate was normalized to number of cells seeded and to mean of t=0 in isogenic control. n_{Diff}=3, data displayed as mean ± SD.

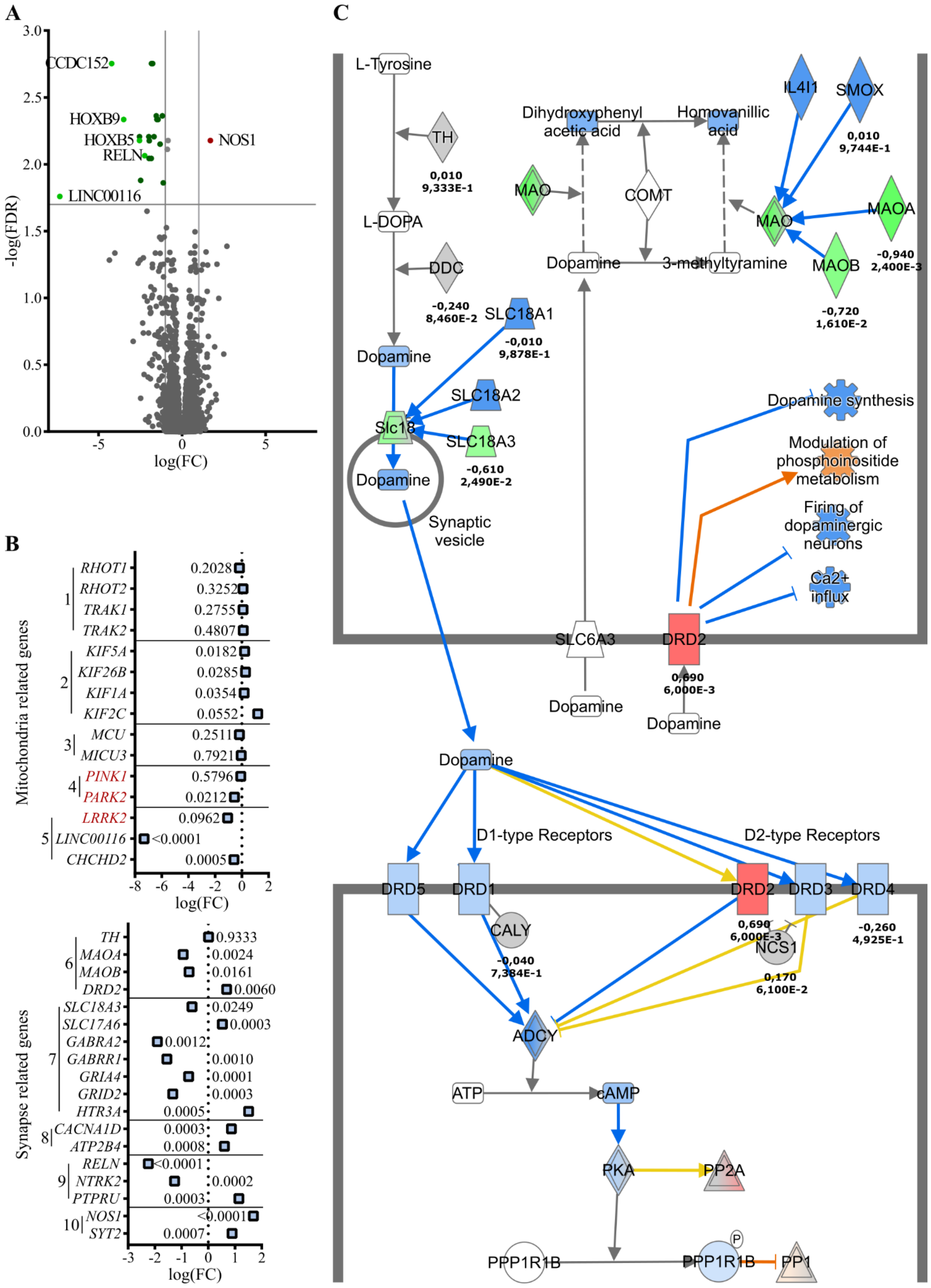
A
3.0
2.5
2.0
1.5
1.0
0.5
0.0
-log(FDR)
CCDC152
HOXB9
HOXB5
RELN
LINC00116
NOS1
-5
0
5
log(FC)
B
Mitochondria related genes
1
RHOT1
RHOT2
TRAK1
TRAK2
2
KIF5A
KIF26B
KIF1A
KIF2C
3
MCU
MICU3
4
PINK1
PARK2
5
LRRK2
LINC00116
CHCHD2
0.2028
0.3252
0.2755
0.4807
0.0182
0.0285
0.0354
0.0552
0.2511
0.7921
0.5796
0.0212
0.0962
<0.0001
0.0005
-8
-6
-4
-2
0
2
log(FC)
Synapse related genes
6
TH
MAOA
MAOB
DRD2
7
SLC18A3
SLC17A6
GABRA2
GABRR1
GRIA4
GRID2
HTR3A
8
CACNA1D
ATP2B4
9
RELN
NTRK2
PTPRU
10
NOS1
SYT2
0.9333
0.0024
0.0161
0.0060
0.0249
0.0003
0.0012
0.0010
0.0001
0.0003
0.0005
0.0003
0.0008
<0.0001
0.0002
0.0003
<0.0001
0.0007
-3
-2
-1
0
1
2
log(FC)
C
L-Tyrosine
TH
0,010
9,333E-1
L-DOPA
DDC
-0,240
8,460E-2
SLC18A1
-0,010
9,878E-1
Dopamine
SLC18A2
Slc18
SLC18A3
-0,610
2,490E-2
Dopamine
Synaptic vesicle
Dihydroxyphenyl acetic acid
Homovanillic acid
IL4I1
SMOX
0,010
9,744E-1
MAO
COMT
MAO
MAOA
-0,940
2,400E-3
Dopamine
3-methyltyramine
MAOB
-0,720
1,610E-2
Dopamine synthesis
Modulation of phosphoinositide metabolism
Firing of dopaminergic neurons
Ca2+ influx
SLC6A3
DRD2
0,690
6,000E-3
Dopamine
Dopamine
Dopamine
D1-type Receptors
D2-type Receptors
DRD5
DRD1
DRD2
DRD3
DRD4
0,690
6,000E-3
-0,260
4,925E-1
CALY
-0,040
7,384E-1
NCS1
0,170
6,100E-2
ADCY
ATP
cAMP
PKA
PP2A
PPP1R1B
P
PPP1R1B
PP1

Supplementary Figure 2: (A) RNA sequencing of hDaNs. Volcano plot depicting differentially regulated genes in Miro1 R272Q compared to isogenic control. Plotted lines indicate threshold at -log(FDR) = 1.7 and log(FC) = ±1. Red dots indicate upregulation above threshold, green dots indicate downregulation below threshold. n_{Diff}=3; data represents mean**. (B)** Expression of mitochondria and synapse related genes in Miro1 R272Q compared to isogenic control. Genes were grouped according to their function: (1) mitochondrial movement adaptors, (2) kinesins, (3) mitochondrial calcium uptake, (4) Mitochondrial quality control, (5) other mitochondrial functions, (6) dopaminergic neuron signaling, (7) other neurotransmitter-specific signaling, (8) neuronal calcium handling, (9) neuronal development, (10) other neuronal functions. Genes highlighted in red are PD-genes. Data shown as fold change to isogenic control. n_{Diff}=3; data represents mean. **(C)** Ingenuity pathway analysis of differentially regulated genes in Miro1 R272Q compared to isogenic control. Pathways assessed were dopamine receptor signalling in the presynapse and synaptic long-term potentiation.

Supplementary Table 1: GOrilla pathway analysis of differentially regulated genes in Miro1 R272Q compared to isogenic control with $p < 0.05$ as target dataset and all genes detected in the RNA sequencing as background. List of top five results in categories function, process and component.

	GO Term	**Description**	**P-value**	**FDR**
Function	GO:0038023	signaling receptor activity	9.05E-7	3.57E-3
	GO:0060089	molecular transducer activity	1.79E-6	3.53E-3
	GO:0022839	ion gated channel activity	1.84E-6	2.42E-3
	GO:0022836	gated channel activity	3.05E-6	3.01E-3
	GO:0005509	calcium ion binding	7.42E-6	5.85E-3
Component	GO:0031226	intrinsic component of plasma membrane	2.14E-13	3.91E-10
	GO:0044459	plasma membrane part	1.54E-12	1.4E-9
	GO:0005887	integral component of plasma membrane	2.64E-12	1.61E-9
	GO:0031224	intrinsic component of membrane	4.6E-12	2.1E-9
	GO:0044456	synapse part	1.73E-11	6.31E-9
Process	GO:0023052	signaling	1.75E-15	2.41E-11
	GO:0009653	anatomical structure morphogenesis	3.14E-15	2.16E-11
	GO:0007267	cell-cell signaling	7.43E-14	3.41E-10
	GO:0032501	multicellular organismal process	6.78E-13	2.33E-9
	GO:0007155	cell adhesion	7.94E-13	2.19E-9

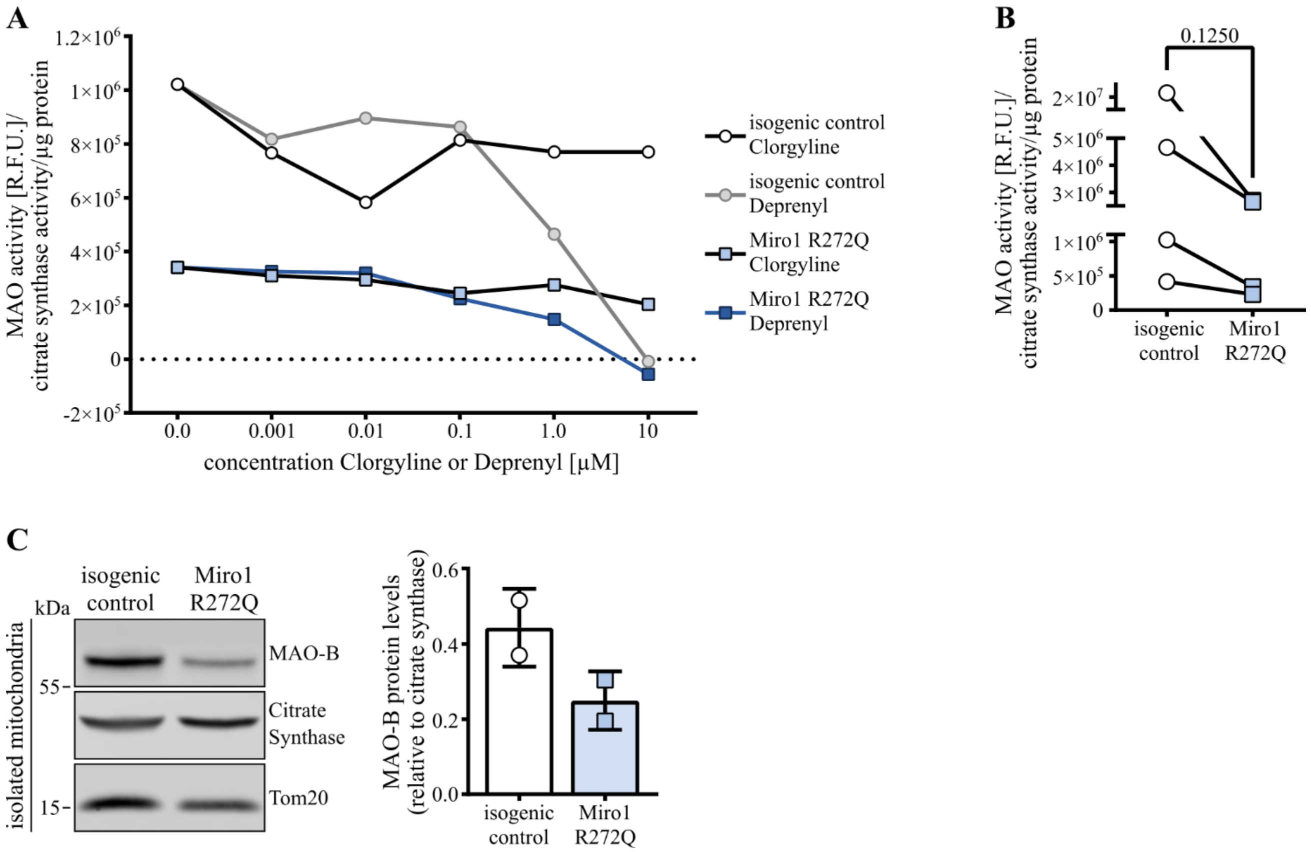

Supplementary Figure 3: (A) Analysis of MAO enzyme activity in mitochondria isolated from isogenic control and Miro1 R272Q hDaNs normalized to citrate synthase enzyme activity. MAO enzyme activity was measured in the presence of MAO-A and MAO-B inhibitors Clorgyline and Deprenyl, respectively, at the indicated concentrations. n_{Diff}=1, data displayed as mean. **(B)** MAO enzyme activity in untreated mitochondria isolated from isogenic control and Miro1 R272Q hDaNs. n_{Diff}=4, data displayed as mean ± SD. Wilcoxon test (two-tailed) **(C)** Representative blot showing MAO-B, citrate synthase and Tom20 in isolated mitochondria used for testing enzyme activity. Quantification of intensity of MAO-B band relative to citrate synthase. n_{Diff}=2, data displayed as mean ± SD.

Supplementary Methods

1 RT-qPCR

Primer sequences are listed in Supplementary Table 1.

Gene	Forward	Reverse
GAPDH	CGAGATCCCTCCAAAATCAAG	GCAGAGATGATGACCCTTTTG
MAP2	CCGTGTGGACCATGGGGCTG	GTCGTCGGGGTGATGCCACG
TH	TGTCTGAGGAGCCTGAGATTCG	GCTTGTCCTTGGCGTCACTG
MAP2	CCGTGTGGACCATGGGGCTG	GTCGTCGGGGTGATGCCACG
FOXA2	CCATGCACTCGGCTTCCAG	TGTTGCTCACGGAGGAGT
RHOT1	TGTCACCCCAGAGAGAGTTC	GCCTGCTGTCTTTGTCTGTT
RHOT2	ATTGAGACCTGCGTGGAGTG	AAGCGTTGAGCTCTTCGTCA

2 Immunofluorescence

hDaNs on Matrigel-coated coverslips were fixed in 4% PFA. For permeabilization for Tom20 staining, hDaNs were incubated 5 min with 0.5% TritonX-100 in PBS at room temperature. After blocking with 10% normal goat serum in wash buffer (0.01% TritonX-100 in PBS), antibodies were diluted in 5% normal goat serum in wash buffer and incubated over-night at 4°C (primary) and 1-2 h at room temperature. Hoechst (Molecular Devices, #H3569) was used to stain nuclei prior to mounting with Dako fluorescent mounting medium (Aligent, #S3023). Z-stacks were taken using a Zeiss Imager.Z1 equipped with an ApoTome.2 and an AxioCam MRm. Representative images of TH/MAP2 staining for characterization were projected with maximum intensity using ZEN software (blue edition, Zeiss) with subsequent adjustment of brightness and contrast. For analysis of TH+ neurons in fiji, z-stacks were projected with maximum intensity and brightness and contrast were adjusted (comparable between images). Counting of MAP+ and TH+ cells was done using cell counter plugin. 10 images were counted per differentiation, (n_{Diff}=3) and sum of MAP+ and TH+ per differentiation was used to calculate percentage TH+ of MAP+ cells; the percentage of one differentiation was used as a data point for statistics.

3 Analysis of mitochondrial movement

Two to four days prior to imaging, 100,000 hDaNs were seeded on Poly-L-Ornithine (PLO, Sigma-Aldrich, #P8638-25MG)-Matrigel double-coated ibidi dishes. For labeling of mitochondria, hDaNs were stained for 7 min at 37°C with 5% CO_2 with 100 nM MitoTracker green (Thermo Fisher Scientific, #M7514). For imaging, medium was replaced with phenol red-free maturation medium and a Leica DMi8 Microscope (40× objective) with the LASX software was used to acquire 61 frames (5 min/5 sec interval). Prior to selection of neurites for analysis, first and last frames were compared to exclude mobile neurites. After cropping, neurites were straightened (Kocsis et al., 1991) with maintenance of movement directionality (anterograde: left to right). For generation of kymographs, time lapses were re-sliced with default settings and then projected with maximum intensity followed by LUT inversion. For classification using displacement into stationary (≤ 2 µm), mobile (> 2 µm), or oscillating (≤ 2 µm and amplitude > 1.5 µm), the Pythagorean theorem was used for calculation. Per differentiation, two data sets were acquired. Per dataset representing one datapoint in the statistical analysis, the sum of all mitochondria analyzed per genotype was used to calculate fractions. Mean mitochondrial speed was measured using fiji-plugin TrackMate (Tinevez et al., 2017) after correcting bleaching with histogram matching and enhancing contrast by 2.5% in all slices. Calibration information was used for TrackMate analysis with LoG detector with an estimated blob diameter of 1 µm with sub-pixel localization and without threshold. Using HyperStack Displayer, automated filtering of spots was applied with manual adjustment where necessary. Particles were tracked using Linear motion LAP tracker searching a radius of 5 µm with a maximum frame gap of 2. Per dataset, 10 timelapses were analyzed, each of which was used as datapoint for statistical analysis.

4 Mitochondrial morphology and membrane potential

Two to three days prior to imaging, 150,000 hDaNs were seeded on Matrigel-coated ibidi dishes. For labeling of mitochondria and indicating mitochondrial membrane potenital, hDaNs were stained for 7 min at 37°C with 5% CO_2 with 100 nM MitoTracker green (Thermo Fisher Scientific, #M7514) and 25 nM Image-iT™ TMRM reagent (Thermo Fisher Scientific, #I34361), respectively. For imaging, medium was replaced with phenol red-free maturation medium and a Leica DMi8 Microscope (40× objective) with the LASX software was used to acquire Z-stacks with a slice interval of 0.88 µm. For analysis in Fiji, stacks of each channel were projected with average intensity and converted to 8-bit greyscale. Prior to generating binary images for the assessing mitochondrial morphology using and adapted protocol (Merrill, Flippo et al. 2017), images were convolved (0 0 −1 0 0/0 −1 −1 −1 0/-1 −1 24 −1 −1/0 −1 −1 −1 0/0 0 −1 0 0) with subsequent subtraction of background using a rolling ball radius of 10 px and unfast enhancement of local contrast with a blocksize of 9 and maximum slope of 4. Next, images were processed with the tubeness tool using sigma = 0.24156 with calibration information followed by despeckling, conversion into 8-bit and thresholding to create a binary image. Measuring area, shape descriptors, perimeter (used to calculate form factor$=\mathrm{perimeter}^2/4\pi\cdot\mathrm{area}$) and fit ellipse of particles bigger than 1.5 px with a circularity of 0-1 was used to calculate the mean of all particles per image for each descriptor which was used as data point in statistics. TMRM corrected total fluorescence (CTF=$\mathrm{IndDen}_{\mathrm{Particle}}$ - ($\mathrm{area}_{\mathrm{Particle}}$ · mean grey $\mathrm{value}_{\mathrm{Background}}$) of each particle measured (bigger than 1.5 px and circularity 0-1) was normalized to MitoTracker green CTF. MitoTracker green binary images, generated by thresholding after subtracting background with a rolling ball radius of 15 px, were used to define the area for measuring area, integrated density and mean grey value of each channel. One datapoint in statistical analysis represents the mean TMRM:MitoTracker green CTF per image.

5 Electron microscopy

Following fixation, samples were washed in 0.1 M Sodium Cacodylate Buffer and further fixed with osmium tetroxide (Sigma Aldrich). Samples were dehydrated by passing through a series of washes with increasing ethanol concentration (50%, 70%, 80%, 90%, 100% Ethanol, 30 min for each concentration). Samples were incubated in propylene oxide/Araldite overnight and then embedded by infiltration of pure Araldite. Semi-thin sections of 350nm were cut first using a Ultracut R-Microtome (Leica Microsystems, Germany) and stained with Richardson-Solution to identify regions of interest. Afterwards, the ultra-thin sections of 60nm were cut for electron microscopy.

6 MitoTimer analysis

For transfection with pMitoTimer plasmid (Addgene, #52659; (Hernandez et al., 2013)) using Fugene HD (Promega, #E2311), according to the manufacturer’s instructions, 80,000 hDaNs per Matrigel-coated glass coverslip were seeded. Two days after transfection cells were fixed with subsequent staining with Tom20 as described above. For acquisition of 14 Z-stacks per differentiation with a slice interval of 0.72 µm and the same exposure times for each channel, a Zeiss Imager.Z1 equipped with an ApoTome.2 and an AxioCam MRm was used. In Fiji, stacks were projected with average intensity followed by conversion to 8-bit greyscale. Binary Tom20 generated by thresholding was used to define the area for measuring mean grey value of particles bigger than 1.5 px with circularity 0-1 of green and red channels. The mean of each channel per image was used to calculate the ratio between red and green representing a datapoint in statistics.

7 Respiratory analysis

Two to five days prior to the experiment 60,000-85,000 hDaNs were seeded into a Seahorse cell plate coated with Matrigel. Respiration was measured in DMEM base medium (without phenol red; Sigma-Aldrich, #D5030 1L) supplemented with 4.5 mg/mL D-Glucose, 0.22 mg/mL pyruvate, and 2 mM glutamine with subsequent injections of (a) medium or5 µM ionomycin, (b) 0.8 µM Oligomycin, (c) 2.7 µM CCCP, and (d) 0.8 µM Rotenone with 4 µM Antimycin A. (a) was measured five times, (b-d) three times. Measurements were normalized to number of hDaNs seeded. Basal respiration after injection of (a) was calculated subtracting mean of measurements after (d) from mean after (a); spare respiratory capacity is the percentage of maximal respiration (mean after (c)-mean after(d)) and basal respiration (last basal measurement-mean (d)).

8 Calcium imaging

Calcium transients were analyzed in hDaN and undifferentiated SH-SY5Y neuroblastoma cells. hDaNs were seeded on PLO-Matrigel and SH-SY5Ys on Collagen. SH-SY5Y were transfected three consecutive days starting four days prior to imaging with non-targeting siRNA (Dharmacon; #D-001206-14-05) or *RHOT1* siRNA (Dharmacon, #M-010365-01-0005) with transfection reagent (Dharmacon, #T-2001-01/T-2004-01) following the manufacturer’s instructions. For imaging of matrix calcium, SH-SY5Y were transfected with CMV-Mito4x-jRCaMP1b (Addgene, #127873; (Ashrafi et al., 2020)) using Fugene HD transfection reagent following the manufacturer’s instructions two days prior to imaging. Prior to imaging, hDaNs and SH-SY5Ys were first treated for 2 h with 2 µM and 10 µM Mitoxantrone, respectively, and for imaging of cytosolic calcium then stained with FLUO-4 (Invitrogen, #F10471) following the manufacturer’s instructions. To chelate extracellular calcium, cells were incubated with 3µM EGTA for 10 min prior to stimulation with an acute injection of 5 µM Thapsigargin. Timelapses were taken under controlled environment (37°C/5% CO2) in phenol red-free maturation medium (hDaN) or maintenance medium (SH-SY5Y) in 5 sec intervals for 3 min using a Leica DMi8 Microscope (40× objective) with the LASX software. Timelapses were then processed, analyzed and measured with Fiji: the frames were segmented into single regions of interest (ROIs) corresponding to cells and the single ROI´s signal intensity measured. The resulting matrix of values, with every column corresponding to a single ROI or cell, and every row to a different frame, was processed through a MATLAB script. The script first normalized the matrix by subtracting the signal intensity corresponding to the background and then also subtracting the signal intensity corresponding to t_0 of every ROI. Second the script partially corrected for desynchronization both intra- and inter-field of views by trying to align the curves following an arbitrary increase in signal intensity that would correspond to the beginning of a calcium transient. The curves generated from the output matrices of the MATLAB script were fitted according to the closest possible model using GraphPad Prism 8.4.0. For the SHSY-5Y model, the rise of the calcium signal was fitted to a linear increase, while the calcium buffering for them was fitted to a one phase exponential decay. For the hDAN model, both the cytosolic calcium increase, and the buffering were fitted to a linear response.

9 Dopamine staining

Two days prior to staining, 50,000 hDaNs were seeded on PLO-Matrigel double-coated glass coverslips. hDaNs were treated for either 24 h with 5 µM L-DOPA or 0.5 h with 5 µM ionomycin before staining using STAINperfect (Immusmol, #SP-A-1000) following manufacturer's instructions (secondary antibodies: Jackson ImmunoResearch, # 103-545-155; Thermo Fisher, A#11077, #A21245) with Hoechst stain for nuclei. For acquisition of 10 Z-stacks per differentiation with a slice interval of 1 µm, fixed exposure times for each channel were used. Images were processed and analyzed in Fiji. First, stacks were projected with average intensity and converted to 8-bit greyscale. For measuring area, mean grey value and integrated density MAP2 channel was used to define a ROI. MAP2 greyscale images were first converted into a binary image by applying thresholding after subtracting background with a rolling ball radius of 25 px, then the binary image was used to create a selection that was applied to greyscale images of all channels for measurement and calculation of CTF. Each image analyzed represents one data point in statistics.

10 Measurement of MAO enzyme activity

For measurement of MAO enzyme activity, a crude mitochondrial preparation from hDaNs was performed. Neurons were washed with PBS before addition of mitochondria isolation buffer () supplemented with protease and phosphatase inhibitors (Millipore Sigma, #11873580001 and Sigma-Aldrich, #4906837001). Detached cells were homogenized by pipetting and subsequent passes through different needle sizes (8x 20G/8x 27G/8x 30G). After centrifugation for 5 min at 1000 xg at 4°C, supernatant was saved and pellet was resuspended in mitochondria isolation buffer and further homogenized by eight passes through a 30G needle. After for 5 min at 1000 xg at 4°C, supernatant was pooled with previous one (pellet was discarded) and centrifuged for 15 min at 10,000 xg at 4°C. The supernatant (cytosolic fraction) was saved and the pellet (mitochondrial fraction) resuspended in MAO assay buffer (100 mM HEPES, 5% Glycerol, protease and phosphatase inhibitors). After measuring protein concentration using Bradford, 45-100 µg protein of mitochondrial fraction were used for measurement of MAO enzyme activity with MAO-Glo assay (Promega, #V1401; (Valley et al., 2006) following the manufacturer's instructions using MAO-B reaction buffer. To assess specificity of the assay, inhibitors Clorgyline (abcam, #ab145646) and Deprenyl (abcam, #ab120604) were added to the assay in concentrations of 0.001/0.01/0.1/1/10 µM. As negative control, the enzyme activity was measured without enzyme. Chemiluminescence was measured after incubation with the detection reagent for 30 min at room temperature using a FLUOstar OMEGA (BMG Labtech). Obtained values were background corrected using the negative control and for amount of protein used. As a control experiment, citrate synthase activity was measured (Shepherd and Garland, 1969). 10 µg protein (isolated mitochondria) was mixed with assay buffer (100 mM Tris pH 8.0, 0.1% TritonX-100), 10 µM Acetyl-CoA and 200 µM DTNB (freshly dissolved in water). Reaction was started by addition of 20 µM Oxaloacetate (freshly dissolved in water) or assay buffer as reference and measured at room temperature for 10 min with a 30 sec interval at 412 nm using a SpectraMax M2e plate reader (Molecular devices). Each value was normalized to t=0 prior to calculation of the slope, which was normalized to amount of protein used for the assay.

11 Transcriptomics

RNA quality from three independent hDaN differentiations was assessed with an Agilent 2100 Bioanalyzer and the Agilent RNA 6000 Nano kit (Agilent). Samples with very high RNA integrity number were selected for library construction. For polyA enrichment, total RNA was subjected to polyA enrichment and cDNA libraries were constructed using the resulting mRNA and the NEBNext Ultra II Directional RNA Library Prep Kit (New England BioLabs). Libraries were sequenced on a NextSeq500 (Illumina) with a depth of >25 million reads each. Library preparation and sequencing procedures were performed by the same individual and a design aimed to minimize technical batch effects was chosen. Read quality of RNA-seq data in fastq files was assessed using QoRTs to identify sequencing cycles with low average quality, adaptor contamination, or repetitive sequences from PCR amplification. Reads were aligned using STAR allowing gapped alignments to account for splicing against a custom-built genome composed of the Ensembl Homo Sapiens GRCh37 and Alignment quality was analyzed using samtools and visually inspected in the Integrative Genome Viewer. Normalized read counts for all genes were obtained using Subread and edgeR. EdgeR uses an exact test for the negative binomial distribution, which has strong parallels with Fisher's exact test, to compute exact *p* values that can be used to assess differential expression. Transcripts covered with less than 1 count-per-million in at least 1 sample were excluded from the analysis for determining differential expression in each of the pair-wise comparisons between experimental groups. For depicting the results in a volcano plot, differentially regulated transcripts were added to a GraphPad Prism file and -log(FDR) and log(FC) values were used as y and x values, respectively. As threshold (indicated in graph by line), a -log(FDR) of 1.7 and log(FC) of ±1 were chosen; values above both thresholds were considered as up- and downregulated and labelled with red and green dots, respectively. Targeted pathway analysis using Qiagen software Ingenuity was performed on the pathways dopamine receptor signalling and synaptic long term potentiation. For Gorilla pathway analysis (Eden et al., 2007, Eden et al., 2009) all differentially regulated genes with $p < 0.5$ were chosen as target dataset and all detected genes as background dataset. The generation of *p* values by the Gorilla pathway algorithm is described in Eden et al., 2009. The top five results in the categories function, process and component were used for the figure. For displaying of mitochondria related and synapse related genes, we plotted the selected genes on the y axis and their corresponding log(FC) on the x axis. *P* values indicate difference between isogenic control and Miro1 R272Q. We provide the list of transcripts (CTRL versus Miro1 R272Q) ranked by LogFC and significance, which was used to run the Gorilla pathway analysis in Supplementary Table 1.

12 References

ASHRAFI, G., DE JUAN-SANZ, J., FARRELL, R. J. & RYAN, T. A. 2020. Molecular Tuning of the Axonal Mitochondrial Ca(2+) Uniporter Ensures Metabolic Flexibility of Neurotransmission. *Neuron,* 105**,** 678-687 e5.

EDEN, E., LIPSON, D., YOGEV, S. & YAKHINI, Z. 2007. Discovering motifs in ranked lists of DNA sequences. *PLoS Comput Biol,* 3**,** e39.

EDEN, E., NAVON, R., STEINFELD, I., LIPSON, D. & YAKHINI, Z. 2009. GOrilla: a tool for discovery and visualization of enriched GO terms in ranked gene lists. *BMC Bioinformatics,* 10**,** 48.

HERNANDEZ, G., THORNTON, C., STOTLAND, A., LUI, D., SIN, J., RAMIL, J., MAGEE, N., ANDRES, A., QUARATO, G., CARREIRA, R. S., SAYEN, M. R., WOLKOWICZ, R. &

GOTTLIEB, R. A. 2013. MitoTimer: a novel tool for monitoring mitochondrial turnover. *Autophagy,* 9**,** 1852-61.

KOCSIS, E., TRUS, B. L., STEER, C. J., BISHER, M. E. & STEVEN, A. C. 1991. Image averaging of flexible fibrous macromolecules: The clathrin triskelion has an elastic proximal segment. *Journal of Structural Biology,* 107**,** 6-14.

SHEPHERD, D. & GARLAND, P. B. 1969. The kinetic properties of citrate synthase from rat liver mitochondria. *Biochemical Journal,* 114**,** 597-610.

TINEVEZ, J. Y., PERRY, N., SCHINDELIN, J., HOOPES, G. M., REYNOLDS, G. D., LAPLANTINE, E., BEDNAREK, S. Y., SHORTE, S. L. & ELICEIRI, K. W. 2017. TrackMate: An open and extensible platform for single-particle tracking. *Methods,* 115**,** 80-90.

VALLEY, M. P., ZHOU, W., HAWKINS, E. M., SHULTZ, J., CALI, J. J., WORZELLA, T., BERNAD, L., GOOD, T., GOOD, D., RISS, T. L., KLAUBERT, D. H. & WOOD, K. V. 2006. A bioluminescent assay for monoamine oxidase activity. *Anal Biochem,* 359**,** 238-46.